OPTIMISATION OF STORAGE RINGS AND RF ACCELERATORS VIA ADVANCED OPTICAL FIBRE-BASED DETECTORS

Thesis submitted in accordance with the requirements of the University of Liverpool for the degree of Doctor in Philosophy by

Maria Kastriotou

May 2018

ABSTRACT

In particle accelerators, diverse causes may lead to the unwanted deviation of the beam particles from the nominal beam orbit and their loss in the machine. To protect from dangerous beam losses and provide valuable information on the accelerator operation, Beam Loss Monitors (BLMs) are being employed. Conventional BLMs are localised detectors, with a wide range of characteristics, depending on which, the appropriate monitor for each application is selected. The optical fibre BLM is an alternative type of detector, used and examined in various facilities for its ability to cover and effectively protect long parts (of the order of 100 m) of an accelerator.

The Compact Linear Collider (CLIC) is a proposal for a future $e^- - e^+$ collider, based on the simultaneous operation of two parallel beam lines, aiming to reach a 3 TeV center of mass energy at approximately 48 km of machine length.

In the present work an optical fibre based detector was developed, consisting of a quartz optical fibre coupled with an Silicon Photon Multiplier (SiPM), to be studied as a beam loss monitor for RF accelerators, such as CLIC, and storage rings. A dedicated housing was fabricated for the photosensor and the related electronics, which optimised the system in terms of sensitivity, low noise and robustness. Instead of the most commonly used, for such detectors, Photo Multiplier Tubes (PMTs), this study made use of the SiPMs taking advantage of their insensitivity to magnetic fields and their efficiency in terms of cost and required power.

The developed system was characterised for its capabilities as a BLM in the CLIC Test Facility 3 (CTF3) and in the Australian Synchrotron Light Source (ASLS). A remarkable intrinsic time resolution of 260 ps was measured, and a discrimination in beam losses with a 25 cm spacing between them was demonstrated for single bunch beams. For 350 ns long electron beams, in order to distinguish simultaneous beam losses on different locations, a distance of 3 m between them was required. The ability of the detector to monitor steady state losses was validated, and a method to assess all beam loss locations utilising only one initially identified, was demonstrated. The limitations introduced to BLMs from the beam loss crosstalk effect in parallel beam lines was investigated, while the sensitivity limitations induced by the RF cavity electron field emission background were estimated as not significant. The optical fibre based detector, combined with appropriate localised detectors at high risk locations, was proven a promising system for the monitoring of beam losses, for both linear accelerators and storage rings.

Finally, a modified, highly sensitive version of the detector was introduced as an advanced RF cavity diagnostics tool. This was proven able of monitoring RF breakdowns and field emitted electrons along with estimating the Fowler-Nordheim field enhancement factor. Additionally, both measurements and simulations confirmed the presence of high energy electrons in the radiation environment of accelerating structures due to electron field emission.

ACKNOWLEDGEMENTS

The present thesis is the outcome of the influence, contribution, advice and support of numerous people within the past years. It is a pleasure to thank all those who made it possible.

I would like to thank my University of Liverpool supervisor Prof. Carsten P. Welsch, for offering me the opportunity to perform this work under his valuable guidance and become a member of the QUASAR Group and the Cockcroft Institute. I owe my deepest gratitude to Eduardo Nebot del Busto, for trusting me to work with him in one of the most prestigious research institutions in the world, and for the invaluable knowledge and experience I gained and the support I received under his close supervision. I would also like to acknowledge Eva Barbara Holzer for the fruitful discussions and the encouragement offered.

I am grateful to Thibaut Lefevre, for his generous advices and insightful comments. I warmly thank Mark Boland for the sterling opportunity and pleasure of collaborating with him at the Australian Synchrotron Light Source, from which I have greatly benefited. I would like to also thank Walter Wuensch, who introduced me to the RF community, which was to me a source of great interest and knowledge.

I would like to thank all my colleagues at the CERN BE-BI-BL section, with whom I enjoyed both working and having coffee. I am indebted to Ewald Effinger, William Viganó, Steve Fernando de Sousa, Raymond Tissier and Christiane Schillinger for their kind availability, their help with hardware and electronics and for teaching me how to solder.

I am particularly grateful to Davide Gamba, Jose Luis Navarro Quirante, Frank Tecker, Theodoros Argyropoulos, Alberto Degiovanni, Ben Woolley, for their generous support in the experiments performed in CTF3 and XBOX-2 and for all the illuminating discussions. I would like to extend these thanks to Roberto Corsini, Steffen Doebert, Wilfrid Farabolini and Piotr Skowronski for their constructive comments and contribution in the conduction of the CLEX experiments, and to all the CTF3 colleagues and operators. A deep thank you to all the colleagues and operators of the Australian Synchrotron Light Source, and especially to Noel Basten, Tom Lucas, Paul Giansiracusa and Steve Martin, for their invaluable support in the installation and the conduction of the experiments and their warm welcome in Melbourne.

I appreciate the feedback of the QUASARs Mark Ibison, James Hunt, Joseph Wolfenden and Lee Robert Carver, who reviewed parts of this thesis. A special thanks to Miguel Abreu Fernandes, for always having an answer to all my University related questions.

I am grateful towards the very good friends that have encouraged me during the last few years, and especially towards Anastasios Mangelis, Vivian Anastasiou, Vassia Vardakastani and Nikos Fountoulakis, with whom we have continuously shared the troublesome moments of writing as well as the joyful breaks. For all the nice times we have spent together since I arrived in Geneva, I would like to thank Philippe Schoofs and David Martin Clavo. I acknowledge Philippe for also providing me his thesis template. A warm thank you to Andreas Alexopoulos and Pablo Fernandez Martinez, for being both great colleagues and supportive friends.

I am deeply thankful and appreciative towards my extended family, with whom we share all our happy and hard moments and who have been a great source of confidence throughout

these years. My late father, Michalis, and grandparents, Dimitris and Evdoxia, influenced me in the most constructive way, teaching me the values of integrity, patience and persistence. I try to follow their path every day. Above all I would like to thank my mother, Eva. Everything I have achieved is a result of her boundless encouragement and care.

My husband and best friend, Eleftherios Skordis, transformed this challenging trip into the most interesting and delightful adventure. He has always been to me a true example of scientific thinking, my strongest support and greatest comfort. Thank you for our enlightening discussions, for our home, and for sharing with me the greatest gift of all. This thesis is dedicated to my Lily.

AUTHOR'S CONTRIBUTION

Next are listed the contributions of the author for this study, indicating when this was accomplished with the help of other people, and which parts of the project were entirely developed by other people.

Chapter 3 describes the development of the photosensing modules for an optical fibre beam loss monitoring system. The readout board for the SiPM was designed and optimised by Fernando Steve Domingues Sousa and Dr Eduardo Nebot del Busto. The low pass filters and the RF shielded modules and chassis were designed by the author, with the help and advice of William Viganó.

In Chapter 4 the study of the Optical fibre BLM (OBLM) system at the ASLS and the Test Beam Line (TBL) is presented. All measurements were performed together with E. Nebot del Busto as well as the intrinsic time resolution analysis. The ASLS measurements were also performed with the invaluable help of M. J. Boland and the ASLS mockup in MATLAB is a work of D. Zhu. The signal analysis for the different loss scenarios for single- and multi-bunch losses was studied by the author.

In Chapter 5, the OBLM measurements at the ASLS and the preliminary analysis of the losses during the full machine cycle were carried together with E. Nebot del Busto and M. J. Boland, and the final analysis was performed by the author. The case of steady state losses was studied by the author. The crosstalk measurements at the Two Beam Module (TBM) and the analysis of the acquired data was performed by the author.

The analysis of the electron field emission and RF breakdown data described in Chapter 6 was performed by the author. The simulations exploring the optical photon generation in quartz and the RF cavity radiation environment were carried out by the author, with consultation from E. Skordis. The measurements at XBOX2 were carried out by the author with the help of T. Argyropoulos and B. Wooley. The analysis for the Fowler-Nordheim plots was performed by the author.

The optical fibres tested in the scope of this thesis were selected and purchased by S. Mallows and E. Nebot del Busto (ASLS). The electronics and shielded modules used were built by the author.

CONTENTS

CONTENTS ix

LIST OF FIGURES xiii

LIST OF TABLES xvii

INTRODUCTION 1

1 ACCELERATORS AND EXPERIMENTAL FACILITIES 3

1.1 | Introduction 3

1.2 | A short overview of particle accelerators 4

1.3 | Synchrotrons and Storage Rings 5

1.3.1 | Main Principles 5

1.3.2 | Synchrotron Radiation 6

1.3.3 | CERN 7

1.4 | Linear Colliders 10

1.4.1 | Main Principles 10

1.4.2 | The CLIC Project 10

1.5 | High gradient RF cavities 14

1.5.1 | Electron Field Emission 14

1.5.2 | RF Breakdown 16

1.5.3 | The CLIC Main Linac accelerating structure 17

1.6 | Experimental Facilities 19

1.6.1 | The CLIC Test Facility 3 (CTF3) 19

1.6.2 | The Australian Synchrotron Light Source (ASLS) 22

2 BEAM LOSS MONITORING 25

2.1 | Introduction 25

2.2 | Beam Losses 26

2.2.1 | Regular beam losses 27

2.2.2 | Irregular losses 28

2.3 | BLM Physics 29

2.3.1 | Electromagnetic interactions of ionising radiation with matter 29

2.3.2 | Mechanism for generation of secondary particles 33

2.4 | Beam Loss Monitors 35
2.4.1 | Ionisation Chambers 35
2.4.2 | PIN diode BLMs 37
2.4.3 | Secondary Emission Based BLMs 38
2.4.4 | Scintillation Detectors 40
2.5 | Summary 41

3 Optical fibre Based Detectors 43
3.1 | Theoretical Background 43
3.1.1 | Refractive index and Total Reflection of Light 43
3.1.2 | Cherenkov effect 44
3.2 | Optical fibres 46
3.2.1 | Optical Fibre Principles 47
3.2.2 | Optical Fibre Characteristics 49
3.3 | Photosensors 54
3.3.1 | Silicon Photon Multiplier (SiPM) 55
3.3.2 | Photo Multiplier Tube (PMT) 59
3.4 | An advanced optical fibre detector 61
3.4.1 | System characteristics 61
3.4.2 | A novel system design 67

4 Position Resolution Studies of Distributed BLMs 71
4.1 | Introduction - Beam loss detection with distributed monitors 71
4.2 | Experimental Setup 72
4.2.1 | Installation at the ASLS 72
4.2.2 | Installation at the TBL 74
4.3 | Studies with short electron pulses 76
4.3.1 | Signal analysis 76
4.3.2 | Signal analysis of unidentified beam losses 83
4.3.3 | Intrinsic time resolution 87
4.4 | Studies with long electron pulses 90
4.4.1 | Multi bunch beam studies at the ASLS 90
4.4.2 | Single- and multi-location losses at the TBL 91
4.5 | Summary 96

5 Beam Loss Monitors in challenging environments 97
5.1 | Introduction 97

5.2 | Operational Losses in a Synchrotron Light Source 97
5.2.1 | Installation 98
5.2.2 | Operational Losses at the Booster 99
5.2.3 | Steady State Losses 102
5.3 | Beam Loss Crosstalk: A BLM limitation in parallel beam lines 109
5.3.1 | Installation 109
5.3.2 | Main Beam to Drive Beam crosstalk 111
5.3.3 | Drive Beam to Main Beam crosstalk 114
5.4 | Summary 118

6 AN ADVANCED DIAGNOSTICS TOOL FOR RF CAVITIES 119
6.1 | Introduction 120
6.2 | X-ray detection by OBLMs 120
6.2.1 | The FLUKA code 121
6.2.2 | Simulating optical photon generation 121
6.3 | RF cavity background radiation due to electron field emission 122
6.3.1 | Measurements with a T24 accelerating structure 122
6.3.2 | Simulation studies 128
6.4 | RF Breakdown radiation detection 136
6.5 | Optical fibre BLMs as RF cavity diagnostics 137
6.5.1 | RF Breakdown prediction from previous pulse 138
6.5.2 | Electron field emission studies during small input power variations 139
6.5.3 | Field Enhancement Factor β_{FN} 141
6.5.4 | Characterisation of a nominal CLIC accelerating structure 143
6.6 | Summary 146

CONCLUSIONS AND OUTLOOK 147

BIBLIOGRAPHY 151

LIST OF FIGURES

1.1 Arial view of the Geneva districts and the main CERN machines and experiments 8
1.2 Illustration of the CERN accelerator complex 9
1.3 CLIC layout at 3 TeV 11
1.4 A CLIC PETS 12
1.5 The CLIC two-beam acceleration 13
1.6 The CLIC Two-Beam Module 13
1.7 Schematic layout of CLIC type-0 module. 14
1.8 Trajectories of dark current emitted in an accelerating structure 15
1.9 SEM image of an RF Breakdown crater 17
1.10 CLIC accelerating structure cells 18
1.11 TD18 and TD24-Open CLIC accelerating structures 18
1.12 Layout of the CLIC Test Facility at CERN 20
1.13 Layout of the Test Beam line 21
1.14 Layout of the CLIC two-beam module at CLEX 21
1.15 Schematic of the Australian Synchrotron Light Source 22
1.16 Elements of the ASLS 23
1.17 Aerial view of the Australian Synchrotron Light Source 23

2.1 Radiation damage to different elements 27
2.2 Mean Energy Loss of muons in different materials [1]. 30
2.3 Stopping power at minimum ionisation with a fit (straight line) for Z>6 [1]. 31
2.4 Collision, radiative and total stopping power for electrons in nitrogen and Bethe-Bloch (B-B) evaluation [2] 32
2.5 Dominant interaction process for photons of energy E_γ in a material of atomic number Z, and angular distribution of the Compton scattered photons 33
2.6 Development of an electromagnetic and hadronic cascade 34
2.7 Schematic of different regions of ionisation chambers 36
2.8 PIN diodes 38
2.9 SEM and operating principle of ACEM 39
2.10 Scintillator operating principles and geometries 40

3.1 Illustration of Snell's law for the refraction, critical angle and total internal reflection. 44
3.2 Atom polarisation from a charged particle travelling through a medium. 45
3.3 Emitted wavelets along the track of a charged particle 46
3.4 Illustration of an optical fibre cable elements. 47
3.5 The acceptance angle of an optical fibre. 48
3.6 Typical attenuation coefficient α of a GeO_2-doped silica fibre 49

3.7 Changes in the 780 nm transmission of an MMF before, during and after a 35 ns irradiation pulse of 1 MeV X-rays [3]. 52
3.8 Irradiation tests of optical fibres with a ^{60}Co source 53
3.9 SiPM circuit and topology 56
3.10 SiPM pixels and photon counting 57
3.11 SiPM dark counts, crosstalk, afterpulses and responce 58
3.12 PMT operation principle and types 60
3.13 Definition of PMT rise, fall, and electron transit time [4]. 61
3.14 Operation principle of optical fibre radiation monitors. 62
3.15 Scheme of the crossing of an optical fibre by a charged particle 63
3.16 The photon trapping probabilities of an optical fibre 64
3.17 The Cherenkov photon yield and the spectrum attenuation after propagating in different lengths of optical fibre 65
3.18 Photon detection efficiency of two models of SiPM (MPPC) by Hamamatsu 67
3.19 The readout board 68
3.20 The SiPM readout board and the complete OBLM chassis 69
3.21 The developed shielded module 69

4.1 Details on the ASLS storage ring and OBLM installation 72
4.2 Sketch of the installed optical fibre BLMs at the Australian Synchrotron Light Source 73
4.3 Image of the CTF3 TBL and the optical fibre installed 75
4.4 Sketch of the installation of OBLMs at the TBL 75
4.5 Signal of the upstream end of the Scraper fibre, when a single bunch beam is injected at the storage ring and the scrapers are closed. 76
4.6 Signal of the Upstream end of the Scraper fibre, when a single bunch beam is injected at the storage ring and the storage ring scrapers are closed, and its derivative 77
4.7 Signal of the Upstream end of the Scraper fibre, when a single bunch beam is injected at the storage ring and the storage ring scrapers are closed, for open and closed BTS scrapers. 78
4.8 Sketch for the analysis of the beam loss signals in the Scraper fibre of the ASLS, when the beam is lost at the BTS scrapers and at the injection point. 79
4.9 Signal of the upstream end of the Scraper fibre, when a single bunch beam is injected at the storage ring and the storage ring scrapers are closed (red) or open (blue). 80
4.10 Sketch for the analysis of the beam loss signals in the Scraper fibre of the ASLS, when the beam is lost in different turns 81
4.11 Sketch for the analysis of the beam loss signals in the Scraper fibre of the ASLS, when fraction of the light is reflected at the opposite end of the fibre 82
4.12 The extraction of the Scraper and RF optical fibres at Sector 2 84
4.13 Calculation of the time difference between two beam loss signals arriving at the upstream end of a fibre. 85

4.14 Single bunch beam loss signal in the ASLS storage ring with closed scrapers, as detected from the downstream end of the Scraper fibre. 86
4.15 First turn single bunch losses observed in the RF fibre when the IVU3 is open and closed 87
4.16 Simulation of the horizontal and vertical beta function of the storage ring double bend achromat, provided by the Australian Synchrotron Light Source. A mockup of the machine elements has been added. 88
4.17 Leading edge of the OBLM signal generated at the scrapers by single bunches injected consecutively into buckets 1 to 10. 89
4.18 Distribution of the photon arrival time at the upstream end of the fibre for ten consecutive buckets. 89
4.19 Distribution of Δt (blue dots) and its Gaussian fit (red line). 90
4.20 Multi bunch generated OBLM signals in the upstream of the Scraper fibre. 91
4.21 Multi bunch generated OBLM signals in the upstream of the RF fibre. 92
4.22 Signals from the TBL signal fibre, the background fibre, and the TBL BLM signal after the background extraction 92
4.23 BLM and BPM signals of the TBL for nominal beam transmission, and when one quadrupole is turned off 93
4.24 BLM signals and the respective BPM intensities for the nominal beam transmission and for the three cases described in Table 4.4. 95

5.1 Sketch of the optical fibre BLM system at the Australian Synchrotron Light Source 98
5.2 Installation of the booster optical fibres 99
5.3 Average of the background measurement of the two OBLMs covering the Linac, Booster and BTS line. 100
5.4 Beam losses during the booster cycle as detected by the OBLMs 102
5.5 Beam losses during the last milliseconds of the booster cycle 103
5.6 Average OBLM signals of the single bunch case measurements of steady state losses 104
5.7 Average OBLM signals of the multi bunch case measurements of steady state losses 105
5.8 Average of the background measurement for the fibres covering the storage ring. . 107
5.9 Comparison of the detected current in the single and the multi bunch case 108
5.10 The LIC support and integration on the TBM 109
5.11 Layout of the BLM installation at the nominal CLIC Two-Beam Module at CLEX . 110
5.12 Installation of the LICs and the optical fibre on the TBM main beam 110
5.13 Installation of the LICs and the optical fibre on the TBM drive beam 111
5.14 OBLM and LIC BLM signals for CALIFES beams with increasing number of bunches 112
5.15 Crosstalk of main beam losses to drive beam BLMs, as measured by OBLMs and LICs 113
5.16 Average signals of the drive beam BPM located upstream of the TBM for different drive beam currents. 114
5.17 Average beam loss signals of the OBLMs drive beam and crosstalk signals of the main beam 115

5.18 Average beam loss signals of the drive beam and crosstalk signals of the main beam LICs . . . 115
5.19 Crosstalk of main beam losses to drive beam BLMs, as measured by OBLMs and LICs 116
5.20 Crosstalk of three different LIC setups . . . 117

6.1 Optical photon generation in quartz, due to electron and photon beams of different energies . . . 122
6.2 The optical fibre installed above the T24 accelerating structure at the CTF3 dogleg line . . . 123
6.3 Simplified schematics of the MPPC transimpedance amplifier readout circuit . . . 123
6.4 OBLM signals observed during the unloaded operation of the T24 RF cavity, attributed to the electron field emission . . . 124
6.5 OBLM detected charge during the five data-taking periods . . . 125
6.6 Double differential number of photons detected by the MPPC per electron crossing the middle of an optical fibre . . . 126
6.7 OBLM signals during normal RF cavity operation in terms of detected photons, and approximation of the relativistic electrons crossing the fibre . . . 127
6.8 3D view of the cavity geometry and the following elements in FLUKA . . . 129
6.9 The cross section at the middle of an accelerating structure disc . . . 129
6.10 Simulated geometry and simulation process in FLUKA . . . 130
6.11 Calculation of the impact angle. . . . 131
6.12 Electron and photon current in a cylinder 2.5 cm above the cavity . . . 132
6.13 Optical photon current in a cylinder 2.5 cm above the cavity . . . 133
6.14 Particle fluence and energy deposition for 15 MeV primary electrons . . . 134
6.15 Particle fluence and energy deposition for 5 MeV primary electrons . . . 135
6.16 OBLM signal observed during an RF breakdown at the unloaded T24 RF cavity . . . 137
6.17 OBLM signals during RF Breakdowns, in terms of detected photons and an approximation of relativistic electrons crossing the fibre . . . 138
6.18 Comparison of the field emission signals during normal operation of the RF cavity to the field emission of the pulse previous to RF breakdowns . . . 139
6.19 Installation of the optical fibre on the XBOX2 accelerating structure . . . 140
6.20 Field emitted electron signal of the T24-Open cavity, and its fit function . . . 141
6.21 Fowler-Nordheim plot from data acquired by a T24-open accelerating structure at the CERN XBOX2 installation . . . 142
6.22 Fowler-Nordheim plot from data acquired by a T24 accelerating structure at the CERN XBOX1 installation . . . 143
6.23 The optical fibre installed above the TD26 accelerating structure at the CTF3 dogleg line . . . 144
6.24 Field emitted electron signal and their mean value in TD26 . . . 145

LIST OF TABLES

2.1 Summary of the detection characteristics of different Beam Loss Monitors 41

3.1 Threshold energy $E_{kin,th}$ for the emission of Cherenkov radiation in Silica, and the kinetic energy of particles for $\beta = 0.999$, for different particles typically found in a beam loss particle shower. 46
3.2 The Hamamatsu MPPC models used in the present work and their main characteristics [5, 6]. 70

4.1 Length of the fibre parts extracting the signal to the photosensors at the ASLS . . . 73
4.2 Characteristics of the digitisers used for the OBLM data acquisition at the ASLS and TBL. 74
4.3 Linear extrapolation for peak estimation at the ASLS 77
4.4 Multi location loss setup at the TBL 94

5.1 Experimental cases examined as part of the steady-state loss study. 103
5.2 Fibre characteristics of the OBLMs tested at the TBM 111

6.1 Time period, mean input power and statistics of the data collected from the dogleg experiment in 2014. 124
6.2 Estimation of expected dark current signals on the OBLM 128
6.3 The electron field emission cases considered for the FLUKA simulations 131

GLOSSARY

ACEM Aluminium Cathode Electron Multiplier.

APD Avalanche Photodiode.

ASLS Australian Synchrotron Light Source.

BLM Beam Loss Monitor.

BPM Beam Position Monitor.

BTS Booster to Storage ring.

CALIFES Concept d'Accélérateur Linéaire pour Faisceau d'Electron Sonde.

CCDR Cladding Core Diameter Ratio.

CERN European Organisation for Nuclear Research.

CLEAR CERN Linear Electron Accelerator for Research.

CLEX CLIC Experimental Area.

CLIC Compact Linear Collider.

COTS Commercial Off-The-Shelf.

CTF3 CLIC Test Facility 3.

DAQ Data Acquisition.

DBRC Drive Beam Recombination Complex.

EM electromagnetic.

FEL Free-Electron Laser.

Flair FLUKA Advanced Interface.

HEP High Energy Physics.

IC Ionisation Chamber.

IVU In-Vacuum Undulator.

LHC Large Hadron Collider.

LIC Little Ionisation Chamber.

linac Linear Accelerator.

MIP Minimum Ionising Particle.

MMF multi-mode fibre.

MPPC Multi-Pixel Photon Counter.

NA numerical aperture.

OBLM Optical fibre BLM.

PDE Photon Detection Efficiency.

PETS Power Extraction and Transfer Structures.

PLIC Panofsky Long Ionisation Chamber.

PMT Photo Multiplier Tube.

PS Proton Synchrotron.

RF Radiofrequency.

RIA Radiation Induced Attenuation.

RIE Radiation Induced Emission.

SEE Single-Event Effects.

SEM Secondary Emission Monitor.

SI step-index.

SiPM Silicon Photon Multiplier.

TBL Test Beam Line.

TBM Two Beam Module.

UFO Unidentified Falling Object.

INTRODUCTION

Particle accelerators are widely used for research purposes in a wide selection of sciences, such as in particle, nuclear and solid-state physics, as well as for medical and industrial applications. Among the various types of accelerators, storage rings and linear accelerators are of the most common. The present thesis was performed at CERN, the largest accelerator complex worldwide.

During accelerator operation, small fractions of the beam escape its nominal orbit, which is defined by the beam envelope equation, and are lost in the machine. Furthermore, unexpected behaviour of the accelerator elements may cause larger parts or the entire beam to be lost. Beam losses result in the activation, degradation or even damage of the machine components. By monitoring them, beam loss monitors contribute both in the protecting the machine as well as in providing valuable information for beam diagnostics, two functions that render them a vital member of the accelerator instrumentation family.

Different types of detectors are being used as Beam Loss Monitors (BLMs), however most of them are localized and therefore cover a very small part of the beam line. To overcome this fact, optical fibres coupled to photosensors have been introduced as an alternative beam loss measuring technique. The operating principle is based on the generation of Cherenkov photons inside the optical fibre by the beam loss particles crossing it and the detection of these photons by a photosensor attached at the end of the fibre. Such monitors can cover large parts of the accelerator with minimal cost and installation requirements, greatly reducing the overall impact of the beam loss monitoring system and avoiding blind spots leading to beam losses going undetected. The characteristics of these fibre based detectors can be modulated depending on the fibre and the photodetector specifications. Within the past decade, optical fibre beam loss monitors have been tested and used in various facilities, at both linear machines and storage rings. Among them stand DELTA [7] and FLASH [8] (Dortmund and Hamburg respectively, Germany), NSLS-II at Brookhaven (USA) [9], and SPring-8 Free-Electron Laser (FEL) [10] and KEK Photon Factory [11] in Japan. The main similarity among these detectors is that as a photosensor a Photo Multiplier Tube (PMT) is being used while the possibility of using a photodiode has also been examined.

In the extent of this thesis, optical fibre based detectors are being studied over their performance and their potential to optimize the operation of storage rings and linear accelerators. The initiative of this study has been the Compact Linear Collider (CLIC), a proposal for a future 48 km electron (e^-) - positron (e^+) linear collider that may reach up to 3 TeV of centre of mass energy. To efficiently protect such a large machine more than 40,000 conventional detectors like ionization chambers are required, while a distributed BLM system might be a cost-effective alternative. As such, a very sensitive, low noise optical fibre BLM system with a Silicon Photon Multiplier (SiPM) in place of the regularly used PMT has been designed and examined over various aspects of its performance: to begin with, in terms of its ability to localize the beam losses occurring in various positions in the accelerator, for different beam lengths. Secondly, concerning the sensitivity limitations introduced in the case of parallel

beam lines from crosstalk, i.e. the background on the BLMs protecting the one beam line due to losses occurring in the other one. Moreover, regarding the capabilities of the detector to protect the damping rings of linear colliders, and consequently, storage rings. The possibility of these monitors to detect the steady state losses was also investigated. Furthermore, the sensitivity limitations caused by the RF cavity background, a question triggered by the presence of thousands of accelerating structures in CLIC, was explored. Finally, the use of fibre based detectors as an RF cavity diagnostics tool has been examined. The coupling of optical fibres to SiPMs for beam loss monitoring has been studied in FERMI@Elettra (Trieste, Italy) [12] and ALICE (Daresbury, UK) [13].

The experimental part of the studies were performed in the CLIC Test Facility 3 at CERN, in the Australian Synchrotron Light Source in Melbourne, and in the high gradient RF cavity test stand XBOX2, at CERN. A description of these facilities as well as CERN and CLIC, together with a summary of the basic theory of particle accelerators and RF cavities are presented in the first chapter.

The second chapter contains the basic theory behind beam loss monitoring. This includes a description of the different types of beam losses and the many purposes beam loss monitors serve in an accelerator, both as a machine protection and as a beam diagnostics tool. Lastly, the main aspects of beam loss related physics are summarized and the most widely used BLMs and their characteristics are listed.

The third chapter focuses on the optical fibre BLM system, describing the Cherenkov effect and the operation of optical fibres, as well as the main characteristics of fibres and photosensors. The development of such a system which uses silicon photomultipliers as end detectors, and which is the main implementation of the optical fibre BLM system (OBLM) used in this thesis, is presented.

The ability of the OBLMs for location determination for single bunch beams and long electron pulses in the case of single- and multi-loss location and the position resolution of this system is measured in chapter four. Additionally, the possibility of identifying the origin of unknown beam losses is demonstrated.

In Chapter five the OBLM system is examined under challenging accelerator environments, namely in a synchrotron facility and in parallel beam lines. In the former, the system is tested for the detection of steady-state losses and of beam losses during the full machine cycle, while in the latter for the sensitivity limitations the neighbouring beam lines introduce to an accelerator's beam loss monitors.

Finally, chapter six expands on the use of fibre based detectors in the vicinity of high gradient RF cavities. The radiation field of the cavities and its effects on the sensitivity of OBLMs is examined through simulation and experimental data, while the possibility for RF breakdown detection is also studied. Finally, the potential of using fibres as an RF cavity diagnostics tool, with focus on the measurement of the Fowler-Nordheim field enhancement factor, is explored.

1

First Chapter

Accelerators and Experimental Facilities

This chapter is an introduction to particle accelerators and the constituent elements and machines relevant to the present work. Section 1.2 provides an overview of particle accelerators, including some of their basic principles and applications. Section 1.3.1 focuses on circular colliders and storage rings, referring to the European Organisation for Nuclear Research (CERN) accelerator complex, where the largest part of this work was performed (Subsection 1.3.1 and 1.3.3 respectively). Section 1.4 describes linear machines, including a proposal for a high energy $e^- - e^+$ linear collider, the Compact Linear Collider (CLIC), presented in Subsection 1.4.2. Due to its original and challenging layout, the latter is of particular interest for Beam Loss Monitor (BLM) system studies. In Section 1.5 a deeper insight in Radiofrequency (RF) cavities principles is given, with the phenomena of electron field emission and RF breakdowns described in Subsections 1.5.1 and 1.5.2 respectively. In Subsection 1.5.3 the highest gradient to date RF cavity, the CLIC accelerating structure, is described. Finally, Section1.6 summarises the experimental facilities where the measurements presented on this thesis were performed: The CLIC Test Facility 3 (CTF3) at CERN and the Australian Synchrotron Light Source (ASLS) (Subsections 1.6.1 and 1.6.2 respectively).

1.1 Introduction

In the present work an optical fibre based detector was developed and explored in terms of characteristics and capabilities. The motivation for this study was the investigation for the beam loss monitoring system of machines such as CLIC, a collider proposal designed to reach a center-of-mass energy of 3 TeV in a total length of 48 km. To efficiently protect this machine, more than 45,500 localised BLMs would be required [14]. The Optical fibre BLM (OBLM) was proposed as a cost effective alternative, since one detector may cover approximately 100 m

of beam line, and therefore fewer monitors and acquisition electronics are required for the protection of the machine. The developed system was tested in CTF3, which was a versatile facility with a variable electron beam and machines operating as a CLIC proof-of-principle.

The ASLS is a user-friendly facility with beam characteristics very similar to those of the CLIC/ILC damping rings and a wide flexibility in the beam and machine settings. Therefore, it was selected as a machine where both the detector capabilities and the possibility of using it for the protection of the damping and storage rings could be explored.

The principal design of CLIC includes more than 40,000 RF cavities, the electron field emission of which may be the source of background radiation for BLMs. This possibility was examined in the scope of this thesis.

This chapter summarises the main principles of particle accelerators and describes the CLIC machine and the CTF3 and ASLS facilities. Furthermore, the CLIC accelerating structures and the electron field emission and RF breakdown phenomena are presented.

1.2 A short overview of particle accelerators

Particle accelerator research is driven by a need of obtaining sources of particles with controlled energies and intensities. Its development has been mainly pushed forward by the High Energy Physics (HEP) community and its requirements to produce new, usually short-lived particles at extremely high energies.

The most essential part for the construction and design of a particle accelerator are the electromagnetic (EM) fields. While electric fields are responsible for providing an energy boost to a beam of charged particles, magnetic fields are employed to guide its trajectory and control its movement in the transverse plane of motion. The elements used towards beam acceleration are the accelerating structures or cavities: dedicated metallic structures, suitable for the excitation of RF modes with electric fields pointing in the particle momentum direction. When a charged particle with charge $q \cdot e$, with $q = 1, 2, \ldots, N$ and $e = 1.6 \times 10^{-19}$C the charge of an electron, travels through the structures, it experiences a variation to its energy equal to

$$\Delta E = q \cdot e \cdot \Delta V \tag{1.1}$$

In the case of a DC cavity, ΔV is the voltage crossed by the particle, and in case of an RF cavity, $\Delta V = V_0 \sin(\omega_{RF} t + \phi)$ is the effective gap voltage. In the latter, V_0 is the effective peak accelerating voltage, ω_{RF} the RF frequency, t the time travelled in the cavity, and ϕ the phase angle.

For the beam manipulation a variety of magnets are used: dipoles are responsible for the beam bending and quadrupoles for the beam size modifications while higher order magnets, such as sextupoles, control any beam and geometric aberrations.

The construction of a particle accelerator demands a variety of other components, such as electron/ion sources, vacuum pumps, beam dumps, kicker magnets and beam instrumentation, more information on which can be found in [15, 16, 17].

Nowadays particle accelerators are an essential tool in a wide range of applications in research, medicine and the industrial sector. Some examples of such applications are: for the former, the isotope production as well as the ever demanding particle physics fundamental research. In the medical field, X-rays are used for medical imaging and radiation treatment, while proton and ion beams have been introduced as a mean of advanced cancer therapy. Finally, particle accelerators are broadly used in industry, such as the semiconductor manufacturing industry where ion implantation techniques are applied and the food industry, where accelerators are used for food sterilisation.

There is different classifications of particle accelerators depending on their main operation principles, as an example linear or circular machines, electrostatic or RF, continuous or bunched [16]. Thereafter, various accelerator designs exist, such as Van de Graaff generators, cyclotrons, synchrotrons and linear accelerators, which are described in detail in [15, 16, 17]. The following sections focus on those types mostly associated to the present study.

1.3 Synchrotrons and Storage Rings

1.3.1 | Main Principles

Circular accelerators present the advantage of using a single accelerating cavity to provide an energy increase for the beam every time the device is crossed. In order to keep the charged particles in orbit, the application of magnetic fields is required. Due to the Lorentz force, when an ultra-relativistic particle of charge $q \cdot e$ and energy E moves in a magnetic field B perpendicular to its direction of motion, it describes an orbit with a bending radius R_b equal to

$$R_b = \frac{E}{ecB}, \tag{1.2}$$

with $c \simeq 2.99 \times 10^8$m/s the speed of light in vacuum. On the other hand, the charged particle will get an energy boost everytime it crosses the RF cavity, i.e. in every turn. Therefore, keeping the bending radius constant for a given circular machine requires the ramping of the dipole magnetic field synchronously to the particle energy increase. Hence, such machines are called *synchrotrons*. The maximum energy that a synchrotron can reach is given by the machine radius R and the maximum magnetic field B, as

$$E_{max}[\text{GeV}] = C_p B[\text{T}] R[\text{m}], \tag{1.3}$$

where $C_p = 0.2998\,\text{GeV/c}$ [17]. To reach even higher energies, a first, small synchrotron might act as a booster, injecting the accelerated particles to another, larger circular machine as is the case in the CERN accelerator complex, Subsection 1.3.3.

In the case of electron synchrotrons, the limit in particle acceleration is set by the parallel emission of synchrotron radiation, described in the following subsection. In the case of ions, it is set by the machine dipole field.

1.3.2 | Synchrotron Radiation

When particles are bent perpendicular to their direction of motion, electromagnetic radiation is emitted. Considering a relativistic particle, the total irradiated power is given by the Liénard formula [15]

$$P_s = \frac{e^2 c}{6\pi\epsilon_0}\frac{1}{(m_0c^2)^4}\frac{E^4}{R^2} \tag{1.4}$$

where E is the particle energy, m_0 the particle rest mass, $\epsilon_0 \simeq 8.85\times10^{-12}\mathrm{CV}^{-1}\mathrm{m}^{-1}$ the vacuum permittivity and R is the bending radius of the orbit. Due to the $\sim 1/m^4$ dependence, synchrotron radiation is an important limitation in electron circular machines. It can be easily calculated that the power radiated by a proton is roughly 13 orders of magnitude lower than that of an electron of the same energy [*]. Hence, synchrotron radiation is only significant in proton machines of a very high energy (~100 GeV).

From Equation 1.4, the energy emitted (lost) by a particle in one turn in a circular accelerator is

$$\Delta E = P_s t_b = \frac{e^2}{3\epsilon_0(m_0c^2)^4}\frac{E^4}{R}, \tag{1.5}$$

where $t_b = \frac{2\pi R}{c}$ the duration of its bending in the machine dipoles. For an electron, Equation 1.5 is rewritten as

$$\Delta E[\mathrm{keV}] = 88.5\frac{E^4\mathrm{GeV}^4}{R[\mathrm{m}]} \tag{1.6}$$

For relativistic particles, synchrotron radiation is emitted in a cone of a half-opening angle θ with respect to the momentum direction, which is given by

$$\theta \approx \frac{1}{\gamma} \tag{1.7}$$

where γ is the Lorentz factor. Therefore, a 1 GeV electron beam emits synchrotron radiation in a cone with angle of 0.03 mrad. Consequently, the emitted radiation is highly collimated, with the ability of providing high photon fluxes in small and well-defined areas [18].

The spectral distribution of synchrotron radiation is continuous, extending from the infra-red to X-rays, with a cut-off wavelength that depends on the machine parameters γ and R,

$$\lambda_{\mathrm{cutoff}} = \frac{2\pi R}{\gamma^3} \tag{1.8}$$

Other characteristics of the synchrotron radiation are its pulsed nature (when it is generated from a pulsed beam), polarisation and high stability. Together with its high flux and broad spectrum, the above transforms synchrotron radiation from an accelerator limitation into a significant scientific tool. Its applications include, but are not limited to, structural analysis of crystals, proteins and non-crystalline systems through X-ray diffraction, elemental analysis using X-ray fluorescence, infra-red spectroscopy of solids, lithography and medical imaging [18]. Additionally, the continuity of the spectrum gives the possibility of wavelength selection depending on the application requirements [17, 18]. As a result, synchrotron light facilities are very popular machines, with more than 47 existing worldwide [19].

*. The rest masses of an electron and a proton are $m_e c^2 = 0.511\,\mathrm{MeV}$ and $m_p c^2 = 938.19\,\mathrm{MeV}$ respectively.

Storage Rings

Storage rings are machines developed to accumulate and store particle beams at a fixed energy. Such accelerators are mainly serving two purposes [15]:

— To generate synchrotron radiation for scientific and industrial applications, known as synchrotron light sources.

— To collide beams towards elementary particle research, also known as circular colliders.

Since storage rings operate at fixed energies, the beam injected must be already accelerated. For that purpose a Linear Accelerator (linac) or a synchrotron are used as boosters of the particles involved. However, storage rings which accelerate the beam prior to storing it also exist (i.e. some of the CERN accelerators, described in Subsection 1.3.3).

A decisive criterion of the quality of a storage ring is the beam lifetime, which for electron machines is determined mainly by the phenomena of electron-gas scattering and the intra-beam Touschek scattering [20]. For a beam containing N_{beam} particles, the lifetime τ_{beam} is given by

$$\frac{1}{\tau_{beam}} = -\frac{1}{N_{beam}} \frac{dN}{dt} \tag{1.9}$$

where $\frac{dN}{dt}$ is the loss rate of the beam. In order to achieve high beam lifetimes of the order of many hours, modern machines use ultra-high vacuum and efficient magnet systems for beam manipulation. In the case of electrons and very high energy ions, when the radiative losses from synchrotron radiation are high, the energy lost has to be restored by RF cavities.

Circular Colliders

In circular coliders, two particle beams are stored in the machine and circulate in opposite directions. They collide in a region surrounded by a complex detector system, known as interaction region. Among all the factors determining the performance of a collider, the most significant are the beam energy and *luminosity*: a higher beam energy can lead to discovery of new particles, while a higher luminosity gives a higher precision in the results, as it corresponds to more interactions [16]. The luminosity L is a measure of the probability of the two beams colliding, and is given by:

$$L = \frac{1}{4\pi} \frac{f N_1 N_2}{\sigma_x \sigma_y} \tag{1.10}$$

where f corresponds to the frequency of the beam collisions, N_i to the number of particles per beam and σ_x, σ_y to the beam horizontal and vertical size. For circular machines $f = f_{rev}$ with f_{rev} being the beam revolution frequency in the machine.

1.3.3 | CERN

The European Organisation for Nuclear Research, known as CERN (which is derived from the past french “Conseil Européen pour la Recherche Nucléaire”) is a research organisation founded by 12 european countries in 1954, dedicated to investigating the structure and interactions of subatomic particles. Today, CERN consists of 22 member states, 2 countries that

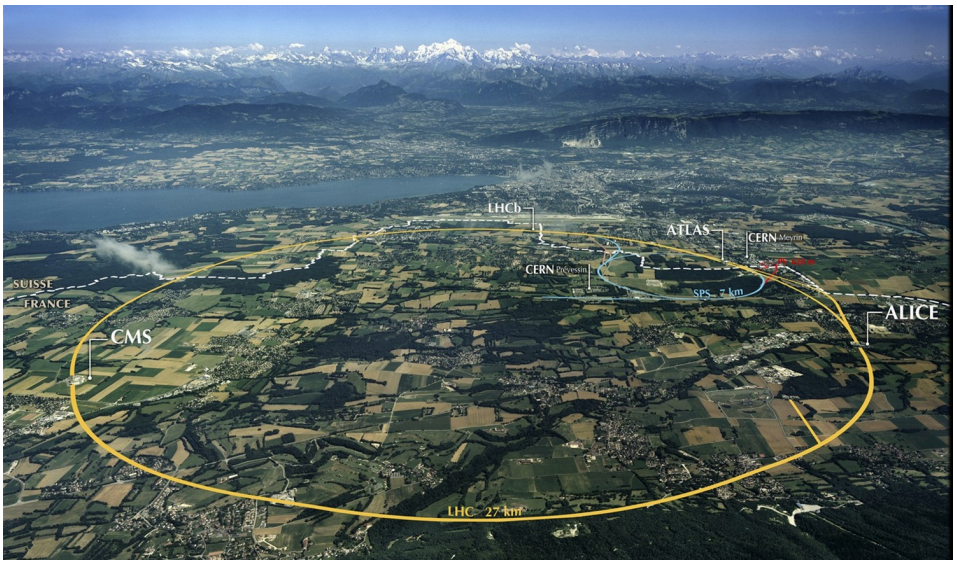

Figure 1.1 – Arial view of the Geneva district. The LHC ring over the Franco-Swiss borders (yellow), its four main experiments and the CERN SPS (blue) and PS (red) machines are indicated

are in the pre-stage to membership and 4 associate member states [21]. With an elaborate accelerator complex located along the Franco-Swiss borders, close to the city of Geneva as shown in Figure 1.1, CERN operates the largest particle physics laboratory worldwide.

The hallmark of CERN is the Large Hadron Collider (LHC), a proton (ion) collider with a 27 km circumference and a design peak momentum of 7 TeV per nucleon [22]. The greatest achievement of the LHC has been the discovery, in 2012, of a Higgs-compatible boson at an energy of 125 GeV/s. This granted P. Higgs and F. Englert, who in the 1960s predicted the existence of such a boson, the 2013 Nobel Price in Physics [23, 24, 25].

However, the latter is only one of the CERN achievements since its foundation, among a list of others such as:

1965 - The first observation of an antinuclei (antideuteron), at the Proton Synchrotron [26]

1968 - The development of the “multiwire proportional chamber” by G. Charpak [27] (1992 Nobel Prize in Physics)

1983 - The discovery of W and Z particles [28] (1984 Nobel Prize in Physics for C. Rubbia and S. van de Meer)

1993 - The World-Wide Web development by Sir T. Berners-Lee [29]

The CERN accelerator complex

The machines of the CERN accelerator complex stand as an excellent demonstration of accelerator combinations in order to develop different experiments and reach higher energies. Figure 1.2 shows the complete CERN accelerator complex, including some information on the machines comprising it.

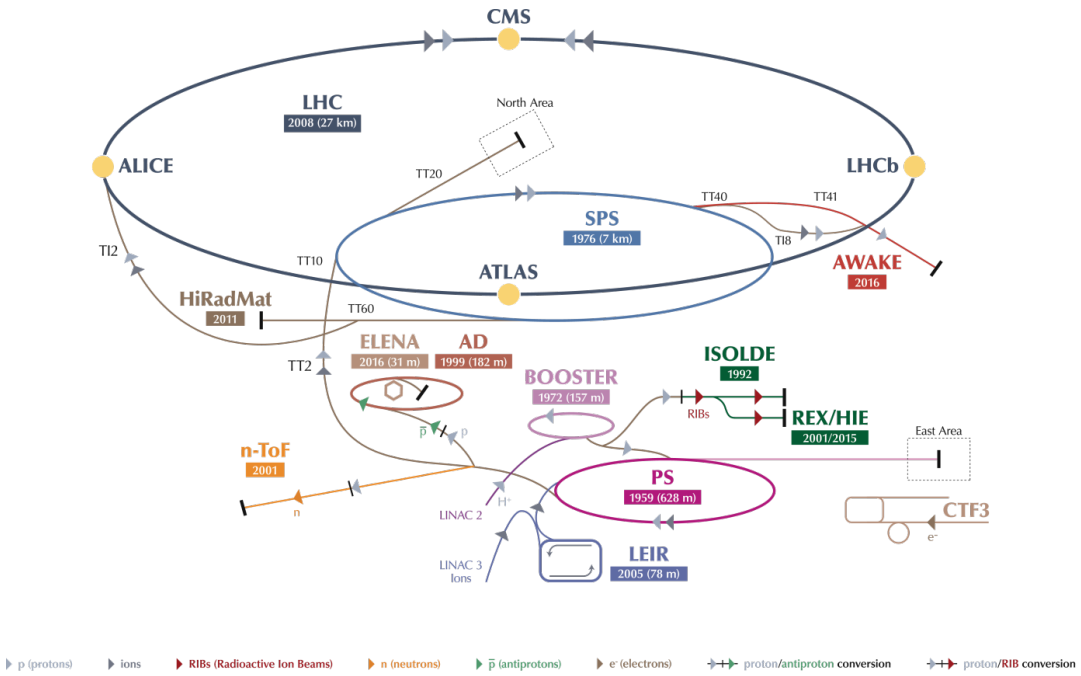

Figure 1.2 – Illustration of the CERN accelerator complex [30]

At the 27-kilometer Large Hadron Collider (LHC), protons are accelerated up to 7 TeV per beam; to this end the protons entering the machine should already have an energy of 450 GeV. This is achieved via a sequence of four other accelerators: The LINear ACcelerator LINAC2 (up to 50 MeV), the Proton Synchrotron Booster (PSB, up to 1.4 GeV), the Proton Synchrotron (PS, up to 28 GeV) and finally the Super Proton Synchrotron (SPS, up to 450 GeV). In the case of ions, these are accelerated in the linear LINAC3 (up to 4.2 MeV/n) and are injected to the Low Energy Ion Ring (LEIR), to reach an energy of 72 MeV/n in approximately 2.5 s. Subsequently, the ions follow the same machines, i.e. the PS (up to 5.9 GeV/n), where the last of the ion electrons are stripped away, the SPS (up to 177 GeV/n) and the LHC, to arrive at 1.38 TeV [31].

At the LHC interaction regions, four large-scale detectors (ATLAS, CMS, ALICE, LHCb) were built to track and analyse the data of the collisions. These experiments aim to examine the predictions of the Standard Model and expand to areas beyond it; discover new particles, examine the state of quark-gluon plasma formed just after the Big Bang and shed light into CP violation (or the domination of matter over antimatter in our universe) [22]. The PS, SPS and LHC ring in the Geneva district, as well as the four main LHC detectors, are illustrated in Figure 1.1.

As presented in Figure 1.2, various additional machines, beam lines and experimental facilities complete the CERN accelerator complex. The High-Radiation to Materials (HiRadMat) and East and North Area are irradiation facilities using primary or secondary beams, latter produced when the former ones impinge onto targets. The neutron Time-Of -Flight

(n_TOF) is a facility designed to study neutron-nucleus interactions for neutron kinetic energies ranging from a few meV to several GeV [32]. In the Isotope mass Separator On-Line facility (ISOLDE) low-energy beams of a vast variety of radioactive nuclides are produced, while in High Intensity and Energy ISOLDE (HIE) the nuclei will be able to reach up to 10 MeV/n. The Antiproton Decelerator (AD) produces and decelerates antiprotons down to 5.3 MeV for antimatter studies [33]. Coupled to it, the Extra Low ENergy Antiproton (ELENA) ring aims to further reduce the antiproton energy down to just 0.1 MeV [34, 35]. As far as the Advanced WAKefield Experiment (AWAKE) is concerned, this is a proof-of-principle project aiming to investigate particle acceleration via proton driven plasma wakefields [36, 37]. Finally, the CERN Linear Electron Accelerator for Research (CLEAR) is an electron linac reaching energies up to 220 MeV, which primarily focuses on accelerator R&D and component studies, for applications in existing and possible future machines [38]. The CLEAR line has been established in the previous CTF3 facility, which stopped operation in December 2016 after fulfilling its experimental program [39]. A major part of the experiments of this thesis was conducted in the CTF3, which is described in detail in Subsection 1.6.1.

1.4 Linear Colliders

1.4.1 | Main Principles

The limitation on electron acceleration in circular machines stems from the high percentage of energy lost due to synchrotron radiation. Therefore, the only plausible solution in order to achieve very high electron energies of the order of 1 TeV are linear accelerators, where the amount of electromagnetic radiation loss is negligible. In contrast to circular machines, the particles in linear accelerators pass the accelerating structures once, and do not require any beam bending. As a result, they contain a large number of RF cavities, quadrupoles and sextupoles for the beam focusing, while dipoles are not required. When used for particle collisions, such machines are called *linear colliders*.

The luminosity of linear machines is given by Equation 1.10. However, since the collision frequency is lower than f_{rev} in a circular machine, sufficient luminosity can only be achieved by reducing the horizontal and vertical beam size σ_x and σ_y. This is accomplished by using dedicated storage rings prior to the final acceleration, called damping rings. There, the damping of energy oscillations is achieved as a result of the synchrotron radiation dependency on particle energy. Particles of an energy higher than the nominal or design emit more synchrotron radiation, while particles of lower energy emit less. Therefore, the particle energy spread of the particles is reduced. The lost energy is restored in the RF cavities through only longitudinal accelerating fields, while the transverse oscillation amplitude is minimised [15, 17].

1.4.2 | The CLIC Project

Following the great discoveries of the LHC, the need for a lepton collider in the multi-TeV scale that can offer a series of complementing precision measurements has been expressed by

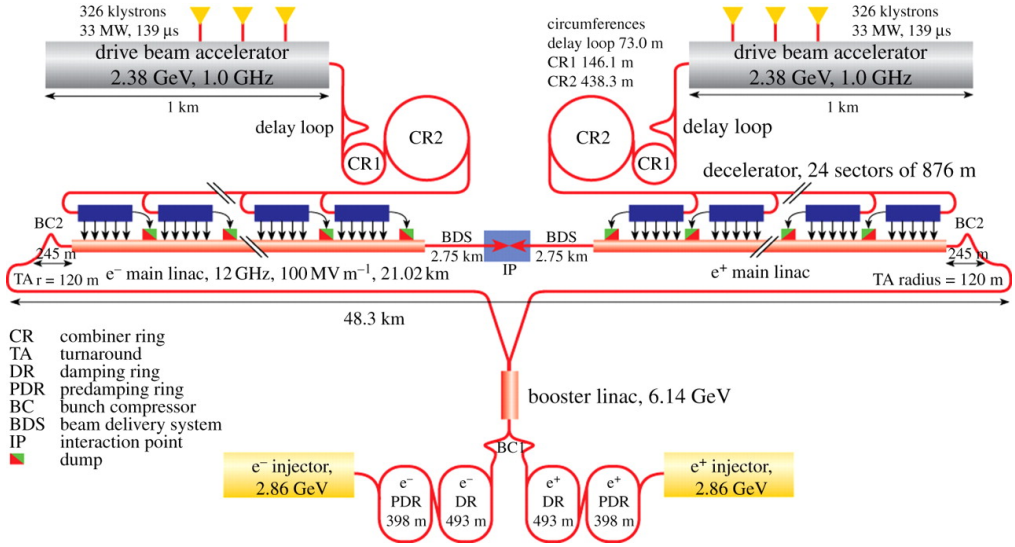

Figure 1.3 – CLIC layout at 3 TeV *(Image: CLIC Collaboration).*

the particle physics community.

CLIC [40] is a proposal for an e^-–e^+ collider with a center-of-mass energy of up to 3 TeV and a luminosity of $2 \times 10^{-34}\,\mathrm{cm}^{-1}\mathrm{s}^{-1}$. To reach electron and positron multi-TeV energies over a reasonable machine length, a novel two-beam acceleration scheme was proposed. The layout of CLIC is illustrated in Figure 1.3, while its operating principles are described in the following subsections.

Main Beam

The Main Beam is generated from a polarised electron and a positron source with a repetition rate of 50 Hz. This is pre-accelerated up to 200 MeV, and injected into a linac to reach an energy of 2.86 GeV. An ultra-low beam emittance is achieved in the following damping rings. The beam is then compressed into a 2 GHz bunch structure with a 1.2 A peak current, while a booster linac further accelerates it to 9 GeV. Starting from this energy the electrons and positrons have to reach up to 1.5 TeV. To achieve such a high energy over a reasonable machine length, the accelerating gradient * of the cavities should be particularly high. For a less than 50 km long machine, the gradient needs to be of the order of 100 MV/m. Since such a gradient cannot be achieved through super conducting technology, a novel design of 12 GHz normal conducting cavities has been proposed [40].

The final length of the linac for a 3 TeV centre-of-mass energy will be 21 km. Each of the two linacs is followed by a 2.75 km beam delivery system, where the electron and positron beams are collimated and focused, prior to their collision at one interaction point in the centre of the CLIC complex.

∗. the acceleration per unit length

Drive Beam

The 2.98 GeV, 4.2 A, 140 µs Drive Beam is generated and accelerated in two 1 GHz linacs, with a bunch repetition frequency of 500 MHz. Through a sequence of several rings and beam lines, this beam targets a very high current of approximately 100 A and a repetition frequency of 12 GHz – equal to the acceleration frequency of the main linac.

A first beam compression is carried out in a delay loop which, as shown in Figure 1.3, consists of both a straight path and a loop, the length of which (72.2 m) corresponds to ~244 ns. An RF deflector sends subsequent 244 ns long bunch trains alternatively into the loop or the straight path. At the end of the loop, the bunches of the delayed train are placed between the bunches of the following one using a second deflector, resulting in an 180° shift between them and in a beam of twice the bunch repetition frequency and twice the average current.

Afterwards, the beam is injected in especially designed circular machines, the so-called combiner rings. The combiner rings are equipped with a set of two RF deflectors, which introduce a closed orbit bump to the circulating particles. Their operation principle is similar to the one of the delay loop: for a combiner ring of a combination factor m, $m-1$ bunches are injected between two beam bunches and a phase shift equal to $\frac{360}{m}$ is introduced. The final beam is characterised by m times the bunch frequency and average current. For the manipulation of the CLIC beam, two combiner rings have been suggested, the first one with a combination factor of three and the second of four. Ultimately and including the delay loop, the drive beam undergoes a combination factor 24, which results in 24 short bunch trains with a repetition frequency and current increased to 12 GHz and 101 A.

The purpose of the drive beam is the transformation of its kinetic energy into RF power for the main beam accelerating structures. This is possible via the drive beam decelerators, i.e. beam lines equipped with passive microwave devices known as Power Extraction and Transfer Structures (PETS) [41]. The PETS are characterised by a periodically loaded waveguide, in which the drive beam bunches excite particular 12 GHz RF modes producing several hundreds MW of 12 GHz RF power. In Figure 1.4 a CLIC PETS prototype is shown.

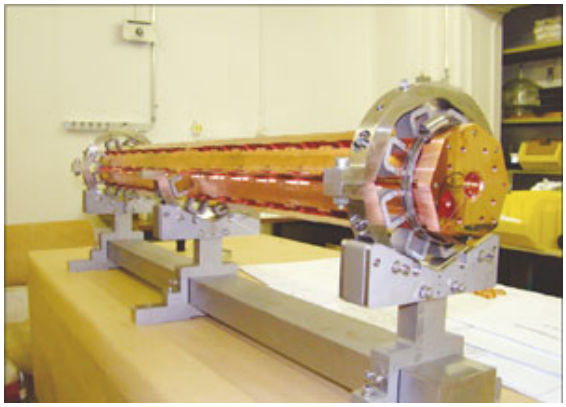

Figure 1.4 – A CLIC PETS *(Image: CLIC Collaboration).*

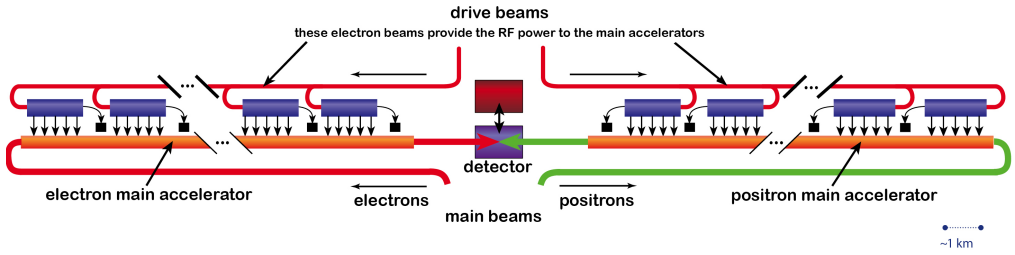

Figure 1.5 – The CLIC two-beam acceleration *(Image: CLIC Collaboration)*.

The two-beam acceleration

The main part of CLIC is divided in 24 sectors, each one covering an average of 878 m and being equipped with approximately 3,000 accelerating structures on the main beam side and one decelerating line on the drive beam side, which runs in parallel to and 60 cm far from the main beam. The drive beam is running in counter flow to the main beam, with one turnaround loop in each sector which directs one of the 24 drive beam bunch trains to one decelerating line. The 12 GHz RF power of each bunch train is extracted from the drive beam via the PETS and is transferred to the main beam accelerating structures through a system of waveguides. In the decelerator the drive beam electrons lose up to 90% of their energy, and they are dumped at the end of each sector. The two-beam acceleration is illustrated in detail in Figure 1.5. Finally, the CLIC two-beam configuration is organised in more than 10,000 “repeated modules” for each linac, known as Two Beam Modules (TBMs) and shown in Figure 1.6.

The CLIC Two Beam Module (TBM)

The principal constituent of CLIC is the TBM, a unit that, when repeated, forms the main CLIC accelerator. A TBM is a combination of PETS, accelerating structures, quadrupoles, Beam Position Monitors (BPMs) and RF waveguides which connect the drive beam to the main beam side. Each PETS is linked to two accelerating structures. Five types of modules are sufficient to

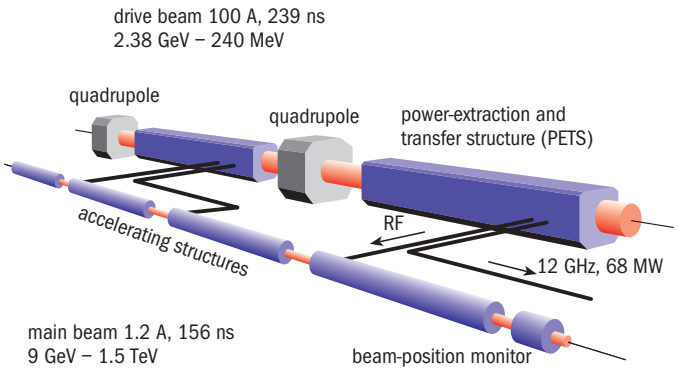

Figure 1.6 – The CLIC Two-Beam Module *(Image: CLIC Collaboration)*.

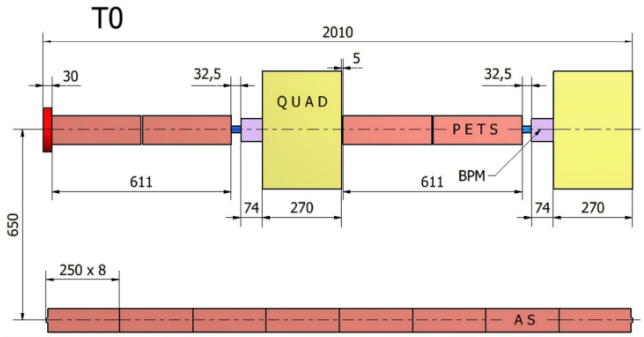

Figure 1.7 – Schematic layout of CLIC type-0 module.

accommodate all necessary configurations towards a complete CLIC machine. Type-0 is the principal module: it contains four PETS, two BPMs and two quadrupoles on the drive beam side and eight accelerating structures on the main beam side, as presented in Figure 1.7. For the other types, one, two, three or four PETS are excluded from the module. These modules are respectively named type-1, -2, -3 and -4. On the main beam side, the equivalent number of accelerating structures, i.e. two, four, six or eight, are also excluded while their space is occupied by one quadrupole per couple of structures.

1.5 High gradient RF cavities

The high gradient normal conducting RF cavities are accelerating structures under investigation for their very high accelerating gradient, which reaches values greater than 100 MV/m [40]. Bearing such an advantage, these cavities succeed to reduce the overall size and cost of linear accelerators. In the past decades, they have been examined for particle acceleration in linear colliders, such as the CLIC [42]. Other attainable applications include the production of high quality electron beams for Free-Electron Lasers (FELs), and the construction of compact linacs for medical purposes, such as proton and carbon ion cancer treatment.

The two following subsections describe physics phenomena taking place in high gradient RF structures of particular interest for the scope of this thesis, namely: electron field emission and RF breakdown.

1.5.1 | Electron Field Emission

Electron field emission represents the phenomenon of electron extraction from metalic surfaces when intense electric fields are applied. In particle accelerator RF cavities, this is of particular interest for various reasons: one is the possibility for a fraction of them to impact on the cavity walls, generating X-rays and, transferring heat to the cavity and increasing the radiation levels of the surroundings. Another is that they can absorb RF power, become bunched and accelerated towards the end of the structure, creating a parasitic beam that will

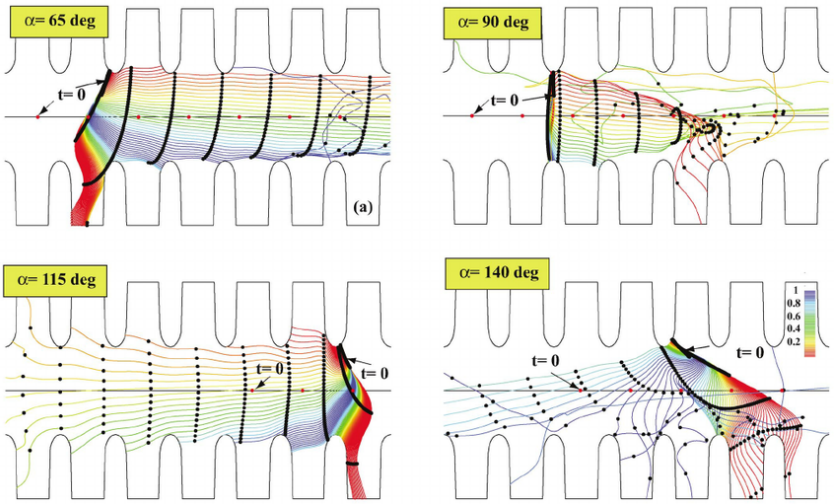

Figure 1.8 – Trajectories (in the x - z plane) of dark current emitted in an accelerating structure for 4 selected emission angles (α). Downstream is to the right (positive z) [44].

waste accelerating power and may potentially induce beam instabilities [43]. The latter is known as dark current [42]. An illustration of field emitted electron trajectories in accelerating structures for different emission angles, calculated and presented in [44], is shown in Figure 1.8.

The phenomenon was first described in 1928 by Fowler and Nordheim [45, 46], who calculated the quantum mechanical tunnelling of the conduction electrons of an ideal, flat metal surface, through the potential barrier of an applied electric field. The field emission current density j_F is given by equation

$$j_F = \frac{1.54 \times 10^{-6} \times 10^{4.52\phi^{-0.5}} \mathcal{E}^2}{\phi} \exp\left(-\frac{6.53 \times 10^9 \phi^{1.5}}{\mathcal{E}}\right) [\mathrm{A/m^2}] \tag{1.11}$$

where $\mathcal{E}$[V/m] is the surface electric field and ϕ[eV] is the work function of the emitting material. In copper, the work function ranges between 4.48 and 4.98 eV, depending on its crystalline structure [47].

In practice, however, the metal surfaces are not perfect. Small variations such as scratches, metallic dust, impurities, metallic surface roughness due to imperfect machining, or even molten craters created by an RF breakdown (described in detail the following subsection), are emitters that can enhance the electric field of the conductor to a local microscopic value $\mathcal{E}_m$. Equation The field enhancement factor β_{F-N} is defined as the fraction

$$\beta_{F-N} = \frac{\mathcal{E}_m}{\mathcal{E}} \tag{1.12}$$

For an effective area A_e [m^2] of the emitter, the field emitted current can be calculated from

Equation 1.11 as

$$I_F = \frac{1.54\times10^{-6}\times10^{4.52\phi^{-0.5}} A_e \beta_{F-N}^2 \mathcal{E}^2}{\phi} \exp\left(-\frac{6.53\times10^9\phi^{1.5}}{\beta_{F-N}\mathcal{E}}\right)[\mathrm{A}] \tag{1.13}$$

For an RF field of the form $\mathcal{E} = \mathcal{E}_0 \sin(\omega t)$ with a period T, where E_0 (V/m) is the amplitude of the surface field, the average field emission current is given from

$$\bar{I}_F = \frac{1}{T}\int_0^T I_F(t)\,dt$$

which can be approximated by:

$$\bar{I}_F = \frac{5.7\times10^{-12}\times10^{1.52\phi^{-0.5}} A_e \beta_{F-N}^2 \mathcal{E}_0^{2.5}}{\phi^{1.75}} \times \exp\left(-\frac{6.53\times10^9\times\phi^{1.5}}{\beta_{F-N}\mathcal{E}_0}\right)[\mathrm{A}] \tag{1.14}$$

The plotting of $\bar{I}_F/\mathcal{E}^2$ versus $1/\mathcal{E}$ is known as Fowler-Nordheim plot. In a semi-logarithmic scale, the field enhancement factor β_{F-N} can be obtained from the slope of the Fowler-Nordheim plot $\frac{d(\log_{10}(\bar{I}_F/\mathcal{E}^{2.5}))}{d(1/\mathcal{E})}$ as

$$\frac{d\left(\log_{10}(\bar{I}_F/\mathcal{E}^{2.5})\right)}{d(1/\mathcal{E})} = -\frac{2.84\times10^9\phi^{1.5}}{\beta_{F-N}} \Rightarrow$$

$$\beta_{F-N} = -\frac{2.84\times10^9\phi^{1.5}}{\frac{d(\log_{10}(\bar{I}_F/\mathcal{E}^{2.5}))}{d(1/\mathcal{E})}} \tag{1.15}$$

The field enhancement factor depends on the geometrical characteristics of the metal surface and the impurities of the material. In this way and therefore it is indicative of the quality of an accelerating structure. A higher field enhancement factor leads to higher electron field emission in the cavity. Typical values for β_{F-N} range between 40 and 100 [46].

The mitigation of the phenomenon is achieved via a process called RF processing or conditioning, during which RF pulses of gradually increasing input power are applied to the cavity. Field emission disappears as the quality of the surface is improved through a slow burning of the field emitters and structure impurities. This clean-up of the surface is a rather empirical process still under investigation and, as described in [46], is " still an art more than a science".

1.5.2 | RF Breakdown

The term RF breakdown refers to an electrical discharge occurring in the RF cavities and is a complex phenomenon still under investigation. It seems that breakdowns occur at locations experiencing an enhanced electric field due to contaminants, geometrical features, crystal defects or a combination of the above. The enhanced electric field leads not only to an increased electron field emission, but also to higher field-evaporation, a process during which the atoms of a metal surface under an applied electric field break their bonds and are extracted

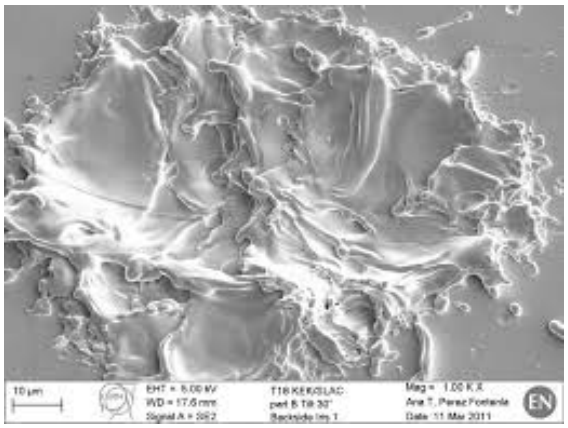

Figure 1.9 – SEM image of an RF Breakdown crater formed in a CLIC X-band accelerating structure, image courtesy of Ana Perez Fontenla [48]

from the material [49]. According to [40], an RF breakdown will develop when the neutral field evaporated atoms exceed a critical value. The field emitted electrons ionise the neutral atoms, creating a plasma locally at the emitter, which expands transversely in the cavity. During the breakdown, a current of the order of 100 A is emitted in few nanoseconds and absorbs nearly all the incoming RF power. Concurrently, when contacting the cavity walls, the plasma may create craters with a diameter of the order of ~10 µm on their surface. Such a crater is presented in Figure 1.9 [48], [50]. Acting as further field electron emitters, these craters may degrade the quality of the accelerating structure.

1.5.3 | The CLIC Main Linac accelerating structure

The CLIC accelerating structure is targeting very high accelerating gradients –of the order of 100 MV/m– at a frequency of almost 12 GHz, while the breakdown (BD) rate should be as low as 10^{-7} BD/pulse/m. To reach these standards and achieve the optimum performance, different designs of X-Band * RF cavities are under investigation [40].

To reach very high gradients normal conducting technology was chosen, and in particular copper, as it is characterised by a low breakdown rate. Most of the RF cavity designs under consideration comprise approximately 20 cells, bonded and baked into one travelling wave structure. The first and last cell encompass the couplers, which are responsible for the input and output of the RF power. In order to maintain a constant accelerating gradient despite the attenuation of the RF power while travelling within the cavity, the structures are tapered [53]. Additionally, structures with cells equipped with wakefield damping waveguides are examined for their performance. In Figure 1.10, accelerating structure cells with (a) and without (b) damping waveguides are shown [54, 55].

Some principal accelerating structure designs which have been investigated over the past

∗. Depending on their operation frequency, RF-cavities are categorised in L-band (1-2 GHz), S-band (2-4 GHz), C-band (4-8 GHz), X-band (8-12 GHz) [51].

(a) (b)

Figure 1.10 – (a) A CLIC accelerating structure cell, without damping [52] (b) The cell of a CLIC accelerating structure with damping waveguides *(Image: CLIC collaboration)*.

years include cavities comprising 24 cells without damping, named T24, and with damping waveguides, known as TD24 *. The former is similar in almost every aspect except the number of cells to the structure of Figure 1.11(a), which is a T18, comprised of 18 cells. The T24 and TD24 structures are being studied in the present work.

Furthermore, a structure of a different manufacturing technique, known as T24-Open, has been examined in the frame of this thesis. The characteristics of this structure are similar to the T24, but its fabrication is based on the milling of two copper blocks as structure halves. The two halves are joined together and are bonded in two bonding surfaces. Between these surfaces and the cavities a finite gap is maintained to ensure high performance [57]. This fabrication technique is illustrated in Figure 1.11(b).

∗. In the naming convention, "T" stands for *tapered*, "D" for the damping waveguides, and the total number of structure cells follows.

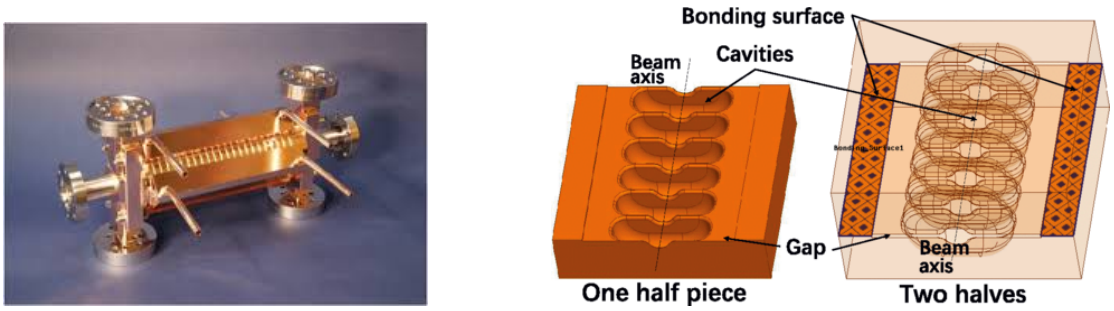

(a) (b)

Figure 1.11 – (a) A CLIC TD18 accelerating structure tested at the SLAC National Accelerator Laboratory [56] (b) 3D Model of the manufacturing of an accelerating structure by joining two milled copper halves [57].

1.6 Experimental Facilities

In this section the experimental facilities where the studies of this thesis were performed, are described.

1.6.1 | The CLIC Test Facility 3 (CTF3)

CTF3 was built at CERN by the CLIC/CTF3 collaboration aiming to prove the feasibility of the CLIC two-beam acceleration technology. The main points to be demonstrated are the drive beam generation and recombination, the RF power production from the drive beam and the two-beam acceleration. For that purpose one drive beam complex and one beam line intending to mimic the main beam, called Concept d'Accélérateur Linéaire pour Faisceau d'Electron Sonde (CALIFES), were established. In the following paragraphs the drive beam complex and its beam lines, namely the dogleg line and the Test Beam Line (TBL) as well as the CALIFES and the two-beam module are presented.

The Drive Beam Complex

The drive beam complex [58] was built as a proof-of-principle demonstrator for beam current and frequency multiplication via delay loops and combiner rings. The complex is able to produce a flexible beam of duration in the range between 140 ns-1.2 µs and a current between 4 and 28 A. Additionally, it houses three experiments: the RF cavity beam loading experiment, beam deceleration beam line and the two-beam acceleration study.

An electron injector generates 4 A of electron beam pulse which is accelerated up to 120 MeV in the 70 m Drive Beam linac. At this point the beam consists of approximately 1.2 µs long trains with eight 140 ns long sub-trains and bunches at an 1.5 GHz bunching frequency. The beam continues into the Drive Beam Recombination Complex (DBRC), where a 42 m long delay loop and an 84 m combiner ring are located. The beam combination in the delay loop will result in four 140 ns long trains of bunches at double frequency (3 GHz) and with an approximately 7.5 A beam current. In the following ring the beam can perform from no full turns, in which case it will not be altered, to up to three full turns. As a result the four trains can be accumulated to down to one single train while the beam current is multiplied by a factor of up to four. Nominally, in the factor four combination, the drive beam exits the DBRC consisting of 140 ns long pulses with bunches at a 12 GHz frequency and spaced by 6.6 ns, and with a current of approximately 30 A. In the case of a factor two (three) multiplication, the beam should reach a value of 15 A (22.5 A). Due to beam loses during the recombination process, the beam current values are lower, and in the nominal case reach the 28 A [59].

At this point the drive beam enters the so-called CLIC Experimental Area (CLEX) and is directed either to the decelerator line TBL, or towards a nominal TBM. The former aims to study the drive beam deceleration through the PETS, while the latter targets to validate the two-beam acceleration. The layout of CTF3, including the drive beam accelerator, the combination beam lines and the CLEX facility is presented in Figure 1.12.

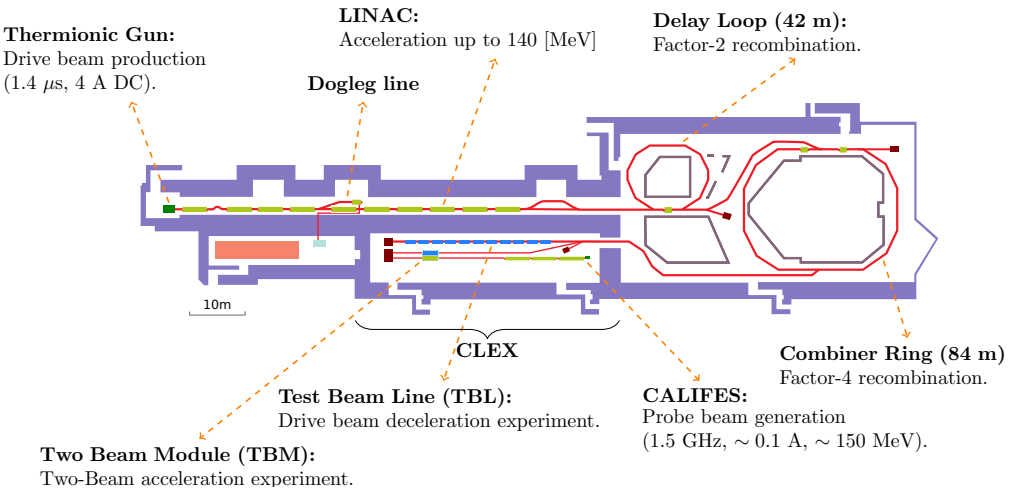

Figure 1.12 – Layout of the CLIC Test Facility at CERN (CTF3) showing the main parts. The beam path is identified by solid red lines. Accelerating structures are identified by a green block on the beam path, while blue blocks represent the PETS *(Image: Davide Gamba, CTF3)*.

The beam loading experiment at the dogleg line

Midway along the drive beam linac, where the drive beam has an energy of 120 MeV and a pulse length of up to 250 ns, a dogleg-like line branches off to transport the beam into a parallel path. This line leads to an RF cavity, where an experiment studying the performance of high gradient accelerating structures, and in particular CLIC RF cavities, with and without beam loading takes place.

The necessary power for the cavity operation is provided by a klystron, producing up to 50 MW of 12 GHZ RF power. RF pulses of 1.5 µs duration are delivered to the structure at a 50 Hz rate via a combination of waveguides and RF components. Directional couplers are installed close to the structure to detect the RF power forwarded to the structure, transmitted through it and reflected at it, which are then measured by logarithmic detectors. A detailed description of the line and the experimental setup can be found in [60].

The TBL

The TBL is a 22.5 m long decelerating linac consisting of eight FODO cells, built to study the suitability of power extraction via beam deceleration. Each FODO cell is 2.8 m long and is equipped with two quadrupoles, two PETS and two BPMs, as illustrated in Figure 1.13. In order to produce the 135 MW, 12 GHz RF power required for CLIC from the lower CTF3 drive beam energy, the active length of the PETS is four times longer compared to that of the CLIC nominal design. At the end of the beam line the beam has lost approximately 50% of its initial energy.

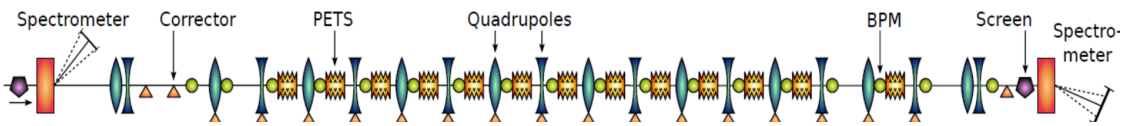

Figure 1.13 – Layout of the Test Beam line *(Image: CLIC collaboration).*

Califes

The CALIFES is a 26 m electron linac built in CLEX to mimic the CLIC main beam. CALIFES delivers flexible electron beams ranging from single bunch to bunch trains of up to 300 bunches, with a bunch charge of 0.05 - 0.6 nC and a bunching frequency of 1.5 GHz. This electron beam, known also as probe beam, is provided from a Cs_2Te photoinjector pulsed by a UV laser, and after being bunched in a buncher structure it is accelerated in two accelerating structures to approximately 200 MeV [61]. The CALIFES beam continues downstream to the installed TBM, for the proof-of-principle of the operation of a nominal CLIC module.

The Two Beam Module

The TBM is a prototype of the CLIC lattice, aiming to simultaneously test all of its components during operation. It is a half Type-0 module, containing two PETS and two quadrupoles on the drive beam and four CLIC accelerating structures on the main beam side, as shown in Figure 1.14. The instrumentation of the module includes one BPM on each beam side and two wakefield monitors [62] on the main beam. The RF power is extracted from the drive beam via PETS and is transferred to the RF cavities through RF waveguides, which accelerate the probe beam supplied from CALIFES. Following the two-beam acceleration, both beam lines are equipped with BPMs, beam current monitors, scintillating screens and a spectrometer, providing information on the beam position, current, profile and energy respectively.

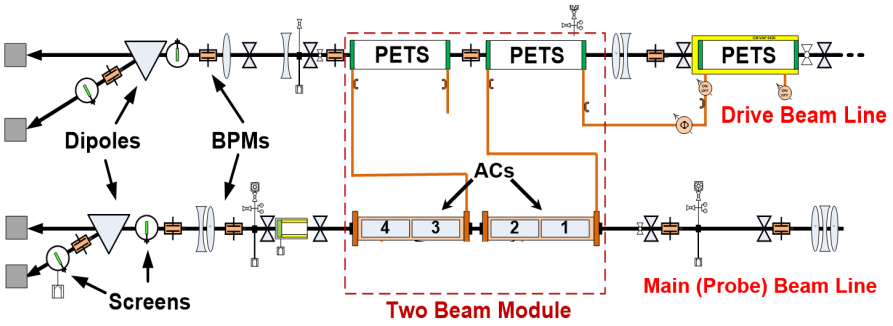

Figure 1.14 – Layout of the nominal CLIC two-beam module installed at CLEX *(Image: Jose Luis Navarro Quirante).*

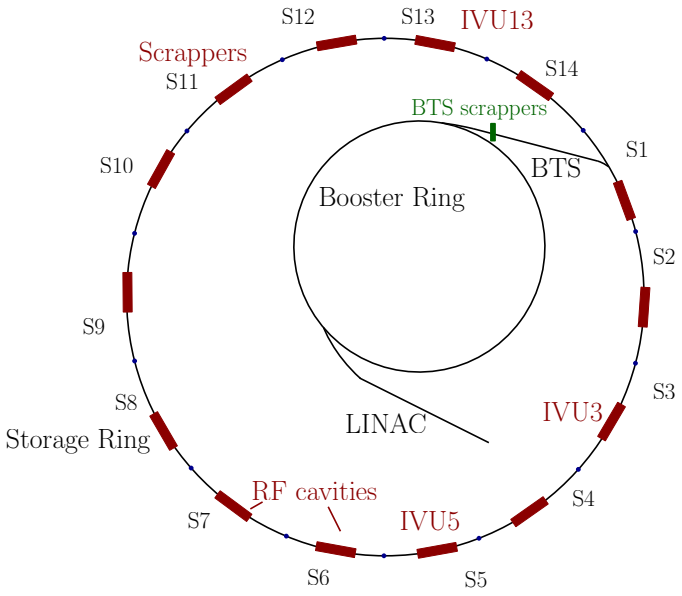

Figure 1.15 – Schematic of the Australian Synchrotron Light Source

1.6.2 | The Australian Synchrotron Light Source (ASLS)

The ASLS is a third generation synchrotron radiation facility located in Clayton, Victoria. The layout of the machine is illustrated in Figure 1.15, while an aerial view of the facility is shown in Figure 1.17.

At the ASLS, the electrons are generated in bunches two nanoseconds apart and are accelerated to 90 keV by a 500 MHz thermionic gun, before entering into a 15 m linac that further accelerates them to 100 MeV. Subsequently, the electrons are injected in a 130 m circumference booster ring equipped with a single 500 MHz RF cavity. A ramping cycle lasts approximately 600 milliseconds, by the end of which they have reached an energy of 3 GeV. During the last few tens of milliseconds of the ramping cycle, the closed orbit is altered via a slow bumping technique. This allows the beam to be centered at the extraction point within the field of the fast magnet that will kick it into the Booster to Storage ring (BTS) transfer line.

At the end of the BTS, another kicker magnet injects the beam into Sector 1 of the 216 m circumference storage ring. The storage ring consists of 14 almost identical sectors with a double bend achromat lattice, each comprising a 4.4 m straight section and an 11 m arc. Two dipoles in each arc are responsible for the particle bending, whereas beam focusing and the corrections in chromaticity and orbit are achieved via six quadrupole and seven sextupole magnets. A segment of the lattice is presented in Figure 1.16(a). The straight section of each sector is equipped with different elements and insertion devices necessary for the machine operation and X-ray production, such as undulators, wigglers, RF cavities and scrapers. In Sectors 3, 5 and 11 In-Vacuum Undulators (IVUs) are situated, with the one of Sector 3 shown in Figure 1.16(b). Sectors 6 and 7 hold the 500 MHz RF cavities to compensate the beam energy lost during synchrotron radiation. Finally, in Sector 11 the beam scrapers concentrate beam

(a) (b)

Figure 1.16 – Elements of the ASLS (a) Elements of the lattice: dipoles (yellow), quadrupoles (red), and sextupoles (green) (b) The Apple II In-Vacuum Undulator of Sector 3.

losses at this location, to protect the insertion devices [63]. The scrapers have one pair of horizontal and one of vertical blades that can close completely so as to stop the full beam or be entirely open resulting in no beam losses. However, at nominal operation the distance between the blades is at 13 mm.

The Australian Synchrotron flexibility renders it an ideal facility for various beam diagnostics experiments. An injection from one bunch to a train of up to 75 bunches is possible, while the bucket in which a single bunch will be injected can be chosen (an RF bucket is the phase-space area which corresponds to a stable synchrotron orbit of a particle in a synchrotron [16]). When operating in single bunch mode, the bunch charge of the machine can be varied from $10^{+5} - 10^{+9}$ electrons [64]. During standard operation the storage ring can hold up to 200 mA of stored current while a beam lifetime of over 200 hours can be reached. The beam is injected in trains of 75 bunches with a current of approximately 0.5 mA and fills approximately 300 of the 320 available 500 MHz RF buckets.

Figure 1.17 – Aerial view of the Australian Synchrotron Light Source *(Image: Australian Synchrotron)*

2

Second Chapter

Beam Loss Monitoring

The current chapter focuses on BLMs, the purpose they serve and the physical principles that lie beneath them. Section 2.1 contains an introduction to beam loss monitoring and a description of BLM uses. In Section 2.2 the main sources of beam losses are presented. Section 2.3 summarises the principal physical processes related to the interaction of lost beam particles with the accelerator materials, as well as their direct and indirect detection by the BLMs. Finally in Section 2.4 the most widely used BLMs and their characteristics are described.

2.1 Introduction

Quoting K. Wittenburg, *"You do not need a Beam Loss Monitoring System as long as you have a perfect machine without any problems. However, you probably do not have such a nice machine, therefore you better install one".*

In an operating accelerator there is a plethora of conditions that may cause part or the entire beam to deviate from its nominal orbit and be lost in it. The BLM system monitors and controls these beam losses and is a vital beam diagnostics system for most particle accelerators, serving many objectives at the same time [65, 66, 67, 68]:

The protection of the machine The interaction of the beam particles with the machine components can lead to their degradation, their destruction or the quenching [†] of superconducting elements, such as magnets and accelerating structures. By monitoring the losses and forcing beam dumps when needed, the BLM system ensures a minimal accelerator performance and protects the machine components from beam induced

†. A quench is the transition of a superconducting material from the superconducting to the normal, resistive state, which inevitably occurs when the temperature, magnetic field or current density of the material exceed a critical value [69]. Transitioning into a normal-conducting state leads to the appearance of a potential difference in the magnet, resulting in an increase in temperature, a thermal expansion of the material and in electro-magnetic forces developed in it [70].

damage. An example of material damage caused by high energy beam is shown in Figure 2.1.

The upkeep of the machine cycle The degradation or destruction of accelerator components may result in a deteriorated machine performance or even a shut-down in order to replace them, a process that can be costly and time consuming. The constant monitoring of beam losses facilitates their preservation below destructive levels, contributing to the upkeep of the machine cycle. To ensure the protection of the accelerator during operation, a critical maximum value of losses (threshold) is applied to the beam loss monitoring system: when beam losses reach this level, the beam is dumped. This results in a downtime which may vary from a few minutes to some hours, affecting the availability and reliability of the machine preventing, however, a greater downtime in the event of machine damage or quench.

The low irradiation and activation of the surroundings The radiation emitted from beam losses ultimately results in the irradiation of the neighbouring equipment, bearing further consequences apart from the core material degradation. These include the effects on the surrounding solid-state electronics, known as Single-Event Effectss (SEEs), and the activation of the surrounding equipment. The former may lead to errors in the acquired data or even in the malfunction of the components, while the latter increases the risk in terms of radiation dose received for the accelerator personnel accessing the facility. In order to reduce this risk, a period for the cool-down of activated materials is often added to the machine downtime when human interventions are required. By identifying beam loss hotspots, BLMs contribute in establishing low irradiation of the surroundings and facilitate mitigation solutions.

Beam diagnostics BLMs are a valuable beam diagnostics tool, as they monitor the behaviour of the beam and provide instantaneous feedback during machine operation and/or commissioning.

The field of beam loss monitoring aims to select the ideal BLM system for each machine, in order to monitor and control the particles that are lost in the accelerator and guarantee its most efficient operation. This chapter aims to provide insight on the various sources of beam losses, the physical principles ruling the interaction of these particles with the accelerator material as well as their detection, and the most common beam loss monitors used today in accelerators worldwide.

2.2 Beam Losses

Depending on their origin, beam losses are classified into two categories; the regular and the irregular beam losses. In this section the two classes are described from information collected from [65, 68, 73], and an insight into the different possible sources of beam losses is provided.

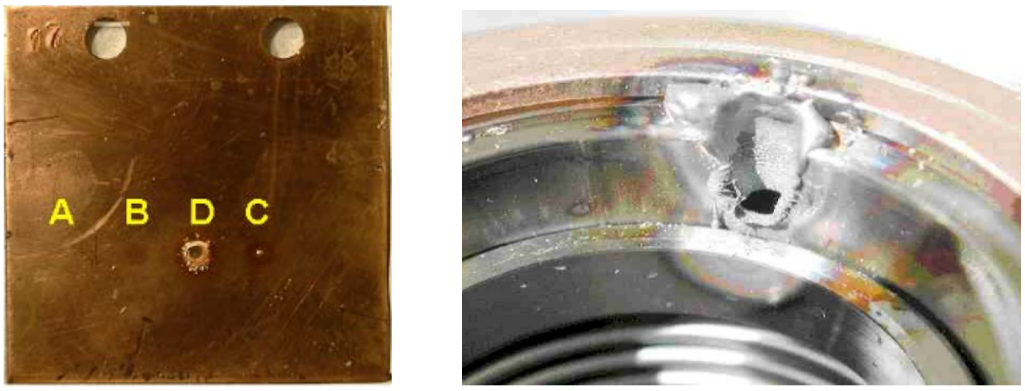

(a) (b)

Figure 2.1 – (a)Radiation damage on 2 mm thick copper plates from 450 GeV/c proton beam with intensities: (A) 1.3×10^{12} (B) 2.6×10^{12} (C) 5.3×10^{12} and (D) 7.9×10^{12} [71] (b) Damage to vacuum components in ELBE, due to direct beam impact, while no BLM system was available at the time [72].

2.2.1 | Regular beam losses

The regular (or controlled, or slow) losses are beam losses, typically unavoidable, that are related principally to the stability of the beam motion and might occur continuously during the machine operation. These type of losses are correlated to the beam transport efficiency and beam lifetime, and BLMs use them to perform machine diagnostics.

In most machines, collimator systems or scrapers are installed to control the regular losses and concentrate them in designated locations, preventing particles from interacting in locations where sensitive equipment of the beam line are installed. However, in the absence of collimators, regular beam losses are also localised in other, normally known, aperture limits of the accelerator. Some sources of regular beam losses are:

Touschek effect The Touschek effect is the Coulomb scattering occurring between two particles of the bunch, resulting in the transformation of a small transverse momentum into large longitudinal momentum [74]. These particles can then exit the longitudinal RF acceptance (buckets), i.e. the region of stable motion in the longitudinal plane, and be therefore lost.

Magnetic field errors and non-linear effects Dipole field and gradient errors as well as small misalignments of the quadrupoles may lead to orbit perturbations. Non-perfect dipoles and quadrupoles introduce high order fields, and therefore linear imperfections in the machine. Both magnetic field errors and non-linear effects result in controlled beam losses in the accelerator.

Collective effects There are three main categories of collective effects * which can result in beam instabilities, blow-up of the emittance and eventually beam losses:

*. The collective effects are the effects related to the beam's own Coulomb force field on itself and on its environment [75].

Beam-beam interactions: In circular colliders, collision points or close to them, beams interact with each other producing large tune spreads and beam instabilities.

Space charge: The space charge effect describes the effect of the beam's own Coulomb field on the beam itself (beam-self interaction), resulting in tune spreads.

Wake fields: The wake fields are EM fields created in the accelerator environment, such as the beam pipe, during the beam passage. These fields can act back on the beam, causing beam instabilities.

Residual gas scattering The beam particles may interact with residual gas particles in the cavity by either elastic or inelastic Coulomb scattering, resulting in direction and momentum modifications leading to or directly causing beam losses.

Halo scraping The beam halo or long tails of the beam distribution are an inevitable feature of the beam and a well-known beam loss source in all machines. The collimation or scraper systems are designed to localise these losses in designated positions in the machine.

2.2.2 | Irregular losses

The irregular (or uncontrolled, or fast) beam losses are usually unexpected losses which usually occur due to the malfunctioning of one or more accelerator elements. These losses are characterised as avoidable [73], since they can be prevented if the entire accelerator equipment is operating correctly. The collimator system might be able to protect from a fraction of these losses depending on the origin. However, since these losses can be highly destructive to the machine elements, their allowed levels for each part of the machine have to be defined and set during normal operation. Sometimes, during machine studies or commissioning, irregular beam losses are set up or allowed in order to examine the machine tolerance. An example of such studies are the superconducting magnet quench tests [76, 77]. Some common sources of irregular beam losses are listed below:

Unforseen aperture limitations The misalignment or only partial retraction of elements that move into the beam, such as girders, collimators, or beam intercepting devices like screens, may be the reason for unforeseen aperture limitations that can induce high beam losses. Another source of aperture limitations may emerge from unforeseen orbit bumps. These might be the result of quadrupole misalignment or false readings of beam instrumentation, such as beam position monitors, which lead to unnecessary beam orbit corrections. Aperture limitations can also arise from the excitation of fraction of the beam to high amplitudes by fast transverse kicker magnets.

Dust In the LHC, particles named as Unidentified Falling Objects (UFOs) were observed to be the source of fast, localised beam losses and were identified as a limitation to the accelerator performance. These events were only observed by the LHC BLM system, and have been attributed to the interaction of the beam with micrometer sized metallic dust [78], giving an indication of how microparticles from the beam line may be the source of irregular losses.

Issues of the RF system (electron machines) Phenomena such as RF trips and drifts of the RF system due to temperature changes in the klystron gallery can be the source of fast beam losses in an accelerator.

Vacuum leaks In the case of even small vacuum leaks the beam interacts with the residual gas, with a fraction of it being lost in the machine. In this way, pressure bumps are distinguished by the BLMs as highly localised loss rates.

Uncaptured beams Due to many mechanisms, such as faulty injection, intra-beam scattering, beam-beam interactions and malfunctioning equipment, a fraction of the bunch may be driven out of the RF acceptance. While the beam is accelerated, these uncaptured particles will then become a source of uncontrolled beam losses.

2.3 BLM Physics

The field of beam loss monitoring requires a good knowledge of particle and nuclear physics for the two steps of the beam loss detection process. The first step, including the interaction of the lost particles with the accelerator materials and the secondary particles at the location of the detector. The second step refers to the interaction of this outcome with the detector, in order to produce a measurable signal. In this section the principal method of particle detection, i.e. the ionisation process, and the generation of particle cascades are summarised.

2.3.1 | Electromagnetic interactions of ionising radiation with matter

Charged particles interact electromagnetically with matter mainly through collisions and radiative losses, as described in the following paragraphs. Depending on the material and the geometry of the absorber, these interactions might be followed by secondary electron emission or scintillation (described in Subsections 2.4.3 and 2.4.4 respectively), while other EM interactions of charged particles include the Cherenkov effect (presented in Section 3.1) and optical transition radiation (described in [1, 79]).

Heavy charged particles

When a charged particle passes through matter, it interacts electromagnetically with the atomic electrons and loses energy due to ionisation and atomic excitation. The average energy loss (or stopping power) of a moderately relativistic heavy particle per unit length is well described by the Bethe formula [1]:

$$-\frac{dE}{dx} = K\frac{Z}{A}\frac{z^2}{\beta^2}\left[\frac{1}{2}\ln\frac{2m_e c^2\beta^2\gamma^2 W_{max}}{I^2} - \beta^2 - \frac{\delta}{2}\right] \tag{2.1}$$

usually given in MeV/(g/cm^2), with Z, A the atomic number and mass weight (in g$\cdot$ mol^{-1}) of the medium and I its mean excitation energy in eV, z the charge of the incident particle,

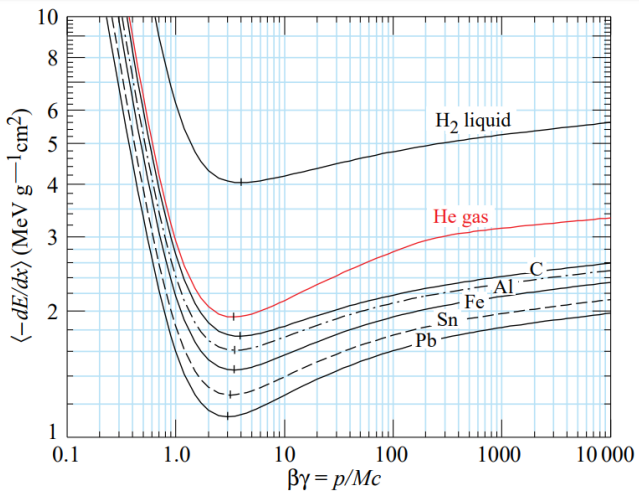

Figure 2.2 – Mean Energy Loss of muons in different materials [1].

$m_e c^2 = 0.511\ MeV$. The factor K is equal to

$$K = 4\pi N_A r_e^2 m_e c^2 = 0.3017\ \frac{cm^2}{mol} \tag{2.2}$$

since $N_A \simeq 6.023 \cdot 10^{23}\ mol^{-1}$ the Avogadro number and $r_e \simeq 2.82\ fm$ the classical electron radius. W_{max} is the maximum energy transfer to an electron in a single collision, and for an incident particle of mass M (MeV/c^2) is given by:

$$W_{max} = \frac{2m_e c^2 \beta^2 \gamma^2}{1 + 2\gamma m_e/M + (m_e/M)^2}. \tag{2.3}$$

Finally, the parameter δ is the density effect correction to ionisation energy loss. The δ describes the screening of the transverse electric field of incident relativistic particles by the charge density of the atomic electrons, and is important in dense absorber materials.

The mean energy loss of moderately relativistic particles in different materials is shown in Figure 2.2. In the beginning, an energy loss proportional to the factor $-\beta^2$ of the Bethe equation is observed until a minimum ionisation is reached. The energy loss pattern is similar for all materials, though it slightly increases with Z with the exception of hydrogen. The logarithmic increase of the Bethe formula follows, showing a similar behaviour for the dense materials due to the density effect correction, and differs only in the He gas where the δ parameter is not applied. In practical cases, most relativistic particles are close to the minimum energy loss rate, and are considered to be Minimum Ionising Particles (MIPs) [1]. The stopping power of minimum ionising particles in different chemical elements is shown in Figure 2.3.1. In light mediums, the energy loss of a MIP is approximated as [79]:

$$\left.\frac{dE}{dx}\right|_{\text{MIP}} \approx 2\ MeV/(g/cm^2) \tag{2.4}$$

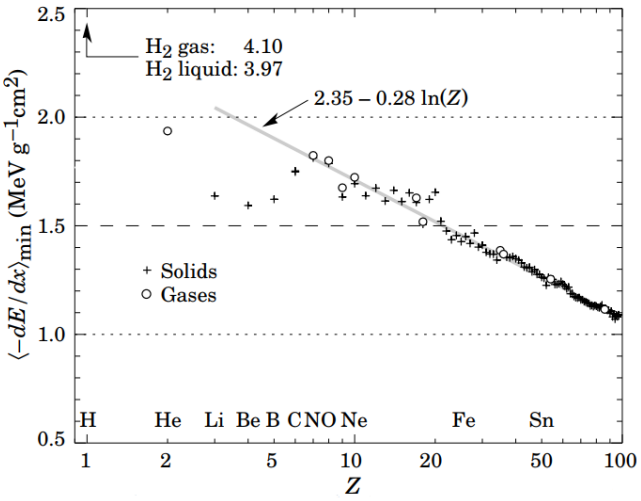

Figure 2.3 – Stopping power at minimum ionisation with a fit (straight line) for Z>6 [1].

At sufficiently high energies (i.e. several hundreds of GeV for muons and pions in iron) the radiative losses (bremsstrahlung, described below) dominate the EM interactions of heavy charged particles. These processes are characterised by low cross sections and hard photon spectra [1].

Fast Electrons

In the case of electrons, the energy loss due to ionisation and atomic excitation can be written as [79]:

$$-\frac{dE}{dx} = K\frac{Z}{A}\frac{1}{\beta^2}\left[\ln\frac{m_e c^2\gamma^2}{2I} - \beta^2 - \frac{\delta}{2}\right] \tag{2.5}$$

in which the differences stem from the fact that the incident particle and the released electron have the same mass, and additionally cannot be distinguished after a collision. Moreover, since the screening effects are different than those of the heavy ion case, the parameter δ takes also different values. Due to their very small mass, electrons fall into the category of MIPs for energies as low as 1 MeV.

Along the ionisation losses, electrons lose energy also due to a phenomenon called *Bremsstrahlung*, or braking radiation, which describes the emission of radiation when a charged particle interacts with and is decelerated by the Coulomb field of a nucleus. The radiative losses are inversely proportional to the square of the particle's mass, and are therefore negligible for heavy particles.

The Bremsstrahlung dominates for electron energies greater than a critical value E_C, i.e. the energy value in which the radiative and the collision losses are equal, which is approximated as:

$$E_C = \frac{(800\,\text{MeV})}{(Z+1.2)} \tag{2.6}$$

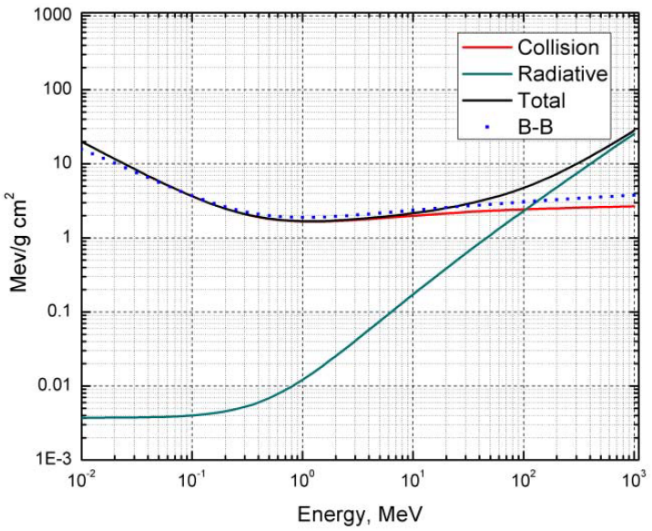

Figure 2.4 – Collision, radiative and total stopping power for electrons in nitrogen and Bethe-Bloch (B-B) evaluation [2]

while the ratio of radiation and collision losses for an electron of energy E_{e^-} in MeV is given by:

$$\frac{(dE/dx)_{rad}}{(dE/dx)_{coll}} \simeq \frac{E_{e^-} \cdot Z}{700} \tag{2.7}$$

Figure 2.3.1 shows a comparison of the radiation and the collision losses for electrons in nitrogen, with respect to the electron energy.

Photons

The photons, in particular gammas and X-rays, are always present as secondaries in a particle accelerator and especially in a beam loss shower. There are three main interactions mechanisms with matter, the photoelectric effect, the Compton effect and the pair production. The energy regions in which each phenomenon is dominant depending on the material of the absorber is shown in Figure 2.5(a). Two other interactions, the photon-photon scattering and the photonuclear interactions, are ruled by very low cross sections [79]. During the latter, a photon of an energy greater than a few MeVs enters and is absorbed by a nucleus, exciting it. The nucleus de-excitation is accompanied by the emission of a proton or a neutron [80].

Photoelectric effect The photoelectric effect is the dominant phenomenon for low photon energies, i.e. below 100 keV. During this effect, the photon with energy E_γ interacts with an atom and completely disappears while kicking out an electron, most probably of the external (K) shell. The photoelectron has an energy E_{e^-} equal to

$$E_{e^-} = E_\gamma - E_b \tag{2.8}$$

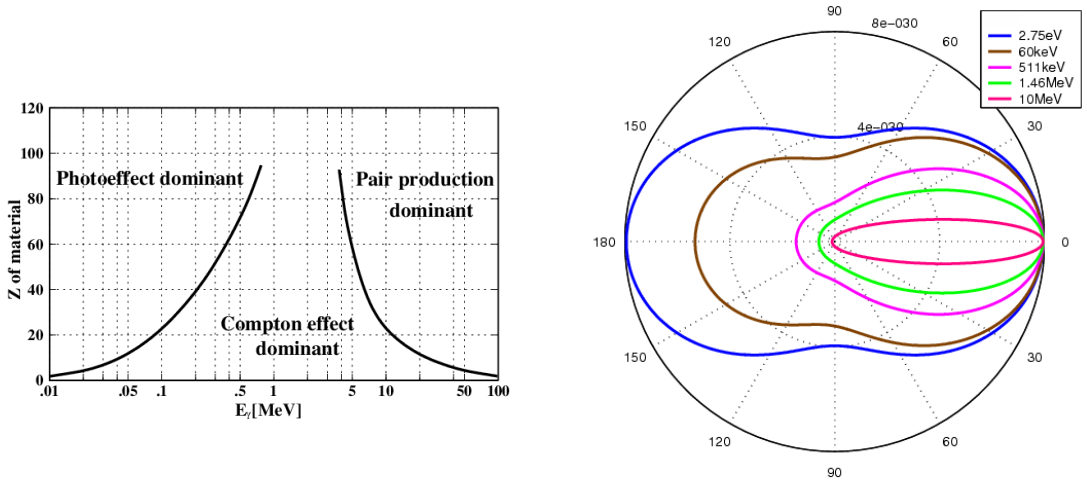

(a) (b)

Figure 2.5 – (a) Dominant interaction process for photons of energy E_γ in a material of atomic number Z (b) Angular distribution of the Compton scattered photons [81]

where E_b is the binding energy of the electron in the atom. During the de-excitation of the atom, one or more characteristic X-rays may be emitted. The cross section of the photoelectric effect is proportional to Z^5.

Compton effect The Compton effect appears at higher photon energies, between approximately 100 keV and 10 MeV, and describes the scattering of the photon by an atomic electron of the medium, known as the recoil electron. The electron is assumed to be at rest before the scattering, and the energy of the scattered photon E'_γ with respect to its scattering angle θ_γ is calculated from:

$$E'_\gamma = \frac{E_\gamma}{1 + \frac{E_\gamma}{m_e c^2}(1 - \cos\theta_\gamma)} \tag{2.9}$$

The angular distribution of the scattered photons is given by the Klein-Nishina formula, which is shown in Figure 2.5(b). It can be observed that at lower photon energies the photon backscattering is highly probable, whereas for higher incident photon energies forward scattering dominates.

Pair production For gamma-ray energies greater than $2m_e c^2$ the pair production takes place, which dominates for $E_\gamma \gtrsim 10$ MeV. When in the Coulomb field of the nucleus or (with lower probability) of an electron, the photon disappears and is replaced by an electron-positron pair.

2.3.2 | Mechanism for generation of secondary particles

The mechanisms for the generation of secondary particles from the interaction of the beam loss particles with the accelerator material are the electromagnetic and the hadronic cascade,

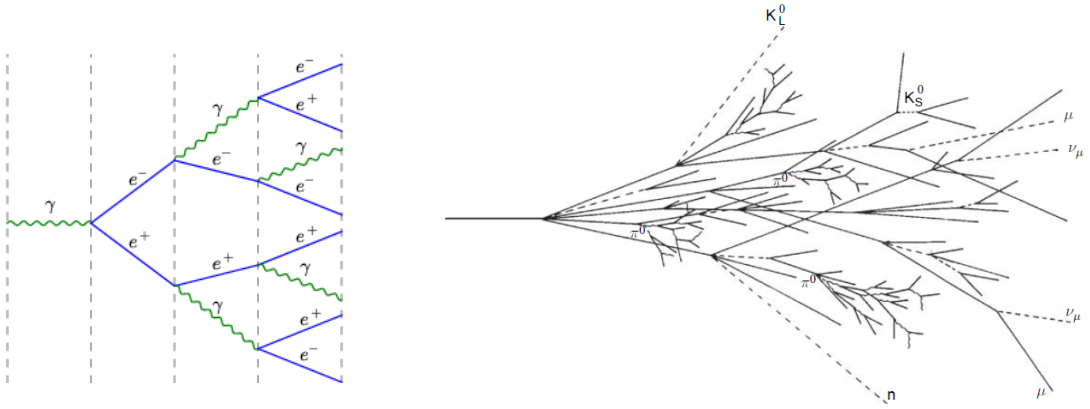

(a) (b)

Figure 2.6 – Development of an electromagnetic (a) and hadron (b) cascade [79].

which are illustrated in Figures 2.6(a) and 2.6(b) respectively.

Electromagnetic cascade An electromagnetic cascade appears when a high energy electron, positron (with $E_{e^-} \gg E_C$) or photon (with $E_\gamma \gg 2m_e c^2$) interact with a medium. The electron generates gamma rays through bremsstrahlung, while the photons are replaced by electron-positron pairs through pair production. As a result a single electron, positron or photon initiates an avalanche or *electromagnetic shower*, which continues developing until the photons arrive to energies below the pair production threshold, and the electrons/positrons below the critical energy.

Hadronic cascade The hadronic cascade appears from the inelastic hadronic processes of an incident hadron, which results in secondary particles, comprising mainly pions (charged and neutral), kaons, nucleons and other hadrons. The secondaries produce a further hadron generation, and this process repeats itself resulting in a cascade. A large component of the secondaries are neutral pions, which quickly decay in two photons ($\pi^0 \longrightarrow \gamma\gamma$) and thus coupling hadronic with electromagnetic showers [79].

The generation and evolution of EM and hadron cascades is a highly complex process. To estimate the expected radiation field in the high risk locations of an accelerator, Monte-Carlo codes are employed. Among the most widely used Monte-Carlo codes are MCNP [82], Geant4 [83] and FLUKA [84, 85]. Combined with some beam dynamics code for the simulation and tracking of the beam loss primaries, the above codes estimate the generation of secondaries and their transport in a medium, and hence the particle shower. The use of such codes is invaluable for the selection of the appropriate detector for each machine, as well as its calibration and ideal location for its installation.

2.4 Beam Loss Monitors

Each accelerator is a unique machine, the choice for the beam loss monitoring system of which strongly depends on its specifications. Some of the parameters to be considered in order to select the most appropriate BLM, as summarised from [2, 66, 73] are:

- Type of output (current-integrating or pulsed).
- Sensitivity and dynamic range.
- Bandwidth (time resolution).
- Radiation hardness. This depends on the material of the detector and the radiation environment of the machine (type of radiation).
- Complexity of system end-to-end online tests
- Calibration aspects: importance and frequency of performing a calibration, ease and uniformity (unit to unit) of calibration, calibration drifts e.g. due to ageing, radiation damage or outgassing.
- Sensitivity to background radiation (e.g. synchrotron radiation, RF cavity background) and possibility of shielding, sensitivity to magnetic fields.
- Sensitivity to voltage drifting.
- Reliability
- Robustness, physical size, positioning.
- Complexity of electronics
- System cost (including the electronics).

As a result of this diversity of requirements, a variety of detectors have been developed and are being used in accelerators as beam loss monitors in the past decades, described in detail in [1, 66, 73, 79, 86]. In this section the detectors commonly used as BLMs are briefly presented. At the end of this section, Table 2.1 summarises the main characteristics of the most widely used BLMs.

2.4.1 | Ionisation Chambers

The Ionisation Chambers (ICs) belong to a well-known family of detectors, used as BLMs in many accelerators. They are chambers filled with gas and containing electrodes, on which high voltages of up to several kV are applied. The most common gases used are argon and nitrogen [2].

The result of ionising particles crossing the detector is the generation of electron-ion pairs in the contained gas. The further operation of the detector depends on the applied voltage, as shown in Figure 2.4.1. If the applied electric field is lower than the Coulomb field in the vicinity of the parent ion, the produced electrons cannot escape it and recombine with the ion. This is the *recombination* region. As the electric field increases, a number of electrons and ions drift towards the anode and the cathode respectively. The number of collected charges increases with higher voltage until a saturation level is reached, when all electrons are collected; this signifies the onset of the *ionisation* region . This region shows no dependence of the collected charge from the bias voltage and is therefore the most typical for ionisation chambers because their sensitivity remains stable for fluctuating voltage. An additional voltage increase leads to

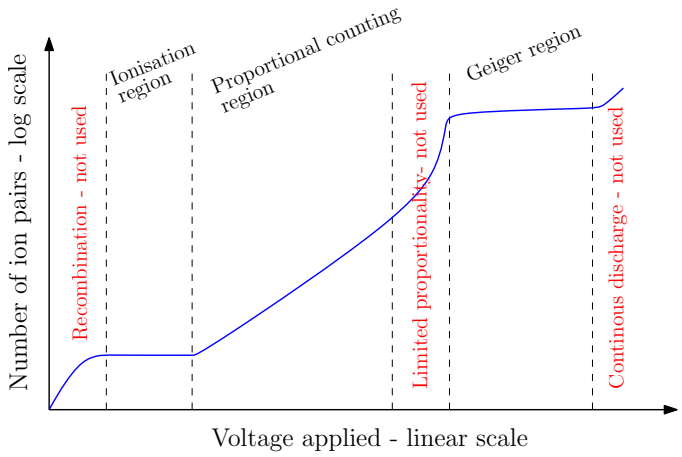

Figure 2.7 – Schematic of different regions of ionisation chambers, based on Figure from [89]

the *proportional* region, where the drifting electrons gain enough energy to produce further ionisations and avalanche on their path. Finally, further raise of the voltage leads to a discharge and breakdown of the gas. This is the *Geiger* region, during which the ions create secondary ionisation and avalanche [2, 73]. The typical mode used for ICs is the ionisation.

The signal of the ionisation chamber is a combination of the detected electrons and ions. The former, travel 10^3 times faster than the later in typical gases, as a result the produced signal starts with a large peak from the detected electrons and an ion tail follows. Compared to other BLMs, the time response of ICs is slow, ranging between 0.1 and 1 µs [87]. Both the time response and the dynamic range of the detector are related to its geometry, while the length of ICs which are used as BLMs may vary from some tens of centimetres to 3 m or longer. The ionisation chambers are today the principal loss monitor of many hadron machines, including the LHC [2].

Advantages The ionisation chambers are very robust detectors and require low maintenance. Additionally, when built with radiation tolerant materials (such as ceramic, glass and metal) and a careful design they are radiation hard. Furthermore, since in the ionisation region the sensitivity remains the same for fluctuating voltage, their calibration is determined only by their geometry. Among their advantages stands also their large dynamic range, which can reach 10^6-10^8 [2, 73]. Finally, their usually large sensitive volume results in a large solid angle coverage [88].

Drawbacks The main disadvantage of the ionisation chambers is their slow time response, with the best one being of the order of 1 µs

Long Ionisation Chamber

In the 1960s very long ionisation chambers were introduced, in order to replace the localised ionisation chambers described above, which protect only a small part of the accelerator,

and achieve a good coverage of large parts of the beam line. These devices are known as Panofsky Long Ionisation Chambers (PLICs), from Panofsky [90] who originally proposed them for SLAC (Stanford Linear Accelerator Laboratory, renamed in 2008 as SLAC National Accelerator Laboratory [91]).

A PLIC is a hollow coaxial cable filled with a gas such as the Ar/CO_2 mixture, with the outer conductor grounded and the inner conductor set to a high voltage of typically 200 to 500 V. Their length usually ranges between 30 and 100 m, however the first one installed at SLAC was 3.5 km long. Today, these monitors are used in various facilities such as the SLC (SLAC Linear Collider) which is nearly entirely covered with a few PLICs, the ELBE (Electron Linac for beams with high Brilliance and low Emittance), the BNL (Brookhaven National Laboratory) 200 MeV linac and the APS (Advanced Photon Source) [73, 92].

Characteristics The PLICs have a uniform sensitivity, similar to that of conventional ionisation chambers. They are radiation hard, with their tolerance to radiation depending on the selection of insulator and spacer. Additionally, they are a cost-effective solution for the coverage of a beam line. Unlike the conventional ICs, designs of the PLICs can be very fast, and a rise time of less than 15 ns and a 150 ns decay time has been demonstrated in APS [93]. The position resolution depends on the PLIC characteristics, i.e. their geometry and the gas filling, and a resolution of about 1.5 m has been achieved for short PLICs. The dynamic range of PLICs is significantly lower than that of conventional ICs, reaching 10^4 with certain amplifiers [73].

2.4.2 | PIN diode BLMs

The electrons existing in crystalline materials are allowed in distinct energy bands, the valence band which represents those electrons that are bound to specific lattice sites, and the conduction band where the electrons freely drift within the crystal. In semiconductors the energy gap between the two bands E_g, called bandgap, is of the order of $E_g \simeq 1\,\text{eV}$ (e.g. $E_g \simeq 1.11\,\text{eV}$ in Si). The radiation that crosses a semiconductor results in the excitation of the electrons to the conduction band generating electron-hole pairs [86].

PIN-diodes are semiconductor parts consisting of three regions, one where positive and one where negative carriers dominate (p-type and n-type respectively), separated by a not doped region called intrinsic or depletion region. This region has a thickness of the order of 100 µm and contributes to a large number of charge carriers. A bias voltage, usually between 5 and 20 V is applied to the diode. When an ionising particle crosses the PIN-diode, it creates electron-hole pairs in the intrinsic region. The bias voltage forces the negative and positive carriers to move towards the cathode and anode respectively, producing a signal [94].

In PIN-diode BLMs, two diodes are mounted face-to-face, in order to count the coincidence caused by particles crossing both detectors and therefore avoid low energy photons such as those emitted by synchrotron radiation (these photons will be absorbed in one of the two diodes). A PIN-diode BLM and its schematic are shown in Figure 2.8.

Advantages The advantages of the PIN diode BLMs include their insensitivity to synchrotron radiation, their fast response of the order of 10 ns and their non-dependence

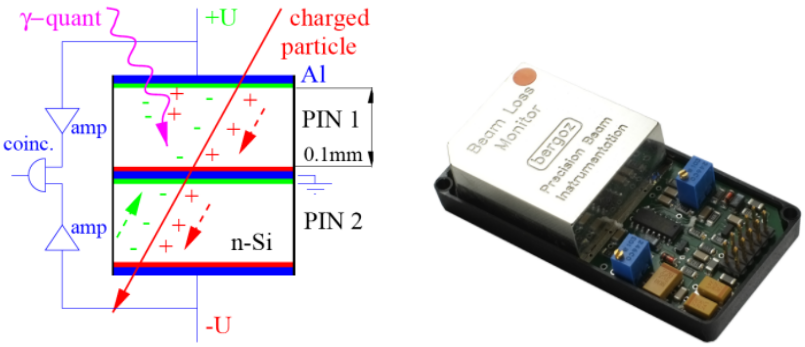

(a) (b)

Figure 2.8 – (a) Scheme of two PIN diodes in coincidence mode [95] (b) A PIN diode [96].

on the bias voltage [87]. Additionally, they are characterised by a large dynamic range reaching values $>10^8$, high sensitivity and a low dark count rate [73, 92]. Finally, PIN-diode BLMs are cost-effective detectors.

Drawbacks Being a silicon detector, PIN diodes are not radiation hard. However, tests in HERA (Hadron-Electron Ring Accelerator) have shown no damage for a dose of 1 MGy [92]. Additionally, their small size provides a small solid angle coverage of the beam loss.

2.4.3 | Secondary Emission Based BLMs

When an energetic charged particle impinges on or emerges from a solid metallic surface, some of the electrons that will be produced during the ionisation processes may migrate to the surface with sufficient energy to escape it. These electrons are low-energetic (for alpha particles on carbon surfaces their energy range is between 60-100 eV) and are conventionally called *secondary electrons*. The dE/dx value of the incident particle can act as predictor of the secondary emission yield, which is higher for heavy ions than for fast electrons. Another important parameter is the work function of the material, with a low work function indicating a higher yield. However, the number of emitted electrons per MIP is for many metals of the order of a few percent [73]. Further information on secondary emission can be found in [97, 98].

In this subsection two secondary emission-based detectors used as BLMs are presented, the Secondary Emission Monitors (SEMs) and the Aluminium Cathode Electron Multipliers (ACEMs).

Secondary Emission Monitor (SEM)

Based on the secondary electron emission, the SEM is a robust and cost-effective monitor, as it comprises of two bias plates and one signal electrode in the middle. The plates are installed in a metal vacuum container. In order to avoid the signal contamination from gas

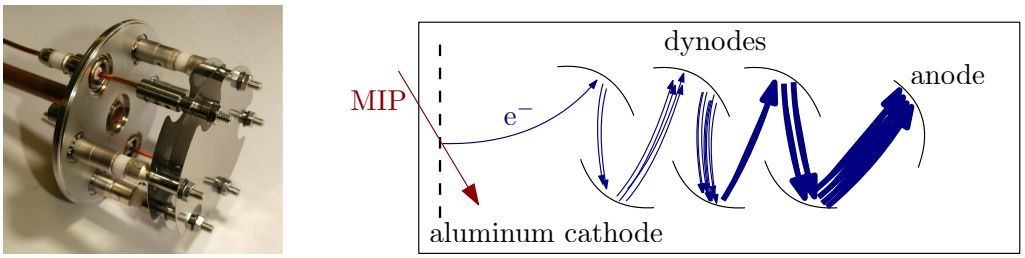

(a) (b)

Figure 2.9 – (a) The SEM of the LHC [98] (b) Scheme of an ACEM

ionisation, a gas pressure lower than 10^{-4} mbar must be reached in the container [98]. The dynamic range of SEMs is expected to be over 10^5. To amplify their signal, the use of current amplifiers or Photo Multiplier Tubes (PMTs) is possible. Together with the ICs, the SEMs are used as the principal BLM system of the LHC [2, 98].

Advantages Consisting principally of metallic parts (when no PMT or amplifier is used), the SEM is robust and very radiation hard, ideal for high radiation areas. Additionally, being based on the very fast phenomenon of secondary emission, the SEM is a very fast detector with response of the order of few nanoseconds. Finally, the monitor is characterised by very high linearity [73, 98].

Drawbacks The main drawback of SEMs is their low sensitivity, which is defined by the secondary electron emission yield as a few percent [2].

Aluminium Cathode Electron Multiplier (ACEM)

The ACEM is essentially a PMT (the PMTs are described in detail in Subsection 3.3.2), the photocathode of which has been replaced by an aluminium cathode. Secondary electrons are emitted by the interaction of beam loss particles with the aluminium cathode, and are multiplied in the dynodes of the device, as shown in Figure 2.9(b) [95]. Like in the case of SEMs, the sensitivity of ACEMs is defined by the secondary electron emission yield. An example of recent ACEM use is the Free Electron Laser in Hamburg (FLASH), where 18 monitors were installed. [92].

Advantages Among the advantages of ACEMs is their high gain and time response, as well as their radiation hardness [88, 92, 95].

Drawbacks Though being radiation hard, the ACEM suffer in terms of homogeneity of their response to the same amount of beam losses, due to the ageing of the PMTs and the darkening of its window. As a result, in high radiation environments like the CERN Proton Synchrotron (PS) they have to be frequently re-calibrated. Additionally, such monitors are small in size, and therefore provide a small solid angle coverage of the beam losses [88]. Finally, their off-the-shelf unavailability renders ACEMs high-priced monitors [92].

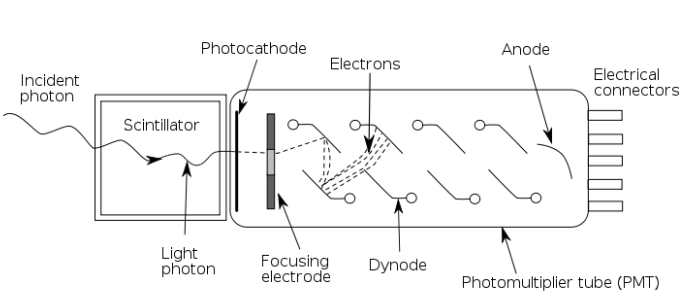

(a)

(b)

Figure 2.10 – (a) The operating principle of a scintillator and (b) Different scintillator geometries [99].

2.4.4 | Scintillation Detectors

Scintillation describes the process under which ionising radiation (charged particles, photons) excites the electron of materials, referred to as scintillating materials. Upon deexcitation, these emit visible radiation, the yield of which is ideally linearly proportional to the deposited energy. Two categories of scintillating materials exist, the organic and inorganic. The former are excited in their molecular energy level structure while the latter in the energy states determined by the crystal lattice of the material. Since the scintillating light is on the visible spectrum, for its transport within the scintillator, this has to be transparent. For charged particles, the scintillation photon yield Y_{sc} can be calculated as:

$$Y_{sc} = R_{sc}\frac{dE}{dx} \tag{2.10}$$

where R_{sc} is the scintillation efficiency, which depends on the material. Indicative values of the scintillation efficiency are for the NaI crystal (inorganic) $R_{sc} = 8 \times 10^4\ \gamma/MeV$ and for the NE102 plastic (organic) $R_{sc} = 2.5 \times 10^4\ \gamma/MeV$ [87]. The scintillation detectors consist of a scintillator coupled to a photosensor. When charged particles interact with the scintillator, the emitted light is guided to the photosensor via light-guides based on the total internal reflection (described in Subsection 3.1.1). Apart from ionising radiation, the plastic scintillators may also detect neutrons due to their scattering with the hydrogen atoms. The absorption of the emitted photons in the scintillator and their escaping (failing internal reflections) are the main reasons for light attenuation in the detector.

Normally as a photosensor for the scintillating light, a PMT is used (described in Subsection 3.3.2). A dynamic range of 10^8 has been measured with such a system [100]. To achieve a good detection efficiency, a good coupling between the PMT and the scintillator is important. This can be achieved by adjusting the light-guide size and the photocathode window and the matching of the scintillator emission spectrum with the PMT spectral response. Moreover, the use of an optical grease between the scintillator and the photosensor to couple their refractive indices (which are similar) contributes to a better coupling of the two by avoiding internal reflections at their connection.

Advantages The scintillators are characterised by their high sensitivity, starting from single photon detection, and a generally high gain and linearity which depends on the PMT and is on the range of $G_{PMT} = 10^5 - 10^8$. Additionally, in the case of organic and liquid scintillators, their fast response between 1 and 10 ns and their great modularity in shapes and size are two considerable advantages.

Drawbacks The main drawback of scintillators is their limited radiation hardness. Depending on their material, the scintillator transmission decreases to $1/e$ of its original one at irradiation levels between 0.01 and 1 MGy. In the inorganic case, their usually slower time response (0.1-1 µs) may constitute a limiting factor [87]. Finally, the varying (within a factor of 10) gain of the same type of PMT is a known disadvantage of the sensor, which can be mitigated via a calibration of all BLM sensitivities through high voltage adjustment and a constant monitoring of the applied voltage.

The following table summarises information on the most commonly used beam loss monitors, including the Cherenkov-based optical fibre BLMs that are described in the following chapter.

Table 2.1 – Summary of the detection characteristics of different Beam Loss Monitors

Detector	**Energy to create one electron [eV/e$^-$]**	**Number of e$^-$/cm/MIP** (depends on $\frac{dE}{dx}$, density)	**approx. Sensitivity [nC/rad]**	**Dynamic range**	**approx. Time Response**
Ionisation chamber	22-95	≈100 *	$500 \cdot G_{elec}$ (1 L)	$10^5 - 10^8$	$(0.1-1)$ms
Plastic scintillator	250-2500	10^3-10^4	$1.7 \cdot 10^4 \cdot G_{PMT}$ (1 L)	limited by PMT	$(1-10)$ns
Inorganic scintillator	50-250	10^4-10^5	$10^5 \cdot G_{PMT}$ (1 L)	limited by PMT	$(0.1-1)$µs
PIN diode	3.6	10^6	$50 \cdot G_{elec}$ (1 cm^3)	$> 10^8$	$(1-10)$ns
SEM/ACEM	2-5%/MIP	0.02-0.05	$2 \cdot 10^{-3} (\cdot G_{ACEM})$ (8 cm^3)	$> 10^5$	< 10 ns
Cherenkov	$10^5 - 10^6$	≈ 10 (H_2O) −200 (SiO_2)	$0.2 \cdot 10^{-3} \cdot G_{PMT}$ (1 m long, ∅ 100 µm)	limited by PMT	instantaneous (limited by PMT)

*. Ar, 1 atm, 20 °C

2.5 Summary

In an accelerator there is a plethora of beam losses, some unavoidable and others usually occurring due to the malfunctioning of accelerator elements, that might be destructive for the machine. Particle detectors are installed to monitor these losses (BLMs), protecting the

machine and providing beam diagnostics. Different types of BLMs are being used today, such as ionisation chambers, secondary emission monitors, scintillators, PIN diodes and Cherenkov detectors, with the underlying detection principle being (with the exemption of the latter) ionisation. For the selection of the appropriate detector, the characteristics of the accelerator and the machine protection requirements have to be taken under consideration. Computer simulations contribute to the BLM choice by estimating the type and levels of radiation in different locations of a machine.

3

Third Chapter

Optical fibre Based Detectors

The current chapter presents the theory behind and the design of an advanced, optical fibre-based beam loss monitor. In Section 3.1 the theoretical background and necessary physical principles are summarised, including the total reflection of light and the Cherenkov effect. In Section 3.2 the operation principles and characteristics of optical fibres are described. Section 3.3 outlines the photosensors relevant to the scope of this thesis: the Silicon Photon Multiplier (SiPM) and the Photo Multiplier Tube (PMT) (Subsections 3.3.1 and 3.3.2 respectively). Finally, in Section 3.4 the combination of optical fibres and photosensors towards the development of the Optical fibre BLM (OBLM), is presented. In particular, Subsection 3.4.1 summarises the characteristics and fundamentals ruling this system, and Subsection 3.4.2 describes the design of a high-sensitivity, low-noise OBLM system.

3.1 Theoretical Background

3.1.1 | Refractive index and Total Reflection of Light

The refractive index n is a fundamental optical property of materials, and is defined as the ratio of the speed of light in space to the speed of light v in one material. Since the latter depend on the light frequency (or wavelength), so does the refractive index which is given by

$$n(\lambda) = \frac{c}{v(\lambda)} \tag{3.1}$$

Typical values of the refractive index in optical frequencies are approximated as $n_{air} \simeq 1.00$ for air, $n_{H_2O} \simeq 1.33$ for water and $n_{SiO_2} \simeq 1.47$ for Silica (SiO_2) [101].

The phenomenon of the total reflection of EM waves on the interface of two mediums can be described using the refractive indices of these mediums. Lets assume an interface between two homogeneous and isotropic media with refracting indices n_1 and n_2 such that $n_1 > n_2$. An EM wave propagating on the medium 1 and impinging on the interface will be totally reflected if the angle of the incident ray to the normal of the interface θ_i is greater than a critical value

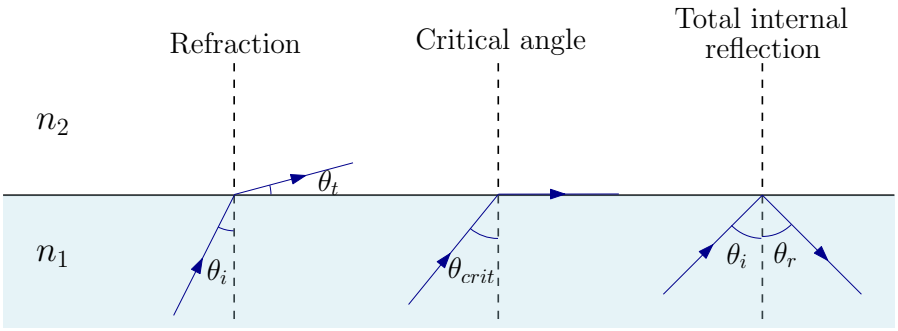

Figure 3.1 – Illustration of Snell's law for the refraction, critical angle and total internal reflection.

θ_{crit}. This value is calculated from the Snell's law of refraction *, as [102]

$$\sin(\theta_{crit}) = \frac{n_2}{n_1} \tag{3.2}$$

During total internal reflection, the angle of the reflected ray to the normal of the interface θ_r, is equal to that of the incident ray, hence $\theta_i = \theta_r$. An illustration of Snell's law for the refraction, critical angle and total internal reflection is shown in Figure 3.1.

3.1.2 | Cherenkov effect

The Cherenkov effect describes radiation which is emitted when a high energy charged particle transverses a medium in which the velocity of the particle $v = \beta c$ (where $\beta = \sqrt{1 - \frac{1}{\gamma^2}}$ and γ is the Lorentz factor), is greater than the phase velocity of light in the same medium. The phenomenon was first observed by P. A. Cherenkov and S. I. Vavilov [103], and was theoretically described by I. E. Tamm and M. Franck in 1937.

The source of Cherenkov radiation is the EM interaction of the particle with the atoms of the medium: in the vicinity of the particle the atoms get polarised, acting as EM dipoles. If the particle is slow ($v < \frac{c}{n}$), these dipoles are distributed symmetrically around it, as illustrated in Figure 3.2(a). Therefore, the polarisation fields are also symmetrical around it and no field, hence no radiation, is observed at large distances.

However, if the particle velocity in the medium is larger than the phase velocity of light in that medium ($v < \frac{c}{n}$), then the induced dipoles are not symmetrically distributed along the particle track. An illustration of this effect is shown in Figure 3.2(b). In this case, the wavelets emitted from the polarised particles will evolve as shown in Figure 3.3(a), interfering constructively and radiating a brief EM pulse known as *Cherenkov radiation*.

It should be stressed at this point that the Cherenkov radiation is emitted by the particles of the medium due to their interaction with the crossing charged particle, and not by the particle itself. In this way, Cherenkov differs from phenomena like bremsstrahlung or synchrotron

*. The Snell's law of refraction is $n_1 \sin\theta_i = n_2 \sin\theta_t$, where θ_t is the the angle of the transmited (refracted) ray to the normal of the interface.

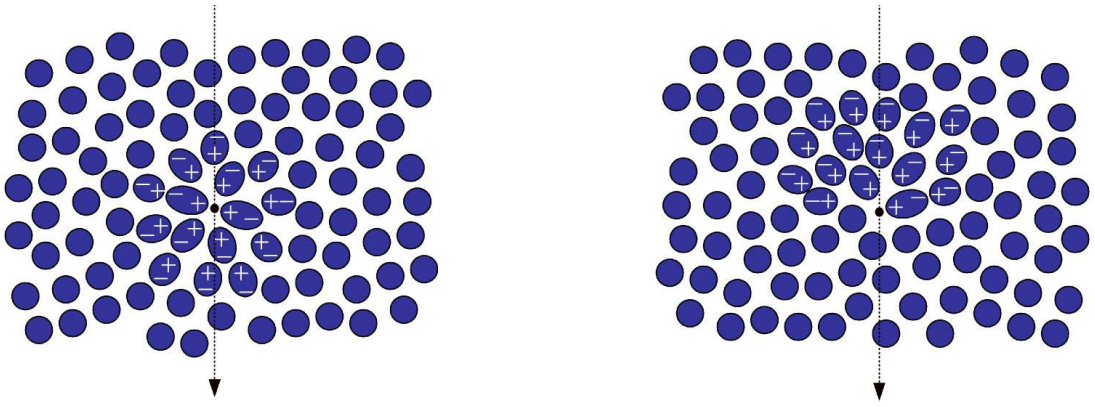

(a) $v < \frac{c}{n}$ (b) $v > \frac{c}{n}$

Figure 3.2 – Atom polarisation from a charged particle travelling through a medium.

radiation. The difference between these phenomena is obvious when observing charged particles with high mass; in this case neither synchrotron radiation nor bremsstrahlung is observed, while on the contrary Cherenkov light is emitted [104].

The emitted radiation is characterised by directionality, and is observed only at a conical plane of a particular angle θ_C with respect to the particle track . This plane is depicted in Figures 3.3(a) and 3.3(b) with a dark red line. At a time t the charged particle has travelled a distance $\beta c t$ and the EM field a distance $\frac{c}{n} \cdot t$. As a result, the Cherenkov radiation is emitted in an angle θ_C, such as:

$$\cos(\theta_C) = \frac{1}{\beta n} \tag{3.3}$$

From Equation 3.3 and for a given refractive index, the threshold velocity for the observation of Cherenkov radiation is estimated by setting the Cherenkov emission angle to zero, therefore:

$$\beta_{th} = \frac{1}{n} \tag{3.4}$$

Furthermore, when the particle is ultra-relativistic and $\beta \rightarrow 1$, the emission angle is maximum and is equal to

$$\theta_{C,max} = \arccos(1/n) \tag{3.5}$$

As an example, in silica the minimum β for Cherenkov radiation is approximated as $\beta_{th} \simeq 0.68$, and the maximum Cherenkov emission angle is $\theta_{C,max} = 47.1°$.

The threshold and maximum kinetic energy can be calculated for $\beta = \beta_{th}$ and $\beta = 0.999$ respectively from the relativistic kinetic energy of a particle E_k:

$$E_k = E_{tot} - E_0 = mc^2\gamma - mc^2$$

$$\Rightarrow E_k = mc^2\left(\frac{1}{\sqrt{1-\beta^2}} - 1\right) \tag{3.6}$$

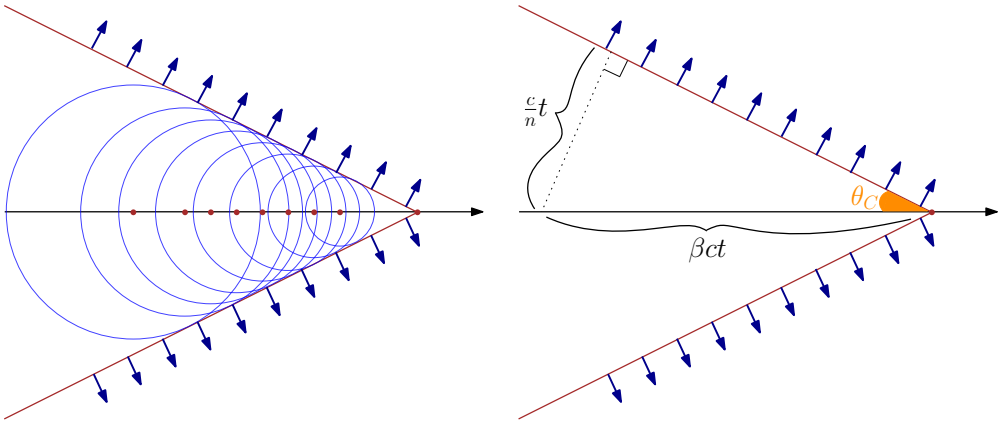

(a) (b)

Figure 3.3 – (a) Emitted wavelets along the particle track, when $v > \frac{c}{n}$, and their constructive interference (b) The geometry of Cherenkov radiation and emission angle.

The results for various charged particles that are typically found in a particle shower, in silica ($n \simeq 1.47$), are summarised in Table 3.1 [105].

Considering a constant refractive index, $n \simeq const.$, the number of Cherenkov photons dN_{ph} emitted per unit path length dL is expressed as a function of the photon wavelength λ as:

$$\frac{dN_{ph}}{dL} = 2\pi\alpha_f z^2 \sin\theta_C \int_{\beta n>1} \frac{d\lambda}{\lambda^2} \tag{3.7}$$

where $z \cdot e$ corresponds to the charge of the particle and α_f is the fine structure coefficient, $\alpha_f \simeq \frac{1}{137}$. For a charged particle with $z = 1$ and $\beta \simeq 1$, the photon yield in quartz is estimated from Equation 3.7 as approximately 100 photons/mm.

3.2 Optical fibres

The invention of the laser in the early 1960s stimulated the interest on optical components which could be used as lightwave elements. In 1966, glass-fabricated dielectric waveguides

Table 3.1 – Threshold energy $E_{kin,th}$ for the emission of Cherenkov radiation in Silica, and the kinetic energy of particles for $\beta = 0.999$, for different particles typically found in a beam loss particle shower.

Particle	$\mathbf{E_0}$ [MeV]	$\mathbf{E_{kin,th}}$ [MeV]	$\mathbf{E_{kin,\beta=0.999}}$ [GeV]
e^-, e^+	0.511	0.186	0.011
p^+, p^-	938.2	341.8	20.02
μ^-, μ^+	105.5	38.5	2.26
π^+, π^-	139.5	50.9	2.98
K^+, K^-	493.7	179.9	10.55

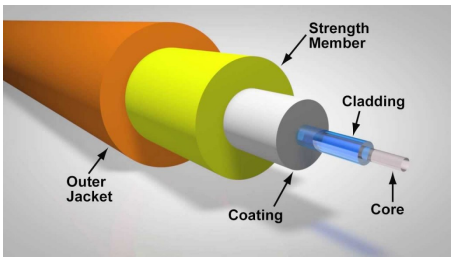

Figure 3.4 – Illustration of an optical fibre cable elements.

were proposed as a novel instrument for optical communication, to become today one of the most effective means of transmitting information: optical fibres. Nowadays, their ability for light propagation expands their spectrum of applications. One of them is the use of optical fibres as particle detectors, based on the radiative losses of particles in the fibre, and in particular on the Cherenkov emission. This chapter outlines the main principles and characteristics of optical fibres in Subsections 3.2.1 and 3.2.2 respectively, while the Cherenkov effect in optical fibres is described later, in Subsection 3.4.1.

3.2.1 | Optical Fibre Principles

The operation of optical fibres is based on the consecutive total internal reflection of light, a phenomenon described in Subsection 3.1.1. The basic optical fibre design demands two materials: one with higher refractive index for the so-called core of the fibre, and one with a lower refractive index around it, known as cladding. The light is continuously reflected in the core-cladding interface and therefore propagates in the core. The fibre material is transparent to light with the most common being fused Silica SiO_2 (also known as quartz), while the core to cladding refractive index ratio is typically 1.1 or 1.2 [105]. A buffer coating, usually of a synthetic material such a polyimide or acrylate, covers the fibre and protects it from mechanical damage, while also protecting the glass from small damages that could lead to the fibre degradation. Usually a strengthen member consisting of elements such as kevlar fibres is used to add robustness to the final product, which is lastly protected externally by an outer layer, the jacket. An illustration of an optical fibre structure is shown in Figure 3.4.

When the boundary between the core and cladding is abrupt, the fibres are called step-index (SI) fibres. One of the most critical parameters of optical fibres is the numerical aperture (NA), which is a dimensionless quantity and is expressed from the core and cladding refractive indices, n_{co} and n_{cl} respectively, as

$$NA = \sqrt{n_{co}^2 - n_{cl}^2} \tag{3.8}$$

Normally, NA ranges from 0.14 to 0.50 [101].

The numerical aperture acts as an indicator of the fibre light-trapping capability, as it is related to the nominal acceptance angle θ_α, shown in Figure 3.5. The nominal acceptance angle defines a cone at the end face of the fibre, and the rays that enter within this cone will be

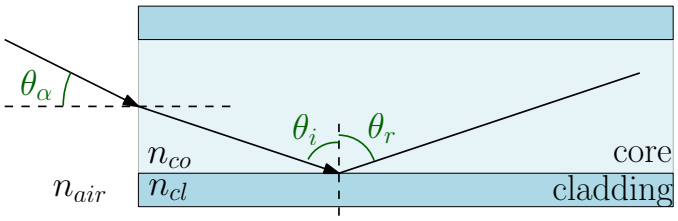

Figure 3.5 – The acceptance angle of an optical fibre.

the ones to eventually propagate. For a fibre in air, the fibre numerical aperture and acceptance cone are connected via:

$$NA = \sin(\theta_\alpha) \tag{3.9}$$

Given the symmetry of light transmission in the fibre, the light that will arrive to the other end of the fibre will also exit within the nominal acceptance cone [106].

Modes and Rays

The propagation of electromagnetic waves in optical fibres is derived in approximation from the *standard wave equations*,

$$\nabla^2\mathbf{E} = \epsilon\mu\frac{\partial^2\mathbf{E}}{\partial t^2} \tag{3.10}$$

for the electric field **E**, and

$$\nabla^2\mathbf{H} = \epsilon\mu\frac{\partial^2\mathbf{H}}{\partial t^2} \tag{3.11}$$

for the magnetic field **H**, where ϵ is the dielectric constant (or permitivity), μ the permeability of the medium and ∇^2 is the Laplacian operator. These equations are generated from the four Maxwell's equations for the behaviour of electric and magnetic fields in a linear, isotropic dielectric material without any currents and free charges [107].

The boundary conditions for the solution of the standard wave equations are imposed by the core-cladding interface, and lead to EM wavefunctions referred to as *modes*. The relevant calculations can be found in [101, 106, 108]. The number of modes that a fibre can support for electromagnetic radiation of wavelength λ is determined by the *normalised frequency* V (or V number), which for a fibre of core radius r is defined by

$$V = \frac{2\pi r}{\lambda}NA \tag{3.12}$$

When $V < 2.405$, only the so-called fundamental hybrid (with E_z and $H_z \neq 0$) electric mode HE_{11} is transmitted through the fibre, which is then called *single-mode*. Alternatively, more than one modes are supported, and the fibre is known as multi-mode fibre (MMF). The number of guided modes M in the multi-mode case can then be approximated as

$$M \simeq \frac{V^2}{2} \tag{3.13}$$

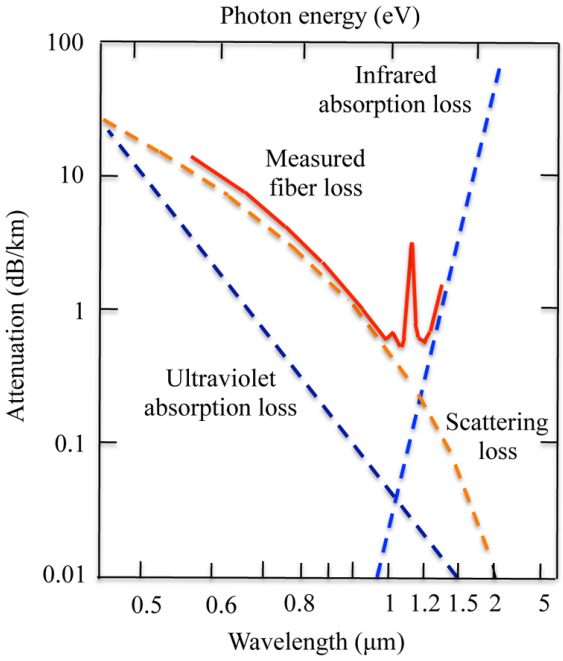

Figure 3.6 – Typical attenuation coefficient α of a GeO_2-doped silica fibre, as a function of wavelength λ [109].

Geometrical optics describe the behaviour of light through a simpler model, ignoring its wave nature and replacing it with a thin *light ray*, which in the wave description of optics is normal to the light phase fronts *. The propagation of light in the optical fibres, depending on the corresponding EM mode, is distinguished in fundamentally two types of rays: meridional and skew rays. The former are the ones that during their passage cross the fibre axis, while the latter propagate in an helical path in the fibre core and never transverse the axis.

3.2.2 | Optical Fibre Characteristics

In this subsection the main characteristics of optical fibres are presented.

Attenuation

When a light signal is travelling in an optical fibre media, the phenomena of absorption and scattering lead to an exponential decrease of the signal power. After covering a length l of the fibre, the resulting power $P(l)$ is given by equation

$$P(l) = P(0) \cdot 10^{-\frac{\alpha l}{10}} \tag{3.14}$$

*. This is valid only when light waves travel in objects much larger than their wavelength.

where $P(0)$ is the incident power. The parameter α is the power attenuation coefficient, which is defined as

$$\alpha[\text{dB/km}] \equiv -\frac{10}{l[\text{km}]}\log_{10}\frac{P(l)}{P(0)} \tag{3.15}$$

The attenuation coefficient of optical fibres strongly depends on the wavelength of the transmitted light λ, as well as the fibre material. An example is presented in Figure 3.6, representing α as a function of the wavelength, for a GeO_2-doped silica fibre. Three main factors contribute to the total attenuation profile: for wavelengths smaller than 0.5 µm, i.e. mainly ultraviolet spectrum, the propagating light is principally lost due to intrinsic material absorption by the electronic absorption bands. In the largest part of optical wavelengths and part of the infra-red, namely in approximately the 0.5-1.5 µm region, the dominant attenuation factor is *Rayleigh scattering*. Finally, in the infra-red region of wavelengths above ~1.5 µm the leading attenuation mechanism is the intrinsic absorption, associated with the atomic vibration bands in the fibre material.

The Rayleigh scattering is essentially the elastic scattering of photons by the atomic electrons of a medium. The oscillating electric fields of the photons interact with the charged particles, leading to their polarisation. Hence, the electrons act as dipoles, whose radiation is the Rayleigh scattered light [110, 111]. The attenuation due to Rayleigh scattering α_R is described as [112]:

$$\alpha_R \simeq \frac{A_R}{\lambda^4} \tag{3.16}$$

where A_R is the Rayleigh scattering coefficient which is entirely dependent on the material. For quartz, α_R can be approximated by [106]

$$\alpha_R = \frac{0.83}{\lambda^4[\mu\text{m}]}[\text{dB/km}] \tag{3.17}$$

As it can be observed in Figure 3.6, the attenuation due to Rayleigh scattering decreases rapidly, which is attributed to the $1/\lambda^4$ factor. The minimum of the attenuation can be found at ~1.5 µm, which consequently corresponds to the frequencies mainly used in telecommunication applications.

The attenuation spike around 1.4 µm is associated to the absorption from water ions in quartz, which are a residue of the fibre fabrication process. Finally, other impurities in the silica material may lead to further spikes in the attenuation coefficient.

Dispersion

A short pulse of light travelling in an optical fibre spreads in time, a phenomenon known as dispersion. There are two main contributions in MM fibers: modal and material dispersion.

The former, also known as multimode of intermodal dispersion, stems from the fact that different EM modes in the optical fibre are characterised by different group velocities. In ray theory, this can be explained by the fact that light can follow different paths with different angles in the fibre, covering various lengths and arriving at different times to its end face.

The maximum time spread per fibre unit length for meridional rays, $\Delta\tau_{mod}$, is approximated as [113]:

$$\Delta\tau_{mod} = \frac{n_{co}L}{c}\left(\frac{n_{co}-n_{cl}}{n_{cl}}\right) \tag{3.18}$$

In the case of skew rays, the dispersion is even larger.

The material dispersion, also known as intramodal or chromatic dispersion, is a consequence of the refractive index dependence on the wavelength, resulting in different group velocities for light of different wavelengths in the fibre. The chromatic dispersion time spread per unit length, $\Delta\tau_{mat}$, for two wavelength components separated by $\Delta\lambda$ is [113]:

$$\Delta\tau_{mat} = \frac{-1}{c}\left[\lambda\frac{d^2n(\lambda)}{d\lambda^2}\right]\Delta\lambda \tag{3.19}$$

The effect of both dispersion mechanisms can be estimated as [114]:

$$\text{Total Dispersion} = \sqrt{\Delta\tau_{mod}^2 + \Delta\tau_{mat}^2} \tag{3.20}$$

Radiation Effects

Optical fibres are used in a variety of applications in harsh radiation environments, such as space missions, military and civil nuclear industry, accelerators, high energy physics and fusion experiments. Therefore, the effects of ionising radiation in them is of considerable importance [3].

The effects of radiation on optical fibres are a result of its interaction with the fibre material, principally direct atomic displacements (knock-on damages) and ionisation processes [3]. The former occur if the incoming radiation particle transfers enough energy to the crystalline structure. In the case of quartz, this corresponds to 10 eV for oxygen atoms and 18 eV for Silicon. The latter leads to electron-hole pairs, which may recombine either radiatively (luminescence) or non-radiatively, through phonon generation or secondary processes, which may result in point defects in the structure.

The most significant macroscopic radiation effects in optical fibres are Radiation Induced Attenuation (RIA), Radiation Induced Emission (RIE) and change of refractive index [3]:

— The Radiation Induced Attenuation is the result of the glass absorption increase due to the generation of radiation-induced defects. The RIA changes with respect to the transmitted wavelength.

— The Radiation Induced Emission is the emission of light within the irradiated sample. This can be either Cherenkov radiation, or luminescence induced by the excitation of existing or radiation-induced point defects.

— Crystal irradiation causes their densification or swelling, leading to modifications of the glass density which depend on the silica type (amorphous, crystalline). These modifications result in changes of the fibre refractive index, and in additional alterations of its bandwidth and mechanical properties.

In general, during an irradiation strong RIA and RIL phenomena take place at the same time, while afterwards the RIA dominates and the transmission of the crystal decreases. An

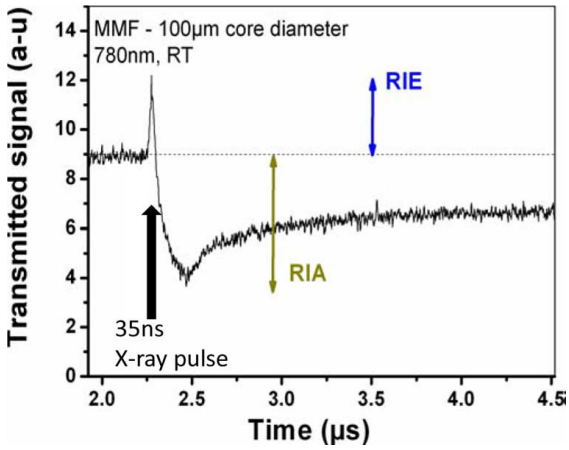

Figure 3.7 – Changes in the 780 nm transmission of an MMF before, during and after a 35 ns irradiation pulse of 1 MeV X-rays [3].

annealing period follows, during which the transmission partially recovers due to the bleaching of point defects. However, some point defects remain stable resulting in the final RIA of the crystal. The processes described are visible in Figure 3.7, which shows the transmission of a multimode optical fibre irradiated with a 35 ns long, 1 MeV X-ray pulse.

The radiation effects on optical fibres depend on a large range of parameters related to the fibre characteristics, the operation and the irradiation conditions, some of which are listed below [3, 105]:

- Fibre characteristics and manufacturing
  - Fibre mode (single-mode, multi mode) and refractive index type (step-index, graded-index)
  - Core, cladding, coating (buffer) material
  - Core and cladding material purity
  - Core and cladding doping and dopant concentration
  - OH content and concentration of other impurities
  - Cladding Core Diameter Ratio (CCDR)
  - Manufacturing method and conditions
- Environmental conditions
  - Type of radiation
  - Dose rate, irradiation length and total dose
  - Irradiation history and annealing periods
  - Temperature
  - Mechanical conditions (stress, bending)
- Operation conditions
  - Optical wavelength
  - Power of transmitted light

The combination of the above factors can result in RIA values bearing a difference of many

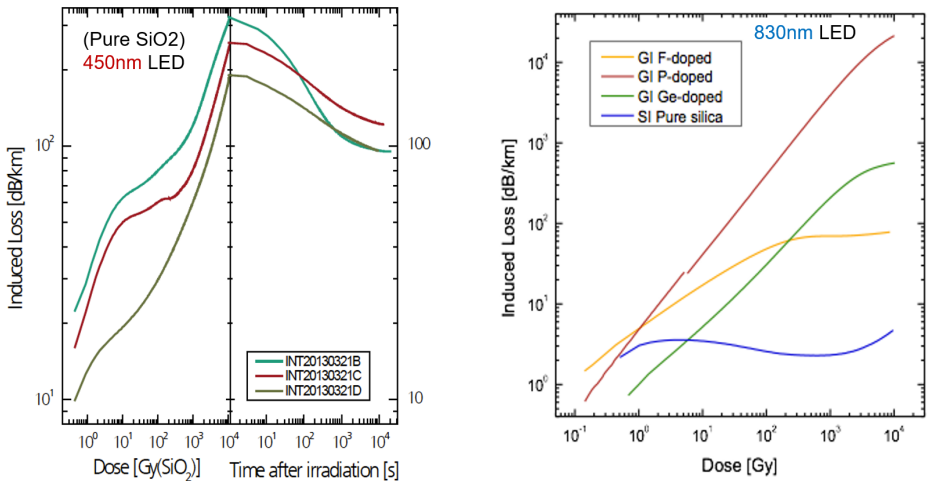

(a) (b)

Figure 3.8 – Irradiation tests of optical fibres with a ^{60}Co source (a) Irradiation of three similar quartz fibres from different producers [115] (b) Irradiation of fibres with different doping materials and refractive index type, as indicated in the legend [116].

orders of magnitude. Furthermore, fibres with very similar behaviour and structural properties before irradiation can show different post-irradiation sensitivities. The following examples demonstrate the influence of the above parameters to the fibre response to irradiation.

Figure 3.8(a) shows the radiation induced loss of three similar quartz fibres at 475 nm, during their irradiation with a ^{60}Co source up to 10 kGy, and their later recovery for 10^4 s. The ^{60}Co source emits photons of a mean energy of 1.25 MeV at a dose rate of 0.22 Gy/s. Though similar, the three fibres show different behaviour not only in the irradiation, but even more in the annealing response, while the fibre showing the highest sensitivity during irradiation is the one with the greatest recovery after that.

In Figure 3.8(b) four fibres with same CCDR, fibre diameter and manufacturer (not indicated) but different core doping materials and refractive index type are compared under the same dose of 10^4 Gy and dose rate. In particular, one fibre is step-index with a quartz core, and three are graded-index with F, P and Ge doping, while the induced loss is measured at 830 nm. The lowest RIA is demonstrated by the step-index quartz fibre, with values of 4-5 dB/km and a relaxation process observable at a total dose of 10^2-10^3 Gy. The graded-index F-doped and Ge-doped fibres show one and two orders of magnitude higher induced losses correspondingly, with saturation effects observable at higher dose levels. Finally, the P-doped fibre shows no resistance to radiation, while the RIA increases almost linearly with the total absorbed dose and reaches a value higher than 10^4 dB/km.

The significance of the core material quality to the fibre performance is discussed in [117], in which fibres drawn by the same company but with preforms from different suppliers show a very different RIA. The effects of the buffer material are demonstrated in [118], in which quartz (core, cladding) fibres with different buffers (aluminium, acrylate, polyimidium, silicone) and

similar but not identical diameters are irradiated with a total dose of 12 Mrad of ^{90}Sr beta particles. The fibres with aluminium buffer show no damage (as measured at the center of the fibre), the fibre with silica buffer broke at 3 Mrad of irradiation and the rest show some radiation damages.

In the past decades, a variety of Commercial Off-The-Shelf (COTS) optical fibres that are less sensitive to radiation have been available. However, many parameters (i.e. the material suppliers, the fibre drawing process followed etc) of the fibre manufacturing are confidential and not accessible to users. Therefore, the radiation response of a COTS fibre cannot be predicted unless performing dedicated irradiation tests [3]. Additionally, unless a uniform fabrication is guaranteed by the manufacturer, supposedly identical fibres from even one single manufacturer might differ significantly, as discussed in [117].

To understand the radiation hardness of an optical fibre, the wavelength spectrum of interest must be taken under consideration. In most studies the fibres are examined for wavelengths related to the data transmission spectrum, i.e. around 0.85, 1.3 or 1.5 μm, as this is their principal industrial application. When used as Cherenkov radiation sensors however, such as in the scope of this thesis, the objective is their radiation hardness for optical wavelentghs. Relevant studies performed for the LHC CMS calorimeter design at CERN [119] give a good indication for such applications. Two optical fibres of quartz core and two different claddings (quartz, plastic) are compared under a 24 GeV proton beam and a total dose of up to 1.25 Grad. The two fibres follow similar responses until 0.5 Grad, where the one of plastic cladding shows a steep increase in attenuation. At 1.25 Grad of total dose, the more radiation tolerant fibre of quartz core and cladding shows very low RIA at around 450 nm, and an almost full post-irradiation recovery. It is interesting to note here that below 380 and above 580 nm the fibre becomes almost opaque and does not recover. For the same application, in [118] it is concluded that quartz fibres (core and cladding) with either no or aluminium buffer are highly resistant to harsh radiation environments.

Further studies on the optical fibre radiation damage have been performed in the scope of the CERN ATLAS experiment, and in particular for the connection of three of the ATLAS subdetectors to their readouts, for which optical fibre links are used [120]. Three fibres from different manufacturers with different core (pure silica, Ge dopant, Ge and P dopant) and cladding (F dopant, pure silica, unknown) configurations have been examined under neutron and gamma irradiation. The operation wavelength of the optical links, and wavelength for which they were tested, is 850 nm, in the near infra-red. After extensive testing the pure Silica core fibres have been classified as radiation hard for the examined wavelength [121] and shown to experience a RIA of only 0.05 dB/m following a total irradiation dose of 33 Mrad.

3.3 Photosensors

There is a large variety of photon detectors for optical communication systems and photosensing applications. Some examples are the PIN diodes, Avalanche Photodiodes (APDs), Silicon Photon Multipliers (SiPMs), PMTs, metal-semiconductor-metal (MSM) and Hybrid Pho-

todetectors (HPD), described in detail in [122,123,124]. In the present section the photosensors relevant to the scope of this thesis will be summarised.

3.3.1 | Silicon Photon Multiplier (SiPM)

SiPMs are detectors built to overcome the drawbacks of previous semiconductor sensors. Their many advantages include a high optical sensitivity, low operating voltage, uniformity from sensor to sensor, low cost, and the ability to be mounted on a PCB [124]. A description of the APD, which is the SiPM constituent, and of the SiPM design and characteristics follows in the next paragraphs.

Avalanche Photodiode (APD)

An APD is a semiconductor detector based on the operation of the photodiode, but with a very high electric field applied to the p-n junction. This electric field provides the electon-hole pairs created during photon detection with sufficient energy for the production of further electron-hole pairs. The outcome is the generation of an avalanche which results in the signal amplification, while the gain is proportional to the applied voltage.

When high electric field applied to an APD is greater than its breakdown voltage *, a very high discharge and therefore output signal is possible. The APD operation at such a voltage level is known as Geiger-mode, and can result in a gain of up to 10^6 . To halt the generated discharge and detect the following photon, the detector must be connected to an external quenching resistor. The resulting photosensor circuit provides single-photon sensitivity [122]. The main drawback of such a design is its inability of recognising multi-photon events, as its output can be considered identical regardless of the number of photons impinging onto it.

SiPM design

The SiPMs are sensors whose design consists of a large matrix of pixels, i.e. parallel connected APDs in Geiger modes and their quench resistors (pixels). The pixels are able to detect photons independently, as illustrated in Figure 3.10(c). The SiPM output charge Q_{SiPM} is the sum of the outputs of all fired pixels N_{fired} and can be calculated as:

$$Q_{SiPM} = C_{pix} \cdot (V_r - V_{br}) \cdot N_{fired} \tag{3.21}$$

with C_{pix} the capacitance of each pixel, V_r the applied reverse bias voltage and V_{br} the breakdown voltage. The factor $C_{pix} \cdot (V_r - V_{br})$ leads to the SiPM gain G, which is expressed as:

$$G = C_{pix} \cdot \frac{(V_r - V_{br})}{e} \tag{3.22}$$

with e being the electron charge.

*. The breakdown voltage of a semiconductor photodetector is the voltage above which the current within the device increases exponentially with increasing reverse bias.

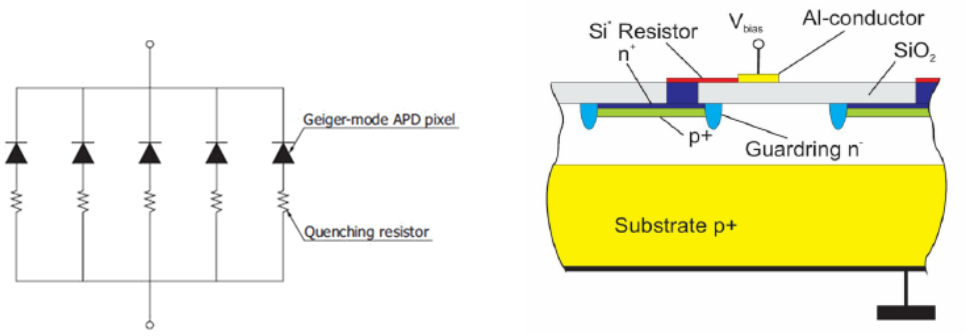

Figure 3.9 – (a) SiPM equivalent circuit [125] (b) Topology of an SiPM [126].

When an SiPM pixel is fired, it produces a signal of a standard height. As a result, when an SiPM is being illuminated at very low intensity, the output charge is characteristic and corresponds to the number of photons impinging onto the sensor. This distribution is shown in Figure 3.10(a), in which the first to the left peak is the pedestal noise, and the following ones give the pulse height in the case of one (1 photon equivalent (p.e.)) and more than one pixels fired simultaneously. A close detail of SiPM pixels is shown in Figure 3.10(b).

SiPM characteristics

This subsection describes the main parameters qualifying the performance of SiPMs.

Photon Detection Efficiency (PDE) The photon detection efficiency indicates the percentage of photons that are detected [124]. The PDE is determined by three factors: the quantum efficiency $QE(\lambda)$, the fill factor ff and the avalanche probability P_{av}. $QE(\lambda)$ corresponds to the ratio of the number of electron-hole pairs created to the number of incident photons, as a function of the incident photon wavelength [127, 128]

$$QE(\lambda) = \frac{e^{-} - h\,\text{pairs}}{\text{Incident Photons}} \tag{3.23}$$

The quantum efficiency depends on the atomic structure and the thickness of the photosensor, and typically range in values of 0.5-0.8 [129].

The total area of the SiPM that is occupied by pixels is the active area of the sensor. However certain regions of each pixel are not sensitive to photons. The fill factor ff is a geometric parameter determined as the ratio of the light detecting (light sensitive) area to the active area of an SiPM. Typical values of the fill factor range between 30 and 80% [130].

The third factor P_{av} is the probability that the carriers generated during photon detection will trigger an avalanche multiplication, and depends on the overvoltage set on the detector.

As a result, the photon detection efficiency of SiPMs is estimated as:

$$PDE(\lambda, V) = \frac{\text{Detected Photons}}{\text{Incident Photons}} = QE(\lambda) \cdot ff \cdot P_{av}(V) \tag{3.24}$$

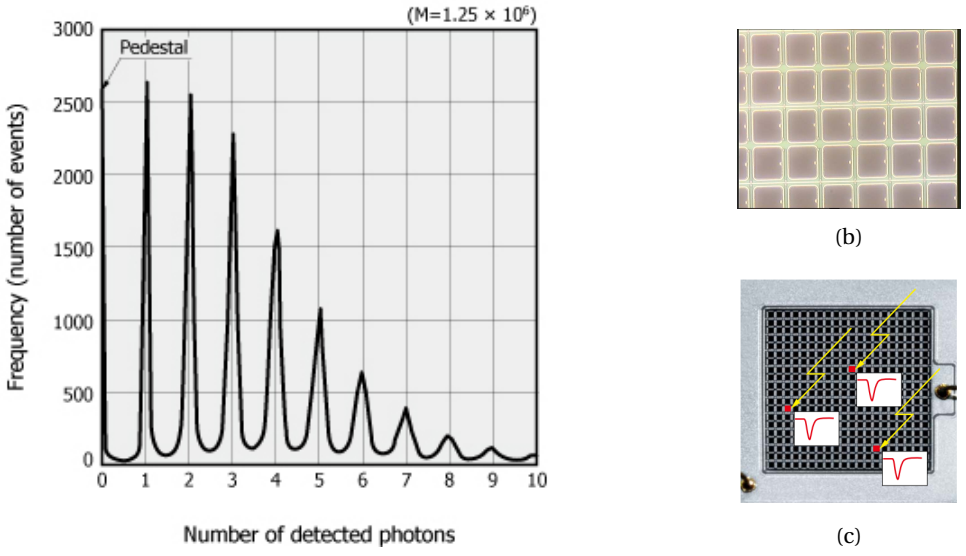

(a) (b) (c)

Figure 3.10 – (a) Photon counting of an SiPM when using an amplifier [131] (b) Zoom onto the SiPM pixels [132] (c) Illustration of an SiPM during photon counting [131].

Typically, the peak PDE is around 30% for SiPMs with 1500 pixels/mm, and higher that 70% for those with 100 pixels/mm [105].

Time response In SiPM the Geiger discharge develops within some hundreds of picoseconds, as a result of the small width of the semiconductor depletion region. Consequently, the SiPM time response is characterised by a quick rise time of the order of some hundred picoseconds in most novel designs [5, 105].

The fall or recovery time of the detector, i.e. the time for the recharge of the pixel capacitance C_{pix}, is larger and its values may vary significantly depending on the photosensor model. It is characterised by the time constant $\tau_{fall} = C_{pix} \cdot R_q$, where R_q is the quenching resistor, and may range from 10 ns up to microseconds. An example of MPPC response for one, two and three detected photons is given in Figure 3.11(a), in which a quick rise time smaller than 1 ns and fall time of around 50 ns can be observed.

Gain Depending on the SiPM model, the gain ranges between 10^4 and 10^6, while it depends strongly on the operation voltage as well as the sensor temperature. To mitigate the gain modifications arising from temperature fluctuations, a cooler may be used. A real-time voltage control depending on the feedback of a temperature sensor is an alternative solution for keeping the SiPM gain constant.

Dark count rate The thermal or field assisted excitation may result in the generation of electron-hole pairs without photon involvement in an SiPM pixel. These pairs may lead to a Geiger-avalanche and result in an unwanted noise signal. Since the dark counts occur

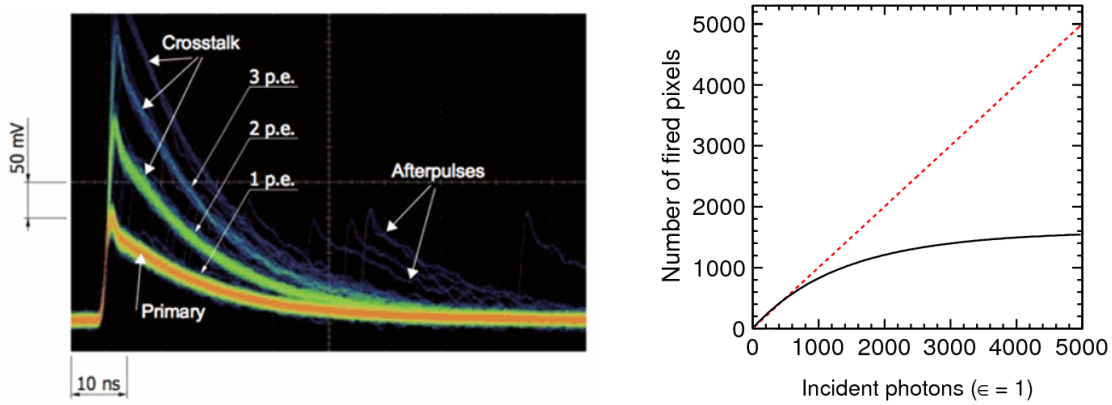

(a) (b)

Figure 3.11 – (a) Dark counts, crosstalk and afterpulses of an SiPM [125], (b) Ideal response of a 1600 pixel SiPM with single photon detection efficiency $\epsilon = 1$ (black solid curve) and response without saturation (red dashed line) [133].

stochastically, usually only one pixel is fired and 1 p.e. dark count is detected. The possibility of more than one pixels firing simultaneously is less likely, however a dark count 2 p.e.or 3 p.e. or 4 p.e. is also observed. This is mostly attributed to the phenomenon of crosstalk, which is described in the following paragraph. The main parameters strongly affecting the dark count rate are the temperature and the applied overvoltage. At room temperature, the typical values are in the 100-1000 kHz/mm^2 range, however lower values have also been achieved [122].

A second noise effect observed in SiPMs are **afterpulses**. These are random pixel discharges, occurring with higher probability shortly after a pixel has been fired. They originate from carriers which are trapped by defects of the semiconductor lattice, to be released at a later time and generate an avalanche. Since they can not be distinguished from real photon-induced signals, afterpulses affect the single-photon counting of the sensor. This phenomenon together with the dark counts of an SiPM for one, two and three photon equivalent signals is shown in Figure 3.11(a).

Crosstalk When an SiPM pixel is fired, a photon generated in the developed avalanche might escape this pixel and fire a neighbouring pixel by generating a new avalanche. This phenomenon is known as optical crosstalk. The probability for optical crosstalk depends on the geometric characteristics and the gain of the detector. For the same gain, smaller pixels have a higher crosstalk probability due to the shorter lengths needed to be covered by the photons in order to escape them. The optical crosstalk is the main source of noise levels higher that 1 p.e. (which are a result of the above described dark count), and this is presented in Figure 3.11(a).

Dynamic range and linearity The response of a perfect photosensor should be linear to the number of illuminating photons, as shown with a dashed line in Figure 3.11(b). However,

the dynamic range of SiPMs is limited by its number of pixels, because they act as counters producing the same output signal when fired, irrespective of the number of photons entering them. As a result, when the sensor illumination increases, the more than one photons that may impinge onto one pixel are not detected. Theoretically, the relation between the number of fired pixels, N_{fired}, and incident photons on the SiPM, $N_{ph,inc}$, is expressed as a binomial distribution [124]

$$N_{fired} = N_{tot}\left(1 - \exp^{-\frac{PDE \cdot N_{ph,inc}}{N_{tot}}}\right) \tag{3.25}$$

and is represented as a black solid line in Figure 3.11(b). The response of the sensor starts linear, but deviates from linearity and saturates with the increase of the number of illuminating photons. In general, up to an illumination of approximately 60% of the pixels the SiPM response is linear, while for higher values the saturation effects appear. The typical SiPM dynamic range is 10^3 (for an SiPM a number of pixels in the order of 4000) [89], however recent advances in SiPM development and the increase of number of pixels have led to dynamic ranges of up to 10^5 [105].

An additional effect of saturation related to the pixel dead time occurs when a second photon impinges on a pixel which has already been fired: if the pixel is not totally recovered and its capacitance is not fully recharged, the resulting pulse will be lower than expected and affect the size of the overall signal.

3.3.2 | Photo Multiplier Tube (PMT)

PMTs are photosensors which have been widely used in the past decades in a variety of applications, such as high energy physics and astrophysics. The PMT characteristics have been thoroughly examined and are well known. Their main advantages include a high sensitivity and large dynamic range, high gain, good timing and low noise.

PMT design

The basic elements of the PMT are a photocathode, an assemble of dynodes and an anode, all incorporated within a tube in vacuum. As shown in Figure 3.12(a), the power voltage is applied to the photocathode and the dynodes through a series of resistors, resulting in a series of voltage steps along the cathode-dynode-output length. The photons enter the PMT through an input window, and continue to the photocathode behind it. The photocathode acts as an electron emitting surface when a photon impinges onto it. The emitted electrons are directed to the series of dynodes due to the applied electric field, while being accelerated at the same time. At each dynode secondary electrons are released, creating an electron cascade which is eventually collected at the anode, resulting in a measurable output signal.

The PMT performance depends significantly on its building elements: The photocathode is responsible for the spectral response, as the photo-emitting probability depends on the photon wavelength. The limitation for short wavelength photons comes from the input window material, which tends to absorb ultraviolet radiation [4].

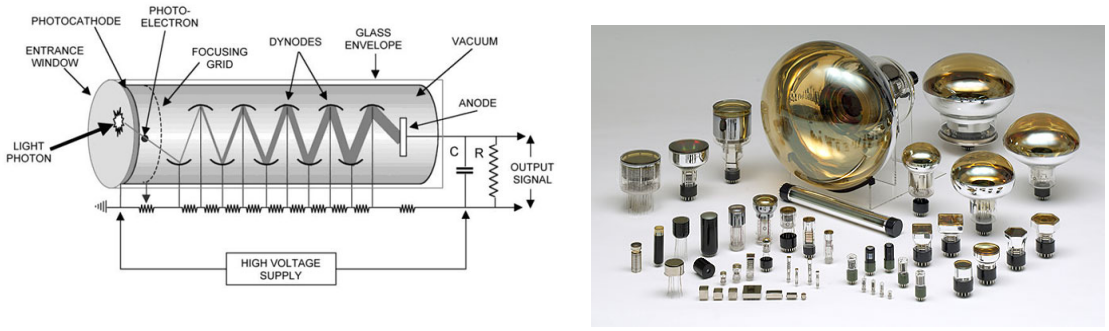

(a) (b)

Figure 3.12 – (a) Operation principle of a PMT [134] (b) Different types of PMTs [135].

There are typically between 8 and 12 dynodes, and may be set in different configurations in space, as can be found in [136]. The number of dynodes N_d is important for the final PMT gain G_{PMT}, which is calculated from [137]

$$G_{PMT} = G_d^{N_d} \tag{3.26}$$

where G_d is the gain of one dynode.

To conclude, PMTs are versatile detectors, available in different shapes, sizes, dynode structure and general characteristics depending on their application. A picture to note the vast variety of these sensors today is shown in Figure 3.12(b).

PMT characteristics

Gain The gain of a PMT depends on the applied voltage. For short light pulses a gain up to 10^9 can be reached, while in the case of continuous pulses the gain is kept lower, usually on the order of 10^7 [136].

Spectral responce The spectral response of the PMT with respect to the incident photon wavelength coincides with the Quantum Efficiency $QE(\lambda)$ of the photocathode. The quantum efficiency depend on the input window and the characteristics of the photocathode, and is estimated as

$$QE(\lambda) = \frac{\text{Produced photoelectrons}}{\text{Incident photons}} \tag{3.27}$$

There is a variety of PMTs in the market with different spectral responses, while a QE of up to 45% is possible at peak wavelength [105].

Dark current The dark current of PMTs is defined as a small current which is still flowing in the absence of any detector illumination. It mainly originates from the thermionic emissions of the cathode and the dynodes. Additional causes among others are the existence of leakage current between the anode and the dynodes, field emission current from the dynodes and the

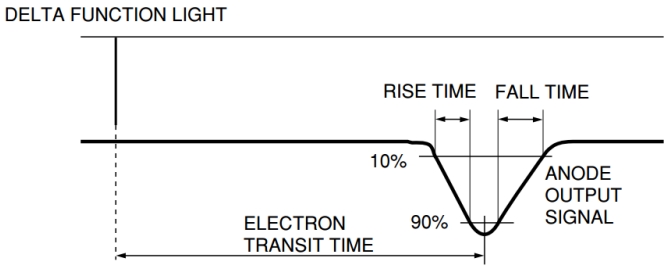

Figure 3.13 – Definition of PMT rise, fall, and electron transit time [4].

ionisation of residual gas in the tube, described in detail in [4]. Typically values of the dark current range between 1 and 10 nA

Linearity - Dynamic range The detector linearity in pulsed operation is defined as the proportionality between the input light and the output current, up to their deviation of 2% and 5% (depending on the manufacturer requirements). The upper limit for the linearity depends on the current flowing in the voltage divider and the maximum current in the anode [138].

Considering the PMT linearity and the dark current, the overall detector dynamic range can be estimated, which reaches usually the order of 10^5-10^6. However, wide-dynamic range PMTs able to cover up to eight orders of magnitude have also been developed [139].

Time response The time response of a PMT is determined by the transit time of the photoelectron from the photocathode to the anode, and the transit time spread, i.e. the different time of arrival to the anode of different photoelectrons. The former depends primarily on the dynode type and internal arrangement and on the supply voltage [4, 136]. Typical values of the electron transit time range between 5 and 40 ns [105], while the transit time spread extends between 0.1 and 20 ns.

The rise (fall) time and fall time of a PMT is the time needed for the output pulse to rise from 10% to 90% (fall from 90% to 10%) of the peak amplitude, when it is illuminated by an instantaneous light pulse. Typically, the fall time is approximately two to three times larger than the rise time, which in the best performing photosensors reaches values down to 0.5 ns [4].

3.4 An advanced optical fibre detector

This section presents the main characteristics of the Cherenkov fibre monitors, and the design of the optical fibre based detector studied in the present thesis.

3.4.1 | System characteristics

The optical fibre radiation monitors studied in the present work are based on the Cherenkov radiation emitted from high energy charged particles in materials such as silica, and the

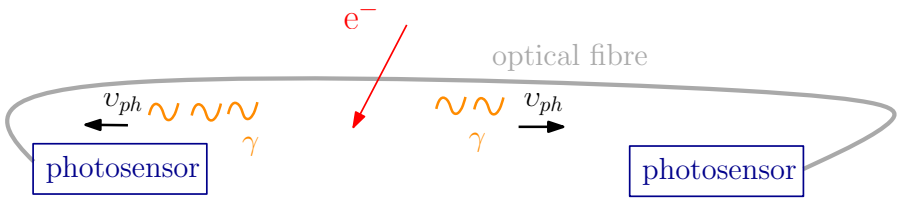

Figure 3.14 – Operation principle of optical fibre radiation monitors.

propagation of light in optical fibres. In particular, they consist of an optical fibre coupled to a photosensor, as shown in Figure 3.14. When high energy charged particles e.g. from a beam loss particle shower cross the fibre, they generate Cherenkov light. Photons with an appropriate emission angle will propagate in the optical fibre with velocity $v = \frac{c}{n_{co}}$, where n_{co} is the refractive index of the fibre core. A fraction of these photons will exit the end face of the fibre, to be detected by the photosensor as a beam loss (or radiation) signal.

To achieve a good understanding of the detector operation, and develop an approximate model which correlates the signal obtained from the photosensor to the number of particles interacting with the fibre, the following aspects should be considered:

1. The photon yield Y generated when a high energy charged particle crosses the fibre core
2. The probability $P_{e,n}$ that a photon is trapped in the fibre and exits within the nominal acceptance cone
3. The attenuation of the Cherenkov light spectrum in the fibre, ϵ_{att}
4. The Photon Detection Efficiency (PDE) of the photosensor, η_{PDE}

Additional factors include the efficiency of the fibre-photosensor coupling, the light dispersion in the optical fibre and the effects of RIA.

Considering the four above aspects, the number of photons detected by the photosensor, $N_{ph,det}$, per charged particle is given by

$$N_{ph,det} = Y \times P_{e,n} \times \epsilon_{att} \times \eta_{PDE} \tag{3.28}$$

Photon Yield

The light yield produced during the passage of a charged particle in an optical fibre can be estimated from Equation 3.7, with L being the particle trajectory as shown in Figure 3.15. The particle crosses the fibre core with an angle a with respect to the axis and a distance b from it. If R is the fibre core radius, the length of this trajectory is given by:

$$L = \frac{2\sqrt{R^2 - b^2}}{|\sin a|} \tag{3.29}$$

Hence, the light yield of a single particle crossing the fibre for a wavelength range between λ_1 and λ_2 can be approximated as:

$$Y = \frac{2\pi}{137}\frac{2\sqrt{R^2-b^2}}{|\sin a|}\left(1-\frac{1}{\beta^2 n^2}\right)\int_{\lambda_1}^{\lambda_2}\frac{1}{\lambda^2}d\lambda \tag{3.30}$$

Replacing the factor $\sqrt{R^2-b^2}$ with its average, which is equal to

$$\frac{1}{R}\int_0^R \sqrt{R^2-b^2}\,db = \frac{\pi R}{4} \tag{3.31}$$

the above equation can be estimated from:

$$Y \simeq \frac{\pi^2 R}{137|\sin a|}\left(1-\frac{1}{\beta^2 n^2}\right)\int_{\lambda_1}^{\lambda_2}\frac{1}{\lambda^2}d\lambda \tag{3.32}$$

For the present application the wavelength range $\lambda_1-\lambda_2$ will be restricted to the optical wavelengths 200-900 nm, due to the relevant quantum efficiency of the relevant light sensors.

Propagation Probability

The operation of an optical fibre beam loss monitor demands that the emitted photons do not only get trapped in the fibre core, but also propagate in it and exit the fibre's end face within a given acceptance angle. For a successful total reflection of the photons in the fibre, the angle ξ between the core-cladding boundary at the reflection location and the photon trajectory must satisfy equation:

$$\xi \geq \arcsin\left(\frac{n_{cl}}{n_{co}}\right) \tag{3.33}$$

where n_{co} and n_{cl} are the core and cladding refractive indices, respectively. The probability that Cherenkov generated photons are trapped in the fibre, P_t, or that they additionally propagate in it and exit the end face, P_e, are described in detail in [140, 141]. Furthermore, the probability that the trapped photons propagate and exit the fibre end face within the nominal acceptance

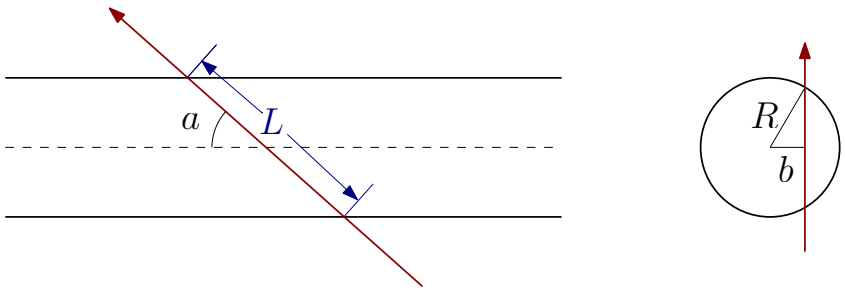

Figure 3.15 – Scheme of the crossing of an optical fibre by a charged particle (dark red line).

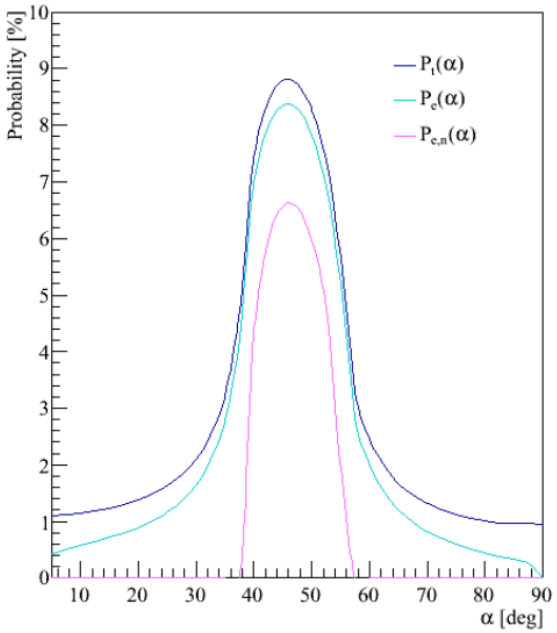

Figure 3.16 – The photon trapping probabilities per incident charged particle as a function of the crossing angle, a, for particles with $\beta = 1$ and $z = 1$ and a fibre in air with $NA = 0.22$. The probability of photon trapping in the fibre P_t is illustrated in dark blue, the probability that photons propagate and successfully exit P_e in light blue and the probability of propagating within the nominal acceptance cone $P_{e,n}$ in magenta [105].

cone, $P_{e,n}$ has been calculated analytically in [141], as:

$$P_{e,n} = \frac{1}{\pi} \arccos\left(\frac{\beta\sqrt{n_{co}^2 - NA} - \cos a}{\sin a \sqrt{\beta^2 n_{co}^2 - 1}} \right) \tag{3.34}$$

Figure 3.16 shows P_t, P_e and $P_{e,n}$ versus the crossing angle a for electrons with $\beta = 1$ propagating in silica ($NA = 0.22$) in dark blue, light blue and magenta colour respectively [105]. It can be observed that the curve reaches a maximum at an angle value similar to the Cherenkov angle in quartz, $a \simeq \theta_C$. This can be intuitively explained by the fact that at such an angle a significant part of the Cherenkov cone propagates nearly in parallel to the fibre axis.

Comparing P_e and $P_{e,n}$, the first is characterised by a tail in the very small and very large angles, while for the same angles $P_{e,n}$ is equal to zero. However, exiting in the nominal acceptance cone guarantees a more efficient fibre-photosensor coupling for two main reasons: A large fraction of the photons exiting outside the cone are refracted with very large angles, and therefore either they cannot be detected by the photosensor active surface, or they get reflected by it. Hence, the coupling efficiency for these angles is very low. Additionally, the photosensor is not homogeneously illuminated, as the largest part of the photons will still be contained within the nominal acceptance cone. This, in the case of photodetectors like the

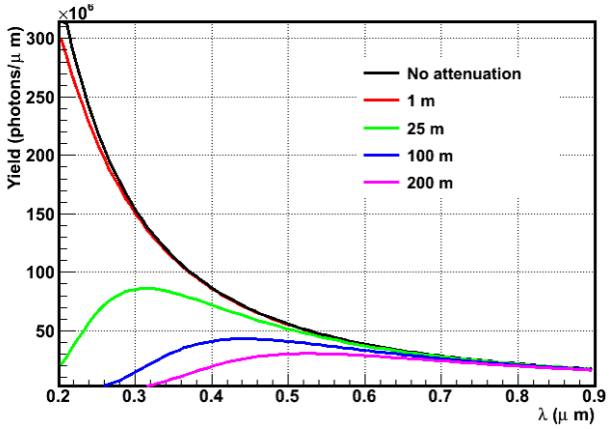

Figure 3.17 – The Cherenkov photon yield in Silica (black line) and the spectrum attenuation after propagating in different lengths of optical fibre [142].

SiPMs, may lead to a very intense illumination of a particular part of the sensor, potentially resulting in its saturation.

On the contrary, the coupling efficiency of the photosensor to photons exiting the fibre within the nominal acceptance cone is very high [105]. To further improve it, the distance of the photosensor to the fibre end face is calculated through the nominal angle and the fibre diameter, so as the entire photosensor surface is illuminated as homogeneously as possible with photons exiting within the acceptance cone.

The yield $Y_{e,n}$ for photons produced, trapped and exiting within the nominal acceptance cone can be expressed by combining Equations 3.32 and 3.34 as:

$$Y_{e,n} \simeq \frac{R\pi}{137|\sin a|}\left(1-\frac{1}{\beta^2 n^2}\right)\int_{\lambda_1}^{\lambda_2}\frac{1}{\lambda^2}d\lambda \arccos\left(\frac{\beta\sqrt{n_{co}^2-NA}-\cos a}{\sin a\sqrt{\beta^2 n_{co}^2-1}}\right) \tag{3.35}$$

The maximum of the yield is found at values of a which correspond to the angles of the Cherenkov emission θ_C, therefore according to Equation 3.3,

$$Y_{e,n,max}(a,\beta) : a \equiv \theta_C = \arccos\frac{1}{\beta n_{co}} \tag{3.36}$$

Since a track parallel to the axis is not possible, regions with $a \to 0°$ and $a \to 180°$ are approximated.

Attenuation

As described in Subsubsection 3.2.2, the main factor of light attenuation in optical fibres in the range of optical wavelengths is Rayleigh scattering. For the scope of this thesis, this will be considered as an approximation for the overall attenuation of the Cherenkov light spectrum

in fibres, while the extrinsic absorptions will be neglected. The attenuation will be expressed from Equations 3.14 and 3.17 as [105]:

$$\epsilon_{att} = \frac{P(l)}{P(0)} \simeq 10^{-\frac{0.83 \cdot L_{fib}[km]}{10 \cdot \lambda^4[\mu m]}} \tag{3.37}$$

where L_{fib} is the length of the fibre.

Combining the above with Equation 3.7 for the photon yield, the Cherenkov light per charged particle of a track length L in the fibre, after a propagation distance L_{fib}, is given by

$$dN_{ph} = 2\pi\alpha_f L z^2 \sin\theta_C \int \frac{10^{-\frac{0.83 \cdot L_{fib}[km]}{10 \cdot \lambda^4[\mu m]}}}{\lambda^2} d\lambda \tag{3.38}$$

The Cherenkov photon spectrum (black curve) and the influence of attenuation on it for different fibre lengths, as calculated from Equation 3.38 is shown in Figure 3.17. The attenuation dependence on the wavelength is clear: the blue/green part of the optical spectrum (up to 400 nm) is drastically reduced with the increase of the fibre length, while the red part (greater than 600 nm) remains almost unaffected.

The attenuation has to be carefully considered during the selection of fibre length and photosensor for an optical fibre BLM system. A photosensor sensitive to the lower optical wavelengths (i.e. the SiPM at approximately 350-450 nm) should be used for fibres principally no longer than 100 m to avoid the complete attenuation of the signal. In the case of low radiation levels or requirement for longer fibres, a photosensor sensitive to the red region of the optical spectrum should be selected.

Photon Detection Efficiency (PDE)

The PDE, or η_{PDE}, is strongly dependent on the wavelength and it varies significantly between different sensors or even from model to model in detectors of the same type. As an example, in Figure 3.18 the PDEs of two Hamamatsu SiPM models of the same principal design are presented. As summarised in Table 3.2 of the following Subsection, the two models essentially differ in the number of pixels and the pixel pitch, with the left one (S12572-010) having a larger number of smaller pixels compared to the right one (S12572-015) [5]. The PDE variations of the two detectors are clearly observed, with the latter showing an approximately double efficiency. As a conclusion, for each application and depending on the photodetector used, $\eta_{PDE}(\lambda)$ factor must be considered separately.

Photon detection

Taking all the above discussed parameters and Equation 3.28 into account, the number of detected photons per charged particle crossing the fibre can be approximated as

$$N_{ph,det} \simeq \frac{R\pi^2}{137|\sin a|}\left(1 - \frac{1}{\beta^2 n^2}\right) P_{e,n} \int_{\lambda_1}^{\lambda_2} \frac{10^{-\frac{0.83 \cdot L_{fib}[km]}{10 \cdot \lambda^4[\mu m]}}}{\lambda^2} \eta_{PDE}(\lambda) d\lambda \tag{3.39}$$

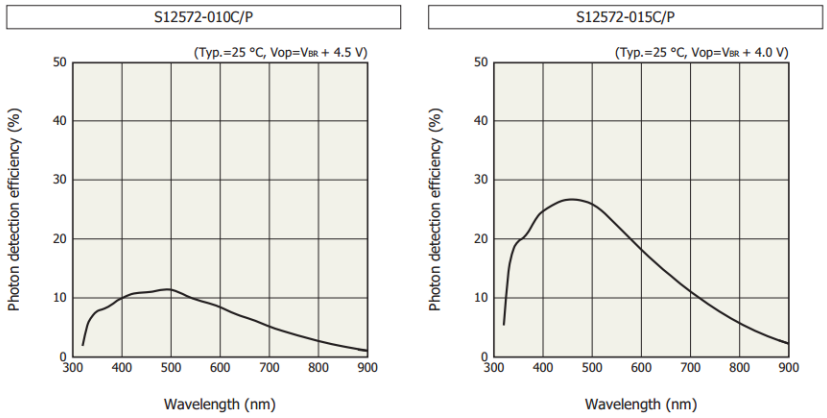

Figure 3.18 – Photon detection efficiency of two models of SiPM (MPPC) by Hamamatsu [5] which differ in the number (and size) of pixels.

For the validity of Equation 3.39, the distance between the photosensor and the optical fibre end face should be such that the full detector surface is illuminated with the fibre nominal acceptance cone. The coupling efficiency can be increased by applying a so-called 'wet' connection, i.e. adding a glue-type material with a similar refractive index as the fibre and the detector window. This minimises the total reflection and refraction of the photons at the end face of the fibre. Another mitigation technique for the photon reflection is the use of fibres with tilted end faces.

3.4.2 | A novel system design

Optical fibre beam loss monitors have been implemented and studied in several accelerator facilities over the past decade, due to the advantages they bear compared to the conventional beam loss detection techniques. These include the very fast detection as a result of the prompt nature of Cherenkov light, which is limited only by the dispersion in the fibre and the photosensor time response. Additionally, being able to cover long parts of the machine with one detector, the optical fibre based BLM requires low resources and ensures that the total of dangerous beam losses will be detected. Furthermore, the monitor is insensitive to low energy photons, which is of high interest for synchrotron light sources. In these applications the PMT is widely used as a photosensor.

An optical fibre sensor has been proposed as one of the candidate technologies for the beam loss monitoring of CLIC [14, 105]. The SiPMs were introduced as a more robust and cost-effective alternative to PMTs, while additionally being insensitive to magnetic fields.

In order to increase the sensitivity of the detector by reducing the noise levels a custom made SiPM module was developed at CERN. The standard modules comprise a low pass filter for the bias voltage and a high pass RC filter (100 nF/50 Ω) readout for the output of the SiPM. A more sensitive version of the modules was also designed, consisting of a transimpedance amplifier readout for the SiPM signal and additional low pass filters for its voltage supply. The

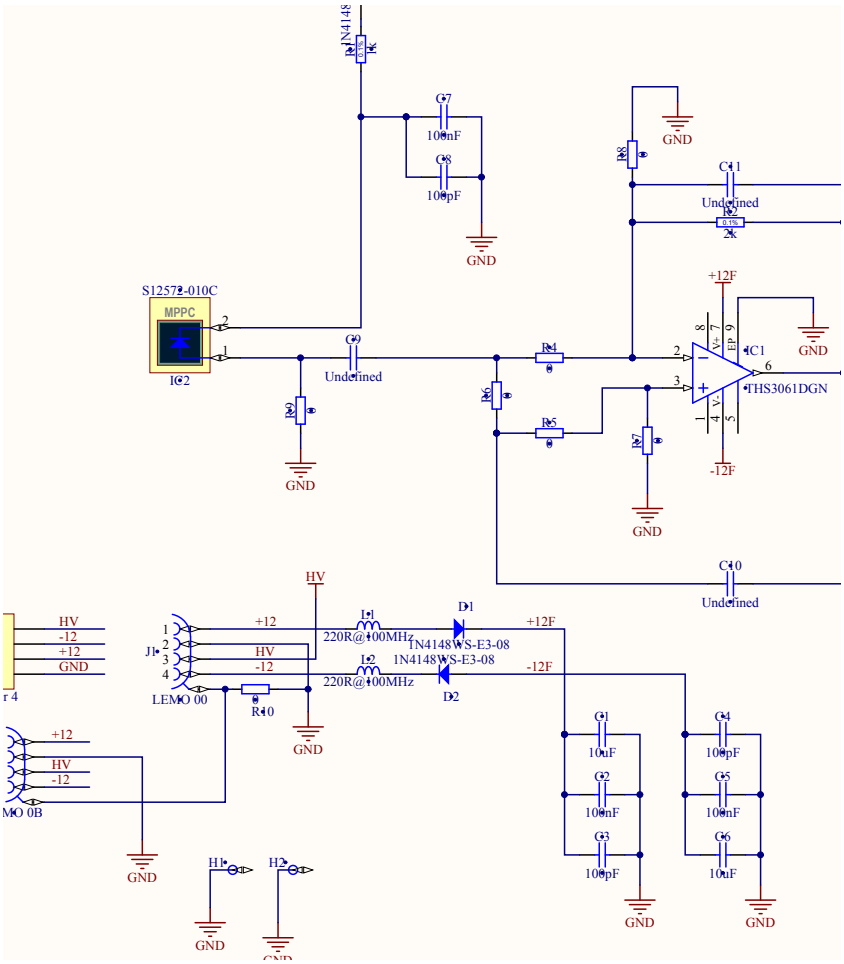

Figure 3.19 – Schematic of the SiPM readout board, courtesy of Fernando Steve Domingues Sousa [143]

schematics of both circuits are illustrated in Figure 3.19. The SiPM connects directly to the readout board, as shown in Figure 3.20(a). An FC-PC connector for the attachment of the optical fibre was implemented on the front of the module, which was designed so as to hold the readout board parallel and centered to the fibre end face. An image of a module and a sketch of its constituents is presented in Figures 3.21(a) and 3.21(b) respectively. To achieve a full illumination of the photosensor active area by the photons exiting the nominal acceptance cone of the fibre, the distance between the two must be determined. This depends on the characteristics of the fibre, namely the diameter and NA, and may vary depending on the required sensitivity of the system. For the adjustment of this distance appropriate spacers were fabricated.

Up to four photosensing modules can fit into a designated chassis equipped with a custom back-plane developed to distribute the power to the modules and provide the grounding. This, together with the RF shielding of the readout, was carefully considered as the biggest potential contributions to noise. The integration of power supply in the chassis allowed to further reduce

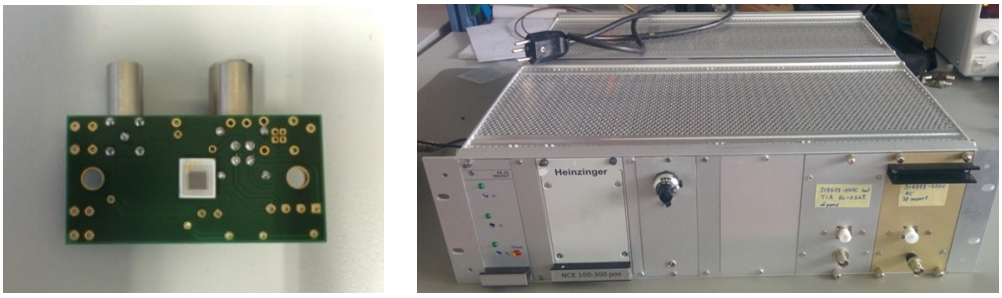

(a) (b)

Figure 3.20 – (a) The SiPM board with the photosensor and the output signal filter. The two connectors serve the input (right) and output (left) of the signal (b) A completed OBLM chassis, with the power supplies (left) and the photosensing modules (right).

the noise levels. Such a chassis is presented in Figure 3.20(b).

The SiPM tested throughout this work is the Multi-Pixel Photon Counter (MPPC) by Hamamatsu. All examined photosensor models have the same dimensions, according to which the readout board was designed. The MPPC are high-quality, cost-effective photosensors, characterised by a low operating voltage, high PDE, spectral response and gain and photon-counting performance. Depending on the sensitivity, gain and dynamic range requirements of each of the tests performed for this thesis, different models of MPPCs were selected. Another factor affecting the model selection was the period when the measurements were performed, as some of the photosensors were commercially released in the course of the present work. The MPPC models used and their main characteristics (number of pixels, gain and operating voltage) are listed in Table 3.2. An MPPC connected on its readout board is shown in Figure 3.20(a).

The sensitivity and dynamic range of the OBLM system can be modulated depending on the selected fibre and photosensor. A very high sensitivity can be achieved by selecting a large core optical fibre and a high-gain SiPM, such as the Hamamatsu S12572-050C, however the dynamic range will be limited due to the photosensor saturation as a result of its small number of pixels and high illumination. An option for both high sensitivity and dynamic range could

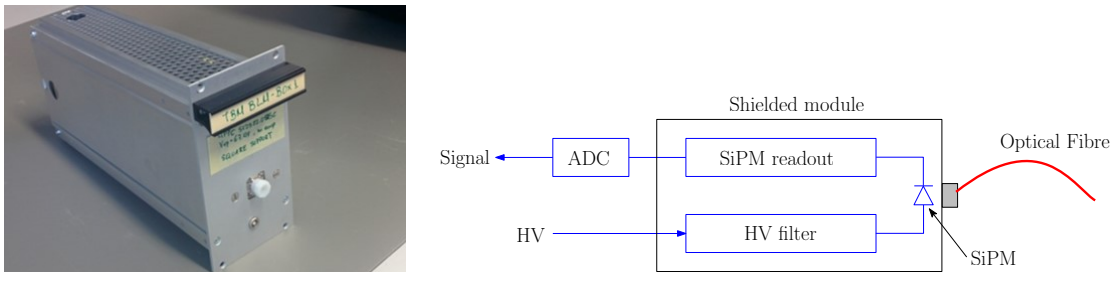

(a) (b)

Figure 3.21 – (a) Design of the shielded module and the elements comprising it (b) The developed shielded module.

Table 3.2 – The Hamamatsu MPPC models used in the present work and their main characteristics [5, 6].

Type	pixels	Gain	V_{op}
S12572-050C	3600	1.25×10^6	67.5
S12572-025C	14400	5.15×10^5	68.5
S12572-015C	40000	2.30×10^5	69.0
S12572-010C	90000	1.35×10^5	69.5

be the use of fibre optic splitters directing a large fraction of the produced light to a high gain SiPM and a smaller one to a sensor with a large number of pixels.

4

FOURTH CHAPTER

POSITION RESOLUTION STUDIES OF DISTRIBUTED BLMS

The identification of the origin of beam losses is critical for a distributed beam loss monitor. In this Chapter the capabilities of the OBLM system described in Subsection 3.4.2 in terms of beam loss location identification and position resolution are examined. To this end, beam losses of different beam types and at different loss locations were generated and studied in two accelerator facilities: the Test Beam Line (TBL) line of CLIC Test Facility 3 (CTF3), and the Australian Synchrotron Light Source (ASLS).

In Section 4.1 the detection of beam losses by distributed detectors is discussed. The installation of OBLMs at the two machines, the ASLS and the TBL is described in Section 4.2 (Subsections 4.2.1 and 4.2.2 respectively). Sections 4.3 and 4.4 examine single- and multi-location loss signals in the case of short and long electron pulses respectively, focusing on the potential to distinguish neighbouring losses. Additionally, in Section 4.3 the level of position resolution that can be achieved by the particular OBLM system is demonstrated.

4.1 Introduction - Beam loss detection with distributed monitors

Beam loss monitors are a beneficial tool not only for the control of beam losses but also for the provision of beam diagnostics. In terms of beam diagnostics, distributed BLMs need to have a high resolution in position, to allow the identification of loss location along a beam line.

Unlike localised detectors, in distributed BLMs the losses are not detected instantaneously, but contrarily throughout the whole period during which the beam travels along the detector. As a result, the time of a loss detection can be correlated to the beam position along the accelerator line. However, the pulse length can be a limiting factor to this correlation. In general, localised beam loss signals are expected to last approximately as long as the beam is passing through the specific location, therefore have a size corresponding to the pulse length.

This phenomenon is not expected to severely affect the beam loss measurement in the case of single bunches or short pulses. However, in the case of long beams the large signals generated may hinder the detection of losses occurring downstream.

OBLMs are the best candidates regarding the time/position resolution, due to the prompt nature of Cherenkov radiation and the advances in photosensor technology, which leads to a photon detection down to few hundreds of picoseconds. Their capabilities, however, are still under investigation and depend on the type of fibres, photosensor, electronics, as well as on the beam characteristics.

Many accelerator facilities have been testing optical fibres, usually with PMTs, as a means of beam loss monitoring. In [11, 144], a position resolution of 30 cm and 30-40 cm has been measured with a single bunch beam and different fibre/photosensor combination. In the present, OBLMs comprising silica fibres coupled to SiPMs, as described in Subsection 3.4.2, are tested with single bunch electron beams and long electron pulses. As explained in [105], the best position resolution is achievable at the upstream end of the fibre. Therefore, unless otherwise stated, this will be the output examined throughout the entire chapter.

Finally, in all calculations presented in the present chapter, the distances are considered in metres (m), the time in nanoseconds (ns) and $c = 0.3\,\mathrm{m/ns}$, while $v = \frac{c}{n} = 0.2041\,\mathrm{m/ns}$ is the speed of light in silica.

4.2 Experimental Setup

4.2.1 | Installation at the ASLS

Two 125 m long optical fibres are sufficient to equip the 216 m circumference storage ring of the Australian Synchrotron. Each fibre has a pure Silica 200 µm core and 245 µm cladding, and a 345 µm acrylate coating, protected by a dark nylon jacket to avoid ambient light and mechanical breakage. The extremes of the fibres are extracted to the roof of the facility, over the storage ring at two locations: Sectors 2 and 9. This setup was selected to ensure that one of

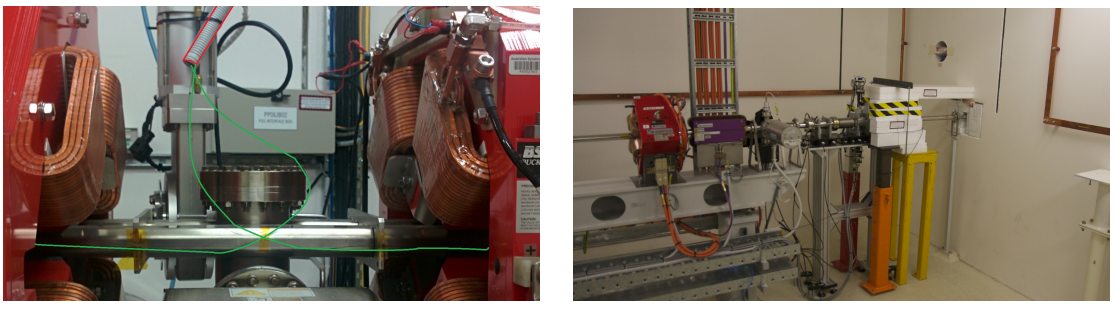

(a) (b)

Figure 4.1 – Details on the ASLS storage ring and OBLM installation (a) The extraction of the two fibres from the storage ring to the roof, at Sector 2. The fibres are noted in green and the extraction tube with a red outline. (b) Part of the BTS line and the wall protecting the storage ring from the scraping losses.

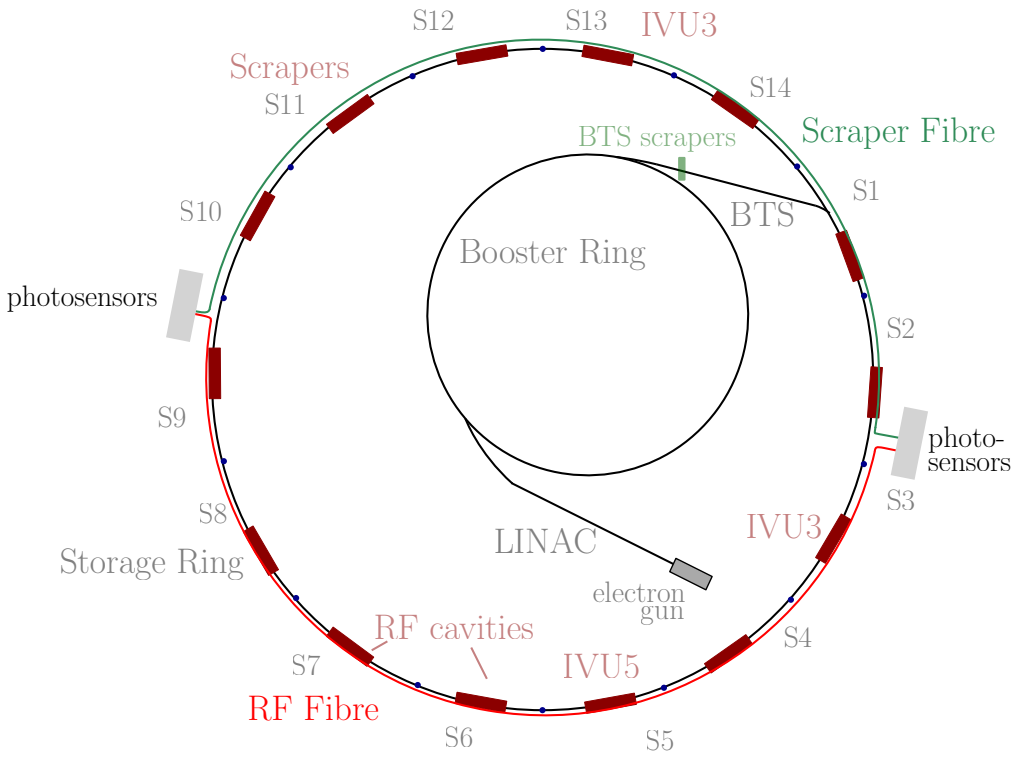

Figure 4.2 – A sketch of the installed optical fibre BLMs at the Australian Synchrotron Light Source. The storage ring is covered by the "Scraper fibre" (green) and the "RF fibre" (red).

Table 4.1 – Length of the fibre parts extracting the signal to the photosensors.

location		symbol	length (m)
Sector 2	Scraper fibre	$x^{extr}_{02,Scr}$	13.5
	RF fibre	$x^{extr}_{02,RF}$	8.0
Sector 9	Scraper fibre	$x^{extr}_{09,Scr}$	3.5
	RF fibre	$x^{extr}_{09,RF}$	9.0

the two fibres would cover two points of reference, i.e.well known loss locations such as the injection point and the scrapers. The fibres arrive to the roof through holes in the ceiling, and their passage is facilitated via plastic tubes, visible in Figure 4.1(a). This Figure shows the two fibres at the extraction location of Sector 2, as they pass through the quadrupoles (red magnets) and enter the tube leading them outside the storage ring area. The storage ring is lined with two optical fibres, installed in the horizontal plane on the inner side of the accelerator. The fibres are fixed externally to the rectangular vacuum chamber and on the inside of the magnets, with a distance of approximately 5.5 cm from the centre of the vacuum chamber. The only exception to that are the larger elements of the storage ring, in particular the IVUs and the RF cavities. Over these elements, the distance between the fibre and the beam is larger. One

fibre is extending from Sector 2 to Sector 9, covering IVU3 in Sector 3, IVU5 in Sector 5 and the RF cavities in Sectors 6 and 7. In the following we will refer to that as "RF fibre". As shown in Figure 4.2, the upstream end of the RF fibre is being extracted and read-out in Sector 2 and the downstream end in Sector 9. The second fibre covers the other half of the storage ring including the scrapers in Sector 11 and the injection point in Sector 1, hence named "Scraper fibre". Its upstream end is extracted in Sector 9 and the downstream in Sector 2. The length of the fibre not parallel to the beam line, i.e. from the extraction location at the storage ring to the photosensors at Sector 2, was measured as approximately 13.5 m (8 m) for the Scraper (RF) fibre, as presented in Figure 4.12. Table 4.1 summarises these measurements and the equivalents at Sector 9. The latter has been calculated from the length of the fibre (125 m) and the storage ring (216 m). For the studies of this chapter, the fibres were coupled to the photosensing modules described in Subsection 3.4.2, with a Hamamatsu MPPC S12572-015C operating at the nominal voltage V_{op}=69.0 V. Finally, for the acquisition of the signals two different Acqiris digitisers (U1071A and U1065A-004), provided by the University of Melbourne, were used [63]. Their characteristics are summarised in Table 4.2. The data acquisition in both Sector 2 and 9 are synchronised with the accelerator timing via a trigger signal which is connected to the electron production by the electron gun. This trigger signal arrives to both acquisition systems through equal length 90 m long coaxial cables.

Table 4.2 – Characteristics of the digitisers used for the OBLM data acquisition at the ASLS and TBL.

	U1071A [145]	**U1065A-004 (DC282)** [146]	**SIS3320** [147]
bandwidth (GHz)	1	2	0.25
sampling rate (GS/s)	1-2	2-8	1.25
resolution (bit)	8	10	10
channels	2	4	8

4.2.2 | Installation at the TBL

The OBLM system installed at the CTF3 TBL consists of two optical fibres: one is 28 m long, and is installed along the beam line and approximately 28 cm above it as shown in Figure 4.3. This fibre is the actual detector, as it covers the entire TBL. The second fibre is 75 m long and extends up to the radiation safe room on top of the accelerator, where the readout equipment is installed. The two fibres are connected via 80% efficiency FC/FC sleeves. Both fibres have a core diameter of 200 µm, and they both contribute to the generated beam loss signals. Aiming to a more accurate measurement of the location of beam losses, only the fraction of the signal the directly equips the accelerator is of interest. This is illustrated in Figure 4.4, where the real detector, covering the TBL, is called "Real signal fibre" and is depicted in magenta colour. The second fibre, which connects the TBL to the radiation safe room, is the "Connecting fibre" and is represented in green. Finally, the full length of both, which will give the final OBLM signal, is referred to as the"Signal fibre" and is illustrated in the Figure with a black colour.

The final OBLM signal contains not only the beam losses occurring at the TBL, but also

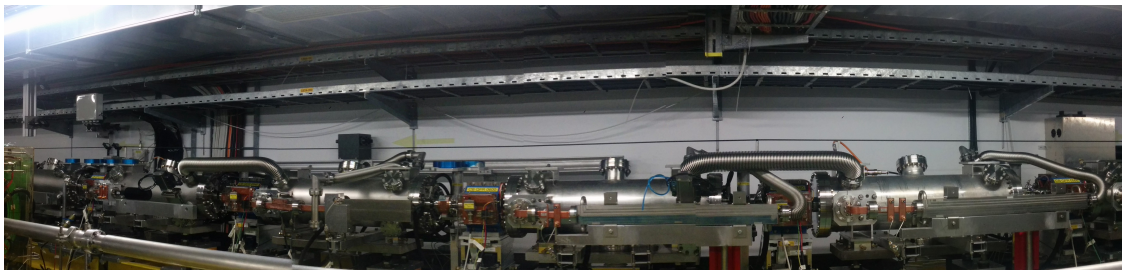

Figure 4.3 – Panoramic image of a part of the CTF3 Test Beam Line. The optical fibre above the beamline is visible.

background signals generated when the particle showers transverse the Connecting fibre. To overcome this complication a second fibre, identical to the "Connecting", has been installed in parallel to the latter. This is shown in blue in the sketch of Figure 4.4 and is called "Background fibre", as its objective is to measure the background signal.

Both fibres ("Connecting" and "Background") are coupled to the photosensing modules described in Subsection 3.4.2. The sensor is a Hamamatsu MPPC S12572-025C, operating at the nominal operating voltage for this model V_{op}=68.5 V. The high-pass MPPC readout consists of a 50 Ω resistor and a 100 nF capacitor. For the signal read-out an SIS3320 acquisition card by Struck [147] was used, the characteristics of which are summarised in Table 4.2.

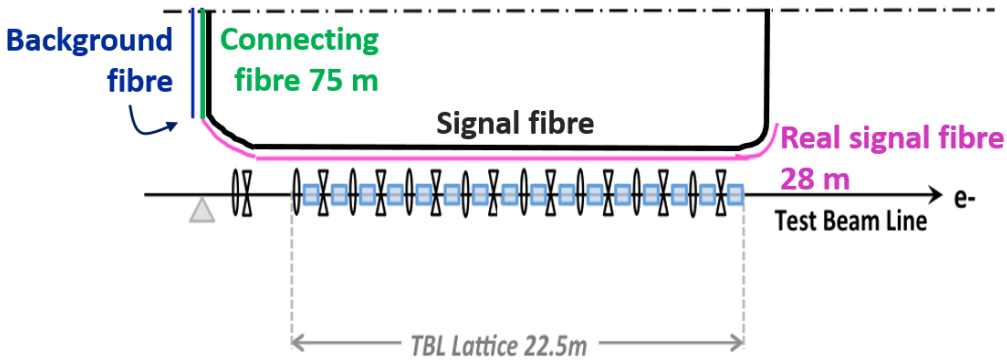

Figure 4.4 – The installation of OBLMs at the TBL. The Real signal fibre (magenta) covers the machine and is connected to the Connecting Fibre (green) for the signal extraction. In parallel to the latter, the Background Fibre (blue).

4.3 Studies with short electron pulses

4.3.1 | Signal analysis

For an initial understanding of the beam loss signals at the ASLS storage ring, the beam losses of a single bunch beam were investigated. Two points of reference were identified: the first was the beam injection in the storage ring, while the second was created by fully closing the scrapers. Beam losses were examined during one turn of the beam in the ring, starting when the beam is entering the storage ring and until the beam scraping. Ten shots were injected under these conditions in a previously empty storage ring, and the average of the Scraper fibre signals is presented in Figure 4.5.

Four peaks are to be observed: one double peak around t=5000 ns, one very large peak with rising edge at approximately t=5206 ns and one smaller at t≃6162 ns. A voltage drop below the background can be noticed following the largest peak and prior to the last one, which is characteristic of the high-pass readout of the photosensor.

To evaluate the beam loss location from the OBLM signal, the photon time of arrival must be estimated. A simple threshold crossing algorithm is not sufficient to cope with complicated beam loss scenarios generating signals close in time. Therefore, an algorithm based on the signal derivative was developed and is presented with red colour, together with the original signal in blue, in Figure 4.6. Four spikes correspond to the four signal peaks, and a threshold of $Y_{thr} = 0.0009$ was set for the determination of their photon time of arrival. For the first and last peak observed the time corresponding to the Y_{thr} is estimated accurately: t_1=4966 ns and t_4=6158 ns. The rest of the peaks were characterised through linear extrapolation, as there were no data points at the threshold: Table 4.3 includes the signal coordinates before and after

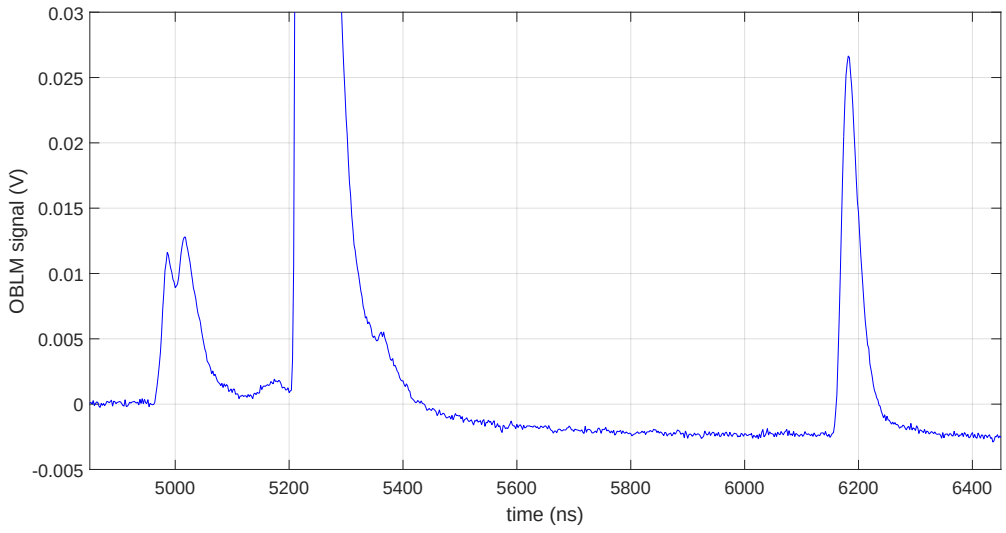

Figure 4.5 – Signal of the upstream end of the Scraper fibre, when a single bunch beam is injected at the storage ring and the scrapers are closed.

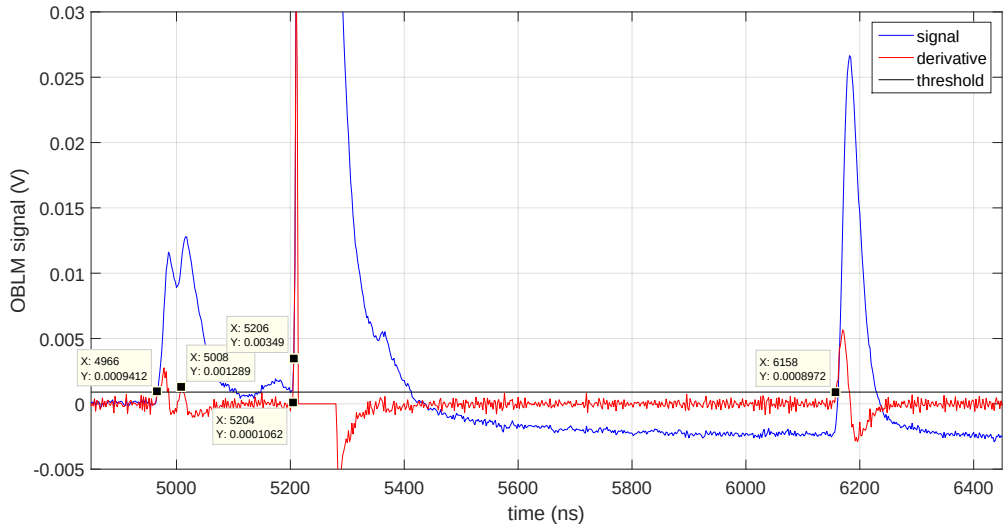

Figure 4.6 – Signal of the Upstream end of the Scraper fibre, when a single bunch beam is injected at the storage ring and the storage ring scrapers are closed (blue), and its derivative (red). The black line depicts the set threshold.

Table 4.3 – Coordinates 1 and 2, between which linear interpolation was applied to estimate the x coordinate at the threshold for peaks 2 and 3.

	peak 2	**peak 3**
coord. 1	(5006, 0.00074)	(5204, 0.00106)
coord. 2	(5008, 0.00129)	(5206, 0.00135)
extrap. t at threshold	(5006.6, 0.0009)	(5204.5, 0.0009)

Y_{thr} (coord. 1 and 2 respectively), as well as the extrapolated t for the Y_{thr}. The latter has been calculated as t_2=5006.6 ns and t_3=5204.5 ns for the second and third peak respectively.

To identify the origin of these peaks a combination of calculations and experimental measurements under different conditions was performed. The results of these studies are described in detail in the following subsubsections.

Unidentified losses in the injection proximity

The first beam loss at the storage ring will occur at the injection point. Therefore, the first signal of Figure 4.5 can be correlated to this instance. The double-peak shape of this signal however, signifies the existence of a second loss location in proximity of the injection point. To identify this second source of beam losses, measurements were performed repeatedly with similar beam conditions (single bunch) but various storage ring settings. Figure 4.7 presents the most significant of the latter: the red line is the average of ten shots during nominal synchrotron operation, similar to Figure 4.5, whereas the blue line is the average of ten shots

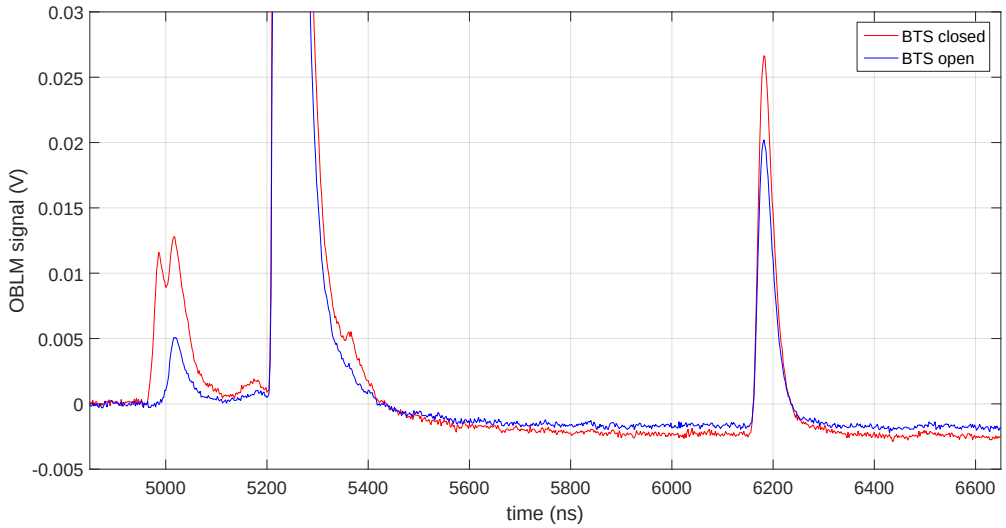

Figure 4.7 – Signal of the Upstream end of the Scraper fibre, when a single bunch beam is injected at the storage ring and the storage ring scrapers are closed, for open (blue) and closed (red) BTS scrapers.

while the BTS line scrapers were open. It is observed that the first of the double peak disappears with the BTS scraper opening. This indicates that the injection losses are represented by the second of the double peak, whereas the first one is attributed to the beam cleaning at the scrapers.

For the validation of this observation the calculation of the time difference between signals generated from BTS scraper and injection losses is necessary. Figure 4.8 shows the signal development according to this hypothesis. The electron shower created by the beam scraping at the BTS travels a distance x_{loss} before reaching the optical fibre at the storage ring. Hence, the generated photons will travel $x_{ph,1}$ metres to reach the upstream photosensors. Meanwhile, the beam covers a distance x_{beam} before being injected in the storage ring, and the Cherenkov photons induced by the injection losses reach the fibre upstream end face after a distance $x_{ph,2}$.

The difference in the arrival time for the photons generated by these two loss locations is given by

$$\begin{aligned} \Delta t &= t_{injection} - t_{BTS} \\ \Rightarrow \Delta t &= \left(\frac{x_{beam}}{c} + \frac{x_{ph,2}}{v}\right) - \left(\frac{x_{loss}}{c} + \frac{x_{ph,1}}{v}\right) \\ \Rightarrow \Delta t &= \frac{x_{beam} - x_{loss}}{c} + \frac{\Delta x}{v} \end{aligned} \tag{4.1}$$

where $\Delta x = x_{ph,2} - x_{ph,1}$ is the distance between the origin of the two beam loss signals. The exact trajectory of the beam lost at the BTS scrapers is not known. However, the assumption

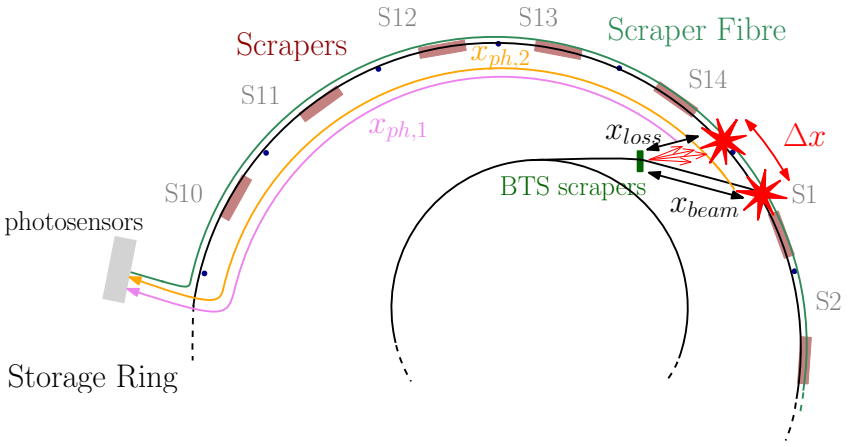

Figure 4.8 – Sketch for the analysis of the beam loss signals in the Scraper fibre of the ASLS, when the beam is lost at the BTS scrapers and at the injection point.

can be made that the electrons lost at the scrapers and the generated particle shower propagate straight at the direction of the beam at that point. With this condition, the length of the loss trajectory can be estimated from the technical drawing of the ASLS as $x_{loss} = (16.34 \pm 0.33)$ m. The distance covered by the electron beam from the BTS scrapers to the kicker magnet at the injection is measured as $x_{beam} = (19.64 \pm 0.47)$ m, and the distance between the two signals on the fibre as $\Delta x = (7.01 \pm 0.41)$ m. In all cases, the errors were calculated via error propagation, from the errors deduced from the technical drawing.

From Equation 4.1 the time difference between beam losses at the BTS scrapers and at the injection point is calculated as $\Delta t = (45.4 \pm 2.6)$ns, with the error estimated via error propagation. The Δt is consistent within 10% with the value experimentally measured by OBLMs as $t_2 - t_1 = 40.6$ ns. Considering the challenges in accurately estimating the trajectory of the beam lost at the scrapers, this difference can be expected. This result confirms that the first observed peak originates from losses produced at the BTS scrapers and the second one is generated during the beam injection in the storage ring.

At the Australian Synchrotron facility, there was no prior direct measurement of losses created at the BTS scrapers. This observation shows the advantages of distributed BLM systems in recognising previously unidentified sources of radiation in the machine, as well as providing detailed information on the machine operation.

Discontinuous beam loss signals

When more than one distributed BLM covers a circular machine, the beam may travel from a part of the machine covered by a particular monitor to a non-covered one, and then return to the first BLM to generate further beam loss signals. In the present study, these types of OBLM signals and the necessary analysis to identify them will be demonstrated. More precisely, the beam losses at the injection point and the scrapers, as detected from the Scraper fibre, are

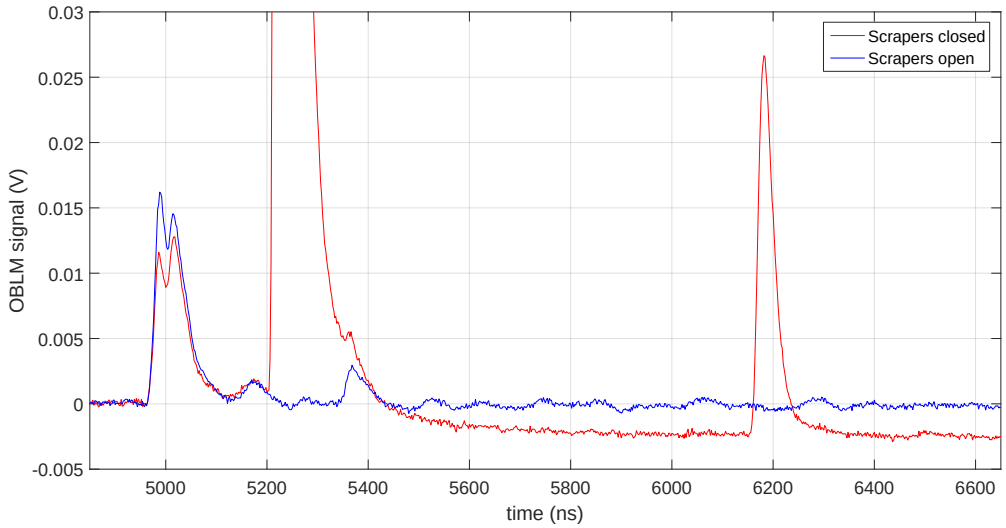

Figure 4.9 – Signal of the upstream end of the Scraper fibre, when a single bunch beam is injected at the storage ring and the storage ring scrapers are closed (red) or open (blue).

examined.

In order to experimentally identify the losses originating from the storage ring scrapers, the OBLM signals while the scrapers were open and closed were compared. To this end, 10 shots with a single bunch beam were acquired for each case. The average signal of the two datasets are shown in Figure 4.9. Two peaks related to the closed scrapers are evident, in particular the third large peak at t_3=5204.5 ns and the last one at t_4=6158 ns. The nature of these two peaks is examined in the present and the following subsubsections. Another peak is observed at a t_5=5356 ns, origin of which is also described in the following subsubsection.

In Figure 4.10 the signal development on the Scraper fibre in the case of closed scrapers is illustrated in red. The Cherenkov photons generated by the beam losses at the injection point are travelling a distance $x_{ph,2}$ to arrive at the upstream end face of the Scraper fibre. Meanwhile the electron beam travels a distance x_{e^-}, before it reaches the storage ring scrapers, where the whole beam is stopped. In this case, the Cherenkov photons in the fibre travel $x_{ph,1}$ to arrive at the photosensor. The arrival time of the photons generated at the injection point at the upstream end of the fibre can be calculated as:

$$t_{ph,2} = \frac{x_{ph,2}}{v}$$

The time of flight to the same end of the fibre of the photons developed due to beam stopping at the scrapers is:

$$t_{ph,1} = \frac{x_{e^-}}{c} + \frac{x_{ph,1}}{v}.$$

As a result the time difference between the two signals will be

$$\Delta t = \frac{x_{e^-}}{c} - \frac{\Delta x}{v} \tag{4.2}$$

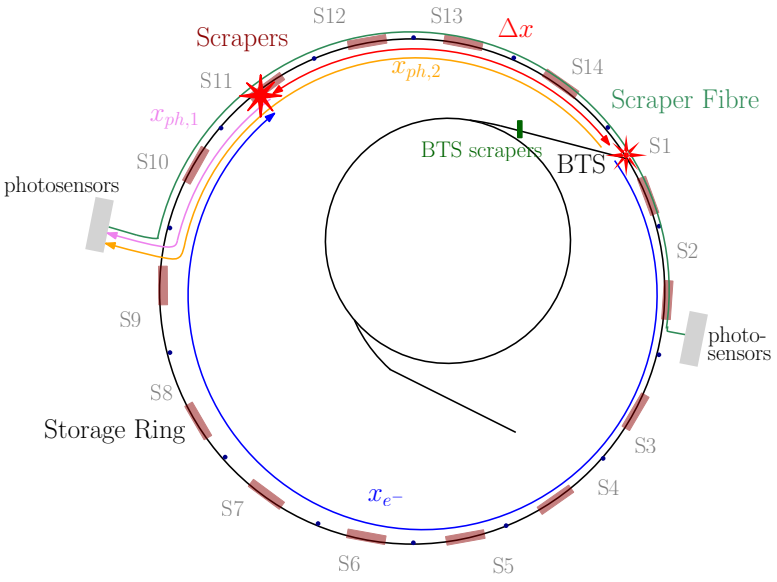

Figure 4.10 – Sketch for the analysis of the beam loss signals in the Scraper fibre of the ASLS, when the beam is lost in different turns [here:injection (turn 1) and scrapers(turn 2)].

where $\Delta x = x_{ph,2} - x_{ph,1}$. Given that $x_{e^-} = L_{ring} - \Delta x$, where $L_{ring} = 216\,\text{m}$ is the ring circumference, the above equation can be rewritten as

$$\Delta t = \frac{L_{ring}}{c} - \frac{\Delta x(1+n)}{c} \tag{4.3}$$

The storage ring of the ASLS is divided in 14 sectors, with length $l_{sec} = \frac{L_{ring}}{14} = 15.4\,\text{m}$. Considering that the injection point and the scrapers positioning at their respective Sectors (1 and 11), the distance between the two locations is measured as 4 sectors, therefore $\Delta x = \frac{4}{14} L_{ring}$. The error in this measurement is calculated as $\delta(\Delta x) = 1.3\,\text{m}$, and stems from the uncertainty on the estimation of the location of the two elements (injection, scrapers) in the technical drawing. The time difference between the two loss signals will be

$$\Delta t = \frac{L_{ring}}{c}\left(1 - \frac{4}{14}(1+n)\right)$$

$$\Rightarrow \Delta t = 211.9\,\text{ns}$$

while the corresponding error is

$$\delta(\Delta t) = \frac{1+n}{c} \cdot \delta(\Delta x) = 10.7\,\text{ns}.$$

To summarize, the time difference between the injection and scraping beam loss signals has been estimated as $\Delta t = (211.9 \pm 10.7\text{ns})$. The peak correlated to injection point, at t_2, and the first peak observed when the scrapers are closed, t_3, are separated by $t_3 - t_2 = 197.9\,\text{ns}$. The

latter agrees within two errors with Δt, with a relative deviation of 6%. Thus, it can be verified that the second peak is generated when the beam enters the storage ring, while the third one corresponds to beam losses at the storage ring scrapers. The origin of the fourth peak, also appearing when the scrapers are closed, is explained in the following Subsubsection.

Photon reflection signals

The accuracy of the above signal interpretation can be confirmed by the identification of the last peak at t_4 = 5204.5 ns. From Figure 4.9 the appearance of this signal when the storage ring scrapers are closed leads to a correlation of the two.

During beam scraping the entire beam is lost at this location, generating a large number of Cherenkov photons in the fibre, which will develop as illustrated in Figure 4.11: One fraction of the photons will travel a distance x to the upstream of the fibre and will be detected by the photosensors. Meanwhile, the largest part of the generated photons propagates to the downstream end of the fibre [105]. A fraction of the latter will cover a distance x_{refl} to reach the downstream end face of the fibre, where they might be reflected. A part of the reflected photons will travel back to the upstream end, to be eventually detected by the photosensor.

The difference in the arrival time at the upstream photosensor of the upstream and the

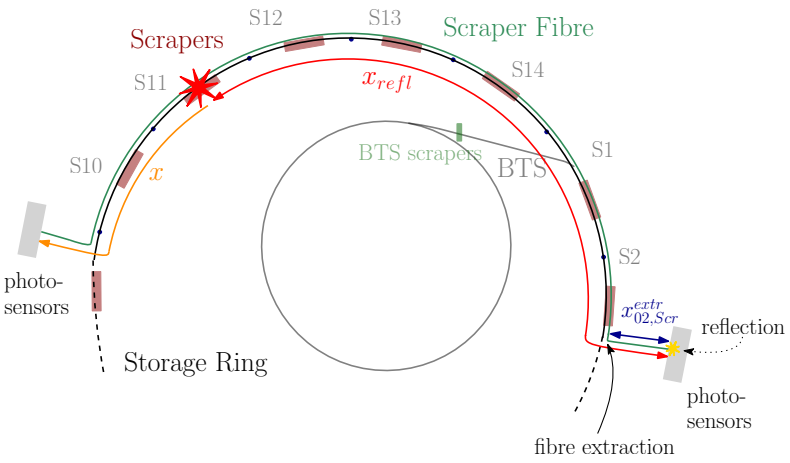

Figure 4.11 – Sketch for the analysis of the beam loss signals in the Scraper fibre of the ASLS, when the beam is lost in the storage ring scrapers. Some of the Cherenkov photons generated travel downstream, are reflected at the end face of the fibre having travelled distance x_{refl} and return to the fibre upstream end.

downstream (reflected) Cherenkov photons is given by

$$\Delta t = t_{refl} - t_{ph}$$
$$\Rightarrow \Delta t = \frac{2 \cdot x_{refl} + x}{v} - \frac{x}{v}$$
$$\Rightarrow \Delta t = \frac{2 \cdot x_{refl}}{v} \tag{4.4}$$

As deducted from Figure 4.11, the distance x_{refl} can be calculated from the distance between the storage ring scrapers and the extraction point at Sector 2, plus the extraction length $x^{extr}_{02,Scr}$. From the ASLS technical drawing, the former can be measured as (83.69 ± 0.47) m. Hence, estimating an additional error of 0.1 m in the extraction length measurement, $x_{refl} = (97.19 \pm 0.48)$ m, and the Δt is calculated as $\Delta t = (952.5 \pm 4.6)$ ns.

The difference in the rising edge of the two last peaks of Figure 4.5, t_3=5204.5 and t_4=6162, is calculated as $t_4 - t_3 = 953.5$ ns, which is compatible with the above calculation. Having a relative deviation of only 0.1%, the calculation and corresponding measurement validate the observation of the losses at the scrapers and their reflection to the opposite fibre end.

A signal similarly created is the peak at t_5=5356 ns observed in Figures 4.6, 4.7 and 4.9, which is attributed to the reflection of the photons generated by the lost bram at the injection point to the downstream end of the fibre. As can be observed in Figure 4.12, these photons will cover a distance equal to $x_1 + x^{extr}_{02,Scr}$ to arrive to the downstream fibre end face. From the technical drawing of the ASLS the length x_1 can be measured as $x_1 = 24.65 \pm 0.6$ m and considering an error of 0.1 m in the extraction length, the Δt can be calculated from Equation 4.4 as $\Delta t = 373 \pm 6$ ns. The time difference between the peak at t_5 and the injection beam loss is $t_5 - t_2 = 5356 - 5008 = 348$ ns. The two values agree within 7.5%, and the deviation between them can be explained by the errors in the estimation of x_1 from the technical drawing.

The signal generated by the reflected photons is very high, and demonstrates the necessity of taking such effects into consideration when performing OBLM signal analysis. As discussed in Subsubsection 3.4.1, a reduction of photon reflections in fibres can be achieved by using tilted fibre end faces or a media that matches the refractive index of the fibre and the photosensor.

4.3.2 | Signal analysis of unidentified beam losses

In this section a method to explore the allocation of undefined beam losses in the machine is described.

Estimation of injection time

As described in Paragraph 4.3.1, the injection point is a standard loss location during machine operation. When identified, this signal renders a very good reference for the position estimation of following losses. However, for an OBLM not protecting the injection area, such

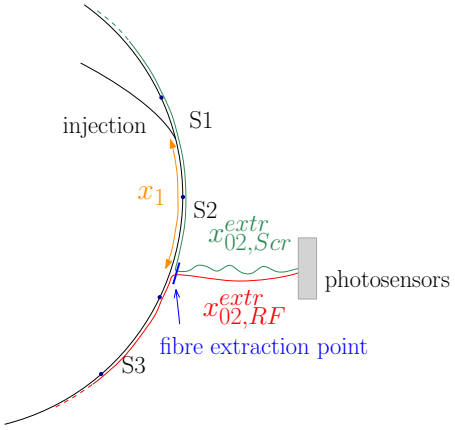

Figure 4.12 – The extraction of the Scraper (green) and RF (red) optical fibres at Sector 2 and the respective lengths of the fibres from the extraction point to the photosensor.

as the RF fibre at the ASLS, such a good reference point does not exist. In this paragraph a sequence of calculations is presented, which aims at identifying the injection time as a reference point for the RF fibre. This will contribute to a correct beam loss location determination for the RF fibre signals.

Figure 4.12 shows an illustration of the storage ring injection location, and the extraction of the Scraper and RF fibres in Sector 2. The distance between the beam injection and the fibre extraction point is outlined as x_1, and the two fibre extraction lengths, $x^{extr}_{02,Scr}$ and $x^{extr}_{02,RF}$ are also shown.

The photons generated by injection beam losses in the Scraper fibre will arrive at its downstream end face in

$$t^{inj}_{02,Scr} = \frac{x_1 + x^{extr}_{02,Scr}}{v}. \tag{4.5}$$

The data acquisition starts with a signal sent from the trigger system, which is synchronised with the ASLS RF gun. The time between the arrival of the trigger signal at the OBLM Data Acquisition (DAQ) system and the injection of the beam in the storage ring can be represented by the variable t_{trig}. Hence, the beam loss signal generated at the Scraper fibre during the beam injection in the ring will be observed at the fibre's downstream end at a time

$$t^{sig,inj}_{02,Scr} = t_{trig} + t^{inj}_{02,Scr} \tag{4.6}$$

The RF fibre will begin detecting beam losses as soon as the beam arrives close to the fibre extraction point of Sector 2, at a distance x_1 from the beam injection location. The Cherenkov photons generated there will cover a distance $x^{extr}_{02,RF}$ to the upstream photosensor. Therefore this signal, which will be referred to here as the leading signal, will arrive to the photosensor at a time

$$t^{lead}_{02,RF} = \frac{x_1}{c} + \frac{x^{extr}_{02,RF}}{v} \tag{4.7}$$

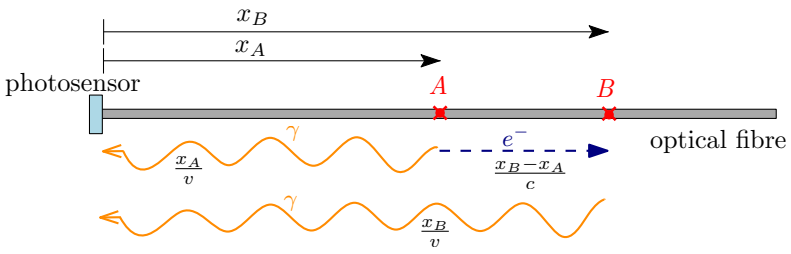

Figure 4.13 – Calculation of the time difference between two beam loss signals arriving at the upstream end of a fibre.

after beam injection. The leading is the first signal to be detected by the RF fibre and corresponds to the moment when the beam starts travelling in the part of the storage ring covered by the RF fibre.

Since the data acquisition commences with the trigger signal, the first signal will be observed at the RF fibre acquisition system at a time

$$t_{02,RF}^{sig,lead} = t_{trig} + t_{02,RF}^{lead} \tag{4.8}$$

From Equations 4.5, 4.6, 4.7 and 4.8, the first beam loss signal at the RF fibre will be detected at:

$$t_{02,RF}^{sig,lead} = t_{02,Scr}^{sig,inj} + \frac{x_1}{c} - \frac{x_1 + (x_{02,Scr}^{extr} - x_{02,Inj}^{extr})}{v} \tag{4.9}$$

Equation 4.9 provides a well defined estimation for the arrival time of the RF fibre leading signal.

Estimation of a beam loss distribution

To calculate the correlation between the distance of two beam loss locations and the difference in their photon arrival time at the upstream end of the fibre, we assume a beam lost at locations A (at a moment $t = 0$) and B of the fibre, as illustrated in Figure 4.13. If with x_A and x_B the distance of A and B from the upstream end of the fibre and t_A, t_B the time of arrival of the generated Cherenkov photons there, then the time difference between the two produced signals can be calculated as:

$$\begin{aligned} t_B - t_A &= \frac{x_B - x_A}{c} + \frac{x_B}{v} - \frac{x_A}{v} \\ \Rightarrow \Delta t &= \frac{\Delta x \cdot (n+1)}{c} \end{aligned} \tag{4.10}$$

where $\frac{x_A}{v}$ ($\frac{x_B}{v}$) is the time for the photons generated in A (B) to reach the photosensor and $\frac{x_B - x_A}{c}$ corresponds to the time it takes for the beam to cover the distance between the two points.

If the photon arrival time for one beam loss location is given, then using Equation 4.10 an OBLM signal with multiple loss locations can be disentangled. In the present study, the signal

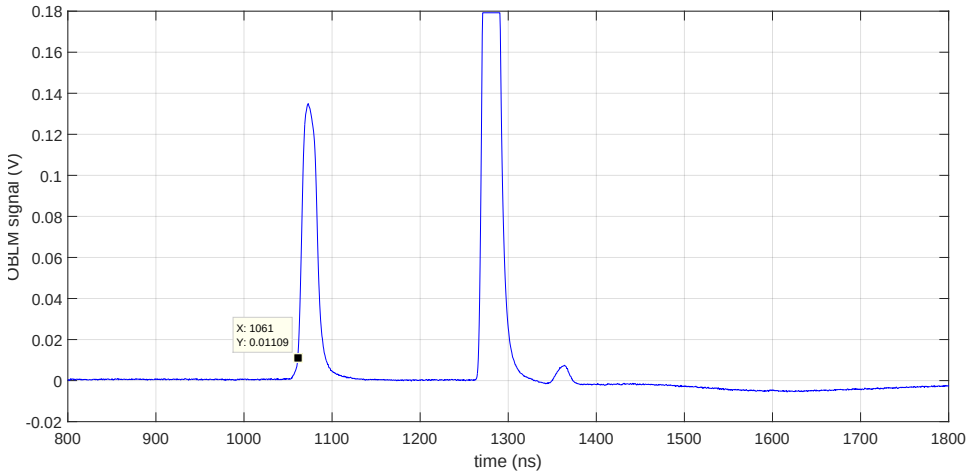

Figure 4.14 – Single bunch beam loss signal in the ASLS storage ring with closed scrapers, as detected from the downstream end of the Scraper fibre.

detected from the upstream end of the RF fibre is examined with the leading signal $t_{02,RF}^{sig,lead}$, the first to be detected by the RF fibre. As explained above this is calculated from Equation 4.9, while to estimate it, the measurement of $t_{02,Scr}^{sig,inj}$ is necessary.

For the estimation of $t_{02,Scr}^{sig,inj}$ the signal from the downstream end of the Scraper fibre, presented in Figure 4.14, is used. This shows the average of ten single bunch injections in the ASLS storage ring, while the scrapers are closed. Three peaks can be observed, in time order: the injection signal, the beam scraping and its reflection (at the opposite fibre end face). The rising edge of the injection signal appears at $t_{02,Scr}^{sig,inj} = 1061\,\text{ns}$ from the beginning of acquisition. From the technical drawing of the ASLS, the length of the fibre from the injection point to the fibre extraction at Sector 2 can be measured as $x_1 = 24.65\,\text{m}$. Therefore, from Equation 4.9 the first beam loss will be detected at $t_{02,RF}^{sig,lead} = 995.4\,\text{ns}$. From this acquisition point on and for a distance of $\frac{L_{ring}}{2}$, the beam is travelling in the part of the ring covered by the RF fibre.

From Equation 4.10 and with $t_{02,RF}^{sig,lead}$ known, when the beam arrives at a location x_1 after the injection point, all the following signals of losses occurring along the path of the RF fibre can be calculated with respect to the injection point, as

$$x = x_1 + \frac{(t - t_{02,RF}^{lead}) \cdot c}{n+1} \tag{4.11}$$

Figure 4.15 shows the average of the RF fibre signal in two cases: when the IVU3 was closed (the undulator gap set at 6.6 cm) in blue colour, and open (the undulator gap set at 38 cm) in red colour. On the horizontal axis the position where the loss occurred with respect to the injection point was calculated from Equation 4.11.

A MATLAB mockup of the Australian Synchrotron machine elements was added on the bottom of the plot. A second horizontal axis shows the relative time of the signal arrival, with

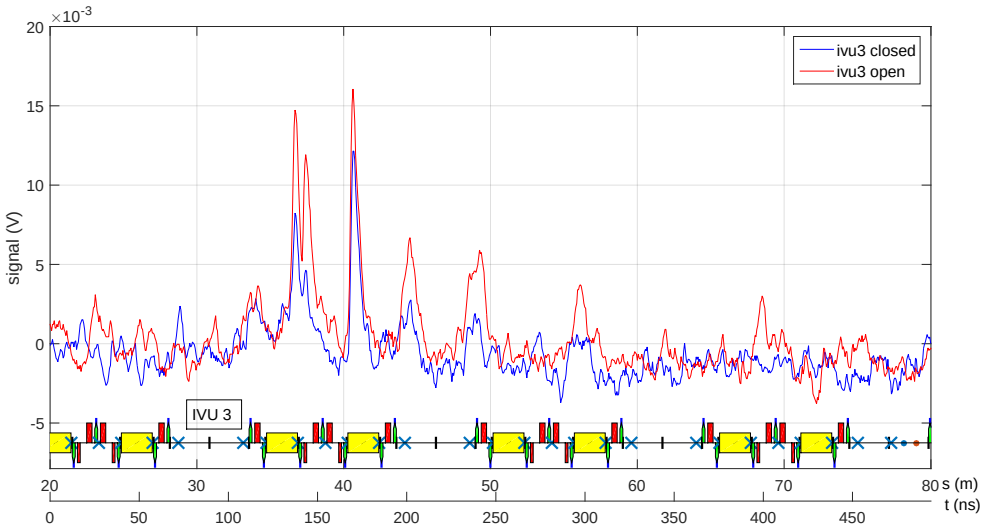

Figure 4.15 – First turn single bunch losses observed in the RF fibre when the IVU3 is open (red) and closed (blue).

$t = 0$ set at the point where the RF fibre starts covering the ring.

The beam loss signals of Figure 4.15 demonstrate the capabilities of longitudinal BLMs: The peaks observed can be attributed to different machine elements. As an example, a difference between the two measurements is visible, with higher signals along the line when IVU3 is closed. This can be explained as the closed IVU3 acts as a collimator, shaping the beam and collimating the halo particles. To support this fact, it can be observed that the peak at the exact location of IVU3 (x = 30 m) for the closed IVU3 is higher than in the case of the open one, due to the beam shaping in the first case. As an outcome of this process, the beam losses at the following quadrupoles are lower than in the case of an open IVU3.

The loss patterns shown in the figure appear to be not incidental, but rather related to the accelerator lattice. In Figure 4.16 a simulation of the ASLS double bend achromat beta functions is presented. The peaks following IVU3, and especially the double at ~140 ns, seem to be related to the horizontal and vertical beta functions. For the confirmation of this observation, more detailed simulations of the beam transport and loss mechanisms are required.

4.3.3 | Intrinsic time resolution

Following the understanding of beam loss location determination, a study on their time resolution potential was performed. With the scrapers closed, single bunch shots were injected consecutively to RF buckets 1 to 10, with the bucket increasing for each shot. Since the ASLS operates at 500 MHz, the successive buckets are separated by 2 ns. This process was repeated more than fifty times, and 540 pulses where acquired in total. As acquisition settings, 20,000 samples with a 2 GS/s sampling rate were selected.

As shown previously in Figure 4.9, the closed scrapers render a well-defined beam loss

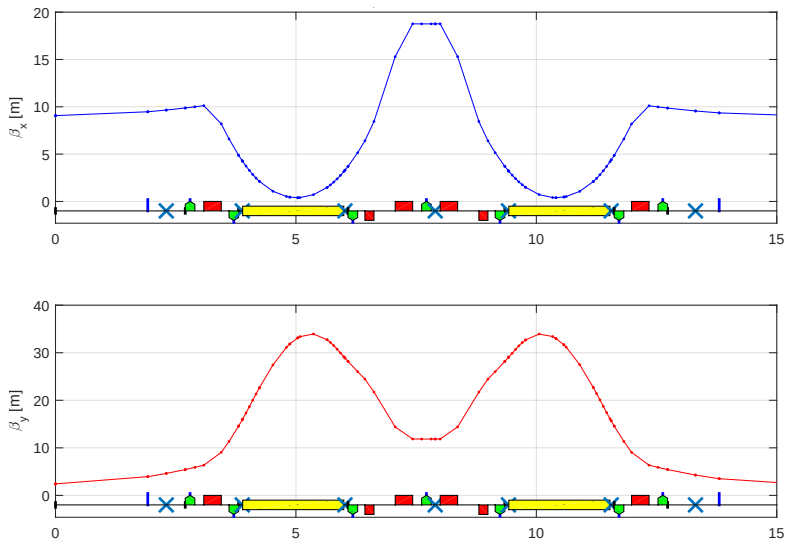

Figure 4.16 – Simulation of the horizontal and vertical beta function of the storage ring double bend achromat, provided by the Australian Synchrotron Light Source. A mockup of the machine elements has been added.

location, providing us a very clear signal at the upstream end of the Scraper fibre. Figure 4.17 shows the leading edge of the signals acquired at this exact location, while each bucket injection is represented by a different colour. A bucket-by-bucket disentanglement, i.e. a 2 ns shift between the signals for each bucket, can be clearly observed on a shot-by-shot basis.

From Equation 4.10 this 2 ns disentanglement corresponds to a clear location discrimination of less than 25 cm. Given the longitudinal spread that characterises the development of beam loss showers, this is satisfactory for the protection of a beam line with one distributed detector, making the discrimination of neighbouring machine elements possible.

To estimate the distribution of the photon arrival time t_{phot}, a threshold value was set at $V_{thres} = 0.1\,\text{V}$. The arrival time t_{phot} was estimated as the time at which the OBLM signal reaches this threshold value, through linear interpolation between the two samples that near V_{thres}. In Figure 4.19 the distribution of the photon arrival time t_{phot} for all acquired pulses is illustrated. As expected, the photon arrival is clearly grouped for the ten consecutive buckets.

The intrinsic time resolution of the system was calculated from the difference of the photon arrival time to the central value t_{cent} of each bucket, $\Delta t = t_{phot} - t_{cent}$. To determine the t_{cent} of the n$^{\text{th}}$ bucket, the t_{cent} of the fourth bucket was estimated initially as the mean value of the Gaussian that can fit the photon arrival distribution for this bucket. The central values of the remaining buckets were deducted from this using the RF period T_{RF} as

$$t_{cent} = t_{cent,4} + \Delta n \cdot T_{RF} \tag{4.12}$$

where $T_{RF} = 2\,\text{ns}$ and Δn is the number of buckets that separates the n$^{\text{th}}$ from the fourth bucket. The Δt distribution for all the acquired signals is illustrated in Figure 4.19, while the red line represents its Gaussian fit. The results show a time resolution of 260 ps, which from Equation 4.10 corresponds to a resolution in position better than 4 cm.

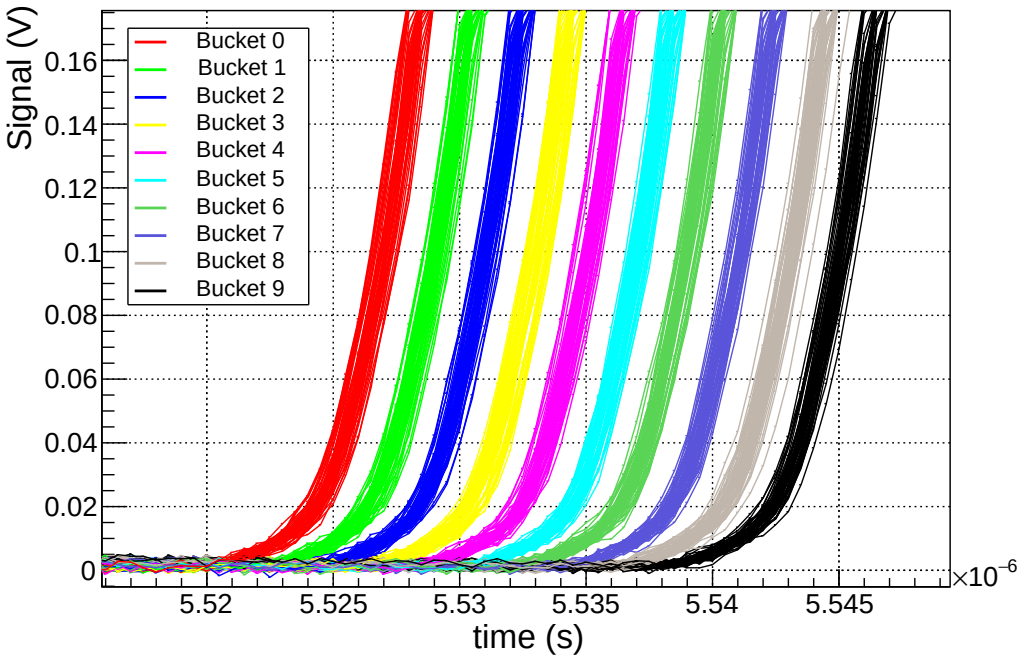

Figure 4.17 – Leading edge of the OBLM signal generated at the scrapers by single bunches injected consecutively into buckets 1 to 10.

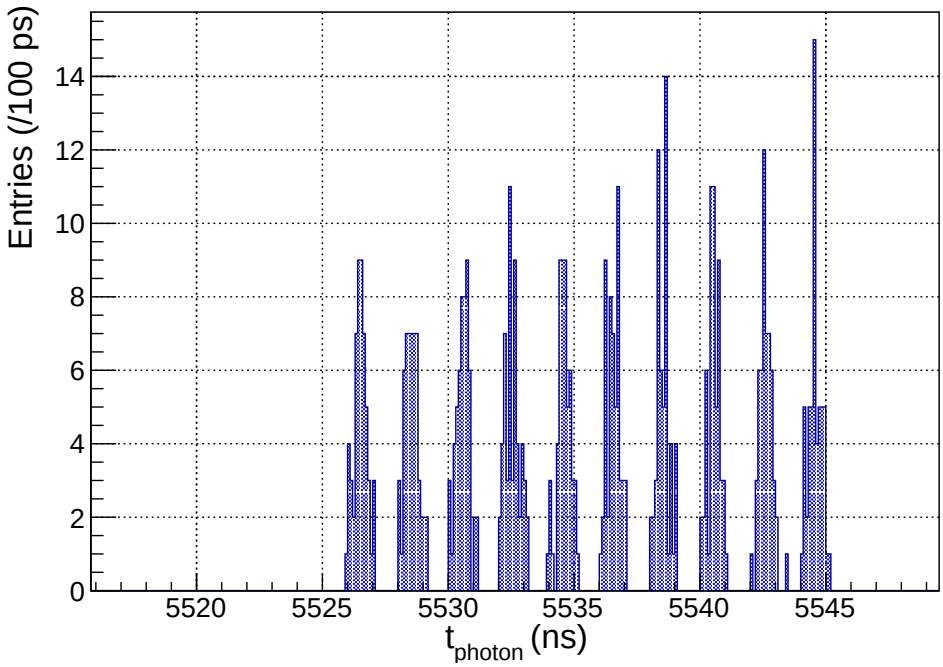

Figure 4.18 – Distribution of the photon arrival time at the upstream end of the fibre for ten consecutive buckets.

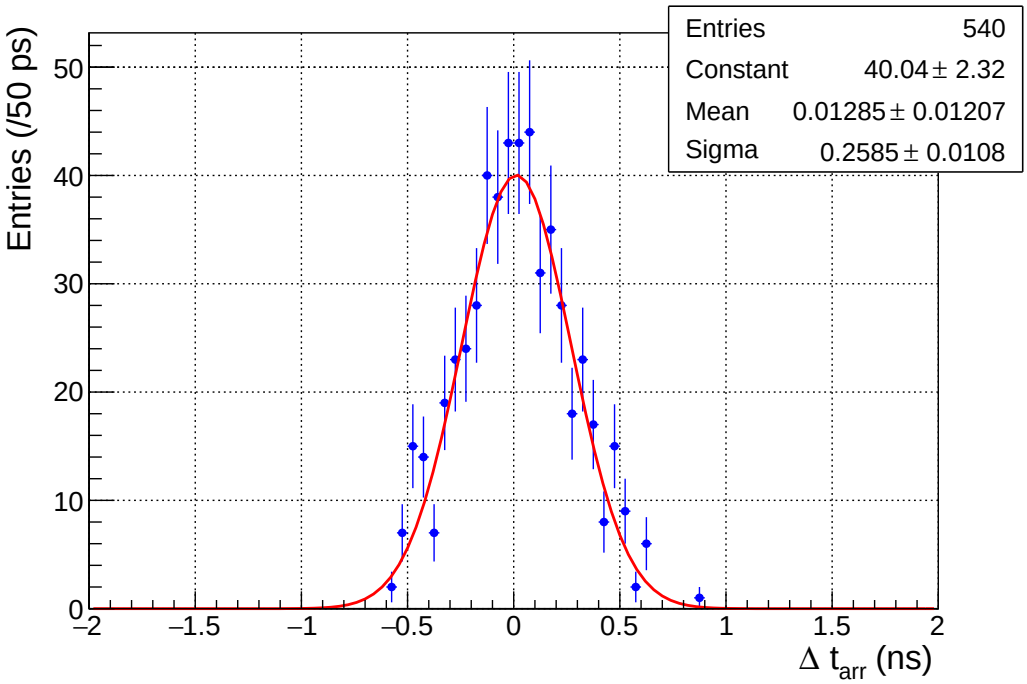

Figure 4.19 – Distribution of Δt (blue dots) and its Gaussian fit (red line).

4.4 Studies with long electron pulses

This section describes several measurements performed at the ASLS and the TBL, aiming to examine the applicability of OBLM systems for beam loss location determination in machines with long electron pulses.

4.4.1 | Multi bunch beam studies at the ASLS

At the ASLS, four beams with different pulse lengths were examined. More specifically the beams consisted of 15, 25, 50 and 75 bunches which correspond to pulse lengths of 30, 50, 100 and 150 ns, respectively. For each case 20 shots of 20,000 datapoints each and with a sampling rate of 2 GHz were acquired. The storage ring scrapers were closed, hence the losses during the first turn were investigated.

To determine the behaviour of signals with a very well known loss pattern, the upstream of the Scraper fibre was used.The average of the OBLM signals for each beam type are presented in Figure 4.20. Compared to the single bunch case of Figure 4.5, a similar structure in the multi bunch case is observable. The first two major peaks correspond to the beam injection and scraping. However, in the first peak, the BTS scraper losses cannot be separated from the injection point, and the double peak of the single bunch case appears here as a large single peak. In the very well defined scraper loss signals, the width of the peak corresponds approximately to the beam pulse length: 30 ns for the 15 bunches, 52 ns for the 25 bunches, 102 ns for the

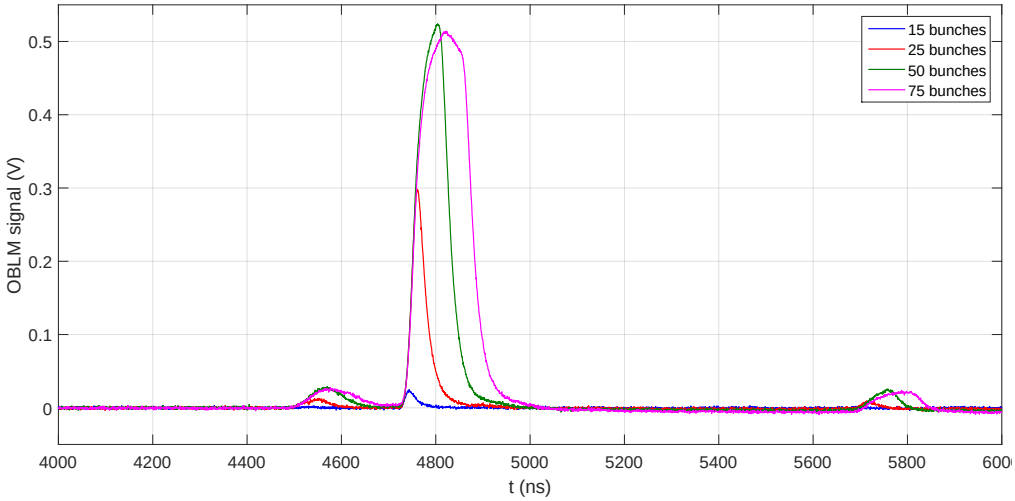

Figure 4.20 – Multi bunch generated OBLM signals in the upstream of the Scraper fibre.

50 bunches and 152 ns at 75 bunches. The slightly larger width than the respective pulse length is a result of the slower falling time of the SiPM. As expected, the reflection of the Cherenkov photons generated during beam scraping is also observed as a third peak.

In Figure 4.21 the average of the signals detected by the upstream end of the RF OBLM for the different pulse lengths are presented. As the exact origin of these losses is unknown,this case could be considered as unidentified beam loss signals. The peak structure shown for the respective single bunch case (Figure 4.15) is still observable. However, the spread of the signal increases with the pulse enlargement. As a result, only four major peaks are observable. Nevertheless, the OBLMs give an indication on the location of the losses, with an accuracy limited by the pulse width.

4.4.2 | Single- and multi-location losses at the TBL

To further examine the resolution that can be achieved in the case of a long electron beam, additional dedicated measurements were performed at the TBL with single- and multi location losses. The fibre installation at the TBL is described in detail in Subsection 4.2.2.

Signal background extraction

To successfully identify the beam loss location at the TBL, it it is necessary to ensure that the measured signal is generated at the Real signal fibre from losses intentionally set up at the TBL quadrupoles, and not at the Connecting Fibre. To that end the Background fibre is used. The background signal is subtracted from the BLM signal, as presented in Figure 4.22: the blue line correspond to the OBLM signal, whereas the black line is the background signal, as detected from the Background Fibre. The magenta line shows the losses as measured by the

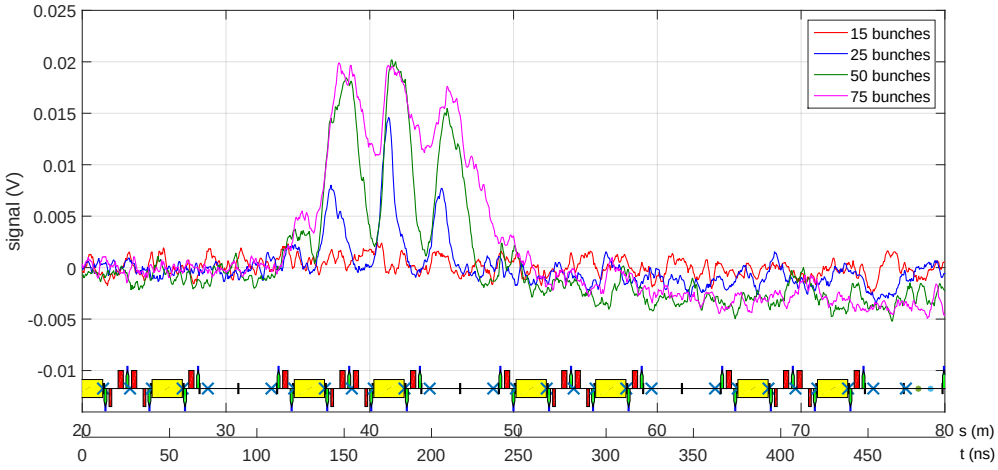

Figure 4.21 – Multi bunch generated OBLM signals in the upstream of the RF fibre.

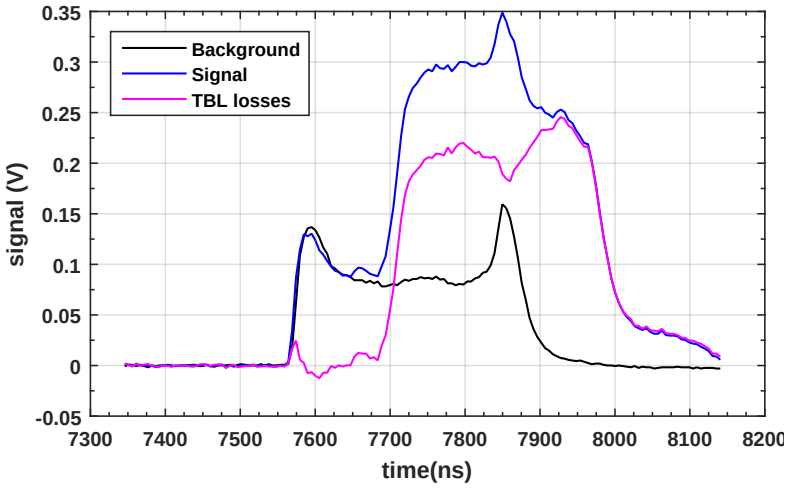

Figure 4.22 – Signals from the TBL signal fibre (blue), the background fibre (black), and the TBL BLM signal after the background extraction (magenta).

TBL fibre (Real signal Fibre), after background subtraction. The contribution of the Connecting fibre to the OBLM signal is important and can be noted from the fact that the final OBLM signal is similar to the one from the Background fibre during the first approximately 100 ns.

Single location losses

At the TBL the generation of single location losses can be achieved by switching off one of the beamline magnets. Five measurements were acquired with different machine settings: one with the nominal beam transmission, and four with one of the quadrupoles 7, 8, 11 and 12 switched off. Fifty shots per quadrupolar setting were acquired, with a 3 A peak current beam

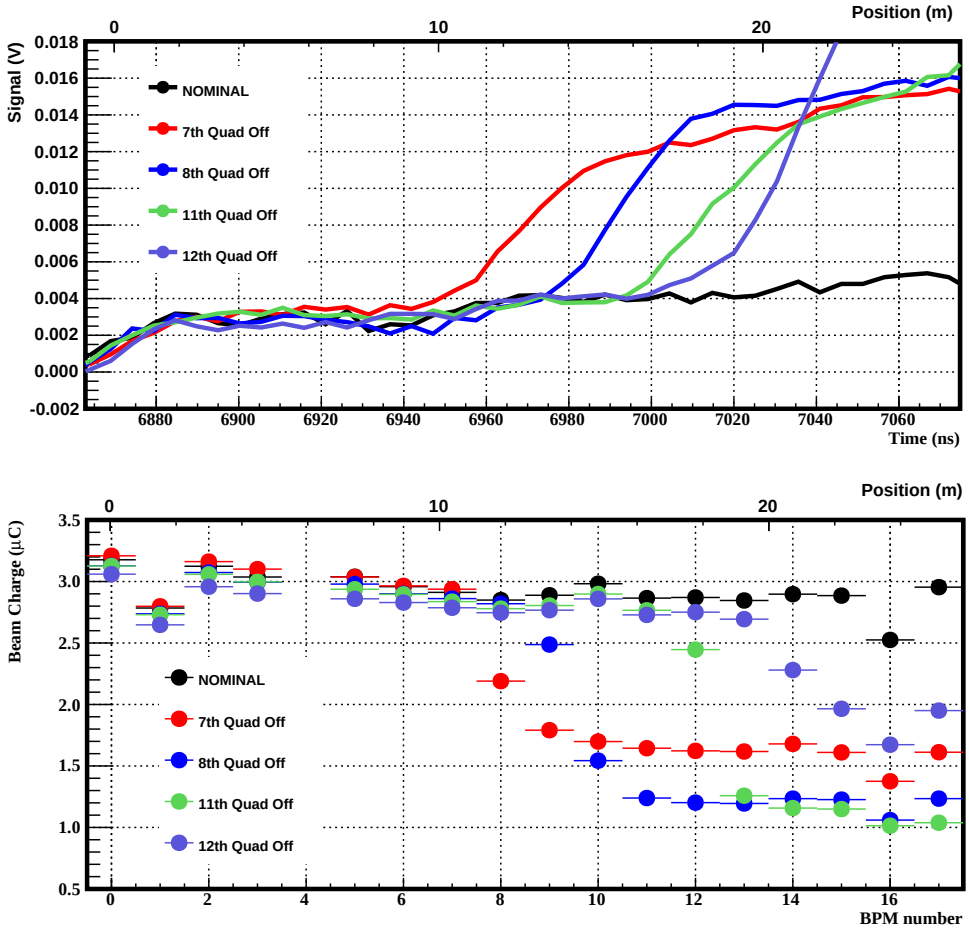

Figure 4.23 – BLM (top) and BPM (bottom) signals of the TBL for nominal beam transmission (black outline), and when one quadrupole is turned off.

and an 1 μs pulse length. Simultaneously, the BPM intensity signals were recorded.

The background signal was subtracted from each of the acquired signals as described above, and the average value of all shots per quadrupole setting was estimated. From the BPM intensity the beam charge was calculated as

$$C_{BPM} = \frac{\sum V(t)}{R} \times t$$

with $R = 50\,\Omega$ the load impedance and $t = 1\,\mu s$ the pulse length.

The results of this analysis are presented in Figure 4.23. The top plot shows the average OBLM signals while the above horizontal axis represents the relative position of the losses in the TBL, as calculated from Equation 4.10. The bottom plot shows the corresponding average BPM signals. Taking into account the 1.4 m distance between the BPMs, their position on the beam line was calculated and added to the horizontal axis on the top of the graph.

Figure 4.23 shows a clear distinction between the different quadrupole settings, in particular a discrimination between the consecutive quadrupoles 7, 8 and 11, 12. This demonstrates a localisation of ~1.4 m in the case of beam losses with long electron pulses, during single location losses.

Multi location losses

The absence of any interception devices in the TBL renders the generation of losses in multiple locations highly challenging. For this experiment, multi-location losses were generated via small modifications in the position of the quadrupole magnets, leading to alterations of the betatron oscillation. The disadvantage of this method is that the losses are not constrained in well defined locations, but are rather spread over a distance.

Three measurements with three different sets of quadrupoles shifted in position followed one measurement of nominal beam transmission. The three cases, the quadrupoles that were shifted and the distance between them are summarised in Table 4.4. In all cases the 5^{th} quadrupole was deviated, and the following shifted magnet varies from one to 2.5 FODO cells downstream. For each case 75 shots were acquired, with a beam pulse of ~350 ns and ~12 A beam charge.

Table 4.4 – Multi location loss setup at the TBL, with different quadrupole magnets shifting in position and the approximate distance between them.

case	Shifted Quadrupoles	Quadrupole Distance
A	5 and 10	7.0 m
B	5 and 8	4.2 m
C	5 and 7	2.8 m

The results of the experiment are summarised in Figure 4.24. On the top plot, the average BLM signal for the four cases are shown. Like the single location case, the averaging follows the background subtraction. On the top horizontal axis the relative location in the TBL was calculated using Equation 4.10. The lower plot shows the respective mean value of each BPM signal for the 75 shots of each loss scenario. On the top axis the BPM number has been converted into distance in m.

The black line represents the nominal beam transmission, and the coloured lines the three cases where the quadrupole magnets were shifted. The deviation of the 5^{th} quadrupole, which took place in all the three cases, created losses clearly detected by OBLMs. At this location, the latter show signals with an almost identical rising edge.

In case A, quadrupole 10 was shifted simultaneously with the 5^{th} quadrupole. The corresponding OBLM signal shows a plateau after the rising edge attributed to quadrupole 5, followed by a further increase approximately 7.5 m after the first one. This signal is in very good agreement with the BPMs and gives a good indication of the two loss locations. In case B quadrupole 8 was moved, and the OBLM signal differs: the second rising edge is hardly separated from the first one, agreeing once more with the BPM data. The rising of the signal above

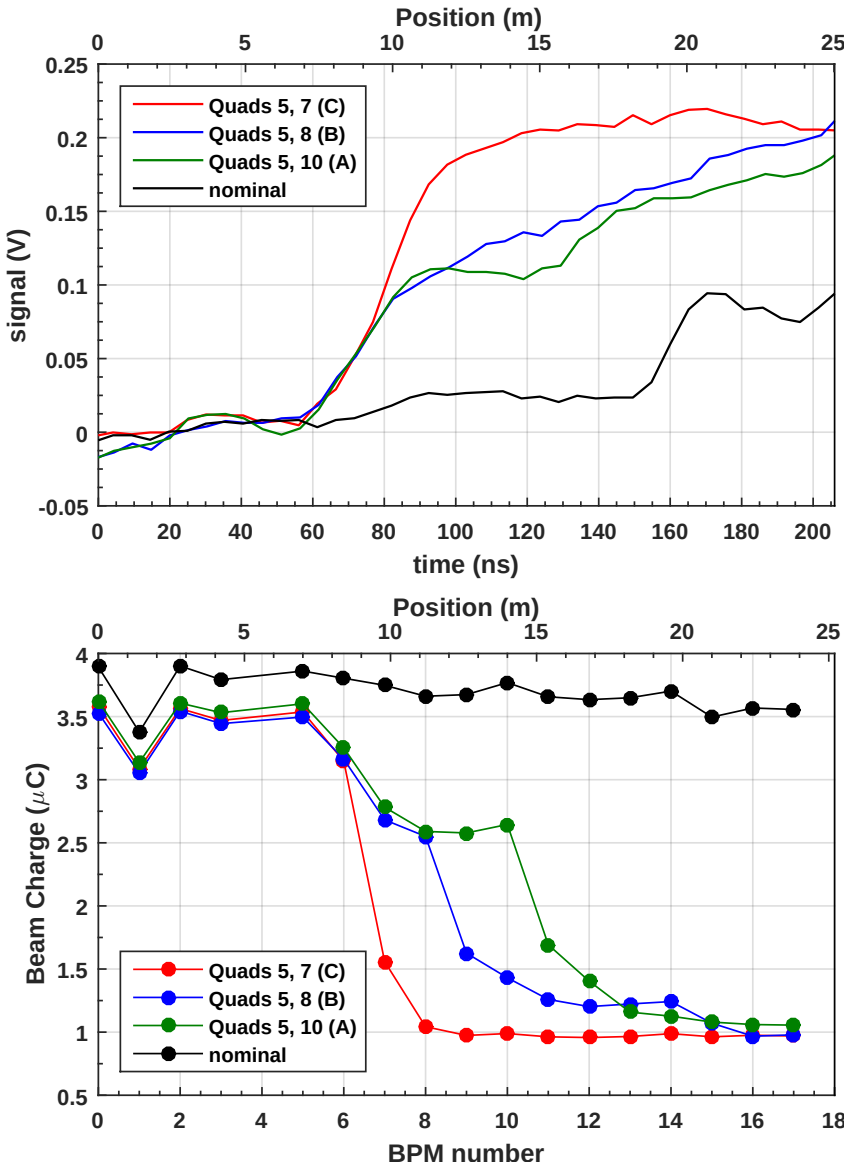

Figure 4.24 – BLM signals (top) and the respective BPM intensities (bottom) for the nominal beam transmission (black) and for the three cases described in Table 4.4.

the plateau of case A signifies the generation of the second beam loss. In case C no distinct second beam loss can be distinguished, but an increase in the slope of the rising edge is visible 20 ns (or approximately 3 m) after the first loss. This indicates a second source of beam losses, information impossible to obtain from the BPM data.

As mentioned above, during the multiple location measurements the beam losses induced are rather distributed, therefore no distinct loss location is expected to be visible. However, even under these conditions the OBLMs provide us with a qualitatively accurate representation of the beam losses, which in all cases agrees with the BPMs, and may grant significant information

on the loss patterns. Considering the agreement with the BPMs, a localisation better than 3 m is feasible under such conditions.

4.5 Summary

In this chapter optical fibre BLMs were examined in terms of their position resolution and the discrimination in the origin of losses they provide in two different machines: the ASLS in Australia and the TBL at CERN.

At the ASLS, different studies were performed towards the understanding of the signal readings in the case of a storage ring covered with OBLMs. The ability to detect and recognise sources of radiation that might otherwise go unidentified was demonstrated with the detection of the beam losses generated at the BTS scrapers of the machine. This also exhibits how distributed beam loss monitors can provide useful and detailed information for the machine operation and optimisation. Additionally, the case of discontinuous beam losses, i.e. when the beam travels in a part of a machine covered by a fibre, to continue in a non-covered section and then return to the first one, has been studied. The recognition of signals produced by photon reflection in the opposite end of a fibre has also been examined. Moreover, a method to unravel the origin of beam losses detected by a fibre covering a part of the machine with no recognised loss locations, when another fibre covers a part of the machine with well-known loss positions has been developed. Simulations of the beam transport and losses in the machine and the particle showers generated in its vicinity, with codes such as with MADX, FLUKA or BSDIM of Geant4, are necessary for a better understanding of beam loss signals and patterns acquired by OBLMs.

The system was demonstrated to disentangle a 2 ns shift in time, which corresponds to a capability for position discrimination better than 25 cm. This gives the possibility of distinguishing consecutive machine elements such as magnets or, in the case of linear accelerators like CLIC, accelerating structures. The intrinsic time resolution of the system was measured to be 260 ps, corresponding in a position resolution better than 4 cm with a single bunch beam.

The case of long electron pulses measurements at the ASLS shows that the OBLMs may give an indication of the origin of beam losses, but are limited by the pulse width. At the TBL, a localisation of approximately 1.4 m was achieved with 1 µm long electron pulses and a single loss location. In the case of multiple loss locations of a 350 ns long beam, a localisation better than 3 m was demonstrated. Given the spread of beam losses in the case of long pulses, such a localisation is satisfactory for the beam loss monitoring and protection of a machine with a distributed detector.

Finally, the installation of the fibres in the two machines provides additional information regarding the OBLM system. In the case of the ASLS, the successful coverage of the entire 216 m storage ring with only two 125 m long optical fibres has been demonstrated. At the TBL, where the beam loss signal is transmitted to a shielded location where the photosensing modules are installed, the use of a second fibre for the extraction of the background generated along the connection of the beam line and the modules was validated.

5

Fifth Chapter

Beam Loss Monitors in challenging accelerator environments

5.1 Introduction

Beam Loss Monitors are a very important machine protection and diagnostics tool. However, they suffer from limitations, most of which are associated either with their nature (e.g. sensitivity, dynamic range, radiation hardness) or with their location outside the beam pipe. The latter renders BLMs vulnerable to other radiation sources which can act as background signals and reduce the detector sensitivity.

This chapter presents measurements on BLM capabilities and limitations. In Section 5.2 the protection of a synchrotron light source by distributed OBLMs will be demonstrated. This includes in Subsection 5.2.2 the measurement of standard operational losses during the full machine cycle, and in Subsection 5.2.3 the detection of steady state beam losses during the normal operation of a storage ring. The results of this study can be applied to machines similar to light sources, such as damping rings, as well as to different accelerator types, i.e. circular storage rings and linacs. Section 5.3 focuses on BLM limitations, in particular the beam loss crosstalk phenomenon occurring in parallel beam lines. For that reason two different detectors, i.e. OBLMs and Little Ionisation Chambers (LICs), were examined at the first nominal two-beam module installed in CTF3.

5.2 Operational Losses in a Synchrotron Light Source

In this chapter OBLM capabilities for the protection of accelerators will be demonstrated through measurements conducted at the ASLS. In addition, the performance of two different photosensors in such applications will be examined.

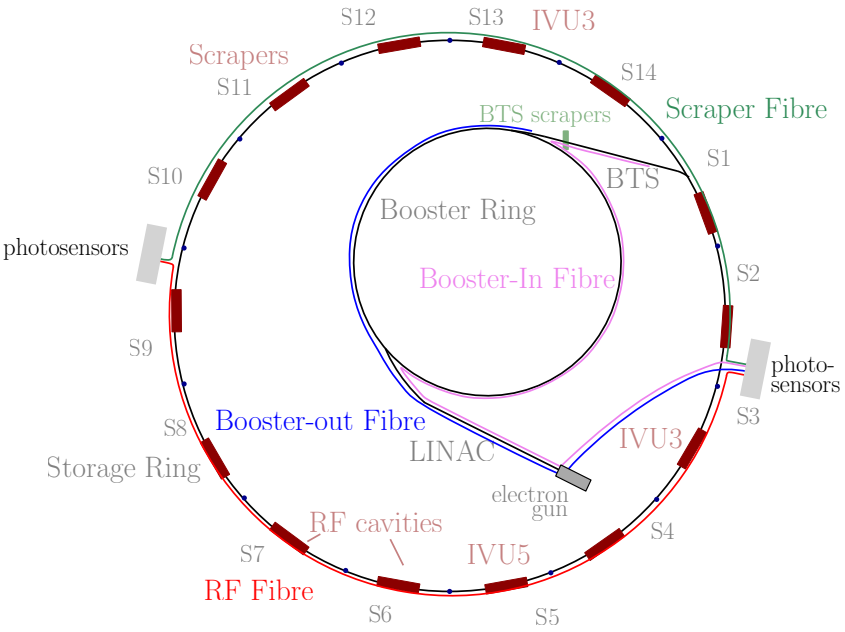

Figure 5.1 – Sketch of the optical fibre BLM system at the Australian Synchrotron Light Source. Four optical fibres are installed, the Scraper fibre (green) and the RF fibre (red) covering the Storage Ring, the Booster-In and -Out fibres (magenta and blue) covering the linac, half the booster and the BTS line

5.2.1 | Installation

The installation of the optical fibres in the storage ring has been discussed in Section 4. Here, the description focusses on those optical cables installed for the observation of beam losses at the LINAC and Booster accelerators, which are parts of the ASLS comprising no other BLMs. The two fibres are 125 m long and have a 200 µm (245 µm pure Silica core (cladding), a 345 µm acrylate coating and a dark nylon jacket. Initially, they cover the linac symmetrically, one being fixed on each side of it as shown in Figure 5.2(a). The fibre on the right side of the linac was named “Booster-In fibre” and the other “Booster-Out fibre”. The two fibres then separate, with each covering approximately half of the booster. In addition, the “Booster-In” fibre covers a large fraction of the BTS transfer line, the BTS scrapers and the booster-to-BTS extraction point, as illustrated in Figure 5.1. As shown in Figure 5.2(b), the fibres were fixed on the beam pipe, through the inner sides of the quadrupoles and dipoles. Furthermore, the only optical end of these fibres which arrives at the roof of the facility where the photosensors are located, is the end upstream of the linac line, which is extracted at Sector 2. To prevent any ambient light from being detected by the photosensors, the modules were covered with a thick black fabric.

For safe fibre extraction a light-tight and robust tube was used, also shown in Figure 5.2(a). For data acquisition an Acqiris U1071A digitiser was used, provided by the University of Melbourne. The latter is equipped with two channels, characterised by an 1 GHz sampling rate, an 8-bit resolution and a bandwidth of 2 GS/s. The trigger signal for commensing acquisition comes from an Event Generator-Event Receiver (EVG-EVR) system described in detail in [148],

(a) (b)

Figure 5.2 – Installation of the booster optical fibres. (a) The extraction of the two fibres from the linac to the roof. One fibre is fixed on the left and the other on the right side of the linac. (b) The fibres passing through a quadrupole and next to a corrector magnet, at the ASLS booster.

and is correlated with the central trigger for the beam injection. A time delay applied to the former enables the OBLM data to be acquired at different times after the injection.

5.2.2 | Operational Losses at the Booster

In this study, the capability of OBLMs to follow the beam losses during a complete machine cycle, in particular during the booster cycle of the ASLS, is examined. The booster cycle starts with the beam injection into the booster ring. The beam energy ramping follows, lasting approximately 0.5 ms, and in the end of the cycle the beam is extracted to the storage ring.

Method

Two different photosensors were used, to combine studies of beam loss measurements during the booster cycle with the performance and the limitations of the photodetectors themselves. The upstream end of the Booster-In fibre was connected to a Hamamatsu fast PMT H10721-210 (OBLM-A) [149] and the upstream end of the Booster-Out fibre to a Hamamatsu MPPC S12572-015C [5] coupled to a transimpedance amplifier with a numerical gain of 500, for higher sensitivity. This comprised a Texas Instruments THS3061 amplifier [150] and a 0.5 kΩ feedback resistor. During the measurements, a multi bunch beam of an approximately 191 nC total charge was injected in the booster, whereas the BTS scrapers were at their nominal position, i.e. leaving an 11 mm gap from the centre of the beam.

For this experiment the data was acquired in sets of 25,000 samples at 1 GHz frequency. Therefore, a total signal duration of 25 µs was obtained with each trigger. To study the losses during the complete booster cycle, lasting approximately one second, multiple measurements at different timestamps, starting from the injection of the beam until its extraction to the storage ring, should be acquired. This was achieved by shifting the trigger time, which corresponds to the timestamp of the data acquisition onset for each measurement. Depending on which

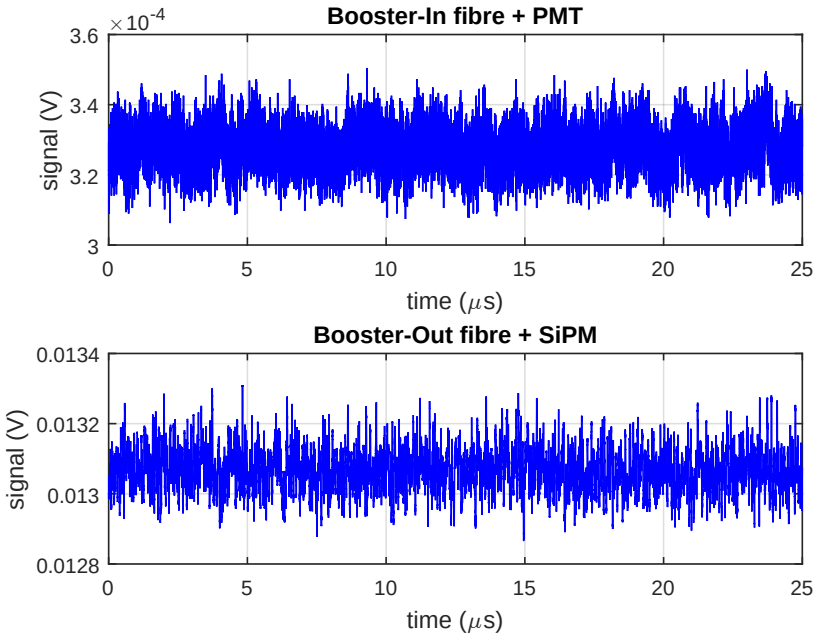

Figure 5.3 – Average of the background measurement of the two OBLMs covering the Linac, Booster and BTS line.

periods of the booster cycle were of interest, this shift varied from 25 µs to 100 ms. In particular, the beam injection and extraction to and from the booster are periods of high interest, therefore the time shift is set at 25 µs to enable a higher collection of data. Contrarily, during the ramping less information is required, and the trigger time was changed by 50-100 ns. For each timestamp a dataset of 50 shots was acquired.

The beam loss measurements during a full machine cycle demand a good knowledge of the machine and detector background, i.e. the signal generated by the OBLM system that is not generated by beam losses. Such a signal can be triggered by radiation sources in the machine, such as high gradient RF cavities, by ambient light or by the dark noise of the photosensor itself. To that end, 30 background shots of the OBLM signal were acquired in the absence of any circulating beam in the storage ring. The fibre background was estimated as the average of the 30 shots, and is presented in Figure 5.3. The lack of major electron or gamma-ray sources in the machine during these measurements, and the one order of magnitude difference between the signals of the two sensors, lead to the conclusion that the background is correlated with the dark noise of the photosensors and their corresponding front-end electronics. This is confirmed and further discussed in Paragraph 5.2.3.

To ensure that it is real beam losses which are measured, a voltage value larger than the maximum of the background signals of Figure 5.3 was taken as a cutoff for the beam loss detection. In particular, $V_{cut,A} = 0.00036\,\mathrm{V}$ was taken for the Booster-In fibre and the PMT, and $V_{cut,B} = 0.0134\,\mathrm{V}$ for the Booster-Out fibre and the SiPM. The signal offset V_{off} was estimated as the mean value of the background signal, with $V_{off,A} = 3.28 \times 10^{-4}\,\mathrm{V}$ and $V_{off,B} = 0.0131\,\mathrm{V}$

for OBLM-A and -B respectively. The total charge generated by the photosensors was calculated in the PMT case, for all samples whose value was *higher* than the selected cutoff, as:

$$C_{PMT} = \frac{\sum (V - V_{off,A})_{(V>V_{cut,A})} \times t}{R}, \tag{5.1}$$

where $R = 50\,\Omega$ is the measurement load and $t = 1$ ns is the sample interval. For the SiPM with the transimpedance amplifier readout, the respective value for the generated charge was given by:

$$C_{SiPM} = \frac{2 \times \sum (V - V_{off,B})_{(V>V_{cut,B})} \times t}{R_F}, \tag{5.2}$$

where $R_F = 0.5\,\text{k}\Omega$ is the feedback resistor.

The statistical mean of the detected charge $\overline{C}_{PMT}$ and $\overline{C}_{SiPM}$ and the corresponding standard error of the mean σ_C were computed for each dataset. Finally, given that the time window of each datapoint was equal to 25 000 ns, the mean detected current was estimated as $I = \frac{\overline{C}[\text{nC}]}{25000}\,[\text{A}]$ and the corresponding error as $\delta I = \frac{\sigma_C}{25000}$.

Results

The signals detected by the two booster fibres throughout the full cycle are presented in Figure 5.4, where a similar behaviour is observed in the two photosensors. It is important to mention here that the two signals can be compared qualitatively but not quantitatively, for two reasons: first, the charge produced by the photosensor is measured, and not the number of detected photons. To calculate the detected photons, one should take into account the photosensor gain. Second, the two fibres do not cover exactly the same areas of the facility and therefore detect beam losses occurring in different locations.

The injection into the booster results in rather high OBLM signals, reaching 100 µA for both detectors. In the four milliseconds following, an exponential decay is observed, which is characteristic of the beam damping following the injection process. The decay is followed by a plateau which is compatible with zero signal. However, the values of the current on the plateau are consistently higher than the dark current expected for the two photon sensors, namely: 1 nA for the fast PMT and 100 nA for the SiPM, leading to the conclusion that there is a small background signal during the machine operation. Following the 0.5 ms ramping, the booster cycle ends with the beam extraction into the BTS line, noticeable from the high signal of the Booster-In fibre.

The beam extraction to the storage ring is illustrated in greater detail in Figure 5.5. A gradual increase of the losses in the case of the Booster-In fibre is observed, which is attributed to the slow bump process. In particular, at the ASLS booster a total of four bumper magnets are installed, two before and two after the BTS extraction point. The Booster-Out fibre covers the first magnet but is extracted before the second one, while the Booster-In fibre covers both of the bumpers following. During the slow bump, the first magnet deflects the beam to the outer side of the storage ring and the second straightens it. Due to its location, the Booster-Out fibre will not detect any beam losses stemming from this process. The losses, however, propagating

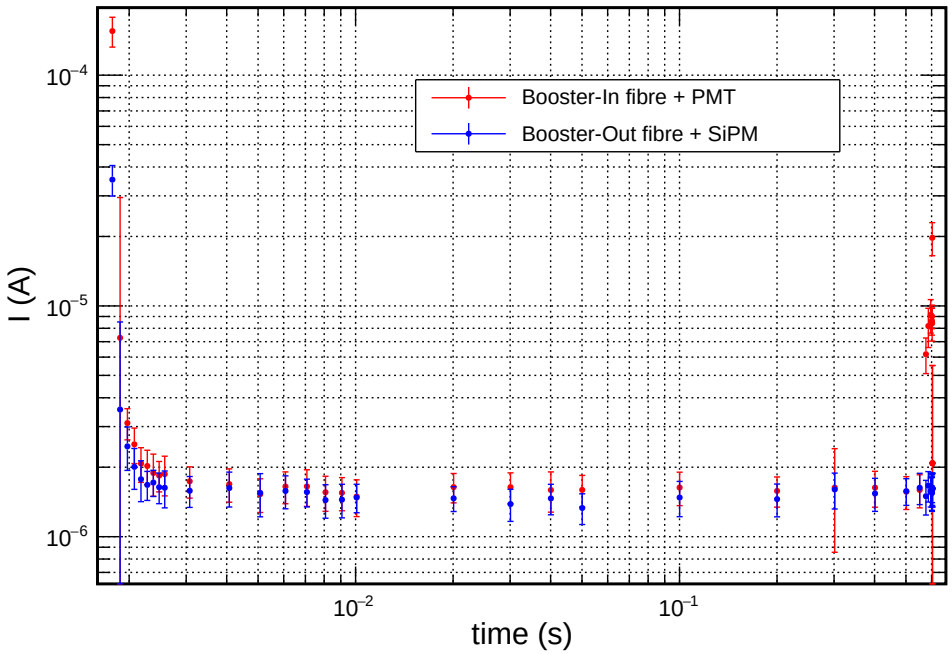

Figure 5.4 – Beam losses during the booster cycle as detected by the Booster-In fibre coupled to a fast-PMT, and the Booster-Out fibre coupled to an SiPM.

downstream, may generate signals in the Booster-In fibre. The latter will additionally detect any beam losses originating from the third and fourth bumper magnet, as well as those developed in the BTS line [151]. With the beam injection in the storage ring the Booster-In fibre signal increases further, to decrease after the injection to the plateau value (last datapoint of the Booster-In fibre in red). The other OBLM, not covering the BTS line region, does not monitor the extraction losses. This phenomenon highlights the main advantage of distributed BLMs compared to localised detectors: the coverage of the entire facility prevents any dangerous losses from going undetected, and aids the beam diagnostics of the entire accelerator.

5.2.3 | Steady State Losses

The following measurements aim to examine the possibility of measuring steady-state beam losses. During the storage ring operation, with a lifetime of approximately 20 hours, the beam losses are expected to be quite low. As a result, it is practically impossible for localised BLMs to detect them. At the ASLS measurements were taken with the distributed OBLMs, in two different cases, and the ability to detect steady state losses with this type of monitor is demonstrated.

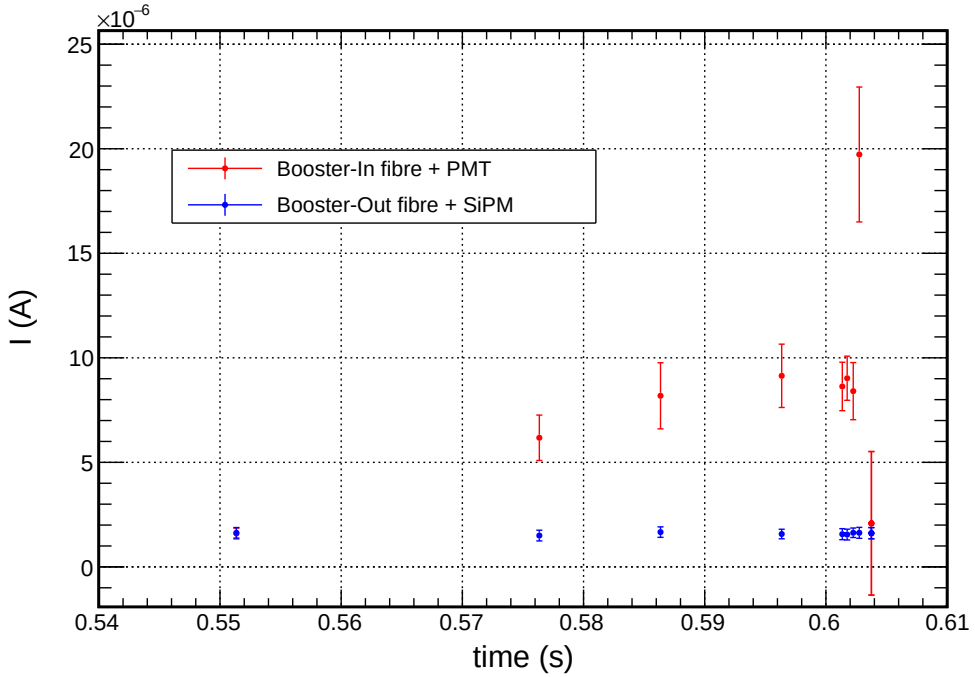

Figure 5.5 – Beam losses during the last milliseconds of the booster cycle before extraction to the storage ring (zoom of Fig. 6).

Method

For this experiment the storage ring OBLMs were used, with the photosensors described in Subsection 5.2.2 installed at Sector 2. The downstream side of the Scraper fibre was connected to the fast-PMT H10721-210 (OBLM-A), whereas the upstream of the RF fibre went to the SiPM S12572-015C, coupled to the transimpedance amplifier circuit (OBLM-B).

To measure steady state losses, two beam loss scenarios were studied. During the first scenario, single bunches were injected into the storage ring, while the beam scrapers were fully open. In this case a beam of approximately 108 mA was already circulating in the storage ring prior to the measurements. During the second case nominal bunch trains of 75 bunches were injected, while the beam scrapers were at standard position, leaving an 11 mm gap. In this case the beams were injected into an empty storage ring.

For the single bunch case the acquisition system was set to store 56,000 samples per trigger with an 1 GHz sampling rate, whereas for the multi bunch one a 0.1 GHZ sampling rate for

Table 5.1 – Experimental cases examined as part of the steady-state loss study.

bunches	scrapers	shots (/trigger)	sample interval	time window
1	open	50	1 ns	56 000 ns
75	nominal	25	10 ns	500 000 ns

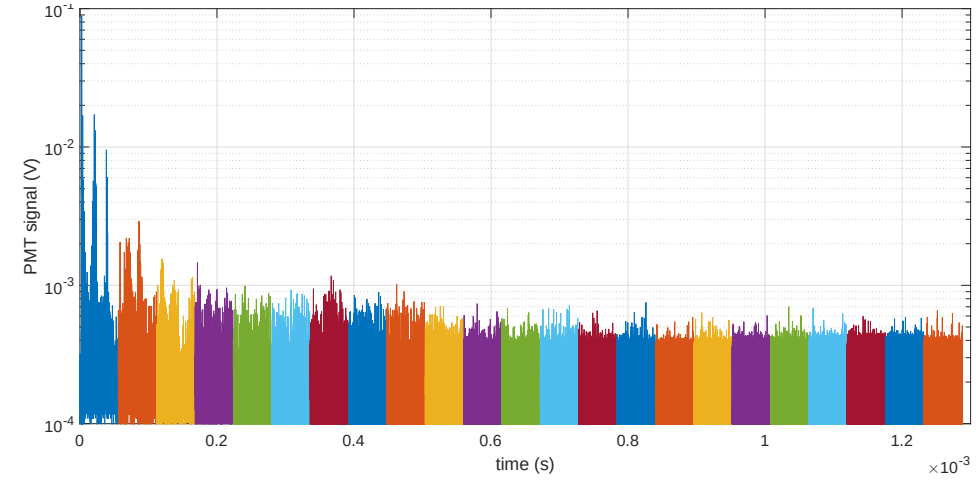

(a)

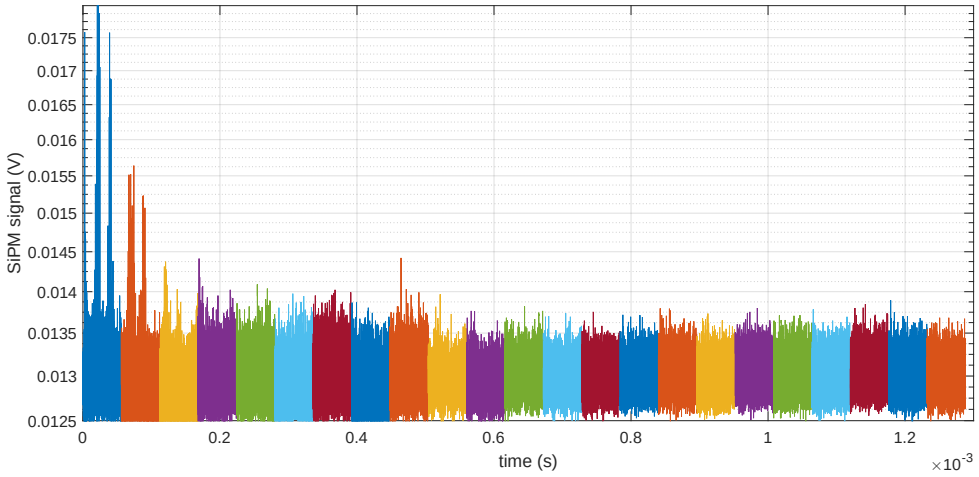

(b)

Figure 5.6 – Average OBLM signals of the single bunch case measurements, concatenated. (a) For OBLM-A, with a fast PMT coupled to the downstream of the Scraper fibre. (b) For OBLM-B, with an SiPM coupled to the upstream of the RF fibre.

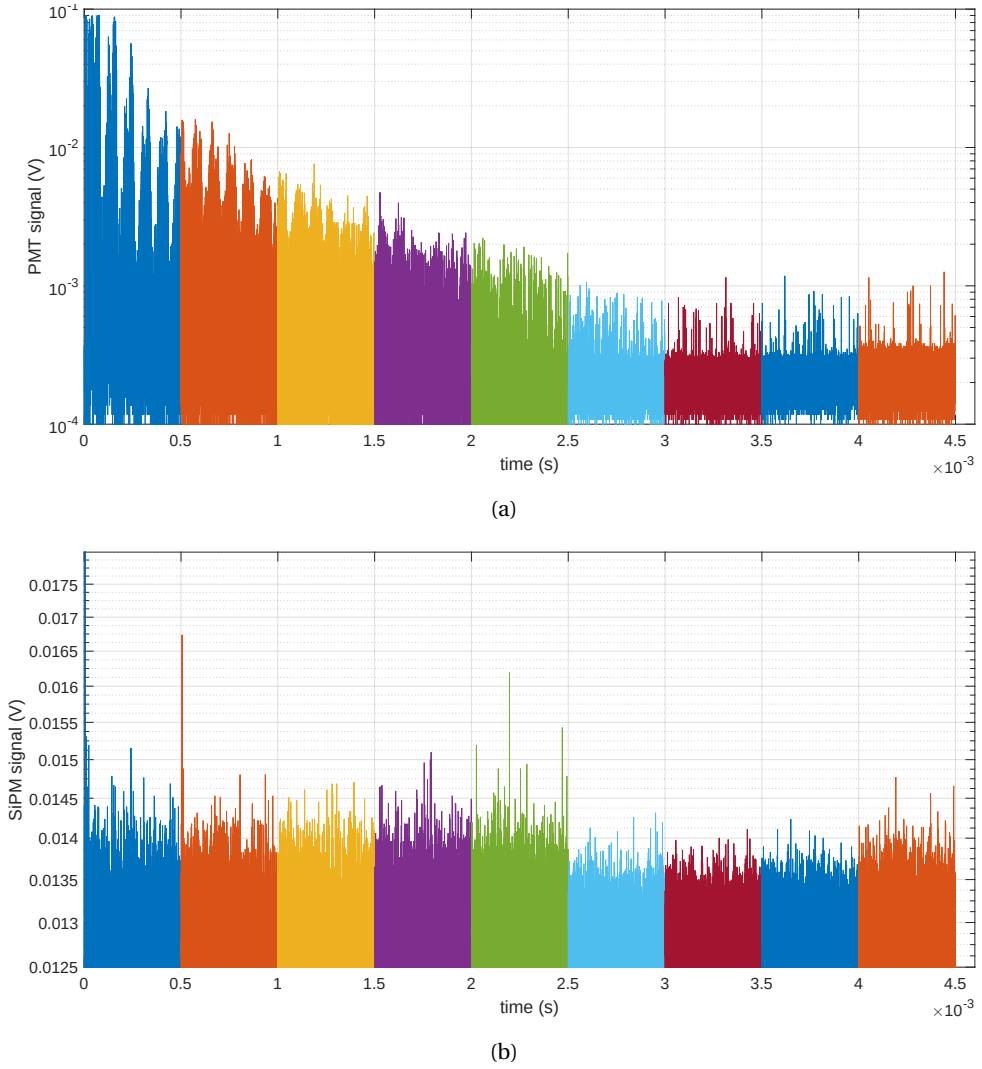

Figure 5.7 – Average OBLM signals of the multi bunch case measurements, concatenated. (a) For OBLM-A, with a fast PMT coupled to the downstream of the Scraper fibre. (b) For OBLM-B, with an SiPM coupled to the upstream of the RF fibre.

50,000 samples was used. As a result, the data acquisition depth of the first case was limited to 56 µs, while for the second scenario the time window was 500 µs. Given this limitation, the trigger time of the data acquisition was delayed in order to look at losses at later times after the beam injection.

During the first scenario 50 shots per trigger were taken. However, since the storage ring can hold up to 200 mA, only 25 shots per trigger could be injected into the ring in the multi bunch case. The characteristics of the two different experimental cases are summarised in Table 5.1.

In Figures 5.6 and 5.7 the two OBLM signals, for the single bunch and the multi bunch case respectively, are illustrated. Each colour represents the average signal of the measurements

taken for each trigger timing, while these signals are shown concatenated. During the storage ring top-up the losses are expected to be very low. In particular considering a 200 mA stored beam, a beam intensity $N_{beam} \approx 9 \times 10^{11}\,e^-$ and a lifetime of approximately 20 h [64], they can be calculated from Equation 1.9 to be of the order of ten electrons per turn. This is supported by the OBLM signals which, after the first few beam turns, approach background values.

Consequently, a good estimation of the OBLM background for this study is also essential. The background measurement was performed similarly to Subsection 5.2.2. Without beam in the machine, 30 background datapoints were acquired and the mean value of the signals obtained was calculated, presented in Fig. 5.8. The storage ring background signals are very similar to the ones observed for the Booster (Figure 5.3), leading to the conclusion that the noise originates mainly from the photosensors themselves and the front-end electronics. The difference between the latter constitutes the difference in the levels of the two signals.

The charge detected (i.e. the charge that the photosensor generates) for the PMT was calculated from Equation 5.1, with a cutoff value estimated as $V_{cut,A} = 0.0006\,\mathrm{V}$, and only samples greater than this value were taken into consideration. For the SiPM, the respective cutoff was set to $V_{cut,B} = 0.0137\,\mathrm{V}$, while Equation 5.2 was used for the calculation of the detected charge. It may be deduced that the PMT noise is approximately one order of magnitude lower than that of the SiPM coupled to the transimpedance amplifier circuit. However, some spikes on the PMT signal can be observed, which were not visible i Figure 5.3 and the Booster-In fibre coupled with the PMT setup. These leads to the conclusion that some sources of background radiation are being measured at the present setup. The signal offset $\mathrm{V_{off}}$ corresponds to the mean value of the background signal, and has been calculated as $V_{off,A} = 1.97 \times 10^{-4}\,\mathrm{V}$ for OBLM-A, and $V_{off,B} = 0\,0129V$ for OBLM-B.

As the single bunch and the multi bunch case were measured within different time windows, the detected charges cannot be compared. To normalise the two cases, the detected current had to be estimated. This was achieved by dividing the statistical mean of the detected charge per dataset, $\overline{C}_{sb}$ and $\overline{C}_{mb}$ by the respective time window. Therefore $I_{sb} = \overline{C}_{sb}/56\,000\,[\mathrm{A}]$ and $I_{mb} = \overline{C}_{mb}/500000[A]$ for the single bunch and the multi bunch case respectively. The corresponding errors were calculated from the standard error of the mean for each dataset, as $\delta I_{sb} = \sigma_{C_{sb}}/56000$ and $\delta I_{mb} = \sigma_{C_{mb}}/500000[A]$.

Results

Figure 5.9 summarises the results of the two measurements, with each point corresponding to the mean value of the current (I) detected, for the number of datapoints acquired per trigger timing. In particular, Figure 5.9(a) represents OBLM-A, for the single bunch (blue) and the multi bunch (red) case. In both of them an exponential loss decay is observed, characteristic of the beam injection process. In the complete set of measurements the losses detected for the multi bunch case, with the scrapers in nominal position, are up to two orders of magnitude higher than those of the single bunch case, during which the scrapers were wide open. The larger beam charge together with the presence of scrapers can explain this pattern. In addition, the signals of the multi bunch beam seem to increase slightly during the final measurements,

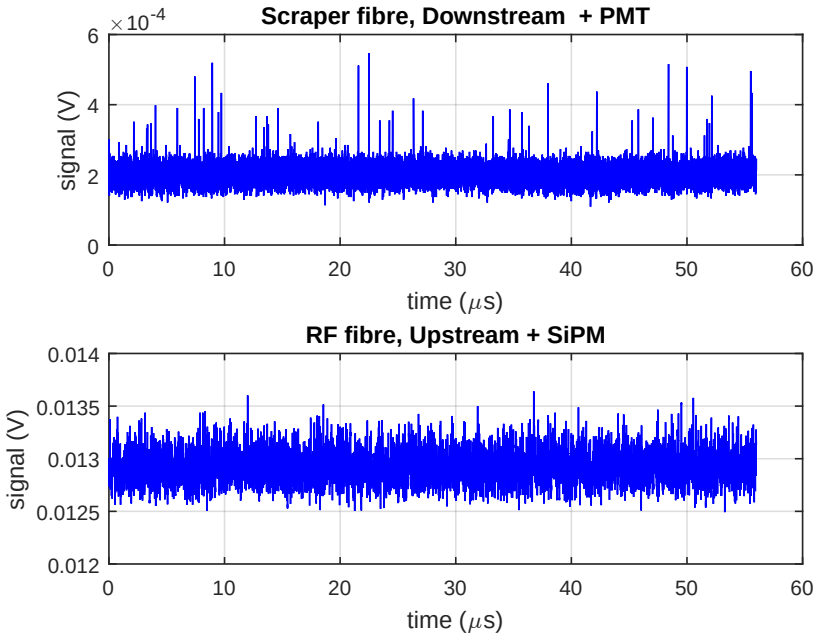

Figure 5.8 – Average of the background measurement for the fibres covering the storage ring.

when reaching the steady-state. This is again attributed to the higher, charge at this point, in the ring and the beam cleaning at the scrapers.

In Figure 5.9(b) the detected charge in the upstream end of the RF fibre (OBLM-B) is summarised. Unlike OBLM-A, in this case injection losses are not observed, apart from the first point in both single and multi bunch measurements which is slightly higher than the rest. This was expected, as the given detector (RF fibre) covers neither the injection point nor the scrapers, where the beam is cleaned and the highest losses occur.

The single bunch case of OBLM-B shows losses constistently higher than the multi bunch one, in which the beam has been previously cleaned. This detection of beam losses which are higher than the signals obtained when a cleaned beam is circulating in the machine, confirms the detection of steady-state losses by the OBLMs.

The fast PMT and the SiPM examined in this study show similar behaviour in beam loss detection. The main difference between the two sensors in this type of measurements is their noise level. The higher noise of the SiPM may introduce challenges to the detection of very low signals. Also taking into consideration the faster time response of the PMTs, they may prove more suitable for applications in storage/damping rings.

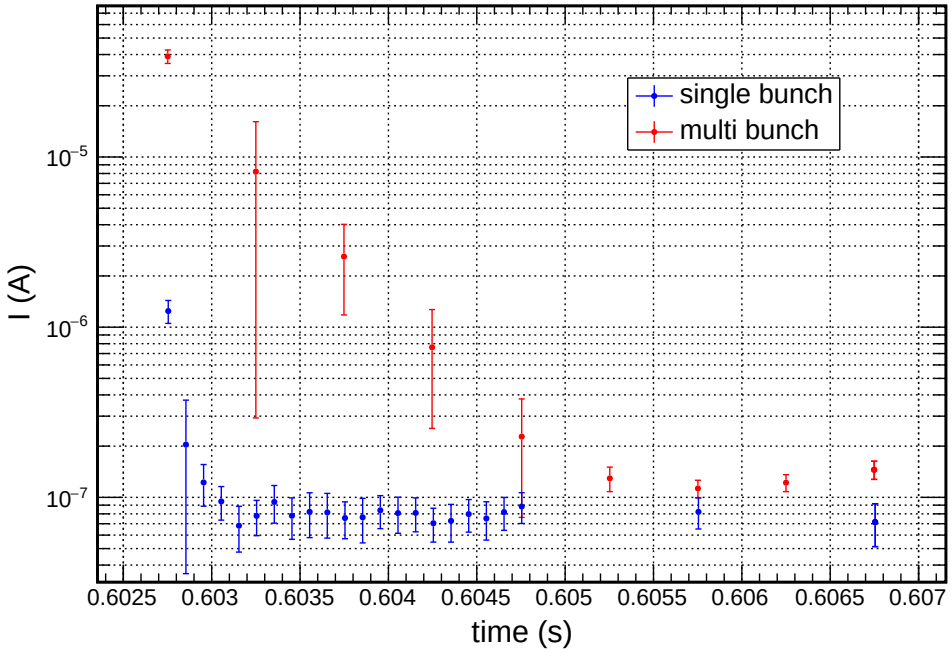

(a)

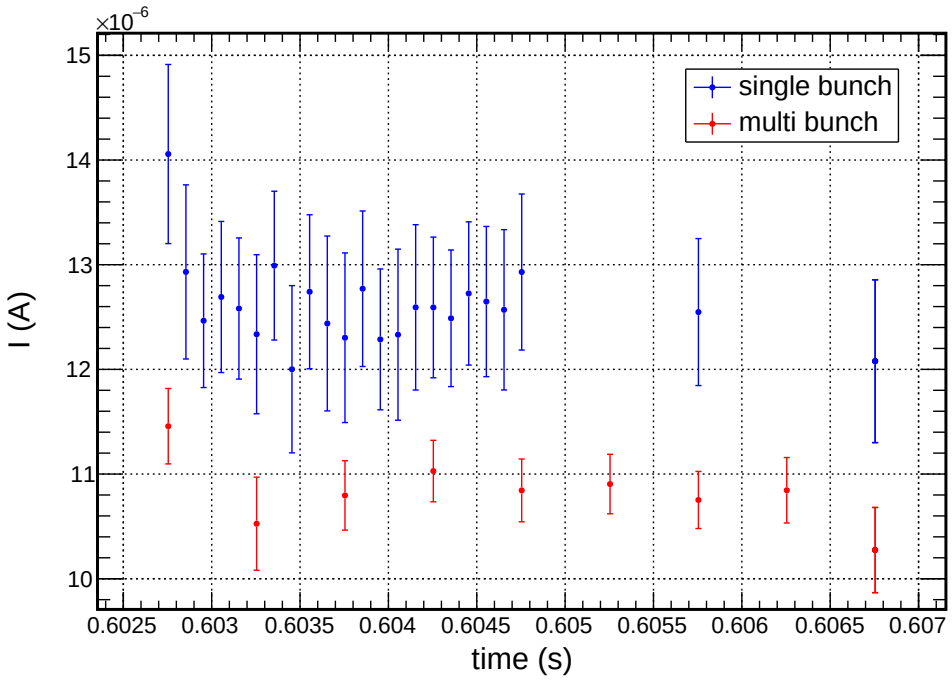

(b)

Figure 5.9 – Comparison of the detected current in the single and the multi bunch case. (a) For OBLM-A, with a fast PMT coupled to the downstream of the Scraper fibre. (b) For OBLM-B, with an SiPM coupled to the upstream of the RF fibre.

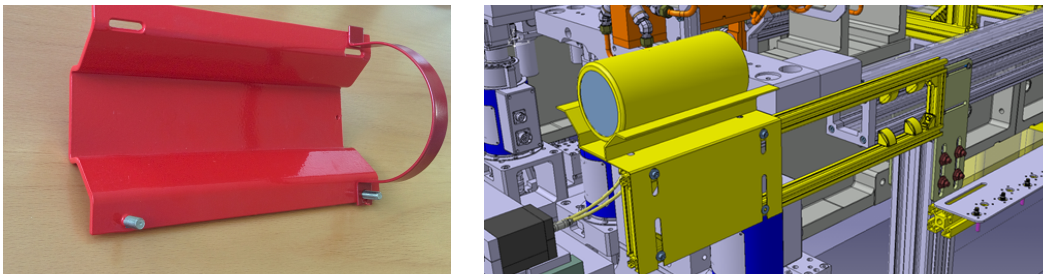

Figure 5.10 – (a) The LIC original support *CERN, BE-BI.* (b) The element designed for the integration of the LICs and the LIC support to the CLIC TBM

5.3 Beam Loss Crosstalk: A BLM limitation in parallel beam lines

High sensitivity together with large dynamic range are important parameters of a BLM for the successful protection of an accelerator. When more than one beam line operates in parallel, a phenomenon that may limit sensitivity of BLMs is introduced: the so-called beam loss crosstalk. The crosstalk refers to the case when beam losses occurring in one of the accelerator lines are detected by the BLMs intended to protect the other one. This hinders the detection of very low losses originating from the beam line the BLM is designated for, hence limiting its sensitivity.

The crosstalk is particularly interesting in the case of the CLIC, where main beam and drive beam beams circulate simultaneously through the two accelerators, and beam loss monitoring requirements demand a highly sensitive BLM system [40]. The CLEX in CTF3 with its two parallel beam lines as described in Paragraph 1.6.1 was regarded as an ideal facility to perform the first BLM crosstalk measurements.

5.3.1 | Installation

LIC installation

The LICs examined consist of three circular, parallel aluminium plates separated by 0.5 cm and filled with N_2 at a pressure of 1.1 bar. The main challenge for the LIC installation at the Two-Beam Module is the limited space for the installation of instrumentation. In addition, for the purposes of demonstration of BLM installation in a future CLIC machine, the detectors should be integrated on the TBM design. The standard LIC support * is presented in Figure 5.10(a). This, together with the LIC, required to be incorporated on the TBM, without interrupting any of the other activities performed on the module or affecting the machine alignment.

For the integration, collaboration with the designers of the TBM, mainly the CERN Modulators and Klystrons section (CERN BE-RF-MK), was necessary. It was decided that the LICs would be installed on the TBM wire protection case, which is fixed on the external sides of the module. An L-shaped part was designed to attach the BLM and its support on the case, as

*. designed by Slava Grishin from the CERN Beam Loss section (CERN BE-BI-BL) and manufactured by the CERN Beams Instrumentation Group (CERN BE-BI).

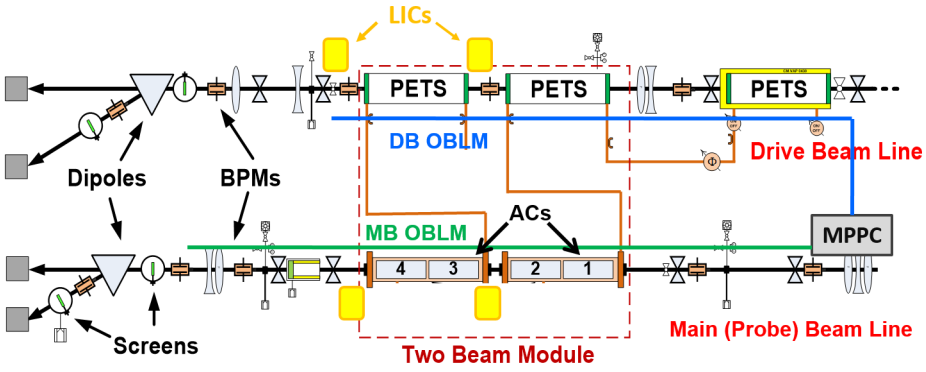

Figure 5.11 – Layout of the BLM installation at the nominal CLIC Two-Beam Module at CLEX. The main beam OBLM (green) and the drive OBLM (blue) are installed above the beam lines, whereas the LICS (yellow) are on the side of the TBM.

shown in Figure 5.10(b) *.

Finally, four LICs were installed on the TBM at CLEX, two of them on the main beam side and approximately 5 cm downstream of the accelerating structures, as presented in Figure 5.12 and two on the drive beam side approximately 10 cm downstream of the quadrupoles, shown in Figure 5.13. Therefore, two detectors are located in the middle and two downstream of the TBM, and the distance between the former and the latter is approximately 1.4 m. The layout of the BLM installation on the CLEX drive beam and main beam-CALIFES line is illustrated in Figure 5.11.

OBLM installation

Two optical fibres were installed along the two beam lines of the TBM. Each fibre is fixed above the beam line and separated from it by 15 cm vertically via mounting posts, attached

*. The LIC integration and design of the L-shaped part was performed by Dmitry Gutkov (CERN).

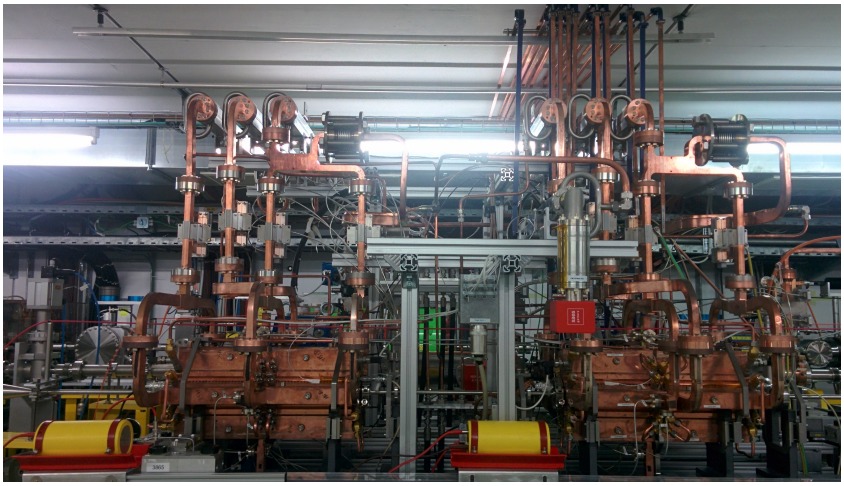

Figure 5.12 – Installation of the LICs (yellow) and the optical fibre (red) on the TBM main beam

on the beam pipe supports. In Figure 5.13 the optical fibre protecting the drive beam and the mounting post supporting it can be observed.

The two fibres are not identical: the drive beam fibre is covering the two TBM PETSs and one PETS located immediately upstream of the TBM, and measures 5 m in length with a 200 µm core diameter.

The main beam fibre, which is 7 m long and 365 µm in core diameter, covers more than two meters on the downstream of the TBM reaching the quadrupoles following it, and another two meters upstream of the module.

The main beam fibre was chosen with a larger core diameter to achieve higher sensitivity for the low intensity CALIFES beam. Figure 5.12 shows the main beam fibre, running above the accelerating structures. The characteristics of the two fibres are summarised in Table 5.2, while their installation layout is also presented in Figure 5.11.

To detect the Cherenkov photons, both upstream fibre ends were coupled to photosensing modules placed under the main beam line. The photosensor used was a Hamamatsu MPPC S12572-010C, coupled to an AC circuit based on a 50 Ω resistor and a 100 nF capacitor. For the beam current measurement a BPM right upstream of the TBM main beam was used.

The data acquisition of all BLMs is performed via a 12-bit, 100 MS/s and 100 MHz SIS3301 ADC card by Struck, controlled via a VME crate [152].

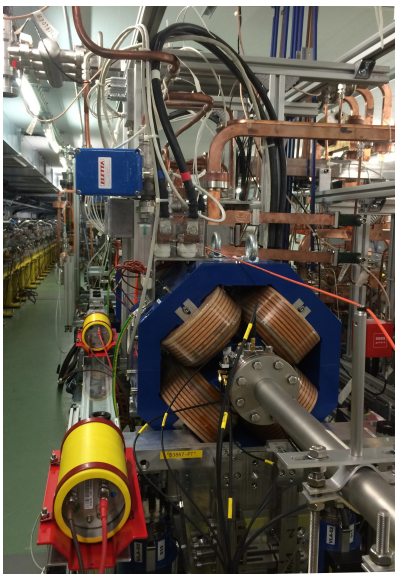

Figure 5.13 – Installation of the LICs (yellow) and the optical fibre (orange) on the TBM drive beam. The mounting post supporting the fibre can be distinguished.

5.3.2 | Main Beam to Drive Beam crosstalk

The first part of this study refers to the crosstalk of the low current CALIFES beam to the BLMs covering the drive beam side. For this purpose, the beam was sent through the CALIFES beam line while the main beam line was off. Forty shots were acquired for each of a total of ten datasets, with an increasing number of bunches. The bunch charge was kept constant

Table 5.2 – Fibre characteristics of the OBLMs tested at the TBM

	Main Beam	**Drive Beam**
length(m)	7	5
core diameter d (µm)	365	200
clad diameter (µm)	400	240
NA	0.22	0.22

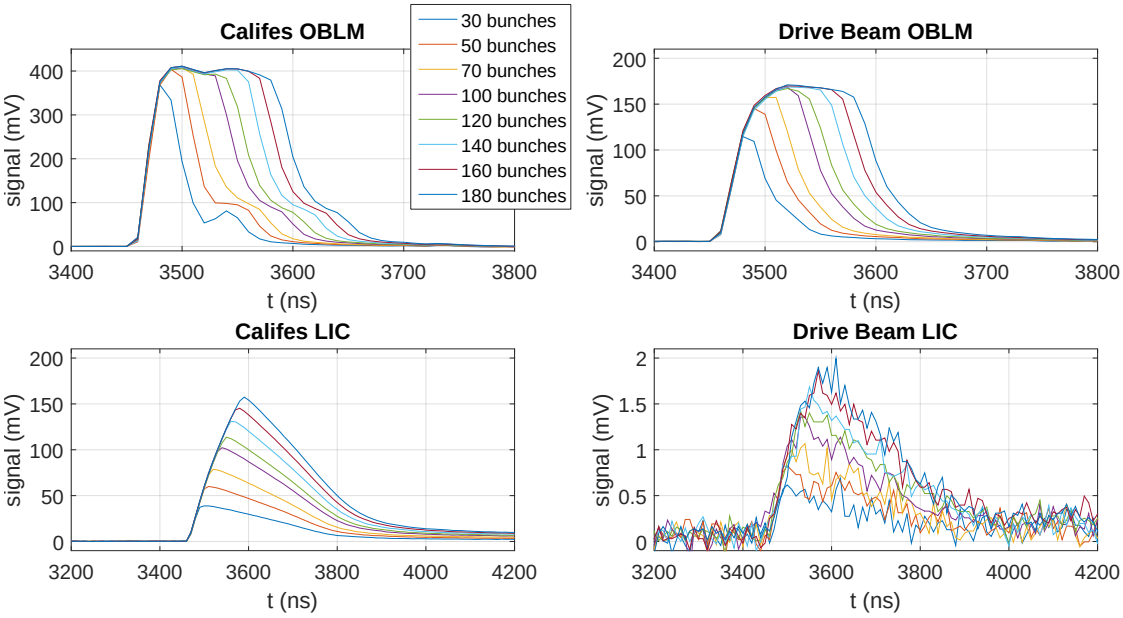

Figure 5.14 – OBLM (up) and LIC (down) BLM signals for CALIFES beams with increasing number of bunches. On the left, the signals of the detectors protecting CALIFES. On the right, the beam loss crosstalk signals on the BLMs protecting the drive beam.

at 0.1 nC, thus each dataset is characterised by a different beam charge. For each shot 512 samples were taken with an 100 MHz sampling rate. In Figure 5.14 the signals of the OBLMs and the LICs located in the middle of the TBM are illustrated, respectively. A saturation of the OBLM photosensors can be observed for beams larger than 50 bunches in the Main beam and larger than 100 bunches in the case of the Drive beam, signifying a large amount of beam lost in the CALIFES line. This saturation is expressed in the first case where the signals create a plateau which drops slightly and then increases further. In the Drive beam case, the acquired signals stops increasing and again a plateau is observed. The amplitude of the signal plateau is different in the two cases. This difference stems from the different core diameters of the two fibers, as the distance between the fibres and the photosensor is the same in the two cases. As a result, in the case of the Drive beam thinner fibre a smaller part of the photosensor is (and therefore less pixels are) illuminated, leading to a lower maximum signal output. In the case of the LICs, the signal of the detector installed downstream of the TBM on the drive beam side was insignificant an hence, for the present study, these LICs were not taken into account.

The detected charge Q_{DB}, Q_{MB} for the drive beam and the main beam respectively was calculated for both BLMs via

$$Q = \frac{1}{R_L}\int_{t_0}^{t_1}(V(t) - V_{off})\,dt \tag{5.3}$$

where $R_L = 50\,\Omega$ is the measurement load, V(t) the BLM signal, (t_0, t_1) = (1796.9, 2005.2) the integration limits that include only the beam loss signal and V_{off} the measurement offset, estimated as the average of the first 50 samples for each shot. In the case of the OBLM, the

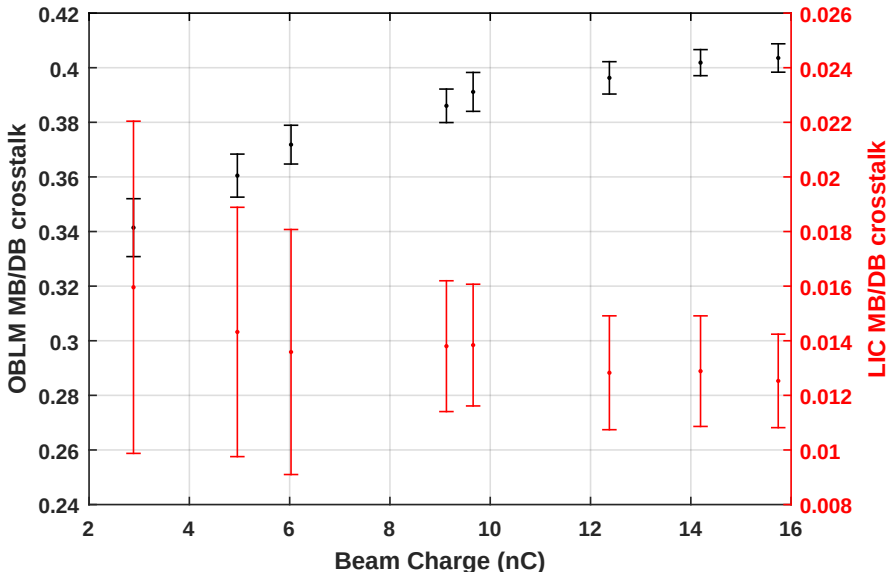

Figure 5.15 – Crosstalk of main beam losses to drive beam BLMs, as measured by OBLMs (black) and LICs (red).

detected charge was multiplied by a normalisation factor to compensate for the fibre diameter difference, in particular

$$Q^{norm}_{OBLM,MB} = Q_{OBLM,MB} \times \frac{d_{DB}}{d_{MB}}$$

For the estimation of the crosstalk of the main beam losses to the drive beam BLMs Equation 5.4 was used, as

$$c_{MB} = \frac{Q_{DB}}{Q_{MB}} \tag{5.4}$$

with $Q^{norm}_{OBLM,MB} = Q_{MB}$ in the OBLM case. Finally, the statistical mean and the statistical mean error of the crosstalk values, $\bar{c}_{MB}$ and $\sigma_{c_{MB}}$, per dataset were calculated. The mean value of the beam charge for each measurement was calculated from the current (I) readings of the BPMs located immediately upstream of the TBM, as

$$Q_{BPM} = \int I(t)dt \tag{5.5}$$

Figure 5.15 shows the crosstalk $\bar{c}_{MB}$ measured by the OBLMs (black) and the LICs located in the middle of the TBM (red) with respect to the average CALIFES beam charge. The crosstalk measured by the OBLMs was found to be one order of magnitude larger than that of the LICs, ranging from 34 - 40% while the $\bar{c}^{LIC}_{MB}$ fluctuates around 1.2%. This large difference is explained by the LIC location on the TBM external sides, in which the TBM elements offer shielding from the CALIFES beam losses. Conversely, the OBLMs are located above the beam lines, and are therefore exposed to a great part of the lost electrons and particle showers.

While the LIC-measured crosstalk appears to be stable within the errors, a significant increase of the OBLM crosstalk is observed. This is attributed to two factors, namely: the satu-

ration of both OBLM photosensors; and the larger momentum dispersion in the CALIFES beam as the number of bunches is increased, which is a result of beam loading. The former limits the beam loss detection of the two detectors. However, up to a beam charge of approximately 100 bunches (~ 9 nC), the main beam OBLM is saturated while on the drive beam the photon detection continues, resulting in the vast increase in the OBLM crosstalk first datapoints. The larger dispersion leads to lower pulse energy and higher beam losses, which may result in the detection of a larger number of lost particles by the drive beam OBLM. At the same time, the drive beam LIC might not be reached by the lower energy beam loss particles and particle showers. Finally, the dispersion might result in modification of the loss location, which also affects the crosstalk signals [153].

5.3.3 | Drive Beam to Main Beam crosstalk

A similar set of measurements was performed for the case of drive to main beam crosstalk. In this case, four different drive beam currents of 8, 16, 24 and 32 A were compared, corresponding to different combination factors in the drive beam Combiner Ring (factor ×1, ×2, ×3 and ×4 respectively), following the delay loop combination. After the latter, the beam pulse length is 140 ns. A total of fifty shots were acquired for each beam current with the same acquisition settings.

Figure 5.16 illustrates the average signals of the BPM located immediately upstream of the TBM for each dataset, where a difference of an approximately 30% in the maximum measured current from the nominal is observed (i.e. in the case of 32 A, a maximum of 24 A is monitored by the BPM). This is attributed to two factors: firstly, imperfections of the beam recombination at the CLEX delay loop, which are confirmed by the low 140 ns current signal preceding the principal beam signal, and secondly the beam losses along the entire beam line [154].

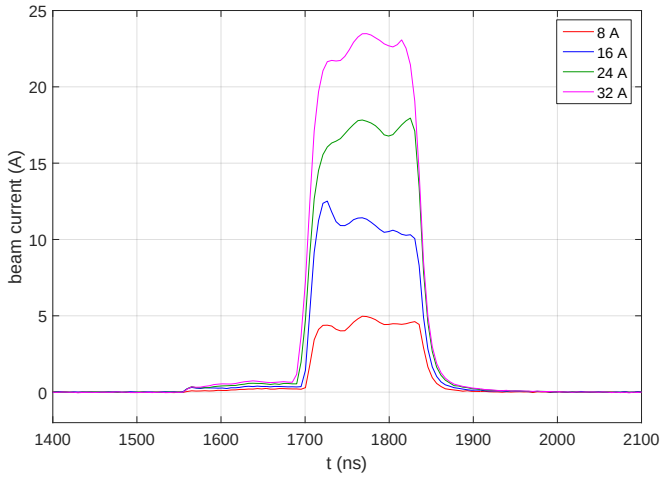

Figure 5.16 – Average signals of the drive beam BPM located upstream of the TBM for different drive beam currents.

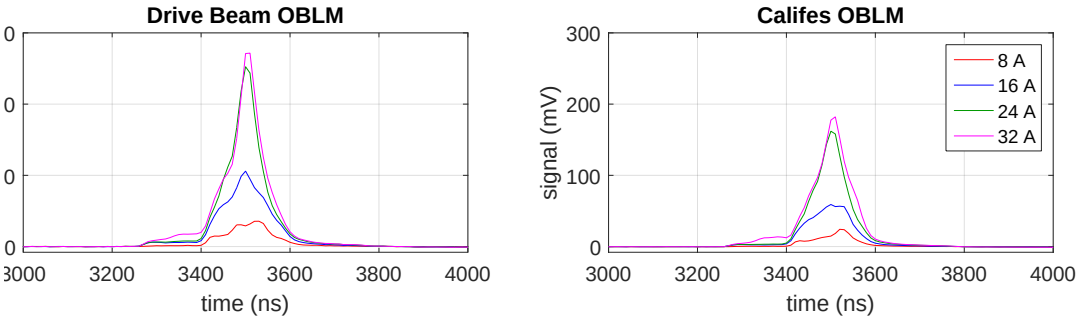

Figure 5.17 – Average beam loss signals of the OBLMs drive beam (left) and crosstalk signals of the main beam (right) of the different drive beam currents.

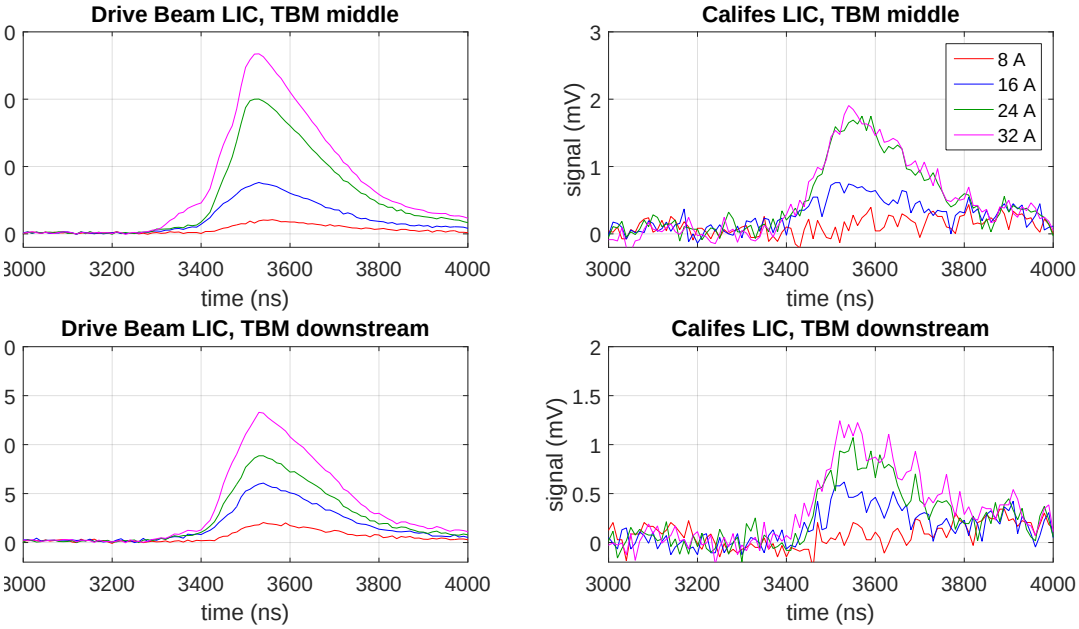

Figure 5.18 – Average beam loss signals of the drive beam (left) and crosstalk signals of the main beam (right) LICs, for different drive beam currents. The upper plots show the signals of the LICs located in the middle of the TBM, whereas in the lower plots the signals of the LICs downstream of the TBM are illustrated.

The average signals of OBLMs and all four ionisation chambers are presented in Figures 5.17 and 5.18 respectively, for the different beam currents. For the OBLM covering the CALIFES line, the normalisation factor $Q_{MB}^{OBLM,norm}$ has been taken into account. In this study, the OBLM and the LIC responses are of a similar shape, all detecting beam losses of the nominal beam. Apart from the latter, the two OBLMs and the LICs protecting the drive beam detect, in the high

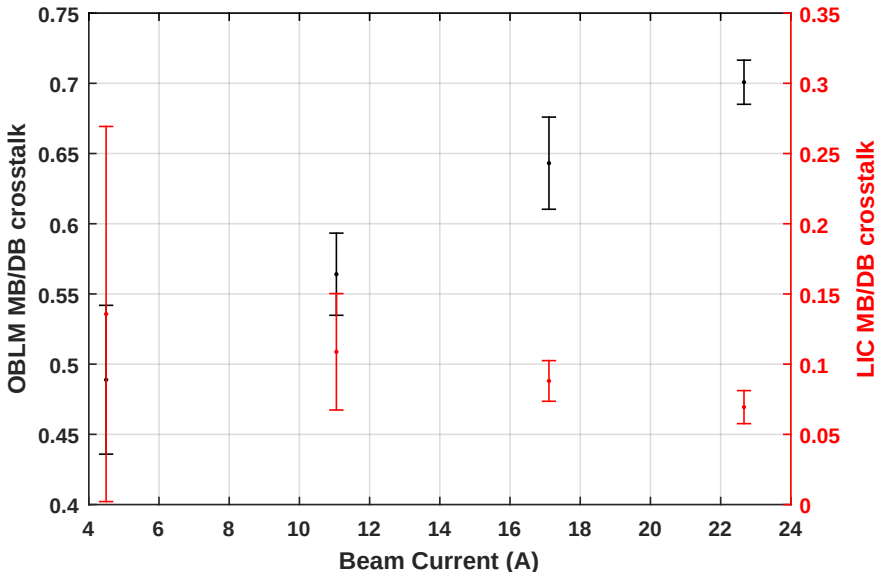

Figure 5.19 – Crosstalk of main beam losses to drive beam BLMs, as measured by OBLMs (black) and LICs (red).

current cases, beam losses created by the very low primary pulse attributed to the incomplete beam recombination at the delay loop. Contrarily, the signals of the LICs located on the main beam side are very low and even close to background in the case of the lowest beam current (8 A).

The detected charge by all BLMs was calculated from Equation 5.3, and the crosstalk for corresponding BLMs was estimated as

$$c_{DB} = \frac{Q_{MB}^{det}}{Q_{DB}^{det}}, \tag{5.6}$$

where "det" corresponds to the OBLM, the LICs in the middle of the TBM or the LICs downstream of the TBM. A second way to calculate the LIC crosstalk is via Equation

$$c_{DB}^{2LICs} = \frac{Q_{MB}^{middle} + Q_{MB}^{down}}{Q_{DB}^{middle} + Q_{DB}^{down}}, \tag{5.7}$$

which combines the signals of both ionisation of chambers of each side.

The statistical mean of the crosstalk values per dataset, $\bar{c}_{DB}^{det}$,and the corresponding statistical error of the mean $\sigma_{c_{DB}}$ were computed. The average of the beam charge for the four measurements was estimated as the average of the plateau in the BPM signal average, between the time limits (t_0, t_1) = (1720, 1830) ns.

The results of this study are summarised in Figure 5.19, showing the $\bar{c}_{DB}^{OBLM}$ for the OBLMs (black points) and $\bar{c}_{DB}^{LIC,middle}$ for the LICs located in the middle of the TBM (red points). The crosstalk measured by the OBLMs varies from 50 to 70%, and seems to be increasing with higher beam current. This agrees with the results of Subsection 5.3.2, however the reason

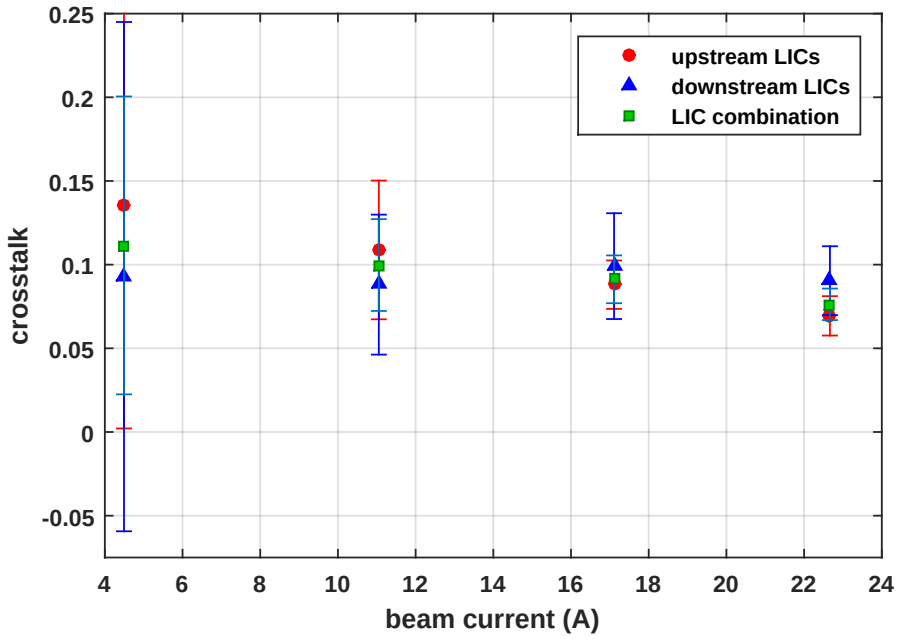

Figure 5.20 – Crosstalk of three different LIC setups: (1) as measured by the LICs installed at the middle of the TBM (red dots), (2) as measured by the LICs installed downstream the TBM (blue triangles), and (3) as calculated from the total of these signals and Equation 5.7 (green squares).

for the increase differs in this case. One explanation is the beam phase-space distribution degradation, as a result of beam recombination. This results in a beam with bigger tails, which can result in higher beam losses and different beam loss shower distribution. Another even more important justification is the difference in the time that the different bunches of a beam have spent in the combiner ring during the recombination process. For example, in the 32 A case, the first quarter of the bunches travels 3.5 times around the combiner ring whereas the last quarter covers only one half of it. The outcome of this process is a beam with bunches which may differ in Twiss parameters, orbit, dispersion, emittance, or even energy. Such a beam will have more losses with different energies and will probably be more distributed, leading to higher crosstalk signals [58, 154]. Contrarily to OBLMs, in the LIC case the crosstalk seems to be stable and of the order of 10% for the different beam currents, with a tendency towards reduction. In this case, the TBM elements interfering between the beam losses and the detector seem to play a major role in shielding the LICs, especially from low energy charged particles.

Figure 5.20 depicts a comparison of the three crosstalk values related to the LICs, $\bar{c}_{DB}^{LIC,middle}$, $\bar{c}_{DB}^{LIC,down}$ and $\bar{c}_{DB}^{2LIs}$. All three cases seem to agree within the error, whereas the value of the crosstalk estimated with Equation 5.7 is consistently between that of the middle and the downstream LICs. Hence for such a setup, the position of the localised detectors, within 1.5 m longitudinally on the machine, is not significant.

In conclusion, in the present machine, the significant crosstalk of the drive beam with the CALIFES BLMs hinders the potential of the latter to detect very low CALIFES losses, and as a result the detector sensitivity is clearly limited. The BLM location, however, plays a major role, and the crosstalk signals are reduced significantly when the shielding provided by the beam lines intervenes.

5.4 Summary

The beam loss detection capabilities of the distributed OBLMs and the limitations of all BLMs have been studied in this chapter. In the first part, OBLMs have been examined for their ability to follow the beam losses during complete machine cycles, and have been proved to be more than sufficient for the beam loss protection and machine diagnostics of storage rings and similar accelerators. Their distributed nature renders possible the detection of beam losses in the entire machine length, many of which would otherwise go undetected. In addition, it contributes to improvements in machine operation and to a better knowledge of radiation sources in the accelerator environment.

Furthermore, the capability of the OBLM in measuring steady-state losses, which are down to a few electrons per turn, in a 3 GeV storage ring was demonstrated. The latter is attributed to the sensitivity of the detector and to the capability of covering the entire machine.

Finally, a first comparison of two different photosensors (an SiPM and a fast-PMT) as parts of the OBLM system during machine operation was performed. The two show similar behaviour; however the fast PMTs are characterised by low noise, resulting in easier detection of very low signals, and a quicker response, and should be considered for storage ring applications.

The second part of this chapter refers to a BLM sensitivity limitation occurring when different beam lines operating at similar frequencies are close to each other: the crosstalk phenomenon, which was examined at the CLIC Test Facility 3. The results of the study highlight the dependence of crosstalk on detector location and beam characteristics, and the negative effect it has on the sensitivity of BLMs protecting parallel beam lines. The crosstalk effect cannot be fully characterised, as it varies with the beam energy, shape, with the type, location and direction of the beam loss. One mitigation technique is installing the detectors protecting the one beam line in a location as much shielded as possible from the other one; in parallel beam lines, that can be their external sides.

Combined with the results of Chapter 4 the conclusion can be drawn, that the developed OBLM is a promising detector with high sensitivity and very good position resolution and ability to distinguish neighbouring beam losses. A beam loss monitoring system consisting of OBLMs and appropriate localised detectors employed at locations of high risk or high interest is proven more than efficient for the protection of linear accelerators and storage rings and the provision of very important beam diagnostics information for their operation.

6

Sixth Chapter

An advanced diagnostics tool for RF cavities

In the present chapter two phenomena relevant to high gradient RF cavities, the electron field emission and the RF breakdown (described in Subsections 1.5.1 and 1.5.2 correspondingly), and their effects on OBLMs are examined. In particular, the RF cavity induced background was measured in different experiments and types of accelerating structures, and conclusions on the sensitivity limitations it introduces to optical fibre beam loss monitors are being drawn. In addition, the possibility of using optical fibre detectors for RF cavity diagnostics is being introduced and examined thoroughly.

The motivation behind this set of studies is summarised in Section 6.1, while Section 6.2 contains a study on the possibility of photon detection by OBLMs. In Section 6.3 the detection by OBLMs of high gradient accelerating structure field emission is demonstrated experimentally (Subsections 6.3.1), while the radiation emitted from an accelerating structure due to electron field emission in terms of electrons and X-rays is examined through simulations in Subsection 6.3.2. In Section 6.4 the possibility of RF breakdown detection is also experimentally validated.

Section 6.5 focuses on the possibility of using OBLMs as an advanced tool for RF cavity diagnostics. The capability to predict an RF breakdown through the detection of the field emitted electrons is studied in Subsection 6.5.1. Subsection 6.5.2 focuses on the detection of very small variations in the accelerating gradient and the field emission, while in Subsection 6.5.3 the field enhancement factor β_{FN} as a determinant of the RF cavity quality is calculated from the OBLM data for different structures. Finally, Subsection 6.5.4 describes the characterisation of a nominal CLIC accelerating structure with this detector, and the limitations the cavities can introduce to BLMs are discussed.

6.1 Introduction

High gradient RF cavities are able to achieve high beam energies in short machine lengths, a characteristic that renders them valuable for a variety of applications. These include linear accelerators for high energy physics, FEL facilities for material science, chemistry or biology, and compact medical linacs for proton and ion treatment [42]. Two phenomena appearing in these structures, namely the electron field emission and the formed dark current, and the RF breakdown, are still under investigation within the high gradient community for limiting the performance of the accelerating structures.

Additionally, the radiation emitted from the RF cavities may limit the operation of instruments close to them. This possibility, together with the large number of accelerating structures found in machines like CLIC, triggered the combined study of RF cavities and OBLMs.

A nominal OBLM system in CLIC would consist of fibres approximately 100 m long, each of which may cover up to 40 structures on the main beam side. Therefore, good knowledge of the RF cavity induced radiation background is essential for the estimation of the limitations it may introduce to the BLM sensitivity.

While it may introduce an obstruction when performing beam loss detection, the field emitted electrons and the dark current provide us with information on the operation of the accelerating structure, which may contribute to a good beam quality and fewer failures. Further insight on the cavity quality is obtained by the emissions generated during RF breakdowns. To detect the radiation emitted during the first phenomenon, different radiation monitors may be used. At CERN Faraday cups are used to detect electrons released inside the cavity during an RF breakdown. These are normally not sensitive enough for the efficient detection of dark current electrons. Additionally, as they are beam intercepting devices, they cannot be used in an operating beam line.

In this chapter the concept of using optical fibre BLMs for RF cavity diagnostics is introduced. Such monitors bear the advantage of insensitivity to a fraction of the X-ray spectrum, which constitute a great part of the RF cavity radiation environment. Additionally, their installation outside the accelerating structure makes RF cavity diagnostics possible, even at operating machines.

6.2 X-ray detection by OBLMs

The fact that quartz crystals may be used for gamma-ray detection [155] triggers a discussion on the partition of the photon spectrum that may generate signals in OBLMs. The detection principle in this case is indirect as neutral particles do not generate Cherenkov light. Here light is produced by high energy electrons or positrons generated primarily by either pair production or the Compton effect in the photon-quartz interaction. Given the Cherenkov threshold of 186 keV for the electrons, shown in Table 3.1, the photons that will give rise to these electrons should have a higher energy in order to be detected. This excludes the X-rays in the conventional definition of the EM spectrum (in which they are defined with energies up

to the order of 100 keV). Actually the spectrum is larger due to the X-rays produced through Bremsstrahlung, which may reach a maximum energy equal to that of the electron generating them.

In order to compare the electron and photon detection efficiency of OBLMs, simulations with the FLUKA [84], [85] code were performed.

6.2.1 | The FLUKA code

FLUKA is a Monte-Carlo tool able to calculate particle transport in and particle interaction with matter. It now is used in a large variety of applications, including accelerator shielding, calorimetry, activation, dosimetry, detector design and neutrino physics.

Electrons and photons are among the more than 60 type of particles that FLUKA is able to accurately simulate in the range of 1 keV to 1 TeV. Additionally, the code is able to simulate optical photons generated due to different phenomena, namely: Cherenkov effect, scintillation and optical transition radiation. Furthermore, one of the main advantages the code bears is the easy recreation of very complex geometries.

For the simulations performed in this thesis the FLUKA Advanced Interface (Flair) [156] was used. Flair is a user-friendly interface, which facilitates the editing and execution of the simulation code and the visualisation of the results. The features of error checking and geometry debugging render it a very useful tool, especially for the development of complicated codes and the design of complex geometries.

6.2.2 | Simulating optical photon generation

To examine the difference on the optical photon yield between electrons and photons, a quartz crystal of a surface $10 \times 10\,\text{cm}^2$ and a width of 5 cm was designed. A pencil beam was generated in the centre of the crystal, and the optical photons with wavelengths 200-900 nm crossing the vertical surface 50 µm downstream of the beam were scored, using the FLUKA *USRYIELD* card. Two different beam particles, namely electrons and photons with energies ranging from 0.5 to 25 MeV, were simulated.

The results of this study are summarised in Figure 6.1, with warm colored (yellow, orange and red) "x"-markers represent the optical photons generated by the electrons and cool colored (green and blue) triangles representing those generated by the photons. The optical photon generation from electrons is similar for all electron energies, and more than two orders of larger than the one of photons. In the case of a photon beam a more than two orders of magnitude difference between the two simulated limits (0.5 MeV, 25 MeV) is observed. This is attributed to the fact that higher energetic photons generate more electrons of higher energies, which will consequently result in greater emission of Cherenkov radiation.

In conclusion, signals obtained with quartz detectors will depend on the radiation environment: in electron richer environments, these are expected to be the main contribution to the signals. However, when photons with energies greater than 5 MeV prevail with approximately two orders of magnitude greater fluences than the electrons, the two types of particles are expected to contribute equally to the detector signal.

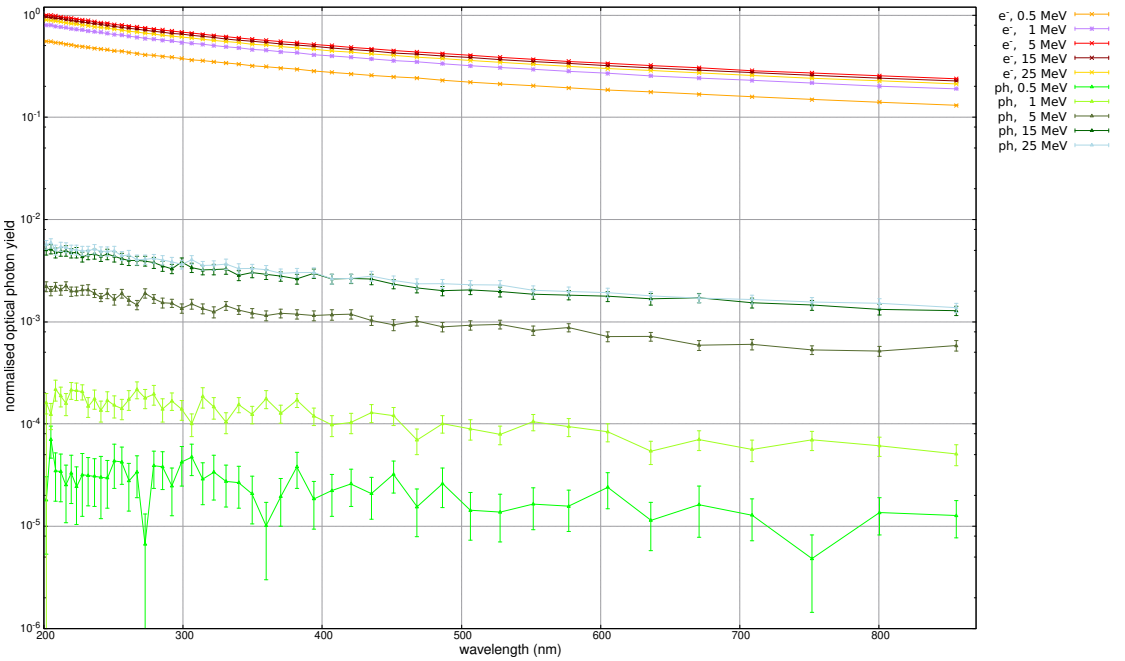

Figure 6.1 – Normalised yield of optical photon generation in quartz, due to electron ("x" points, shades of yellow, orange and red) and photon (triangles, shades of green and blue) beams of different energies.

6.3 RF cavity background radiation due to electron field emission

In this Section measurements of dark current induced radiation with an OBLM are demonstrated, and the limitations this may introduce to the detector sensitivity are discussed. The measurements described were performed at the dogleg line in CTF3 where, as described in Subsubsection 1.6.1, the performance of CLIC X-band accelerating structures is being investigated. This test stand is called XBOX-1. Furthermore, simulations have been performed to study the emission of electrons outside the cavity, as well as the cavity radiation environment.

6.3.1 | Measurements with a T24 accelerating structure

Experimental Setup

The first RF cavity installed at the dogleg line in CTF3 was a CLIC T24 accelerating structure, consisting of 24 cells like the ones illustrated in Figure 1.10(a). The OBLM system installed to measure the RF cavity background was selected to be highly sensitive, so as to detect even very low electron signals. In this context, a COTS 7 m long pure SiO_2 fibre from Thorlabs, with a core diameter of 910 µm, an 1000 µm cladding and a hard polymer buffer was selected [157]. The cable was installed along the accelerating structure and 2.5 cm above it, while extending more that 60 cm to the upstream and 30 cm to the downstream of the structure. The T24 RF

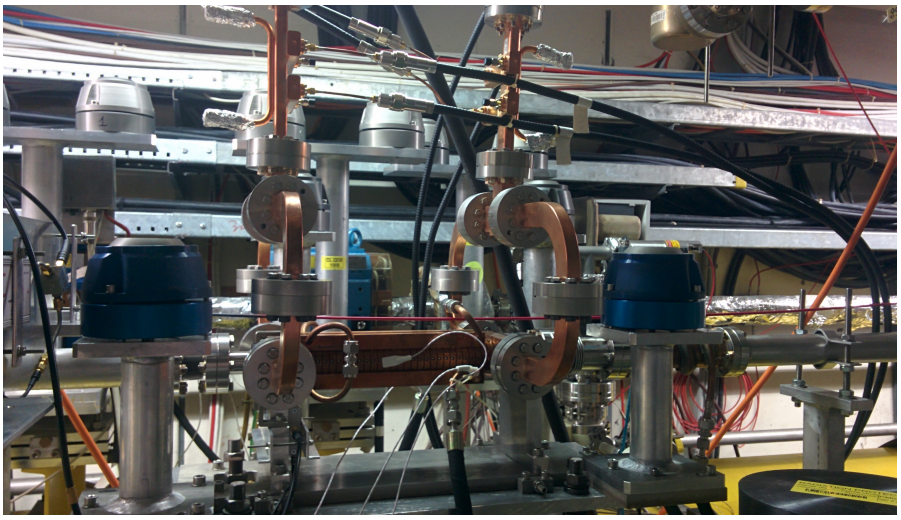

Figure 6.2 – The optical fibre installed above the T24 accelerating structure at the CTF3 dogleg line

cavity and the installed optical fibre are illustrated in Figure 6.2.

On the upsteam side, the length of the rest of the fibre between the beam line and the photosensing module was approximately 2.5 m. In all following studies, only the upstream end of the fibre is examined. The custom made opto-electronic read-out module described in Subsection 3.4.2, was situated on the floor, under the beam line and upstream of the RF cavity. To avoid the detection of ambient light and reduce the noise on the photosensor, the chassis and modules were covered with a dark fabric. The photosensor selected was a Hamamatsu MPPC S127572-050C. As summarised in Table 3.2, the selected MPPC has a high gain, and therefore sensitivity, and allows the detection of very low signals. The main drawback of this photon detector is the low number of pixels which results in an easier saturation of the signal. The photosensor readout board, illustrated in Figure 6.3, included a transimpedance amplifier readout, consisting of a Texas Instruments THS-3061 amplifier [150], a 0.5 kΩ resistor and a 10 nF capacitor.

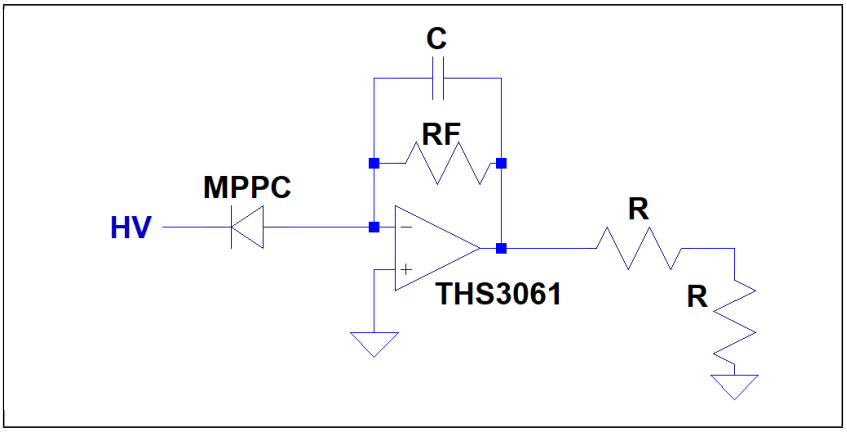

Figure 6.3 – Simplified schematics of the MPPC transimpedance amplifier readout circuit

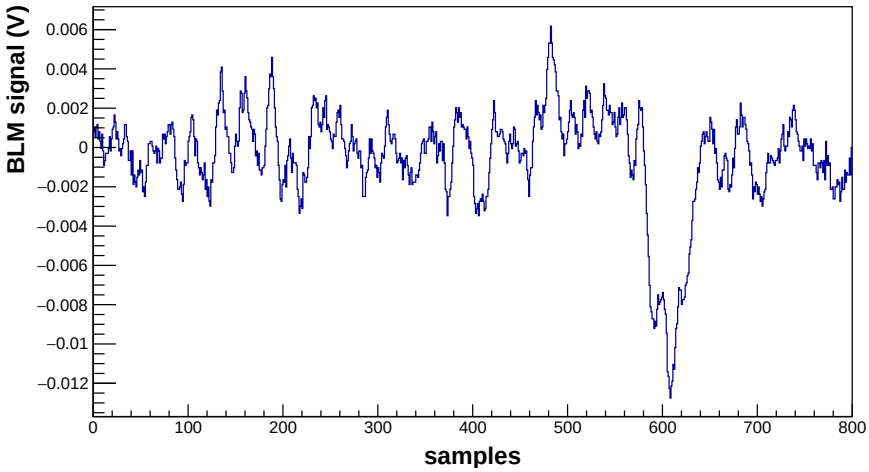

Figure 6.4 – OBLM signals observed during the unloaded operation of the T24 RF cavity, attributed to the electron field emission

The acquisition of the signals was carried out via a NI 5761 National Instruments digitiser at 250 MS/s [158]. A detailed description of the acquisition system can be found in [60, 159, 160].

Method

Due to the low breakdown rate of the CLIC accelerating structures, a long acquisition time was necessary in order to acquire sufficient RF breakdown data for the study of the cavity performance. Five different data-taking periods, each lasting from two to seven days and containing several thousands pulses, have been examined. During each period a different input power was applied in the accelerating structure, while the RF pulse length remained constant at 200 ns. The characteristics of the five periods, including the dates of the data collection, the input power in the structure, the number of pulses that were normally transmitted and the number of those which resulted in an RF breakdown are summarised on Table 6.1.

Table 6.1 – Time period, mean input power and statistics of the data collected from the dogleg experiment in 2014.

Period	Dates	Input Power (MW)	Normal Pulses	Breakdowns
1	06/10 - 09/10	29.0	4178	47
2	16/10 - 20/10	29.0	3697	65
3	20/10 - 27/10	32.5	1539	51
4	05/11 - 07/11	33.0 to 35.0	1187	218
5	10/11 - 13/11	22.0	2280	3

The OBLMs demonstrated to detect signals during the normal operation of the accelerating structure, such as the one presented in Figure 6.4. The signals are negative due to the SiPM readout configuration. Given the above described 250MS/s sampling rate of the acquisition system, one sample every 4 ns is collected. This corresponds to a length of the pulses detected of approximately 200 ns, correlating them to the RF pulse and indicating that they are indeed signals generated by the field emitted electrons in the accelerating structure.

The total charge Q measured by the MPPC sensor was calculated using Equation 6.1:

$$Q = \frac{1}{R_L} \int_{t_0}^{t_1} (V_{meas} - V_{off}) dt \tag{6.1}$$

where $R_L = 50\,\Omega$ is the load used at the signal output, V_{meas} the measured pulse amplitude and (t_0, t_1) define the integration interval, which was set to 240 ns for the case of dark current, in order to include the full length of the detected pulse. The signal offset V_{off} was calculated as the mean value of the first 50 samples and computed for each pulse independently. To study the evolution of the BLM signal with respect to the input power, the maximum of the forward power to the accelerating structure was recorded.

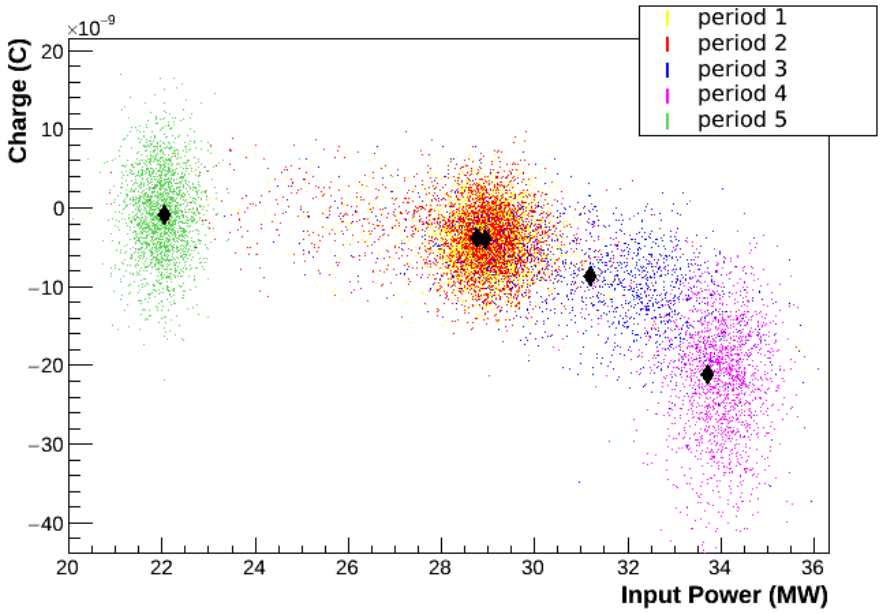

Figure 6.5 – OBLM detected charge during the five data-taking periods, and the mean values for each period (black diamond)

The analysis of the signals was performed with the ROOT Analysis Framework [161]. For all pulses accumulated during each data taking period, the mean value of the detected charge Q and of the input power, as well as the standard error of the mean for the two variables, were calculated. Figure 6.5 illustrates the detected charge with respect to the maximum input power

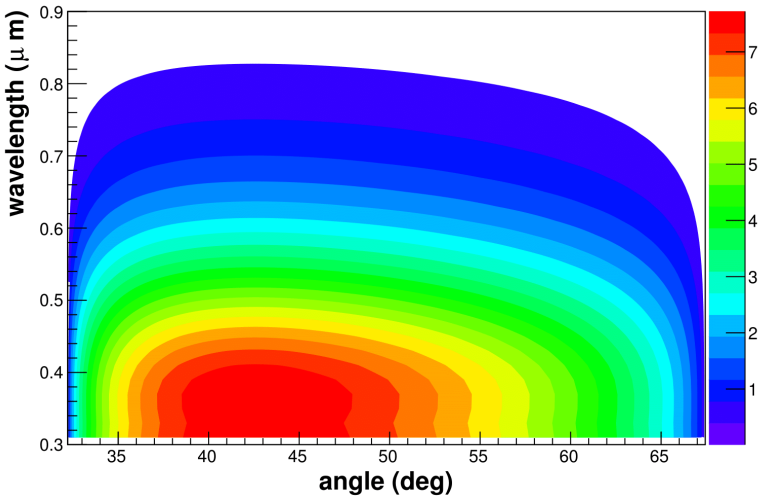

Figure 6.6 – Double differential number of photons detected by the MPPC per electron crossing the middle of an optical fibre like the one installed at the dogleg experiment, as calculated from Equation 3.39.

for all acquired pulses of the five periods, and the average value for each period. Since the SiPM signal is negative, lowest charge in the Figure corresponds to the highest detected signal.

Considering the design of the MPPC readout circuit, shown in Figure 6.3, the number of Cherenkov photons N_{ph} impinging on the photosensor can be estimated from the detected charge Q via Equation 6.2:

$$N_{ph} = \frac{2 \times R_L}{R_F \times G \times q_e} \times Q \tag{6.2}$$

where $R_F = 0.5\,\text{k}\Omega$ is the feedback resistor of the transimpedance amplifier circuit, $G = 1.25 \times 10^6$ is the MPPC gain and $q_e = -1.6 \times 10^{-19}\text{C}$ is the electron charge.

To appreciate the electron field emission outside the RF cavity, the number of electrons necessary to generate such a BLM signal was estimated via Equation 3.39. The calculations performed were approximate, assuming only electrons of a relativistic $\beta = 1$. The following characteristics were implemented for the fibre: the numerical aperture was equal to $NA = 0.22$, the core refractive index $n_{co} = 1.47$ and its radius $R = 450\,\mu\text{m}$. The length of the fibre was 7 m. Since the middle of the fibre was mounted close to the structure, it was also assumed that all electrons cross the fibre at its longitudinal centre, and therefore that the generated photons cover a distance $L_{fib} = 3.5\ m$ until they reach the photosensor.

The double differential yield of detected photons $\frac{d^2N_{ph}}{d\lambda \cdot da}$ for electrons of $\beta = 1$ crossing the fibre and for the above parameters is shown in Figure 6.6. To estimate the number of photons detected per charged particle crossing the fibre, the $\frac{d^2N_{ph}}{d\lambda \cdot da}$ was integrated over all optical wavelengths (200 nm − 900 nm) and trajectory angles (0° − 90°).

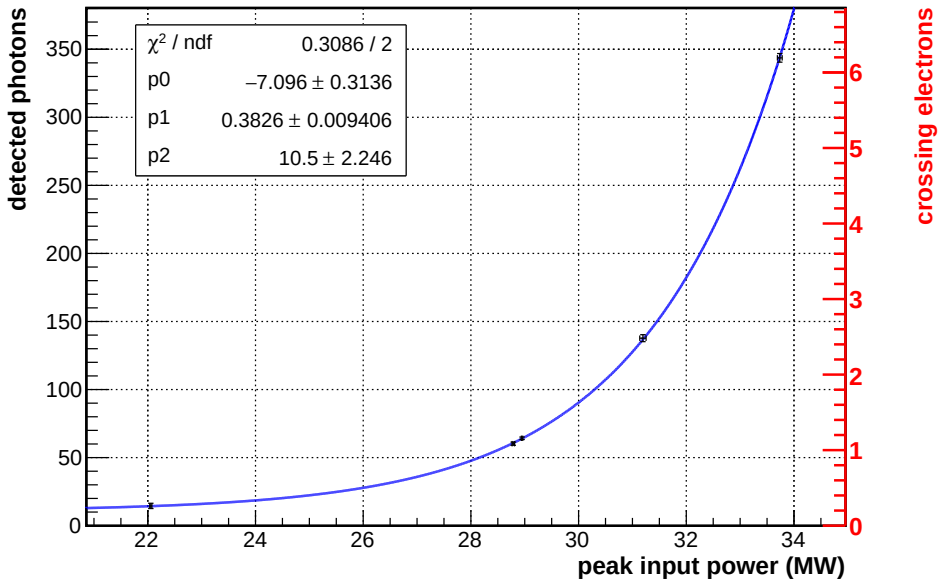

Figure 6.7 – OBLM signals during normal RF cavity operation in terms of detected photons (left axis), and an approximation of the relativistic electrons crossing the fibre (right axis)

Results

The results of the data analysis for the five data taking periods are shown in Figure 6.7. The left axis represents the number of photons detected by the MPPC, calculated from Equation 6.2, while the right red axis shows an estimation of the number of electrons crossing the fibre. It can be observed that the number of electrons estimated to be crossing the fibre is rather low. However, this number refers to only relativistic electrons (energies higher than 11 MeV as shown in Table 3.1) and is only an indication. As will be discussed in the following subsection, the highest percentage of the electrons that reach the fibre are expected to be of much lower energies. Additionally, it was demonstrated in Section 6.2 that high energy X-rays may also generate optical photons in quartz. However, the radiation environment of the cavity is simulated in Subsection 6.3.2, which shows that the largest fraction of the signal can be attributed to electrons. Furthermore, one can note that the data in the figure correspond to a fraction of the electron quantisation. This stems from the fact that the calculation of the number of electrons through Equation 3.39 gives an indicative value for which various approximations have been performed. As described above, only electrons with $\beta = 1$ have been considered, while parameters such as the coupling efficiency have not been taken into account. Moreover, an integration over all incident angles has been estimated, an average of the distance electrons cover in the fibre has been used, while it was assumed that all electrons cross at the longitudinal middle of the fibre. Therefore, the outcome of this calculation is not an exact number of electrons which created the detected signal, but rather the fraction of the

Table 6.2 – Estimation of expected dark current signals on BLM at nominal beam power expressed as number of detected photons, number of crossing electrons and integrated charge detected

	40 MW	**60 MW**
photons	2.19×10^{5}	4.10×10^{8}
electrons	3.95×10^{3}	7.39×10^{6}
charge (C)	2.19×10^{-7}	4.10×10^{-4}

electron charge which would be required in order to generate it under the above described conditions.

The detected signals follow an exponential behaviour, that can be described by the following function:

$$N(x) = exp(p0 + p1 \cdot x) + p2 \tag{6.3}$$

The best encountered fit is represented in Figure 6.7 with a blue line, where the respective free parameters are computed by the fitting algorithm as:

$$p0 \simeq -7.19 \pm 0.31,\ p1 \simeq 0.38 \pm 0.01,\ p2 = 10.5 \pm 2.2$$

The rapid exponential increase of the signal with input power is in good agreement with the increase of field emitted electron current described by the well known Fowler-Nordheim equation [45], which is discussed in Section 1.5. This is further demonstrated in Subsection 6.5.3.

The electron field emission consists a background radiation source for the OBLMs, which may obstruct them from detecting very low beam losses, limiting therefore their sensitivity. To assess this limitation in the case of a CLIC machine, extrapolations of Equation 6.3 were performed for the nominal input power of the CLIC accelerating structure. This in the case of an unloaded (i.e. without beam) machine corresponds to 40 MW, while it reaches 60 MW when beam is loading the cavities.

The calculated BLM background from field emitted electrons is summarised in Table 6.2. According to this extrapolation, the dark current signals reach very high values, i.e. approximately 220 nC of BLM detected charge at 40 MW and 410 µC at 60 MW. Such large signals can cause a significant limitation in the sensitivity and therefore reduce the dynamic range of the detectors. However, it should be mentioned that for the particular experiment, a very sensitive OBLM system was deployed. In a nominal OBLM system all these factors and hence the sensitivity of the detector will be reduced, and the limitations induced by the RF cavity radiation are expected to be lower.

6.3.2 | Simulation studies

The radiation environment of RF cavities is expected to consist principally of X-rays [162, 163] produced by the bremsstrahlung of lost electrons. However, as discussed in Section 6.2, the optical fibre BLM system detects principally electrons, and is characterised by a low

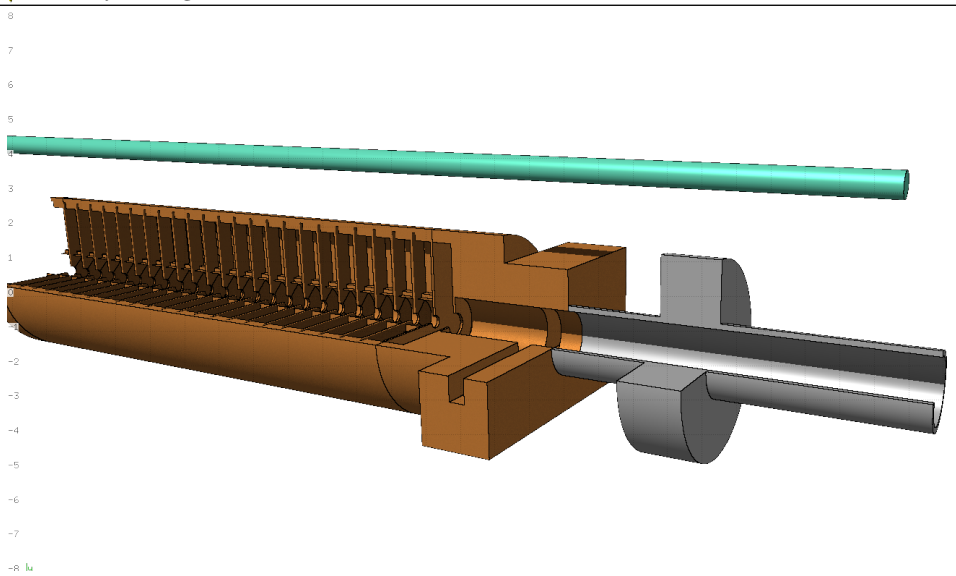

Figure 6.8 – 3D view of the cavity geometry and the following elements in FLUKA

sensitivity to X-rays. To examine the origin of the signals detected by the OBLMs, a Monte-Carlo simulation with the FLUKA [84], [85] Monte Carlo code were performed.

The objective of the simulation is to quantify and compare the electron and photon fluences in the optical fibre, when electrons of different energies impact the inner walls of the accelerating structure. Furthermore, it is aimed to examine if the energy of the field emitted electrons and geometrical characteristics of the RF cavity allow for high energy electrons to reach the fibre of the OBLM and prove the major contributors to the detected signal.

To this end, a detailed geometry of a CLIC TD26 accelerating structure was modelled including the designed damping waveguides [54] and tuning holes *. The structure consists

*. The tuning holes are hollow cylindrical parts of the cell, extending from its surface up to the iris. Through these holes, the RF experts can slightly modify the size of the iris, therefore its RF properties, and consequently the RF characteristics of the structure.

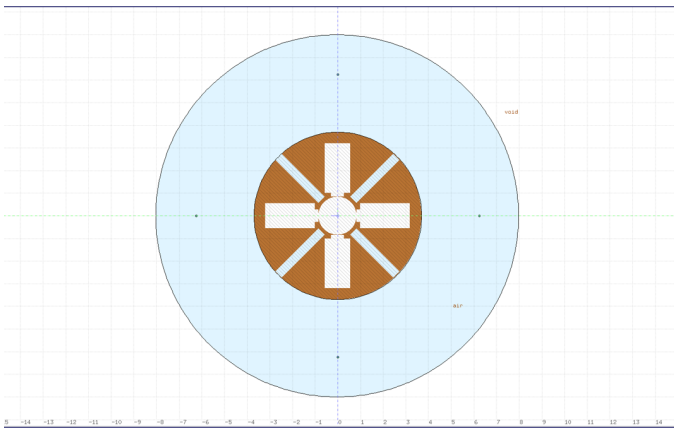

Figure 6.9 – The cross section at the middle of a disc of an accelerating structure with damping waveguides (horizontal and vertical) and tuning holes (forming an X in the cell)

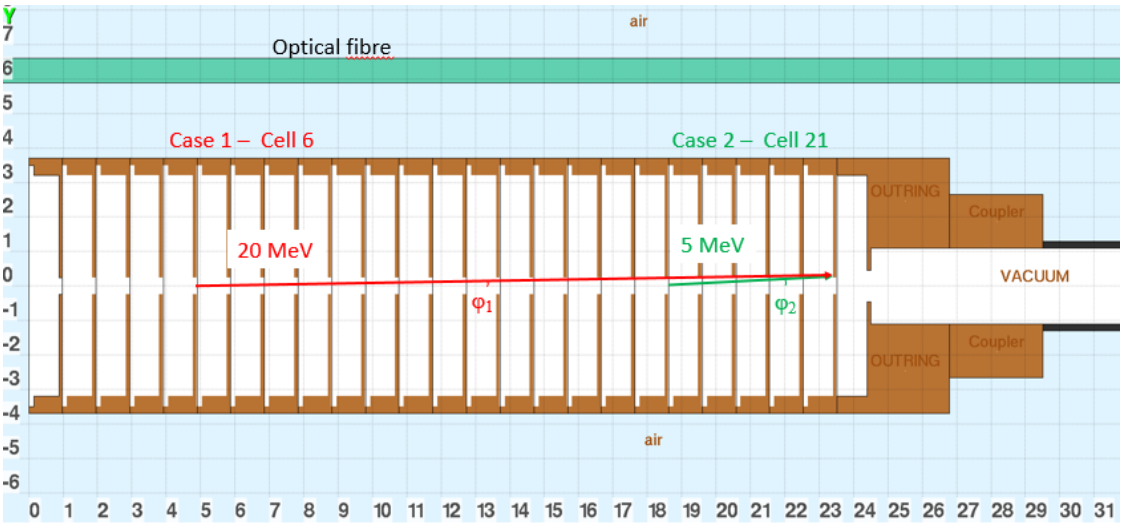

Figure 6.10 – The simulation process in FLUKA. In the first case, an electron emitted at cell 6 gains 20 MeV before impinging on the iris of cell 25 with an angle φ_1. In case 2, the electrons start from disc 21 and gain 5 MeV before the impact at cell 20 with an angle φ_2

of 26 copper discs (cells) of a 3.7 cm radius, 0.98 cm thickness and a variable iris radius. In the simulated geometry, the iris radius is set constant, for simplicity, to the smallest value of 0.494 cm, which is equal to the iris radius of the 25th cell of the structure, with the exception of the last disk which is larger. Following the cavity disks, a copper outer ring and RF coupler with a thickness of 2.3 cm and 2.7 cm respectively were also modelled. Following these components are, the stainless steel beam pipe with a thickness of 2 mm and an external diameter of 2.6 cm, and a stainless steel flange 3.6 cm downstream of the coupler. Figure 6.8 shows a 3D image of the entire simulated structure. An illustration of the cross section at the middle of a disc is shown in Figure 6.9, where both the damping waveguides and the tuning holes are visible.

An optical fibre with similar characteristics to the one tested at CTF3 was also simulated as a quartz cylinder of 9 mm diameter, one order of magnitude larger than the experimentally tested in order to achieve higher statistics. The location of the fibre was selected to replicate the experimental setup, with it running along the structure and 2.5 cm above it. The total length of the simulated detector was 43.12 cm, A 2D view of the model including the illustration of the simulation process that follows, is presented in Figure 6.10.

As described in Section 1.5, the field emitted electrons follow different routes and gain various energies, depending on the length they have travelled in the structure. For this simulation it was assumed that the electrons follow linear paths until they impinge on the iris. Their starting location was set in the radial centre of the cell that emits them and at the very beginning of it (upstream). As interaction location the 25th cell of the cavity was selected as the one with the smallest iris radius (i.e. the limiting aperture) and where the electrons emitted at the beginning of the cavity would have gained high energies. The impact point was chosen to be on the top edge of the iris, so potential secondary radiation would be on average directed

towards the fibre.

The length of the discs composing the accelerating structure is approximately 1 cm. Considering an nominal CLIC accelerating gradient of 100 MV/m, it can be deducted that an electron gains 1 MeV/cm while travelling through the cavity, i.e. approximately 1 MeV per cell. Hence, electrons emitted at different positions will have different energies when they reach the impact point.

For this study electrons starting from different cells and impinging at the interaction location (cell 25) were simulated. These electrons travel different distances in the cavity and are therefore characterised by different energies. As an example, those generated at the first cell cover a length of 25 discs before reaching the impact point, gaining an energy of 25 MeV. The collision angles on the impact point also differ depending on the starting position of the electrons, as shown in Figure 6.11.

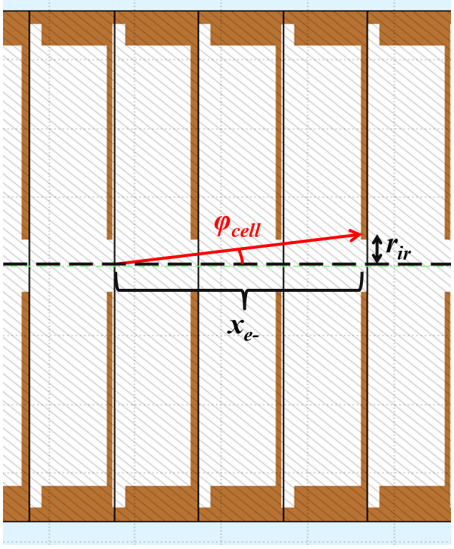

Figure 6.11 – Calculation of the impact angle.

With x_{e^-} the longitudinal distance between the starting and the interaction position and $r_{ir} = 0.494$ cm the radius of the iris, the respective collision angles φ_{cell} for different initial positions were calculated as:

$$\varphi_{cell} = \arctan\left(\frac{r_{ir}}{x_{e^-}}\right) \tag{6.4}$$

An illustration of the simulation process, as described above, is shown in Figure 6.10, while a summary of the five different cases simulated, including the emission cell, the energy obtained by the electrons and the impact angle is presented in Table 6.3.

The scoring region of the simulation was selected to be the volume of the optical fibre, and the scored value was the single differential current of electrons and photons crossing the fibre. Additionally, the particle fluence and the energy deposition in the entire simulated geometry was scored using a spatial cylindrically binned detector.

Table 6.3 – The electron field emission cases considered for the FLUKA simulations

Cell	Energy (MeV)	Impact Angle φ_{cell} (deg)
21	5	5.36
16	10	2.83
11	15	1.89
6	20	1.41
1	25	1.13

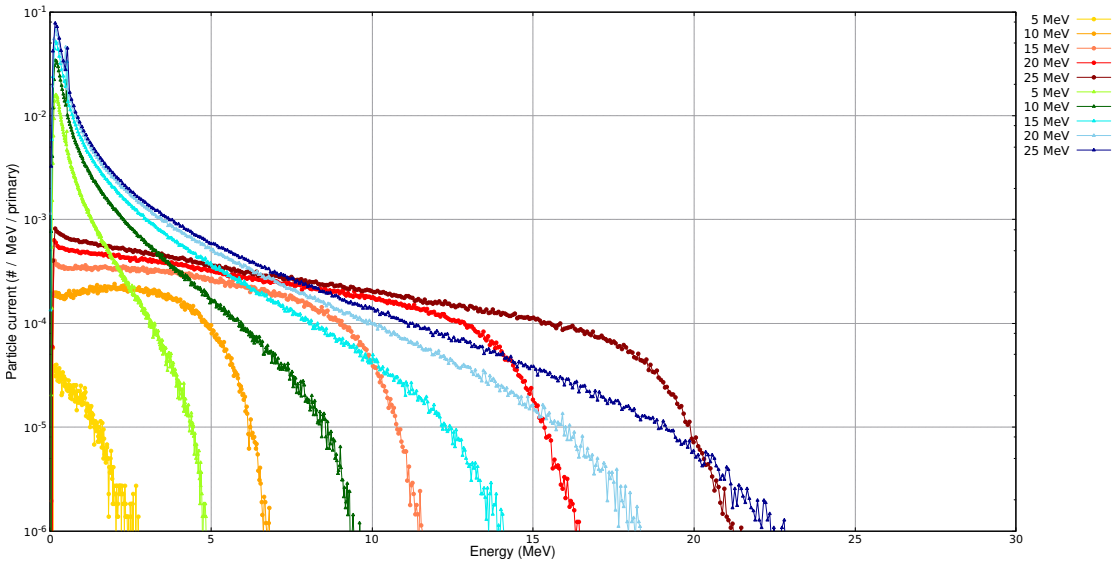

Figure 6.12 – Electron (circular points) and photon (triangular points) current in a cylinder 2.5 cm above the cavity, per MeV and per primary electron impacting the accelerating structure

The results of the simulation are summarised in Figure 6.12 where the number of generated electrons and photons (i.e. the current) in the fibre per energy unit and per primary with respect to the initial electron energy (show in the legend) are shown. The five different cases of primary energies and angles, described in Table 6.3 are superimposed. The circular points and warm colours (red, orange, yellow) represent the electrons crossing the fibre, while the photons are shown as triangular points and cool colors (green, blue).

The radiation environment of the high gradient accelerating structures, as estimated from the simulation, consists of both electrons and photons. The energy spectrum of electrons is mostly confined within an order of magnitude , reaching up to a few MeV below the primary electron energy. The photon distribution shows a large peak at low energy X-rays, and descends to reach energies almost equal to the primary with more than four orders of magnitude smaller current.

Comparing the electron and photon spectra, for low energy primaries (here, in the case of 5 MeV primaries) the photons dominate with an approximately two orders of magnitude difference. Combined with the results of Section 6.2 for the Cherenkov photon yield of electrons and photons in quartz, at these energies the electron contribution to the OBLM signal can be estimated greater. For 10 MeV primaries, the photons continue prevailing but the amount of electrons that reach the fibre is considerably higher and combined with the outcome for the optical photon generation simulations, consists a larger fraction of the OBLM signal.

For primaries with energies from 15 MeV and higher, the electrons are the main signal contributors. The spectrum at energies smaller that 5 MeV, still shows a photon to electron difference that can reach up to two orders of magnitude in the very low energies (below 1 MeV). However, at those energies, the optical photon yield of electrons is more than three orders of magnitude larger than the one of photons, therefore these X-rays do not consist a significant

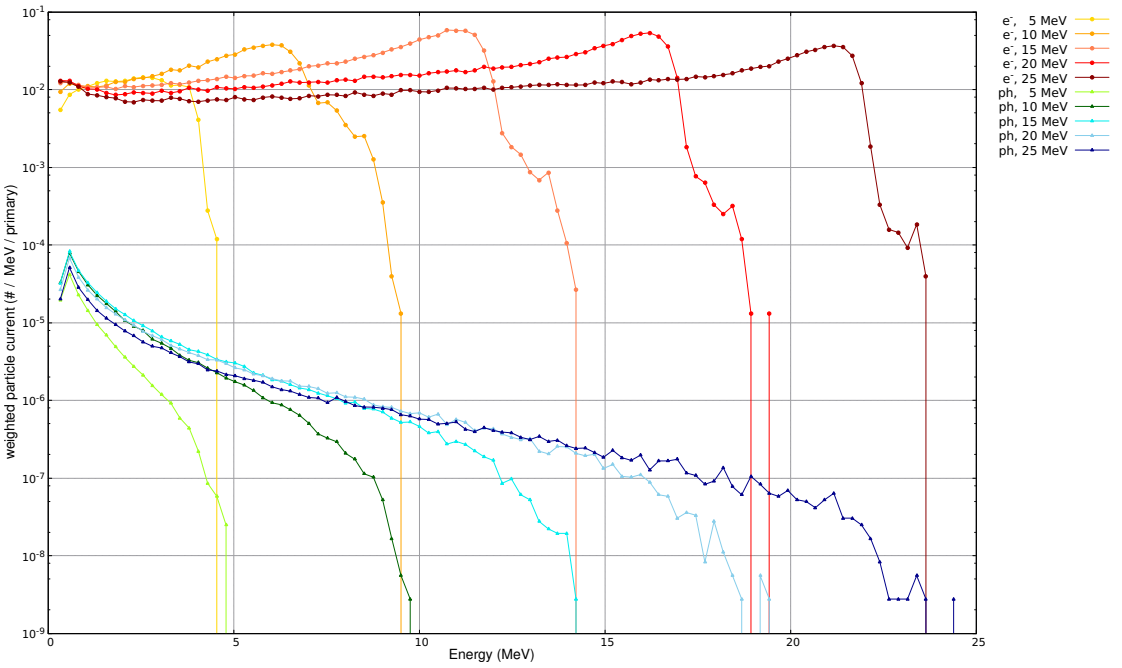

Figure 6.13 – Electron (circular points) and photon (triangular points) current weighted by their relative ability for optical photon generation, in a cylinder 2.5 cm above the cavity, per MeV and per primary electron impacting the accelerating structure

contribution to the optical photon generation. For higher energies and up to a few MeVs below the energy of the primary, the electrons dominate consisting the main fraction of the OBLM signal.

To confirm this estimation of the electron and photon contribution to the detected signal, the data of the present simulation were weighted by the relevant normalised yield, as deducted from Figure 6.1. The values of the simulated curves at a wavelength of 200 nm were used as normalisation factors for each particle and for the five different energies, by which the particle current in the optical fibre was weighted depending on its type and energy. In particular five energy ranges were distinguished for the electron and photon current in the optical fibre, namely (0-0.5] MeV, (0.5-1] MeV, (1-5] MeV, (5-15] MeV and (15-25] MeV, the data of which were multiplied by the normalisation factor corresponding to their greater value. The resulting weighted plot is presented in Figure 6.13 and demonstrates that the OBLM signal is essentially generated only by electrons.

The present simulation describes only few of the numerous possible scenarios of the very complex RF cavity electron field emission, confirming the presence of electrons in the radiation environment of the accelerating structure.

From Figure 6.14(a), which shows an overlay of the electron fluence in the simulated geometry for the intermediate energy of 15 MeV for primary electrons, it can be observed that the largest fraction of electrons escapes through the beam pipe. Comparing this result with Figures 6.14(b) and 6.14(c), which illustrate the photon fluence and the energy deposition

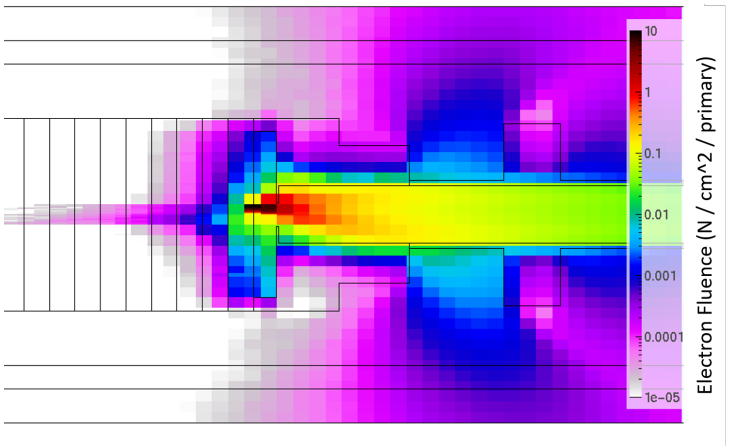

(a)

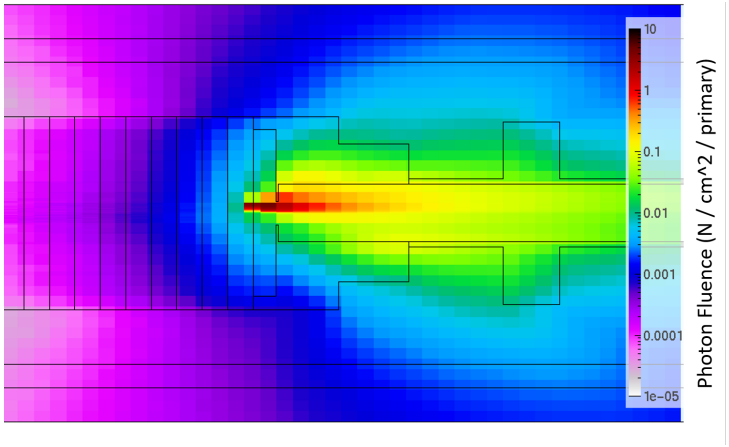

(b)

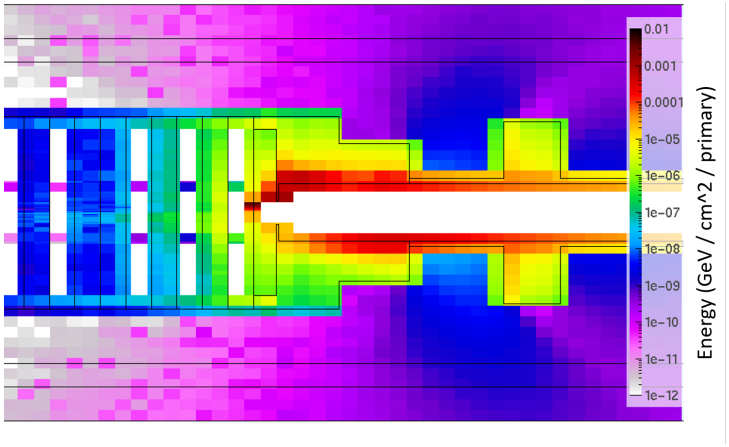

(c)

Figure 6.14 – Fluence of (a) electron and (b) photon fluence, and total energy deposition (c) in the simulated geometry, for 15 MeV primary electrons

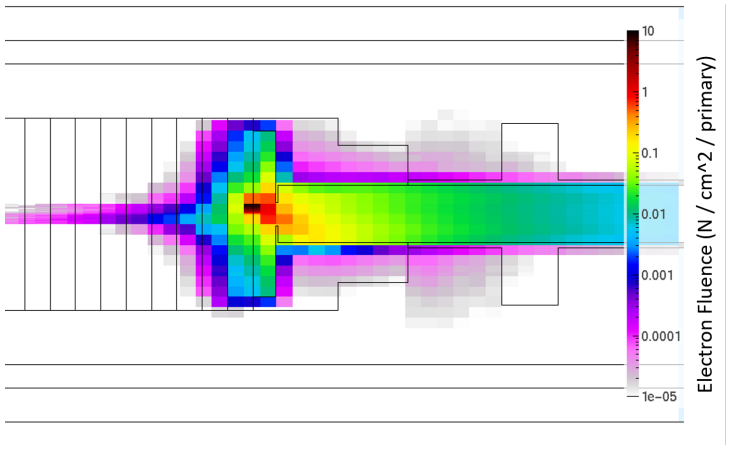

(a)

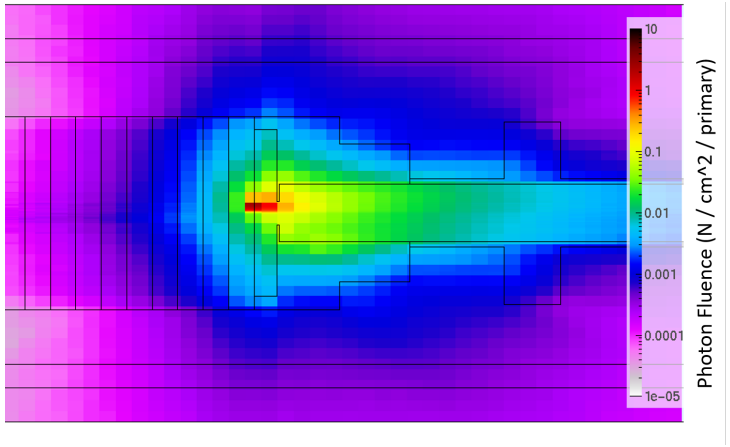

(b)

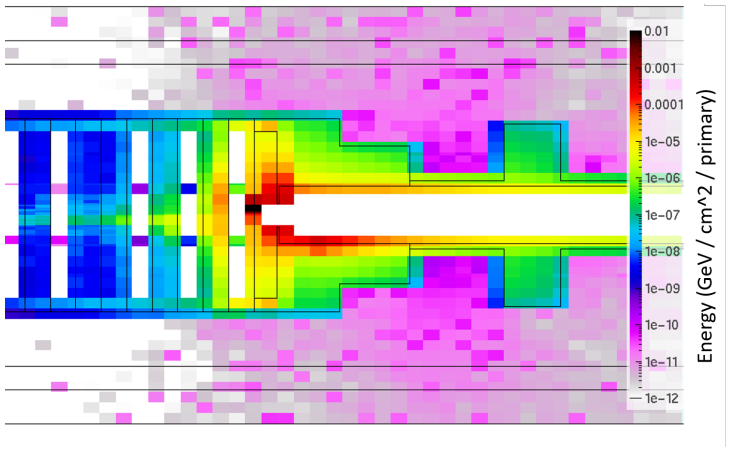

(c)

Figure 6.15 – Fluence of (a) electron and (b) photon fluence, and total energy deposition (c) in the simulated geometry, for 5 MeV primary electrons

correspondingly, the conclusion can be drawn that the main contributor in the energy deposition in the cavity environment are the electrons. The results of this simulation were validated experimentally: after more than one year of operation, the part of the fibre that covered the beam pipe became rigid, while a discolouration of the plastic cover could be observed. However, these alterations did not affect the quality of the measured signals. Figure 6.15 presents the same values in the case of 5 MeV primary electrons. For this primary energy an insignificant fraction of electrons manage to escape from the beam pipe, while the energy deposition outside the RF cavity, compared to the 15 MeV case, is rather low.

6.4 RF Breakdown radiation detection

During an RF breakdown, a large fraction of the power that can reach 50 MW is absorbed, most possibly by the generated electron currents. These collide with the structure walls emitting X-rays [162] and, as simulated in the above section, electrons outside the cavity. To examine the emitted radiation detected by the OBLM, an analysis on the RF breakdown occurrences at the dogleg accelerating structure experiment was performed.

Method

This study was performed in the experimental setup described in Subsection 6.3.1. In the present case, only the RF breakdown pulses are examined.

The acquisition system of the XBOX-1 experimental setup includes a buffer, which stores the two pulses previous to an RF breakdown and merges them with the breakdown signal into one single file. This is presented in Figure 6.16: the two small peaks are the signals of the preceding RF pulses, while the third, large peak appearing is an RF breakdown. From this plot a direct comparison between the signals of the two cases is triggered: during a breakdown a much higher signal, and therefore particle fluence is observed.

The RF breakdown data were acquired during the same data-taking periods as the electron field emission data of Subsection 6.3.1, and are also summarised in Table 6.1. From the Table an increase of the breakdown rate with the input power can be observed, which is in agreement with what is discussed in Section 1.5: as derived from Equation 1.13, the field emitted current increases with the accelerating gradient, hence the input power in the accelerating structure. The increased field emitted current results in a larger RF breakdown rate in the cavity.

For the analysis of the breakdown pulses, the same method as in Subsection 6.3.1 was followed. However, for Equation 6.1 a longer window of 1.6 μs was selected, in order to include the complete development of the breakdown.

Results

The results of the study are summarised in Figure 6.17 in which the average of the OBLM detected signal with respect to the average input power in the cavity is depicted. The tendency

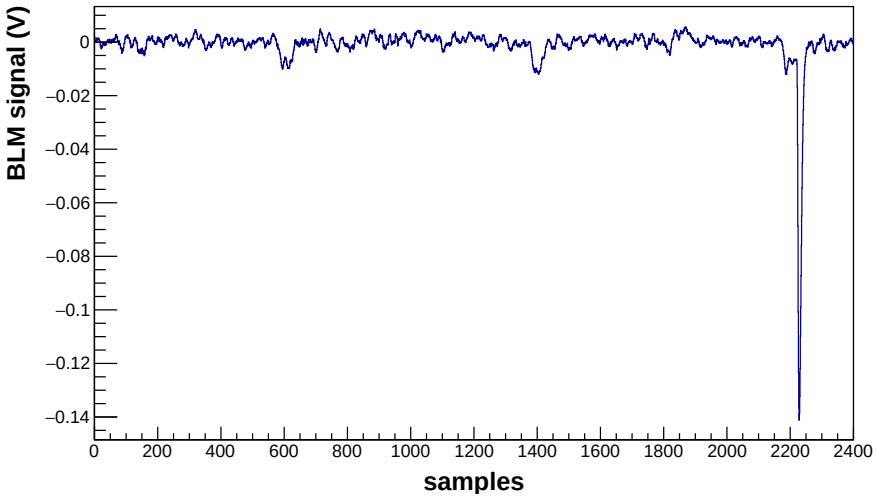

Figure 6.16 – OBLM signal observed during an RF breakdown at the unloaded T24 RF cavity

of an increased signal in the fibre with increasing RF power is observed. This is explained not only from the general higher electron field emission with higher input power, which was demonstrated in the previous Section, but also because during a breakdown the electrons generated in the produced plasma absorb a major fraction of the RF power in the cavity [164]. The higher this power is, the larger the amount of electrons that exit the accelerating structure and are detected by the monitor.

Due to the large error bars of Figure 6.17, the RF breakdown data can be fitted by a variety of functions. However, it was noticed that the highest accuracy was achieved for Equation 6.3, hence this equation was also selected to fit the breakdown case. The fit parameters, indicated on the Figure, are different than in the field emission case and have very large errors. As a result, no accurate prediction of the expected radiation from RF breakdowns occurring at the nominal accelerating gradient can be made.

6.5 Optical fibre BLMs as RF cavity diagnostics

Following the demonstration that OBLMs can detect radiation generated from dark current losses and RF breakdowns, the potential of using them for RF cavity diagnostics was introduced. This led to a set of diagnostics measurements and studies of high gradient accelerating structures, which are described in this section.

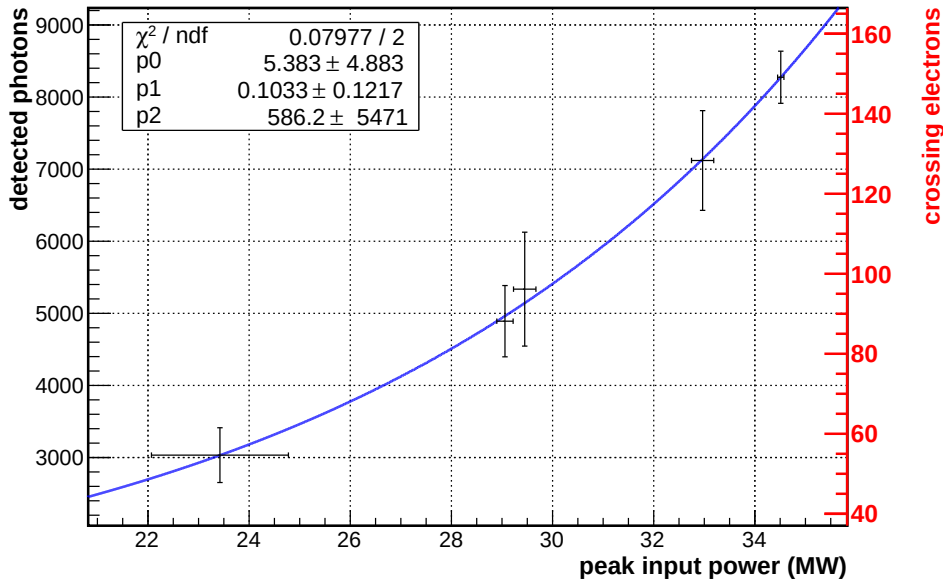

Figure 6.17 – OBLM signals during RF Breakdowns, in terms of detected photons (left axis) and an approximation of relativistic electrons crossing the fibre (right axis)

6.5.1 | RF Breakdown prediction from previous pulse

The ability of detecting both field emitted electrons and RF breakdowns introduces the idea of examining whether the prediction of breakdowns from the signals obtained during normal operation is possible. A potential observation that would help predict a breakdown could be an increase in the level of the field emitted electrons prior to it, however until today such a phenomenon has never been observed. To perform this study, the data from XBOX-1 experiment and the data-taking periods examined in the dark current (Subsection 6.3.1) and RF breakdown case (Section 6.4) were used.

In particular, in Subsection 6.3.1 the mean value of the measured field emission signals for different input powers has been calculated, shown in Figure 6.7. Additionally, in the case of RF breakdowns the two pulses preceding the breakdown are also being logged. The pre-breakdown pulses are visible in Figure 6.16. In order to examine if there is a detectable accumulation of the field emitted electrons in the accelerating structure before an RF breakdown, the charge of the signal of the pulse prior the breakdown was calculated for each event. The integration window used was set at 240 ns. Subsequently, for each data-taking period, the mean value and the average error of the mean for all the pre-breakdown pulses were calculated. Due to the lack of statistics for the fifth period (only three breakdown cases logged), this was excluded from the analysis.

The results of this study are illustrated in Figure 6.18. The black points correspond to the mean value of all field emission signals for the average of the peak input power during these measurements, the blue line is the fit function used for these data, as explained in

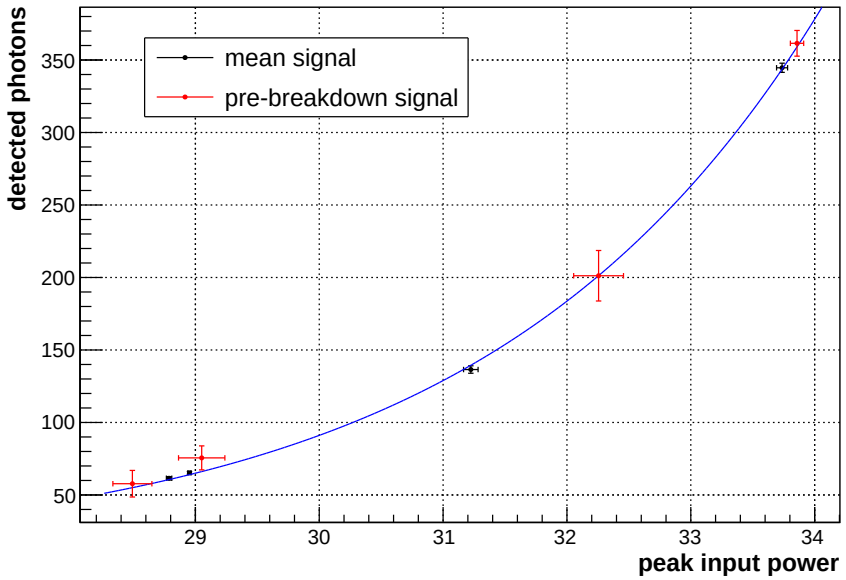

Figure 6.18 – Comparison of the field emission signals during normal operation of the RF cavity (black) to the field emission of the pulse previous to RF breakdowns (red)

Subsection 6.3.1, and the red points represent the mean values of the pre-breakdown pulses. The OBLM signals of the pre-breakdown pulses do not show any significant difference with respect to those in normal operation, and agree within the error with the fit function. It can be concluded that no breakdown predictions can be made with this diagnostics system, something which agrees with all past experience on this subject [165]. An observation that can be made, however, is that in most of the cases the average peak power of the pre-breakdown case is higher than the average peak power of the total of the pulses, which may be an additional parameter triggering the events.

6.5.2 | Electron field emission studies during small input power variations

XBOX-2 is an X-band test stand at CERN [166] aiming to study accelerating structures under high input power. In this test stand the RF cavity is not part of a beam line, but stand-alone. At the XBOX-2 an OBLM system was installed to contribute in the RF cavity diagnostics. This introduced the opportunity to perform additional electron field emission measurements during power scans, i.e. by changing the input power in small steps.

Experimental setup

During the present measurements the RF cavity tested at XBOX-2 is the T24-Open, comprising two halves, which is described in Subsection 1.5.3 and shown in Figure 1.11(b) [57]. The two halves were connected on the vertical axis, i.e. their interface was at the top and at the

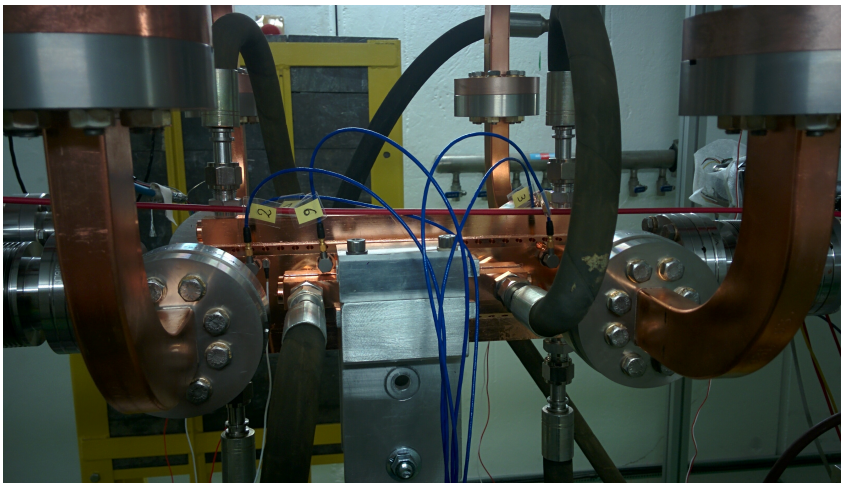

Figure 6.19 – Installation of the optical fibre on the XBOX2 accelerating structure

bottom of the installed structure.

A 5 m optical fibre of a 550 µm (600 µm) core (cladding) was installed at the test stand, above and along the accelerating structure and in contact to it, as shown in Figure 6.19. The chassis including the photosensors and their readouts was located on the floor of the facility, under the girder supporting the accelerating structure. Since the aim was the use of OBLM for RF cavity diagnostics, the high-gain Hamamatsu MPPC S12572-050C was used and coupled to a transimpedance amplifier readout circuit, identical to the one of the CTF3 dogleg line, described at the beginning of this chapter.

Method and Results

For this measurement a scan on the input power was performed starting from 24 MW and reaching up to 33 MW in steps of 0.25 MW. The input power and OBLM data were logged at a rate of 5 Hz. The detected charge, calculated from Equation 6.1 with an integration interval of 240 ns, is illustrated in Figure 6.20. The number of electrons with $\beta = 1$ that would correspond to such a signal has been calculated from Equation 3.39, after implementing the characteristics of the current optical fibre and is shown on the right axis of the Figure.

The electron field emission signal is characterised by a distinct increase with the raising of the input power. The exponential Equation 6.3 was applied to fit the data and is represented with a blue line in Figure 6.20. The same equation was used for the fit of the T24 field emission results, shown (Figure 6.7). The exponential function fits very well with the experimental data, with parameters:

$$p0 = -4.45 \pm 0.06,\ p1 = 0.318 \pm 0.002,\ p2 \simeq 46.0 \pm 0.7$$

Due to the large number and the good quality of the experimental data, the errors of the fit parameters are very low. Comparing the parameters with those of the T24 structure a divergence

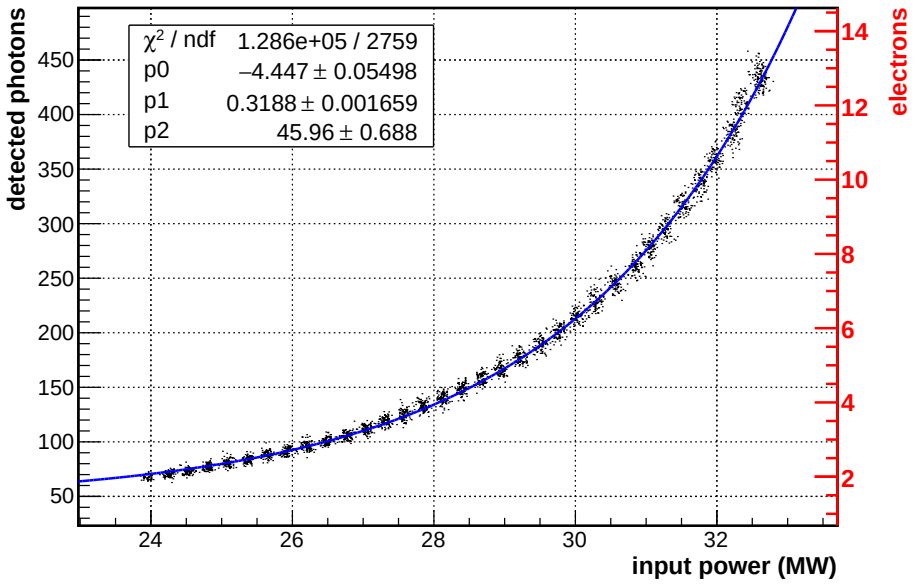

Figure 6.20 – Field emitted electron signal of the T24-Open cavity, and its fit function (blue line)

is observed. This is attributed to the fact that the electron field emission is characteristic of each high gradient RF cavity and may significantly vary depending on the design and condition.

6.5.3 | Field Enhancement Factor β_{FN}

The final step to demonstrate the applicability of OBLMs for RF cavity diagnostics is the extraction of the Fowler-Nordheim plot and the calculation of the field enhancement factor β_{FN}. To that end, the data acquired in XBOX-2 and in the T24 accelerating structure, described in Subsections 6.5.2 and 6.3.1, were used.

As derived in Equation 1.15, the factor β is given from

$$\beta_{FN} = -\frac{2.84 \times 10^9 \phi^{1.5}}{\frac{d(\log_{10}(\bar{I}_F/\mathcal{E}^{2.5}))}{d(1/\mathcal{E})}}$$

where $\phi = 4.7\,\text{eV}$ is the work function of copper. The accelerating gradient $\mathcal{E}$ can be estimated from the input power P in the accelerated structure as [167]

$$\mathcal{E}[MV/m] = \alpha_{acc}\sqrt{P[MW]} \tag{6.5}$$

where the parameter α_{acc} is characteristic of the structure design and can be estimated from the power at which the gradient reaches the 100 MV/m. For the T24-Open structure, this was calculated as $\alpha_{acc} \simeq 15$ [168]. For the electron field emission, however, one is interested in the electric field that develops at the surface of the structure interior $\mathcal{E}_S$ [169], which for the

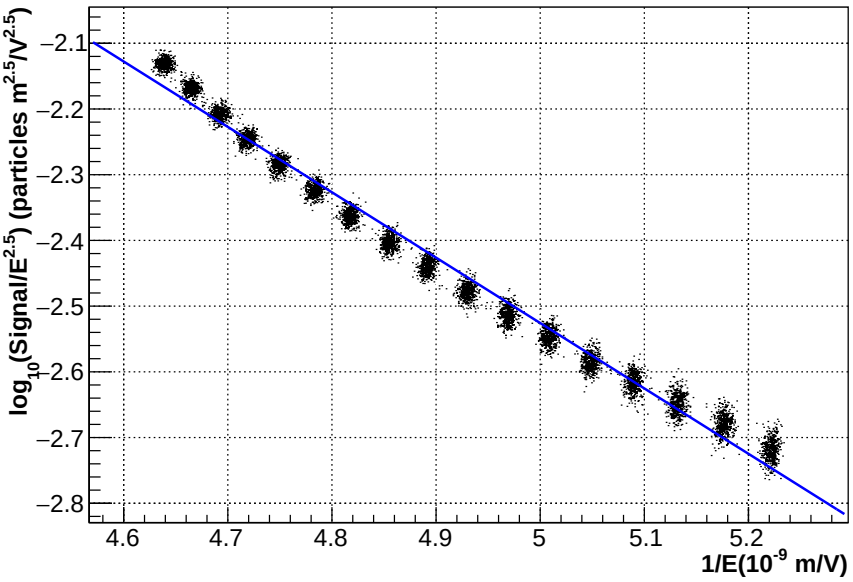

Figure 6.21 – Fowler-Nordheim plot from data acquired by a T24-open accelerating structure at the CERN XBOX2 installation

examined cavity is approximately 2.5 times the accelerating gradient [57, 170]. Therefore for the present calculations:

$$\mathcal{E}_S \simeq 37.5\sqrt{P} \tag{6.6}$$

Replacing the field emitted current $\bar{I}_F$ with the estimated electron emission $Signal_{e^-}$, as calculated from Equation 3.39, and the gradient $\mathcal{E}$ with the electric field at the surface of the structure interior $\mathcal{E}_S$, the Fowler-Nordheim factor β can be given by:

$$\beta_{FN} = -\frac{2.84 \times 10^9 \phi^{1.5}}{\frac{d\left(\log_{10}(Signal_{e^-}/{\mathcal{E}_S}^{2.5})\right)}{d(1/\mathcal{E}_S)}} \tag{6.7}$$

The denominator of the above Equation $\frac{d\left(\log_{10}(Signal_{e^-}/{\mathcal{E}_S}^{2.5})\right)}{d(1/\mathcal{E}_S)}$ can be estimated as the slope of the plot representing the values of $\log_{10}(Signal_{e^-}/{\mathcal{E}_S}^{2.5})$ with respect to the inverse of the electric field $1/\mathcal{E}_S$. This is illustrated in Figure 6.21 and can be fitted by a linear equation shown in blue, with its slope is estimated as $\frac{d\left(\log_{10}(Signal_{e^-}/{\mathcal{E}_S}^{2.5})\right)}{d(1/\mathcal{E}_S)} = -0.995 \times 10^9$. The field enhancement factor β_{FN} is hence calculated for this accelerating structure as $\beta_{FN} = 29.1$.

The same process was followed for the experimental setup of XBOX-1 and the T24 accelerating structure. The maximum surface electric field of this cavity is 2.05 times the field in the structure, while the factor α_{acc} can be calculated as $\alpha_{acc} \simeq 16.1$ [171]. In this case, the Fowler-Nordheim plot was produced for both the signal detected by the photosensor directly (photons) and the estimated number of electrons with $\beta = 1$ that this signal corresponds to.

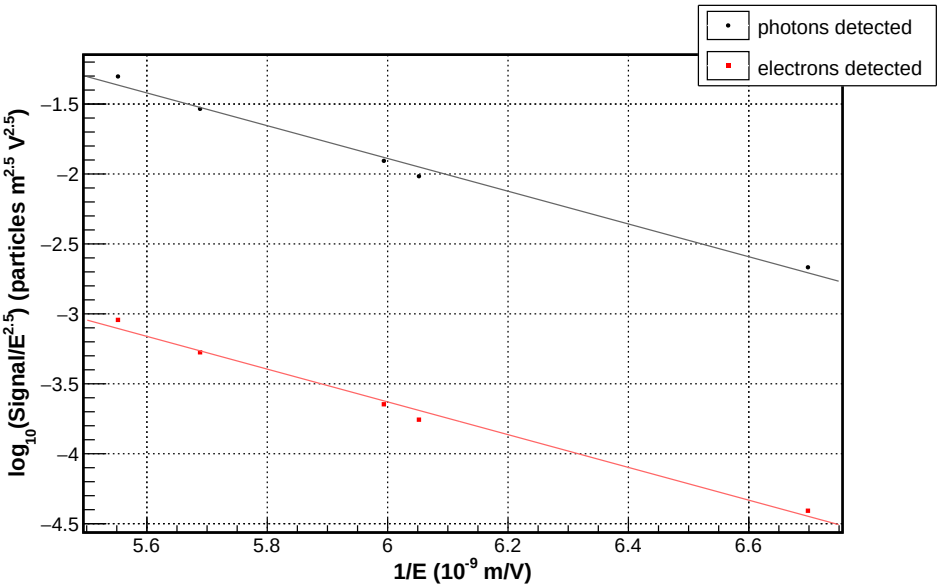

Figure 6.22 – Fowler-Nordheim plot from data acquired by a T24 accelerating structure at the CERN XBOX1 installation

Since the relationship between the two is linear, the two plots are characterised by the same slope, equal to $\frac{d(\log_{10}(Signal_{e^-}/\mathcal{E}_S{}^{2.5}))}{d(1/\mathcal{E}_S)} = -1.171 \times 10^9$. The field enhancement factor can be consequently estimated as $\beta_{FN} = 24.7$ in this case, and is very similar to the one calculated above for the T24-open cavity.

It is worth to stress here that the linear fit of both Figures 6.21 and 6.22 is a product of the applied model and that the data are in reality non-linear. This is due to the fact that the Fowler-Nordheim theory describes the electron field emission in the case of an ideal metal surface, while in the present case the OBLM detects the electrons that have been emitted in the cavity and escaped it. The observed non-linearity stems from the fact that emitted electrons with lower energy may not escape the cavity, while those of higher energy are more likely to be detected by the OBLM.

6.5.4 | Characterisation of a nominal CLIC accelerating structure

At the XBOX-1 experiment a nominal CLIC accelerating structure, the TD26 [60], was installed and tested. As described in Subsection 1.5.3, the TD26 has 26 cells and, in comparison to the previously examined T24, damping waveguides. The difference in the cell geometry leads to different levels of field emission and results in a different shielding of these electrons. Therefore, the radiation measured outside the cavity may deviate significantly from the one measured in the T24 case.

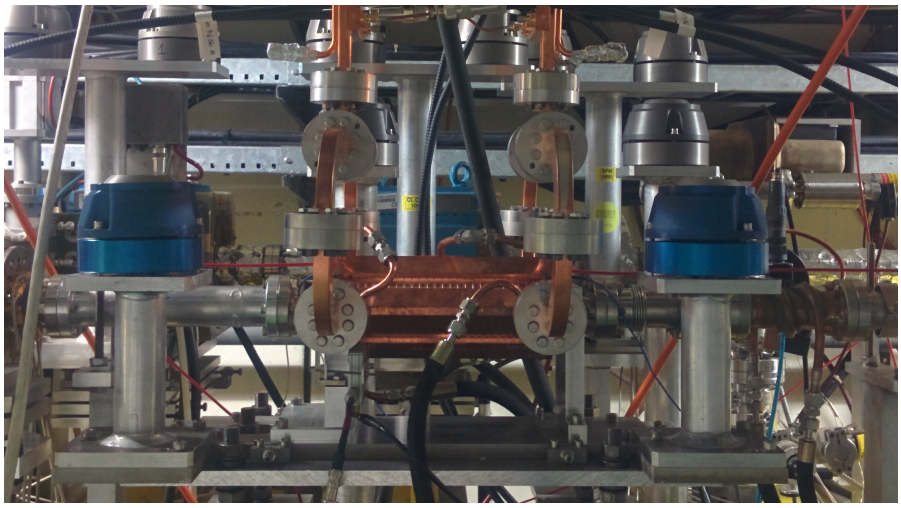

Figure 6.23 – The optical fibre installed above the TD26 accelerating structure at the CTF3 dogleg line

Experimental Setup

To take measurements with the OBLM system a new pure Silica fibre was installed. The fibre was of a smaller core diameter, 550 µm, with a 600 µm cladding and a hard polymer buffer, and also 7 m long [157]. Otherwise, the setup was similar to the one described for the T24 structure, and is shown in Figure 6.23. In comparison to the T24, in this case the fibre is almost in contact with the new cavity.

Method and Results

A total of 6,000 RF pulses were examined during December 2015. The input power in the accelerating structure varied from 34 to 42 MW while the pulse length remained constant at 200 ns.

For the estimation of the detected charge Equation 6.1 was used, with an integration window of 240 ns to include the complete RF pulse and to be comparable to the T24 study. The detected charge for all acquired pulses with respect to the peak input power in the accelerating structure is presented in Figure 6.24. For each MW of input power in the structure the statistical mean of the signals was calculated and is represented in Figure 6.24 as red star points, while the error bars correspond to the standard deviation.

At 42 MW, which corresponds to almost the nominal accelerating gradient of the unloaded CLIC accelerating structure, the dark current signal detected by the OBLM is 2.6 nC. The detected signal is one order of magnitude lower than the one measured with the T24 and presented in Figure 6.5. This can be attributed to various reasons: firstly, the optical fibre diameter in the T24 case is double to the case examined at the present study. Secondly, the different diameter of the cavities (T24 has a diameter of 45 mm whereas TD26 reaches the 74 mm) results in a higher attenuation of the dark current losses in the TD26 structure. Finally,

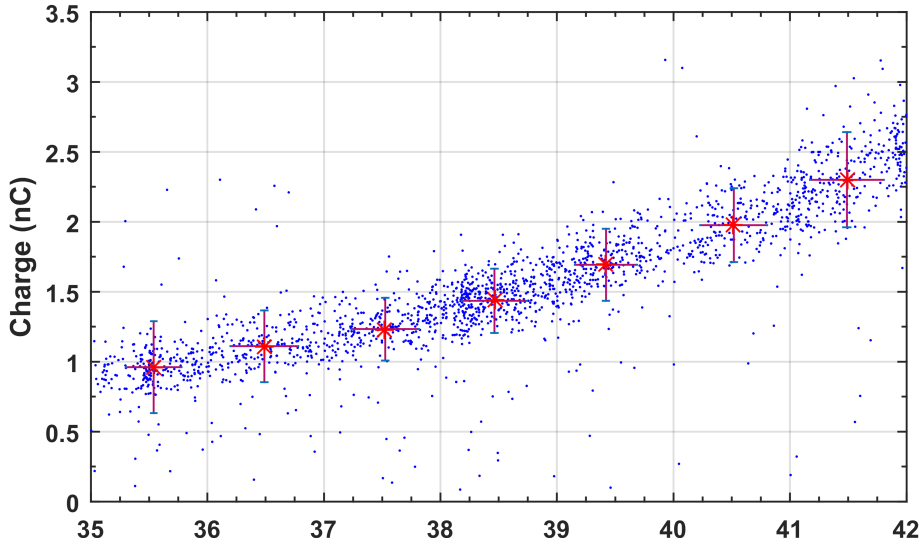

Figure 6.24 – Field emitted electron signal (blue) and their mean value for each MW of input power in the structure (red).

the quality of the accelerating structure plays a significant role: a well-conditioned cavity with fewer contaminants and imperfections experiences lower electron field emission compared to a more flawed one.

It is clear that the field emitted electrons are detectable by the OBLMs in the TD26 RF cavity. However, once more the installed system has a higher sensitivity than the one proposed as a nominal BLM system for machines like CLIC, damping rings or electron storage rings. For such machines, as demonstrated in Chapter 4, a 200 µm optical fibre and a photosensor readout without an amplifier are sufficient.

The use of the amplifiyng readout with the 500 Ω feedback resistor enlarges the signal 10 times compared to the simple high pass filter readout used originally. In addition, the ratio of the two fibres is $\frac{diam_{exp}}{diam_{nom}} = \frac{550}{200} = 2.75$, while the electron path length and hence the Cherenkov photon yield increases linearly linearly with the fibre diameter. Though the measured number of photons depends on and grows with the interaction volume and the solid angle, as a first approximation the linearity with the fibre diameter has been used. As a result, the detected signal during this experiment can be estimated as approximately 27.5 times higher than the one expected for a nominal CLIC BLM system. Therefore, in such a system the background will drop to 3.5% of the value measured at the dogleg, i.e. 0.09 nC, and is not expected to limit the detector sensitivity. This was experimentally confirmed at the TD26 structure: after changing the photosensor MPPC readout into a non-amplifying low pass filter, the dark current signals were not detectable. As a conclusion, the electron field emission of CLIC accelerating structures is not expected to introduce a significant sensitivity limitation to nominal OBLMs.

6.6 Summary

In this chapter, the OBLMs were studied with respect to high gradient RF cavities. Experimental measurements at CTF3 demonstrated that sensitive OBLM systems detect both the electron field emission and the RF breakdown generated radiation. The particle origin of the signals detected was examined through simulations of the optical photon creation in quartz from electrons and photons, as well as the RF cavity radiation environment. From the simulations it is deduced that the major contribution of the OBLM signals originates from electrons.

Additional measurements at the CERN XBOX-2 test-stand demonstrated that OBLMs bear the ability to measure differences in electron field emission during small variations in the accelerating gradient. Additionally, through measurements at two different structures and facilities it was validated that they can be used for the estimation of the Fowler-Nordheim field enhancement factor β_{FN}, a parameter characteristic of the RF cavity. This rendered the fibres an invaluable tool for RF cavity diagnostics, which is confirmed by the fact that they are currently operationally used at the XBOX-2.

The fibres bear as advantage the fact that they are not intercepting the beam, and therefore they can efficiently be used for RF cavity diagnostics in an operational beam line. In such a beam line at the CTF3 facility, a nominal CLIC RF cavity with damping waveguides was examined and the sensitivity limitations its field emission will introduce to a nominal OBLM system was studied. The conclusion reached is that while the RF cavity background can be detected by OBLMs which are modified towards high sensitivity, a nominal, i.e. non-sensitive, OBLM system will not be significantly inhibited by it.

CONCLUSIONS AND OUTLOOK

In the frame of the present work an optical fibre based particle detector was developed and was examined for its characteristics and its capabilities, as a beam loss monitor, in optimising the operation of storage rings and RF accelerators.

The detector consists of a quartz multimode fibre coupled with a Silicon Photomultiplier, integrated in a designed high-pass readout and contained in specially manufactured RF shielded modules. Its operating principle is based on the generation of Cherenkov light when high energy charged particles cross the quartz, and on the photon propagation through the fibre to its end face, where they are detected by the photosensor. Compared to conventional detectors, optical fibre based ones offer greater versatility, providing the maximum possible coverage over the entire length of the accelerator in a cost-effective way. In addition, the system is insensitive to magnetic fields, neutrons and low energy X-rays, while its sensitivity and dynamic range can be modulated depending on the fibre and photosensor characteristics. A nominal composition that was examined in the present work and was demonstrated suitable for beam loss monitoring applications consists of a fibre with a 200 μm core diameter and up to 125 m long, and an SiPM with high dynamic range.

The detector was tested as a beam loss monitor at the Australian Synchrotron Light Source and the CLIC Test Facility 3, at CERN, for different aspects of its performance. The installation of an optical fibre BLM provides the option of stationing the photosensing modules away from the accelerator, e.g. in a radiation shielded location. Under such circumstances, the usage of a second fibre as a background detector between the modules and the accelerator, in order to achieve higher signal accuracy, was presented.

In both ASLS and CTF3 the beam loss location identification capabilities of the detector were examined. In the case of a single bunch beam, a remarkable intrinsic time resolution was measured, equal to 260 ps which corresponds to a position resolution better than 4 cm. Furthermore, an impact location discrimination with 25 cm spacing between beam losses in the machine was demonstrated. When the beam is multi-bunch or long, the loss origin is identifiable but the detector performance is limited by the pulse length. A minimum accuracy of 1.4 m in the localization of loss locations was achieved with a 1 μs long beam. In addition, a distance of 3 m was required in order for two loss positions to become distinguishable when losing a 350 ns long electron pulse. Considering that the lost particles and the generated particle showers are rather spread in the case of long electron pulses, such a loss location discrimination is satisfactory for the efficient protection of a particle accelerator. For single bunch beams, the obtained resolution is sufficient for distinguishing consecutive machine elements such as magnets or even, in linear accelerators such as CLIC, the compact high gradient RF cavities.

The signals obtained from a long monitor such as the OBLM provide more realistic information about the distribution of beam losses, compared to localised detectors. At the ASLS the ability of distributed systems to recognise previously unknown loss locations was presented. Furthermore, aspects related to the analysis of acquired signals, such as the identification

of false signals originating from the photon reflection at the opposite end of the fibre, were explored. Moreover, a method to determine unknown beam loss locations in an OBLM was demonstrated, for the case that a loss position has been identified in a neighbouring fibre. Additionally, the entire ASLS machine was covered with only four fibres, which proved capable of monitoring beam losses during the complete machine cycle and of measuring steady state losses. However, to protect critical locations and particularly during multi-bunch beams, the use of complementary localised detectors such as ionisation chambers that can provide additional information on the beam loss structure is recommended. Compared to the use of PMTs, the SiPM system is insensitive to magnetic fields, inexpensive, and robust, while they require a much lower bias voltage supply. However, the low noise of fast-PMTs might be an advantage for storage ring applications and should be taken under consideration.

The use of a BLM system in situations where it is protecting a beam line located very close to another beam (e.g. LHC, CLIC), may be restricted by sensitivity limitations, due to the crosstalk of beam loss signals. At CTF3 this phenomenon was quantified for OBLMs and ionisation chambers for different values of the beam current. However, it could not be entirely determined as it is strongly correlated with the beam and beam loss characteristics. The shadowing of the detector from the opposite beam line, e.g. by installing it so that the accelerator it protects provides radiation shielding, is an approach that can reduce the crosstalk effect on the BLMs.

Measurements with OBLMs placed close to high gradient accelerating structures at CTF3 demonstrate that a nominal OBLM is not sensitive to the RF cavity background radiation, which is the result of the electron field emission in the structure. However, the optical fibre detector can be modified with a large fibre core, a high sensitivity SiPM and a transimpedance amplifier. In such a case, its capability to detect field emitted electrons that escape the cavity, and RF breakdowns was demonstrated experimentally. The contribution of photons to the generation of Cherenkov radiation (via Compton electrons or pair production) and the RF cavity radiation environment for an electron field emission scenario were calculated with FLUKA simulations. The radiation field of the accelerating structure was shown to be comprised of both electrons and photons, although the contribution of the latter to the OBLM signal is negligible.

The detection of field emitted electrons and its low sensitivity to X-rays introduced the modified fibre sensor as an invaluable diagnostics tool for RF cavities. The detector is able to monitor the field emission variations during very small changes of 0.25 MW on the input power in the accelerating structure. Furthermore, its utilisation for the estimation of the Fowler-Nordheim field enhancement factor was demonstrated.

Among the advantages of OBLMs stands their straightforward installation, which renders their replacement, if necessary, an uncomplicated procedure. Nevertheless, for reasons related both to cost and the protection of the accelerator personnel, this is not a desirable process. The knowledge of the radiation environment levels where the detector will be installed is very important for the proper selection of an optical fibre that will withstand it. In cases of highly localised known radiation sources, the use of OBLMs should be avoided, either through an alternative installation route of the detector or with added shielding. In such locations, a very radiation hard detector, such as an ionisation chamber or a SEM, should be used.

Conclusively, a distributed fibre-based particle detector has been developed and studied as a beam loss monitor in both storage rings and RF accelerators. The OBLM covers the entire accelerator length at a reasonable cost and was proven capable of locating the origin of beam losses with significant accuracy. Moreover, being able to recognize previously unknown beam loss locations, this monitor provides valuable information for the machine operation. In the case of high energy linear colliders such as CLIC, the detector was proven capable of protecting both the linacs and the damping rings. The obtained experience renders the developed OBLM, combined with suitable detectors at very critical locations, a notable system for the machine protection and optimisation of machine operation of particle accelerators and for beam commissioning.

Additionally, the optical fibre based detector is a novel and very promising sensor for RF cavity diagnostics. As a result, the OBLMs installed in the context of this thesis, continue being studied and used in the ASLS, while they are operational for dark current and RF breakdown measurements and RF cavity characterisation at the CERN XBOX-2 test stand. Moreover, the developed design has been commercialised and is proposed as a BLM for different types of accelerators and for further radiation detection applications, such as in nuclear plants.

The following steps towards the optimisation of the OBLM include an extensive study of the achievable sensitivity and dynamic range. Further developments to increase them, could include the use of split fibres that arrive to photosensors of different characteristics or the use of logarithmic amplifiers. Additionally, the design of a system for the calibration of the detector will augment its reliability. Simulations of the beam transport and losses in an accelerator and the particle shower generation along the machine are necessary to confirm the interpretation of the optical fibre signals. Moreover, detailed measurements of the radiation hardness of different types of fibre and of the photosensors for different radiation environments can provide valuable information for the capabilities of the system. Finally, the capabilities of the system can be further explored by examining it in hadron machines and mixed radiation environments.

BIBLIOGRAPHY

[1] C. Patrignani et al., "Review of Particle Physics, 2016-2017," *Chin. Phys. C*, vol. 40, no. 10, p. 100001. 1808 p, 2016. (document), 2.3.1, 2.3.1, 2.2, 2.3.1, 2.3, 2.3.1, 2.4

[2] A. Zhukov, "Beam Loss Monitors (BLMs): Physics, simulations and applications in accelerators," in *Proceedings of 2010 Beam Instrumentation Workshop, BIW10, Santa Fe, New Mexico, US.*, pp. 553–565, 01 2010. http://accelconf.web.cern.ch/AccelConf/BIW2010/papers/thtnb01.pdf. (document), 2.4, 2.4, 2.4.1, 2.4.3

[3] S. Girard, J. Kuhnhenn, A. Gusarov, B. Brichard, M. V. Uffelen, Y. Ouerdane, A. Boukenter, and C. Marcandella, "Radiation effects on silica-based optical fibers: Recent advances and future challenges," *IEEE Transactions on Nuclear Science*, vol. 60, pp. 2015–2036, June 2013. (document), 3.2.2, 3.7, 3.2.2, 3.2.2

[4] Hamamatsu Photonics K.K., "Photomultiplier tubes, basics and applications, third edition." https://www.hamamatsu.com/resources/pdf/etd/PMT_handbook_v3aE.pdf, 2007. Accessed: 02-06-2017. (document), 3.3.2, 3.13, 3.3.2

[5] Hamamatsu Photonics K.K., "MPPC® (multi-pixel photon counter), S12572-010, -015C/P." www.hamamatsu.com/resources/pdf/ssd/s12572-010_etc_kapd1045e.pdf. Data Sheet from Hamamatsu Photonics. (document), 3.3.1, 3.4.1, 3.18, 3.2, 5.2.2

[6] Hamamatsu Photonics K.K., "MPPC® (multi-pixel photon counter), S12572-025, -050, -100C/P." www.hamamatsu.com/resources/pdf/ssd/s12572-025_etc_kapd1043e.pdf. Data Sheet from Hamamatsu Photonics, Accessed 30-05-2017. (document), 3.2

[7] G. Schmidt, E. Kasel, K. Wille, M. Körfer, H. Henschel, and J. Kuhnhenn, "Optical Fibre Beam Loss Monitors for Storage Rings at DELTA," 2002. (document)

[8] F. Wulf and M. Körfer, "Beam loss and beam profile monitoring with optical fibers," pp. WEAOA01, 411–417, 01 2009. (document)

[9] S. L. Kramer, "Cherenkov radiation for Beam Loss Monitor Systems," in *Proceedings, 15th Beam Instrumentation Workshop BIW2012: Newport News, Virginia, USA, April 15-19*, pp. THBP03, 1–5, 2012. (document)

[10] X.-M. Maréchal, Y. Asano, and T. Itoga, "Design, development, and operation of a fiber-based cherenkov beam loss monitor at the spring-8 angstrom compact free electron laser," *Nuclear Instruments and Methods in Physics Research Section A: Accelerators, Spectrometers, Detectors and Associated Equipment*, vol. 673, pp. 32 – 45, 2012. (document)

[11] T. Obina and Y. Yano, "Optical fiber based loss monitor for electron storage ring," in *IBIC 2013: Proceedings of the 2nd International Beam Instrumentation Conference*, pp. 638–643, 12 2013. (document), 4.1

[12] D. D. Giovenale, L. Catani, and L. Fröhlich, "A read-out system for online monitoring of intensity and position of beam losses in electron linacs," *Nuclear Instruments and Methods in Physics Research Section A: Accelerators, Spectrometers, Detectors and Associated Equipment*, vol. 665, pp. 33 – 39, 2011. (document)

[13] A. Intermite, M. Putignano, and A. Wolski, "Cherenkov Fibre Optic Beam Loss Monitor at ALICE," *Conf. Proc.*, vol. C110904, pp. 1383–1385, 2011. (document)

[14] S. Mallows, E. B. Holzer, and J. W. van Hoorne, "Fiber based BLM system research and development at CERN," in *Proceedings of HB2012, Beijing, China* , pp. THO3C05, 596–600, 2012. 1.1, 3.4.2

[15] K. Wille, *The physics of particle accelerators: An introduction*. Oxford, UK: Univ. Pr., 315 p, 2000. 1.2, 1.3.2, 1.3.2, 1.4.1

[16] S. Y. Lee, *Accelerator physics*. Singapore, Singapore: World Scientific, 491 p, 1999. 1.2, 1.3.2, 1.6.2

[17] H. Wiedemann, *Particle accelerator physics I*. Berlin, Germany: Springer, 1999. 1.2, 1.3.1, 1.3.2, 1.4.1

[18] S. Mobilio, F. Boscherini, and C. Meneghini, *Synchrotron radiation: basics, methods and applications*. Berlin: Springer, Aug 2014. 1.3.2, 1.3.2

[19] "Lightsources.org collaboration." `http://www.lightsources.org/regions`. Accessed: 04-04-2017. 1.3.2

[20] T.-Y. Lee, "Practical Definitions of Beam Lifetimes in an Electron Storage Ring," 2005. 1.3.2

[21] "Cern council." `http://council.web.cern.ch/en/content/member-and-associate-states-observers`. Accessed: 05-04-2017. 1.3.3

[22] A. Breskin and R. Voss, *The CERN Large Hadron Collider: Accelerator and Experiments*. Geneva: CERN, 2009. 1.3.3, 1.3.3

[23] G. Aad *et al.*, "Observation of a new particle in the search for the Standard Model Higgs boson with the ATLAS detector at the LHC," *Phys. Lett.*, vol. B716, pp. 1–29, 2012. 1.3.3

[24] S. Chatrchyan *et al.*, "Observation of a new boson at a mass of 125 GeV with the CMS experiment at the LHC," *Phys. Lett.*, vol. B716, pp. 30–61, 2012. 1.3.3

[25] Nobelprize.org, "The Nobel Prize in Physics 2013." `http://www.nobelprize.org/nobel_prizes/physics/laureates/2013/`, Nobel Media AB 2014. Web. 16 Mar 2018. 1.3.3

[26] T. Massam, T. Müller, B. Righini, M. Schneegans, and A. Zichichi, "Experimental observation of antideuteron production," *Nuovo Cimento*, vol. 39, pp. 10–14, 1965. 1.3.3

[27] G. Charpak, "Development of multiwire proportional chambers," Jun 1969. 1.3.3

[28] "Cern courier," November 1983. 1.3.3

[29] T. Berners-Lee, R. Cailliau, J.-F. Groff, and B. Pollermann, "World-Wide Web: the information universe," *Electron. Netw.*, vol. 2, pp. 52–58, 1992. Reprinted in 2010. 1.3.3

[30] C. De Melis, "The CERN accelerator complex. Complexe des accélérateurs du CERN," Jul 2016. General Photo. 1.2

[31] X. C. Vidal and R. C. Manzano, "LHC Pb collisions - Taking a closer look at LHC." `http://www.lhc-closer.es/taking_a_closer_look_at_lhc/0.lhc_pb_collisions`. Accessed: 01-10-2017. 1.3.3

[32] "nTOF." `http://cds.cern.ch/record/1997567`, Dec 2012. Accessed: 01-10-2017. 1.3.3

[33] P. Belochitskii et al., "Commissioning and First Operation of the Antiproton Decelerator (AD)," p. 6 p, Jul 2001. 1.3.3

[34] edited by V. Chohan, *Extra Low ENergy Antiproton (ELENA) ring and its Transfer Lines: Design Report.* CERN Yellow Reports: Monographs, Geneva: CERN, 2014. CERN-2014-002, DOI: 10.5170/CERN–2014–002. 1.3.3

[35] S. Pandolfi, "First antiprotons in ELENA." `http://cds.cern.ch/record/2281940`, Aug 2017. Accessed: 01-10-2017. 1.3.3

[36] E. Gschwendtner, "Starting Up the AWAKE Experiment at CERN," p. TUOBB2. 4 p, 2017. 1.3.3

[37] "AWAKE," Apr 2013. `http://cds.cern.ch/record/1997886`. 1.3.3

[38] D. e. a. Gamba, "The clear user facility at cern," 12 2017. 1.3.3

[39] R. Corsini, "Final Results From the Clic Test Facility (CTF3)," no. CERN-ACC-2017-130, p. TUZB1. 6 p, 2017. 1.3.3

[40] edited by M. Aicheler, P. Burrows, M. Draper, T. Garvey, P. Lebrun, K. Peach, N. Phinney, H. Schmickler, D. Schulte, and N. Toge,
A Multi-TeV linear collider based on the CLIC technology: CLIC Conceptual Design Report. CERN-2012-007, 2012. 1.4.2, 1.4.2, 1.5, 1.5.2, 1.5.3, 5.3

[41] E. A. I. Syratchev, D. Schulte and M. Taborelli, "High RF Power Production for CLIC," in *Proceedings of PAC07, Albuquerque, New Mexico, USA*, pp. WEPMN071 pp. 2194–2196, June 2007. 1.4.2

[42] T. P. Wangler, *RF Linear Accelerators.* Willey-VCH, 2008. 1.5, 1.5.1, 6.1

[43] G. Benvenu, P. Fernandes, and R. Parodi, *An investigation on the field emitted electrons in travelling wave accelerating structures.* Nuclear Instruments and Methods in Physics Research A320, 1992. 1.5.1

[44] K. L. F. Bane, V. A. Dolgashev, T. Raubenheimer, G. V. Stupakov, and J. H. Wu, "Dark currents and their effect on the primary beam in an X-band linac," *Phys. Rev. ST Accel. Beams*, vol. 8, p. 064401, 2005. Available from: `https:`

//www.researchgate.net/publication/255944113_Dark_Currents_and_Their_Effect_on_the_Primary_Beam_in_an_X-band_Linac [accessed Apr 20, 2017]. 1.8, 1.5.1

[45] R. H. Fowler and L. Nordheim, *Electron Emission in Intense Electric Fields*. Proceedings of the Royal Society of London. Series A, Containing Papers of a Mathematical and Physical Character, Vol. 119, No. 781, pp. 173-181, May 1, 1928. 1.5.1, 6.3.1

[46] J. W. Wang and G. A. Loew, *Field emission and RF Breakdown in High-Gradient Room-Temperature Linac Structures*. SLAC-PUB-7684, October 1997. 1.5.1, 1.5.1

[47] C. Kittel, *Introduction to Solid State Physics*. Wiley, 2004. 1.5.1

[48] A. T. Perez Fontenla. Private Communication, July 2016. 1.9, 1.5.2

[49] C. G. Sánchez, A. Y. Lozovoi, and A. Alavi, *Field-evaporation from first-principles*. Molecular Physics, vol. 102, issue 9-10, pp. 1045-1055, 2004. 1.5.2

[50] W. Wuensch, "Advances in the Understanding of the Physical Processes of Vacuum Breakdown," Tech. Rep. CERN-OPEN-2014-028. CLIC-Note-1025, CERN, Geneva, May 2013. 1.5.2

[51] J. W. Wang, *RF properties of periodic accelerating structures for linear colliders*. PhD thesis, Calif. Univ. Stanford, Stanford, CA, 1989. Presented on Jul 1989. *

[52] G. Riddone, W. Wuensch, and R. Zennaro, "Structure production: Cern activities and master schedule." Talk, CLIC08 Workshop, CERN, Geneva, Switzerland. Available from: https://indico.cern.ch/event/30383/contributions/696469/attachments/575611/792742/GR-CLIC08-SMS-Production_RZ_last.pdf [accessed Apr 21, 2017], October 2008. 1.10

[53] K. A. Thompson, C. E. Adolphsen, K. L. F. Bane, H. Deruyter, Z. D. Farkas, H. A. Hoag, K. Ko, G. A. Loew, R. H. Miller, E. M. Nelson, R. B. Palmer, J. M. Paterson, R. D. Ruth, J. W. Wang, P. B. Wilson, N. M. Kroll, X. T. Lin, R. L. Gluckstern, N. Holtkamp, B. W. Littmann, and D. U. L. Yu, "Design and simulation of accelerating structures for future linear colliders," *Part. Accel.*, vol. 47, pp. 65–109. 80 p, Nov 1993. 1.5.3

[54] A. Grudiev and W. Wuensch, "Design of the CLIC Main Linac Accelerating Structure for CLIC Conceptual Design Report," in *Proceedings, 25th International Linear Accelerator Conference, LINAC2010: Tsukuba, Japan, September 12-17, 2010*, p. MOP068, 2011. 1.5.3, 6.3.2

[55] R. Zennaro, A. Grudiev, G. Riddone, A. Samoshkin, W. Wuensch, S. Tantawi, W. J. W, and T. Higo, "Design and fabrication of CLIC test structures," in *Proceedings of LINAC08, Victoria, BC, Canada*, pp. TUP057, 533–535, 2008. 1.5.3

[56] J. Wang, J. Lewandowski, J. Van Pelt, C. Yoneda, D. Gudkov, G. Riddone, T. Higo, and T. Takatomi, "Fabrication Technologies of the High Gradient Accelerator Structures at 100MV/m Range," 2010. 1.11

[57] H. Zha and A. Grudiev, "Design of the compact linear collider main linac accelerating structure made from two halves," *Phys. Rev. Accel. Beams*, vol. 20, p. 042001, Apr 2017. 1.5.3, 1.11, 6.5.2, 6.5.3

[58] D. Gamba and F. Tecker, "Emittance Optimisation in the Drive Beam Recombination Complex at CTF3," in *Proceedings, 6th International Particle Accelerator Conference (IPAC 2014), Dresden, Germany*, pp. TUPRI080, pp. 1754–1754, 2014. 1.6.1, 5.3.3

[59] R. Corsini, P. Skowronski, and F. Tecker, "CTF3 Status, Progress and Plans," *ICFA Beam Dyn. Newslett.*, vol. 62, pp. 165–186, 2013. 1.6.1

[60] F. Tecker *et al.*, "Beam-Loading Effect on Breakdown Rate in High-Gradient Accelerating Structures," in *Proceedings, 7th International Particle Accelerator Conference (IPAC 2016): Busan, Korea, May 8-13, 2016*, p. THPOR031, 2016. 1.6.1, 6.3.1, 6.5.4

[61] J. L. Navarro Quirante *et al.*, "CALIFES: A Multi-Purpose Electron Beam for Accelerator Technology Tests," in *Proceedings, 27th Linear Accelerator Conference, LINAC2014: Geneva, Switzerland, August 31-September 5, 2014*, p. MOPP030, 2014. 1.6.1

[62] R. Lillestøl, E. Adli, R. Corsini, S. Döbert, W. Farabolini, L. Malina, J. Pfingstner, and W. Wuensch, "Wakefield Monitor Experiments with X-Band Accelerating Structures," in *Proceedings, 6th International Particle Accelerator Conference (IPAC 2015): Richmond, Virginia, USA, May 3-8, 2015*, p. MOPTY004, 2015. 1.6.1

[63] E. Nebot Del Busto *et al.*, "Position Resolution of Optical Fibre-Based Beam Loss Monitors Using Long Electron Pulses," in *Proceedings, 4th International Beam Instrumentation Conference, IBIC2015*, p. WEBLA03, 2016. 1.6.2, 4.2.1

[64] E. Nebot del Busto *et al.*, "Measurement of Beam Loss at the Australian Synchrotron," in *Proceedings, 3rd International Beam Instrumentation Conference, IBIC2014*, (Monterey, CA, USA), p. WECZB3, 2014. 1.6.2, 5.2.3

[65] K. Wittenburg, "Beam Loss Monitoring and Control," in *The 8th European Particle Accelerator Conference, Paris, France, 3-7 Jun 2002*, pp. 109–113, Jun 2002. 2.1, 2.2

[66] R. Schafer, "A Tutorial on Beam Loss Monitors," in *Proceedings, 10th Beam Instrumentation Conference: Upton, New York, USA, May 6-9, 2002*, 2002. 2.1, 2.4

[67] E. B. Holzer, "Beam Loss Monitoring for Demanding Environments," in *Proceedings, 4th International Beam Instrumentation Conference, IBIC2015*, p. WEBLA01, 2016. 2.1

[68] CERN, , (Geneva), CERN, 2016. Comments: 17 lectures, 440 pages, published as CERN Yellow Report https://cds.cern.ch/record/1641418. 2.1, 2.2

[69] K. Mess, P. Schmüser, and S. Wolff, *Superconducting Accelerator Magnets*. World Scientific, 1996. †

[70] L. Bottura, "Magnet Quench 101," *WAMSDO 2013: Workshop on Accelerator Magnet, Superconductor, Design and Optimization; 15 - 16 Jan 2013, CERN, Geneva, Switzerland*, p. 9 p, Jan 2014. †

[71] V. Kain, J. Ramillon, R. Schmidt, K. Vorderwinkler, and J. Wenninger, "Material Damage Test with 450GeV LHC-type beam," p. 4 p, Jul 2005. 2.1

[72] P. Michel, "Strahlverlustmonitore für ELBE (in german)." Strahlungsquelle ELBE; ELBE-Palaver, 2002. https://www.hzdr.de/FWL/palaver/michel/Pal_170102/Palaver_BLM-Dateien/v3_document.htm, Accessed: 07-04-2012. 2.1

[73] K. Wittenburg, "Beam loss monitors," 2009. 2.2, 2.2.2, 2.4, 2.4.1, 2.4.1, 2.4.2, 2.4.3

[74] A. Chao and M. Tigner, *Handbook of Accelerator Physics and Engineering*. Handbook of Accelerator Physics and Engineering, World Scientific, 1999. 2.2.1

[75] J. Holmes, S. Henderson, and Y. Zhang, "Review of collective effects." Lecture, US PArticle Accelerator School, Vanderbilt, USA. http://uspas.fnal.gov/materials/09VU/Lecture9b.pdf [accessed Jan 15, 2018], January 2009. *

[76] B. Auchmann, T. Baer, M. Bednarek, G. Bellodi, C. Bracco, R. Bruce, F. Cerutti, V. Chetvertkova, B. Dehning, P. P. Granieri, W. Hofle, E. B. Holzer, A. Lechner, E. Nebot Del Busto, A. Priebe, S. Redaelli, B. Salvachua, M. Sapinski, R. Schmidt, N. Shetty, E. Skordis, M. Solfaroli, J. Steckert, D. Valuch, A. Verweij, J. Wenninger, D. Wollmann, and M. Zerlauth, "Testing beam-induced quench levels of lhc superconducting magnets," *Phys. Rev. ST Accel. Beams*, vol. 18, p. 061002, Jun 2015. 2.2.2

[77] E. Skordis, R. Bruce, F. Cerutti, A. Ferrari, P. Hermes, A. Lechner, A. Mereghetti, S. Redaelli, B. Salvachua, V. Vlachoudis, and C. Welsch, "Study of the 2015 Top Energy LHC Collimation Quench Tests Through an Advanced Simulation Chain," no. CERN-ACC-2017-300, p. MOPAB012. 4 p, 2017. 2.2.2

[78] T. Baer, G. Arduini, M. J. Barnes, W. Bartmann, C. Bracco, E. Carlier, F. Cerutti, B. Dehning, L. Ducimetière, A. Ferrari, M. Ferro-Luzzi, N. Garrel, A. Gerardin, B. Goddard, E. B. Holzer, S. Jackson, J. M. Jimenez, V. Kain, F. Zimmermann, A. Lechner, V. Mertens, M. Misiowiec, E. Nebot Del Busto, R. Morón Ballester, L. Norderhaug Drosdal, A. Nordt, G. Papotti, S. Redaelli, J. Uythoven, B. Velghe, V. Vlachoudis, J. Wenninger, C. Zamantzas, M. Zerlauth, and N. Fuster Martinez, "UFOs: Observations, Studies and Extrapolations," 2012. 2.2.2

[79] C. Grupen and B. Shwartz, *Particle Detectors; 2nd ed.* Cambridge monographs on particle physics, nuclear physics, and cosmology, Cambridge: Cambridge Univ. Press, 2008. 2.3.1, 2.3.1, 2.3.1, 2.3.1, 2.6, 2.3.2, 2.4

[80] F. H. Attix, *Introduction to radiological physics and radiation dosimetry*. Physics textbook, Weinheim: Wiley, 2004. 2.3.1

[81] "Klein-Nishina formula." https://en.wikipedia.org/wiki/Klein\T1\textendashNishina_formula. Accessed: 19-01-2018. 2.5

[82] J. T. Goorley, M. R. James, T. E. Booth, F. B. Brown, J. S. Bull, L. J. Cox, J. W. J. Durkee, J. S. Elson, M. L. Fensin, R. A. I. Forster, J. S. Hendricks, H. G. I. Hughes, R. C. Johns, B. C. Kiedrowski, R. L. Martz, S. G. Mashnik, G. W. McKinney, D. B. Pelowitz, R. E. Prael,

J. E. Sweezy, L. S. Waters, T. Wilcox, and A. J. Zukaitis, "Initial mcnp6 release overview - mcnp6 version 1.0," 6 2013. 2.3.2

[83] S. Agostinelli *et al.*, "GEANT4: A Simulation toolkit," *Nucl. Instrum. Meth.*, vol. A506, pp. 250–303, 2003. 2.3.2

[84] A. Ferrari, P. R. Sala, A. Fassò, and J. Ranft, *FLUKA: A multi-particle transport code (program version 2005)*. Geneva: CERN, 2005. 2.3.2, 6.2, 6.3.2

[85] T. T. Böhlen, F. Cerutti, M. P. W. Chin, A. Fassò, A. Ferrari, P. G. Ortega, A. Mairani, P. R. Sala, G. Smirnov, and V. Vlachoudis, "The FLUKA Code: Developments and Challenges for High Energy and Medical Applications," *Nucl. Data Sheets*, vol. 120, pp. 211–214. 4 p, 2014. 2.3.2, 6.2, 6.3.2

[86] G. F. Knoll, *Radiation detection and measurement; 4th ed.* New York, NY: Wiley, 2010. 2.4, 2.4.2

[87] E. Nebot del Busto, "Beam Loss Technology." ACAS School for Accelerator Physics 2016, Clayton, Victoria, Australia. Available from: `https://events.synchrotron.org.au/event/6/contribution/14/material/slides/0.pdf` [accessed Jun 25, 2017], January 2016. 2.4.1, 2.4.2, 2.4.4, 2.4.4

[88] S. S. Gilardoni, S. Aumon, E. Effinger, J. Gil-Flores, and U. Wienands, "Beam loss monitors comparison at the CERN Proton Synchrotron," p. 3 p, Sep 2011. 2.4.1, 2.4.3

[89] C. Leroy and P.-G. Rancoita, *Principles of radiation interaction in matter and detection; 4th ed.* Hackensack, NJ: World Scientific, 2016. 2.7, 3.3.1

[90] W. K. H. Panofsky, "The use of a long coaxial ion chamber along the accelerator," 1963. SLAC-TN-63-057. 2.4.1

[91] "SLAC renamed to SLAC Natl. Accelerator Laboratory." The Stanford Daily, Volume 234, Issue 20, 16 October 2008. `https://stanforddailyarchive.com/cgi-bin/stanford?a=d&d=stanford20081016-01.2.7`, Accessed: 31-05-2018. 2.4.1

[92] L. Frölich, "Beam Loss Monitors." Invited talk, ERL instrumentation workshop, Cornell University, Ithaca, USA, June 2008. Available from: `http://www.larsfroehlich.de/download/ERL_instrumentation_ws_2008_BLMs.pdf` [accessed Mar 26, 2018]. 2.4.1, 2.4.2, 2.4.3

[93] D. R. Patterson, "Preliminary design of the beam loss monitor system for the Advanced Photon Source," *AIP Conf. Proc.*, vol. 281, pp. 194–203, 1992. 2.4.1

[94] D. Bailey and E. Wright, *Practical fiber optics.* Practical, Oxford: Newnes, 2003. 2.4.2

[95] P. Forck, *Lecture notes on beam instrumentation and diagnostics: Joint University Accelerator School, January - March 2010.* [S.l.]: [s.n.], 2010. 2.8, 2.4.3

[96] Bergoz Instrumentation, "Beam Loss Monitor." `http://www.bergoz.com/en/blm`. Accessed: 03-04-2018. 2.8

[97] J. I. Goldstein, *Scanning electron microscopy and X-ray microanalysis; 3rd ed.* Berlin: Springer, 2007. The book can be consulted by contacting: EN-STI: Czapski, Michal Adam. 2.4.3

[98] D. Kramer, B. Dehning, and M. Sulc, *Design and Implementation of a Detector for High Flux Mixed Radiation Fields*. PhD thesis, 2008. Presented on 01 Sep 2008. 2.4.3, 2.9

[99] bib:Detec, "Scintillation materials." `https://en.wikipedia.org/wiki/Klein\T1\textendashNishina_formula`. Accessed: 11-04-2017. 2.10

[100] K. Wittenburg, "Specific instrumentation and diagnostics for high-intensity hadron beams," p. 58 p, Mar 2013. Comments: 58 pages, contribution to the CAS - CERN Accelerator School: Course on High Power Hadron Machines; 24 May - 2 Jun 2011, Bilbao, Spain. 2.4.4

[101] G. Keiser, *Optical fiber communications; 4th ed.* Boston, MA: McGraw-Hill, 2008. International edition. 3.1.1, 3.2.1, 3.2.1

[102] A. Boudrioua, *Photonic waveguides: theory and applications*. London: ISTE, 2009. 3.1.1

[103] J. V. Jelley, *Cherenkov radiation and its applications*. London: Pergamon, 1958. 3.1.2

[104] L. D. Landau, E. M. Lifshitz, and L. P. Pitaevskii, *Electrodynamics of continuous media; 2nd ed.* Course of theoretical physics, Oxford: Butterworth, 1984. 3.1.2

[105] J. W. van Hoorne, C. F. Fabjan, and E. B. Holzer, "Cherenkov Fibers for Beam Loss Monitoring at the CLIC Two Beam Module," May 2012. Presented 28 Jun 2012. 3.1.2, 3.2.1, 3.2.2, 3.3.1, 3.3.1, 3.3.1, 3.3.2, 3.3.2, 3.16, 3.4.1, 3.4.1, 3.4.2, 4.1, 4.3.1

[106] J. M. Senior, *Optical fiber communications: principles and practice*. Prentice-Hall Internat. Ser. in Optoelec., Englewood Cliffs, NJ: Prentice-Hall, 1985. 3.2.1, 3.2.1, 3.2.2

[107] J. D. Jackson, *Classical electrodynamics; 3rd ed.* New York, NY: Wiley, 1999. 3.2.1

[108] D. Marcuse, *Theory of dielectric optical waveguides; 2nd ed.* Quant. Electron, New York, NY: Academic Press, 1991. 3.2.1

[109] G. Keiser, F. Xiong, Y. Cui, and P. P. Shum, "Review of diverse optical fibers used in biomedical research and clinical practice," *Journal of Biomedical Optics*, vol. 19, no. 8, p. 080902, 2014. 3.6

[110] L. Kissel and R. H. Pratt, "Rayleigh scattering: elastic photon scattering by bound electrons," Tech. Rep. PITT-304, Pittsburgh Univ. Ist. Fís., Pittsburgh, PA, Sep 1983. 3.2.2

[111] C. F. Bohren and D. R. Huffman, *Absorption and scattering of light by small particles*. Wiley science series, New York, NY: Wiley, 1983. Reprint by Wiley in 2004. 3.2.2

[112] K. Tsujikawa, K. Tajima, and M. Ohashi, "Rayleigh scattering reduction method for silica-based optical fiber," *Journal of Lightwave Technology*, vol. 18, pp. 1528–1532, Nov 2000. 3.2.2

[113] R. Hui and M. O'Sullivan, *Fiber Optic Measurement Techniques*. Burlington, MA: Elsevier Academic Press, 2009. 3.2.2, 3.2.2

[114] H. R. J. and E. A. Lacy, *Fiber Optics*. New Jersey: Prentice Hall PTR, 1993. 3.2.2

[115] J. Kuhnhenn, "Fiber irradiation test at fraunhofer institute," 2012. not published. 3.8

[116] J. Kuhnhenn, "Fibre optic sensors at accelerators - considerations and pitfalls." Presentation, 7th DITANET Topical Workshop on Beam Loss Monitoring, DESY, Hamburg, Germany. Available from: `https://indico.cern.ch/event/154172/contributions/1399500/attachments/163433/230548/Kuhnhenn_DITANET_2011.pdf` [accessed June 13, 2017], December 2011. 3.8

[117] J. P. Merlo, I. Dumanoglu, N. Akchurin, U. Akgun, S. Ayan, P. Brücken, E. Eskut, A. Fenyvesi, A. Kayis-Topaksu, N. Koca, K. Makónyi, D. Novák, Y. M. Önel, G. Onengüt, and A. Polatoz, "Radiation-hardness studies of high OH**- content quartz fibres irradiated with 500 MeV electrons," *Nucl. Instrum. Methods Phys. Res., A*, vol. 490, no. 3, pp. 444–455, 2002. 3.2.2

[118] V. Hagopian, "Radiation Damage of Quartz Fibers," Tech. Rep. CMS-CR-1999-002, CERN, Geneva, Jan 1999. 3.2.2

[119] K. Cankocak, N. M. Bakirci, S. Cerci, E. Gülmez, J.-P. Merlo, Y. Onel, F. Ozok, I. Schmidt, and N. Sonmez, "Radiation-Hardness Measurements of High OH^{-} Content Quartz Fibres Irradiated with 24 GeV Protons up to 1.25 Grad," Tech. Rep. CMS-NOTE-2007-003, CERN, Geneva, Jan 2007. 3.2.2

[120] G. Mahout, M. Pearce, M. L. Andrieux, C. B. Arvidsson, D. G. Charlton, B. Dinkespiler, J. D. Dowell, L. Gallin-Martel, R. J. Homer, P. Jovanovic, I. R. Kenyon, G. Kuyt, J. M. Lundqvist, I. Mandic, O. Martin, H. R. Shaylor, R. Stroynowski, J. K. Troska, R. L. Wastie, A. R. Weidberg, J. A. Wilson, and J. Ye, "Irradiation studies of multimode optical fibres for use in ATLAS front-end links," *Nucl. Instrum. Methods Phys. Res., A*, vol. 446, no. 3, pp. 426–34, 2000. 3.2.2

[121] A. Abdesselam, P. Allport, R. Apsimon, C. Band, C. Barr, L. Batchelor, R. Bates, P. Bell, J. Bernabeu, J. Bizzell, R. Brenner, T. Brodbeck, P. Bruckman De Renstrom, C. Buttar, J. Carter, D. Charlton, A. Cheplakov, A. Chilingarov, M.-L. Chu, A.-P. Colijn, I. Dawson, B. Demirkõz, P. de Jong, P. Dervan, Z. Dolezal, J. Dowell, P. Escobar, E. Spencer, T. J. C. Ekelöf, L. Eklund, D. Ferrere, T. Fraser, M. French, R. French, J. Fuster, B. Gallop, C. García, M. Goodrick, A. Greenall, A. Grillo, J. Grosse-Knetter, F. Hartjes, N. Hessey, J. C. Hill, J. Homer, L. Hou, G. Hughes, Y. Ikegami, C. Issever, J. Jackson, M. Jones, T. J. Jones, P. Jovanovic, E. Koffeman, P. Kodys, T. Kohriki, S.-C. Lee, C. Lester, M. Limper, S. W. Lindsay, M. Lozano, C. Macwaters, C. Magrath, G. Mahout, I. Mandic, J. Matheson, T. McMahon, B. Mikulec, A. Muijs, M. Morrissey, A. Nichols, R. Nickerson, V. O'Shea, S. Pagenis, M. Parker, J. Pater, E. Perrin, H. Pernegger, S. Peeters, P. Phillips, M. Postranecky, D. Robinson, A. Robson, A. Rudge, H. Sandaker, K. Sedlak, N. A. Smith, S. Stapnes, B. Stugu, P. K. Teng, S. Terada, A. Tricoli, M. Tyndel, N. Ujiie, M. Ullán, Y. Unno, E. van der Kraaij, I. Van Vulpen, G. Viehhauser, J. H. Vossebeld, M. Warren, R. Wastie, A. Weidberg, P. Wells,

D. White, and J. Wilson, "The Optical Links of the ATLAS SemiConductor Tracker," Tech. Rep. ATL-INDET-PUB-2007-013. ATL-COM-INDET-2007-016, CERN, Geneva, Aug 2007. Paper published 2007 JINST 2 P0903 Submitted as an ATLAS note for completeness and ease of reference. 3.2.2

[122] T. Yoshizawa, *Handbook of optical metrology: principles and applications; 2nd ed.* Boca Raton, FL: CRC Press, 2015. 3.3, 3.3.1, 3.3.1

[123] C. DeCusatis and C. J. S. DeCusatis, *Fiber Optic Essentials.* Burlington, MA: Elsevier, 2005. 3.3

[124] S. Awadalla, *Solid-state radiation detectors: technology and applications.* Devices, circuits, and systems, Boca Raton, FL: CRC Press, Apr 2015. 3.3, 3.3.1, 3.3.1, 3.3.1

[125] Hamamatsu Photonics K.K., "Hamamatsu guide to detector selection." `http://www.hamamatsu.com/jp/en/community/optical_sensors/articles/guide_to_detector_selection/index.html`. Accessed: 30-05-2017. 3.9, 3.11

[126] M. Teshima, B. Dolgoshein, R. Mirzoyan, J. Nincovic, and E. Popova, "SiPM Development for Astroparticle Physics Applications," in *30th International Cosmic Ray Conference in Merida*, no. arXiv:0709.1808, Sep 2007. 3.9

[127] Hamamatsu Photonics K.K., "Si APD (Avalanche Photodiode)." `https://www.hamamatsu.com/resources/pdf/ssd/si_apd_kapd0001e.pdf`. Data Sheet from Hamamatsu Photonics. 3.3.1

[128] S. K. Saha, *High resolution imaging: detectors and applications.* Singapore: Pan Stanford Publ., 2015. 3.3.1

[129] P. Buzhan *et al.*, "An advanced study of silicon photomultiplier," *ICFA Instrum. Bull.*, vol. 23, pp. 28–41, 2001. 3.3.1

[130] Slawomir Piatek, Hamamatsu Photonics K.K., "A technical guide to silicon photomultipliers (sipm)." `https://www.hamamatsu.com/us/en/community/optical_sensors/articles/technical_guide_to_silicon_photomultipliers_sipm/index.html`. Accessed: 10-04-2018. 3.3.1

[131] Hamamatsu Photonics K.K., "What is mppc." `https://www.hamamatsu.com/us/en/community/mppc/4392.html`. Accessed: 19-06-2017. 3.10

[132] C. Xu, R. Klanner, E. Garutti, and W.-L. Hellweg, "Influence of X-ray Irradiation on the Properties of the Hamamatsu Silicon Photomultiplier S10362-11-050C," *Nucl. Instrum. Meth.*, vol. A762, pp. 149–161, 2014. 3.10

[133] K. Kotera, W. Choi, and T. Takeshita, "Describing the response of saturated SiPMs," *ArXiv e-prints*, 2015. 3.11

[134] "Sense, ultimate low light-level sensor development." https://www.sense-pro.org/lll-sensors/pmt. Accessed: 02-06-2017. 3.12

[135] Hamamatsu Photonics K.K., "Glass processing technology." http://www.hamamatsu.com/eu/en/technology/innovation/glass/index.html. Accessed: 02-06-2017. 3.12

[136] J. M. Moore, C. C. Davis, and M. A. Coplan, *Building scientific apparatus; 4th ed.* Cambridge: Cambridge Univ. Press, 2009. 3.3.2, 3.3.2, 3.3.2

[137] N. Menn, *Practical optics.* Amsterdam: Elsevier, 2004. 3.3.2

[138] Hamamatsu Photonics K.K., "Photomultiplier tubes and assemblies for scintillation counting and high energy physics." http://www.hamamatsu.com/resources/pdf/etd/High_energy_PMT_TPMZ0003E.pdf, 2017. Accessed: 04-06-2017. 3.3.2

[139] Hamamatsu Photonics K.K., "Wide Dynamic Range Photomultiplier Tube Unit." https://www.hamamatsu.com/resources/pdf/etd/H13126_C12918_TPMO1068E.pdf, 2015. Data Sheet from Hamamatsu Photonics. 3.3.2

[140] P. Gorodetzky, D. Lazic, G. Anzivino, E. Chiavassa, A. Contin, G. Dellacasa, N. De Marco, R. DeSalvo, M. Gallio, P. Guaita, K. F. Johnson, P. Juillot, M. Lundin, M. Marino, A. Musso, A. Piccotti, E. Scomparin, and E. Vercellin, "Quartz fiber calorimetry," *Nucl. Instrum. Methods Phys. Res., A*, vol. 361, pp. 161–179. 51 p, Jul 1995. 3.4.1

[141] S. H. Law, S. C. Fleming, N. Suchowerska, and D. R. McKenzie, "Optical fiber design and the trapping of Cerenkov radiation," *Appl. Opt.*, vol. 45(36), p. 9151–9159, December 2006. 3.4.1

[142] E. Nebot del Busto, E. Branger, E. B. Holzer, M. Kastriotou, S. Mallows, and C. P. Welsch, "Blm investigations at ctf3." CLIC/CTF3 experimental verification meeting, CERN, Geneva, Switzerland. Available from: https://indico.cern.ch/event/316306/contributions/731324/attachments/607412/835855/ENebot_CTF3_ExpVerification_29_04_2014.pdf [accessed Jun 20, 2017], April 2014. 3.17

[143] F. S. Domingues Sousa. Private Communication of Schematic design, June 2014. 3.19

[144] I. Chaikovska, L. Burmistrov, N. Delerue, and A. Variola, "Optical fiber beam loss monitor for the PHIL and ThomX facilities." 5th International Particle Accelerator Conference IPAC'14, June 2014. 4.1

[145] Agilent Technologies, "Agilent U1071A, Acqiris DP1400 High-Speed PCI Digitizer." http://literature.cdn.keysight.com/litweb/pdf/5989-7100EN.pdf?id=1291180,www.agilent.com. Data Sheet from Agilent Technologies. 4.2

[146] Agilent Technologies, "Agilent U1065A, Acqiris High-Speed cPCI Digitizers." http://literature.cdn.keysight.com/litweb/pdf/5989-7443EN.pdf?id=1306645,www.agilent.com. Data Sheet from Agilent Technologies. 4.2

[147] Struck Innovative Systeme. http://www.struck.de,www.struck.de/sis3320.htm. 4.2, 4.2.2

[148] E. van Garderen, M. ten Have, G. LeBlanc, A. Starritt, and K. Zingre, "Upgrade of the timing system at the Australian Synchrotron," in *Proceedings, 9th European Workshop on Beam Diagnostics and Instrumentation for Particle Accelerators (DIPAC 09): Basel, Switzerland, May 25-27, 2009*, p. TUPD27, May 2009. 5.2.1

[149] Hamamatsu Photonics K.K., "Photosensor Modules H10720/H10721 Series." www.hamamatsu.com/resources/pdf/etd/H10720_H10721_TPMO1062E.pdf. Data Sheet from Hamamatsu Photonics. 5.2.2

[150] Texas Instruments Incorporated, "THS3061, Low-Distortion, High Slew Rate, Current-Feedback Amplifiers." http://www.ti.com/lit/ds/symlink/ths3061.pdf. Data Sheet from Texas Instruments. 5.2.2, 6.3.1

[151] M. J. Boland. Private Communication, March 2017. 5.2.2

[152] Struck Innovative Systeme. http://www.struck.de,www.struck.de/sis3300firm.htm. 5.3.1

[153] T. Lefevre. Private Communication, May 2016. 5.3.2

[154] D. Gamba. Private Communication, January 2017. 5.3.3, 5.3.3

[155] B. Sowerby, "Cerenkov detectors for low-energy gamma rays," *Nuclear Instruments and Methods*, vol. 97, no. 1, pp. 145 – 149, 1971. 6.2

[156] V. Vlachoudis, "Flair: A powerful but user friendly graphical interface for fluka," in *International Conference on Mathematics, Computational Methods and Reactor Physics (M&C 2009), Saratoga Springs, New York, USA, May 3-7 2009*, 2009. 6.2.1

[157] Thorlabs, "0.22 NA Hard Polymer Buffer, Silica/Silica Multimode Fiber." https://www.thorlabs.com/drawings/28348c2722f1aa55-EE373FD4-F403-0C00-EE2817F649C436D9/BFH22-910-SpecSheet.pdf. Spec Sheet from Thorlabs. 6.3.1, 6.5.4

[158] National Instruments, "NI 5761R User Guide and Specifications." http://www.ni.com/pdf/manuals/375509a.pdf. Data Sheet from National Instruments. 6.3.1

[159] J. L. Navarro Quirante *et al.*, "Effect of Beam-Loading on the Breakdown Rate of High Gradient Accelerating Structures," in *Proceedings, 27th Linear Accelerator Conference, LINAC2014: Geneva, Switzerland, August 31-September 5, 2014*, p. TUPP033, 2014. 6.3.1

[160] W. Wuensch *et al.*, "Experience Operating an X-band High-Power Test Stand at CERN," in *Proceedings, 5th International Particle Accelerator Conference (IPAC 2014): Dresden, Germany, June 15-20, 2014*, p. WEPME016, 2014. 6.3.1

[161] R. Brun and F. Rademakers, "ROOT: An object oriented data analysis framework," *Nucl. Instrum. Meth.*, vol. A389, pp. 81–86, 1997. 6.3.1

[162] W. Wuensch, "High-Gradient Breakdown in Normal-Conducting RF Cavities," Jun 2002. 6.3.2, 6.4

[163] R. Sandstrom, D. Huang, and J. Norem, "Study of Radiation From RF Cavities," p. 3 p, 2008. 6.3.2

[164] V. Dolgashev. Private Communication, January 2016. 6.4

[165] W. Wuensch and I. Syratchev. Private Communication, November 2015. 6.5.1

[166] B. Woolley, P. K. Ambattu, R. Apsimon, G. Burt, A. Dexter, A. Grudiev, I. Syratchev, R. Wegner, and W. Wuensch, "High Gradient Testing of an X-band Crab Cavity at XBox2," in *Proceedings, 6th International Particle Accelerator Conference (IPAC 2015): Richmond, Virginia, USA, May 3-8, 2015*, p. WEPHA057, 2015. 6.5.2

[167] J. W. Wang, G. A. Loew, R. J. Loewen, R. D. Ruth, A. E. Vlieks, I. H. Wilson, and W. Wuensch, "SLAC/CERN high gradient tests on an X-band accelerating section," May 1995. 6.5.3

[168] N. Catalan Lasheras, A. Grudiev, G. McMonagle, I. Syrachev, B. Woolley, W. Wuensch, H. Zha, G. Bowden, V. Dolgashev, A. Haase, T. Argyropoulos, J. Giner Navarro, D. Pereira, R. Rajamäki, X. Stragier, P. J. Giansiracusa, T. G. Lucas, and M. Volpi, "Fabrication and high-gradient testing of an accelerating structure made from milled halves," in *Proceedings of LINAC16, East Lansing, MI, USA*, pp. THPLR003, 845–847, September 2016. 6.5.3

[169] T. Argyropoulos. Private Communication, March 2016. 6.5.3

[170] H. Zha, V. Dolgashev, and A. Grudiev, "RF Design of the CLIC Structure Prototype Optimized for Manufacturing from Two Halves," no. CERN-ACC-2015-266, p. TUPTY054. 3 p, 2015. 6.5.3

[171] A. Grudiev, "RF Design and Parameters of 12 GHz T24_vg1.8_disk (or 12WNSDVG18, or CLIC_G undamped 12 GHz)." `https://edms.cern.ch/document/1068314/1`, 2008. CERN EDMS document, Accessed 12-01-2018. 6.5.3